NASA-CR-201085

The Aeroacoustics of Supersonic Jets

Final Report on NASA Grant NAG 1-1047

Philip J. Morris and Dennis K. McLaughlin
Department of Aerospace Engineering
The Pennsylvania State University

Feb. 1991 to June 1995

Contents

1 Introduction 2

2 Publications 3

3 Graduate Student Researchers 4

4 Appendix: Graduate Student Theses 5

Chapter 1

Introduction

This is the final report on NASA Grant No. NAG 1-1047 entitled, "The Aeroacoustics of Supersonic Jets." The Principal Investigators are Drs. Philip J. Morris and Dennis K. McLaughlin of the Department of Aerospace Engineering at the Pennsylvania State University.

The research project has been a joint experimental/computational study of noise in supersonic jets. The experiments have been performed in a low to moderate Reynolds number anechoic supersonic jet facility. Computations have focussed on the modeling of the effect of and external shroud on the generation and radiation of jet noise. A summary of the results of the research program are given best in the form of the Masters and Doctoral theses of students who obtained their degrees with the assistance of the research grant. A list of student names, their degrees, and the titles of their dissertations are also provided in this report. In addition, a list of presentations and publications made by the Principal Investigators and the research students is also included.

Chapter 2

Publications

Kinzie, K. W. and McLaughlin, D. K.,"An experimental study of noise radiated from supersonic elliptic jets," *AIAA Paper* 95-0511.

Kinzie, K. W. and McLaughlin, D. K.,"Noise radiated from asymmetric supersonic jets," *CEAS/AIAA Paper* 95-014.

Kinzie, K. W. and McLaughlin, D. K.,"An azimuthal modal decomposition measurement technique for elliptic jets," *AIAA Paper* 96-1669.

McLaughlin, D. K. and Kinzie, K. W.,"A review of large scale turbulent structures in supersonic jet flows," invited paper for presentation at the ASME Fluids Engineering Conference, San Diego, July 7-11, 1996.

Morris, P. J., Chung, C. and Pautet, L. R., "Acoustic scattering: a numerical simulation," 47th APS/Division of Fluid Dynamics Meeting, Atlanta, GA, November 1994.

Pautet, L. R. and Morris, P. J., "A numerical simulation of diffraction by a half-plane," submitted for publication in *J. Computational Acoustics*, May 1996.

Shieh, C.-W. and Morris, P. J., "Analysis of instability waves in non-circular supersonic jets with a finite element method," 47th APS/Division of Fluid Dynamics Meeting, Atlanta, GA, November 1994.

Shieh, C.-W. and Morris, P. J., "Instability wave analysis of confined supersonic jets using the finite element method," accepted for publication in *J. Sound and Vibration*, May 1996.

Chapter 3

Graduate Student Researchers

Kevin W. Kinzie, "Aeroacoustic properties of moderate Reynolds number elliptic and rectangular supersonic jets," **Ph. D.** thesis, Aerospace Engineering, 1995. Present Occupation: Research Engineer at General Electric Aircraft Engines, Cincinnati, OH.

Lucie R. Pautet, "Diffraction by a half-plane using the dispersion relation preserving scheme," **M. S.** thesis, Aerospace Engineering, 1994. Present Occupation: Ph. D. Candidate, Oceanography, University of California, San Diego, CA.

Ching-Wei Shieh, "Instability wave analysis of confined axisymmetric supersonic jets using the finite element method," **M. S.** thesis, Aerospace Engineering, 1995. Present Occupation: Ph. D. Candidate, Aerospace Engineering, Penn State University, PA.

Chapter 4

Appendix: Graduate Student Theses

The Pennsylvania State University

The Graduate School

Department of Aerospace Engineering

AEROACOUSTIC PROPERTIES OF MODERATE REYNOLDS NUMBER ELLIPTIC AND RECTANGULAR SUPERSONIC JETS

A Thesis in

Aerospace Engineering

by

Kevin W. Kinzie

Submitted in Partial Fulfillment
of the Requirements
for the Degree of

Doctor of Philosophy

August 1995

We approve the thesis of Kevin W. Kinzie.

Date of Signature

Dennis K. McLaughlin — June 17, 1995

Dennis K. McLaughlin
Professor of Aerospace Engineering
Head of the Department of Aerospace Engineering
Thesis Advisor
Chair of Committee

Cengiz Camci — 6/2/1995

Cengiz Camci
Associate Professor of Aerospace Engineering

Gerald C. Lauchle — 22 May 1995

Gerald C. Lauchle
Professor of Acoustics

Philip J. Morris — 6/2/1995

Philip J. Morris
Boeing Professor of Aerospace Engineering

ABSTRACT

The aerodynamic and acoustic properties of supersonic elliptic, rectangular, and circular jets are experimentally investigated. All three jets are perfectly expanded with an exit Mach number of approximately 1.5 and are operated in the Reynolds number range of 25,000 to 50,000. The reduced Reynolds number facilitates the use of conventional hot-wire anemometry and a glow discharge excitation technique which preferentially excites the varicose or flapping modes in the jets. In order to simulate the high velocity and low density effects of heated jets, helium is mixed with the air jets. This allows the large-scale structures in the jet shear layer to achieve high enough convective velocity to radiate noise through the Mach wave emission process.

Experiments in the present work focus on comparisons between the cold and simulated heated jet conditions and on the beneficial aeroacoustic properties of non-circular jets. Comparisons are also made between the elliptic and rectangular jets. When helium is added to the jets, the instability wave phase velocity is found to approach or exceed the ambient sound speed. The radiated noise is also louder and directed at a higher angle from the jet axis. In addition, near field hot-wire spectra are found to match the far-field acoustic spectra only for the helium/air mixture case. These results demonstrate that there are significant differences between unheated and heated asymmetric jets in the Mach 1.5 speed range, many of which have been found previously for circular jets. The asymmetric jets were also found to radiate less noise than the round jet at comparable operating conditions. Strong similarities were also

found between the aerodynamic and acoustic properties of the elliptic and rectangular jets.

TABLE OF CONTENTS

LIST OF FIGURES ix

LIST OF TABLES xiv

NOMENCLATURE xv

ACKNOWLEDGEMENTS xix

CHAPTER 1 INTRODUCTION 1

1.1 Overview 1

1.2 Heated Jet Research 5

1.3 Research Objectives 7

1.4 Technical Approach 11

1.5 Thesis Summary 13

CHAPTER 2 EXPERIMENTAL APPARATUS 15

2.1 High Pressure Air Supply 15

2.2 Anechoic Chamber 18

2.3 Vacuum Recovery System 20

2.4 Supersonic Nozzles 21

2.4.1 Elliptic Nozzle 23

2.4.2 Rectangular Nozzle 24

2.4.3 Circular Nozzle 24

2.5 Glow Discharge Excitation System 25

CHAPTER 3 EXPERIMENTAL PROCEDURE 29

3.1 Digital Signal Acquisition 29

3.1.1 Trans-Era System 30

3.1.2 DAS-58 Board 31

3.2 Pressure Measurements 32

3.2.1 Mean Flow Pressure 32

3.2.2 Fluctuating Acoustic Pressure 33

3.3 Hot-Wire Anemometry 33

3.4 Heated Jet Simulation 35

3.4.1 Properties of Gas Mixture 39

3.4.2 Jet Mixture Concentration 43

3.4.3 Helium Concentration in Test Chamber 48

3.4.4 Calculation of Helium Jet Plume Velocity 52

3.4.5 Helium/Air Mixture Hot-Wire Calibration 56

CHAPTER 4 MEAN FLOWFIELD MEASUREMENTS 61

4.1 Helium/Air Jet Mixtures 62

4.1.1 Centerline Mach Number and Velocity Distribution -- Helium Jets 63

4.1.2 Circular Jet Velocity Profiles 65

4.2 Pure Air Jets 69

4.2.1 Centerline Mach Number and Velocity Distribution -- Pure Air Jets 69

4.2.2 Asymmetric Jet Velocity Profiles 72

4.2.3 Vorticity Thickness and Normalized Velocity Profiles . . . 78

4.2.4 Velocity Contour Measurements 87

CHAPTER 5 FLUCTUATING FLOWFIELD MEASUREMENTS 91

5.1 Hot-Wire Fluctuation Amplitudes 91

5.2 Instability Mode Growth Rates 102

5.3 Axial Phase Speed Measurements 104

5.4 Radial Hot-Wire Measurements 114

CHAPTER 6 ACOUSTIC MEASUREMENTS 125

6.1 Sound Pressure Level Directivity 125

6.2 Far-Field Acoustic Spectra 129

6.2.1 Bandpassed Acoustic Spectra 142

6.3 SPL Contours 147

6.4 Modal Decomposition 149

CHAPTER 7 CONCLUSIONS AND FUTURE WORK 165

7.1 Summary of Results 165

7.1.1 Focus on Asymmetric Jets 165

7.1.2 Focus on Helium Simulation 168

7.2 Concluding Remarks 169

7.2.1 Future Work 170

REFERENCES 173

APPENDIX A MODAL DECOMPOSITION THEORY AND CODE 178

APPENDIX B SPECTRAL ANALYSIS CODE 190

APPENDIX C VORTEX MODEL CODE 197

LIST OF FIGURES

Figure 2.1 Schematic of Penn State jet noise and shear layer facilities. 16

Figure 2.2 Diagram of jet noise anechoic chamber. 20

Figure 2.3 Sketches of nozzle exits. 22

Figure 2.4 Measurement coordinate system and nomenclature 23

Figure 2.5 Schematic of the glow discharge system. 27

Figure 2.6 Electrode placement around nozzles. 26

Figure 3.1 Molar concentration of helium in gas mixture as a function of helium mass concentration. 42

Figure 3.2 Gas mixture molecular weight as a function of helium mass concentration. 42

Figure 3.3 Ratio of specific heats (γ) for gas mixture as a function of helium mass concentration. 44

Figure 3.4 Gas constant (R) for gas mixture as a function of helium mass concentration. 44

Figure 3.5 Schematic of upstream supply lines and critical choke points needed to set helium concentration of the jet flow. 46

Figure 3.6 Fliegner's constant (F) as a function of helium mass concentration. . 48

Figure 3.7 Measured helium concentration (by mass) in the chamber as a function of the jet helium concentration. 52

Figure 3.8 Hot-wire calibration for varying helium concentrations (by mass). . . 57

Figure 3.9 Ratio of air jet anemometer output to helium jet anemometer output as a function of axial location. 60

Figure 4.1 Pitot probes used to measure mean jet velocity. 63

Figure 4.2 Helium and air centerline Mach number and velocity distributions for the elliptic jet. 64

Figure 4.3 Dimensional and nondimensional velocity profiles for air and helium axisymmetric jet. 66

Figure 4.4 Centerline Mach number and velocity distributions for pure air jets, $T_j/T_a = 0.69$. 71

Figure 4.5 Velocity profiles for pure air elliptic jet, $T_j/T_a = 0.69$ 74

Figure 4.6 Velocity profiles for pure air rectangular jet, $T_j/T_a = 0.69$ 76

Figure 4.7 Vorticity thickness distribution for pure air jets, $T_j/T_a = 0.69$. 80

Figure 4.8 Graphical definition of vorticity thickness, δ_ω , and 0.99 velocity thickness, δ. 80

Figure 4.9 Normalized velocity profiles of the pure air elliptic jet, $T_j/T_a = 0.69$. 82

Figure 4.10 Normalized velocity profiles of the pure air rectangular jet, $T_j/T_a = 0.69$. 83

Figure 4.11 Thickness parameters used to normalize the jet velocity profiles of figures 4.9 and 4.10, $T_j/T_a = 0.69$. 84

Figure 4.12 Half-velocity points of the pure air elliptic jet for Reynolds numbers of 27,000 and 50,000, $T_j/T_a = 0.69$. 86

Figure 4.13 Vorticity thickness of the pure air elliptic jet for Reynolds numbers of 27,000 and 50,000, $T_j/T_a = 0.69$. 86

Figure 4.14 Velocity contours from pure air elliptic and rectangular jets, $T_j/T_a = 0.69$. 88

Figure 5.1 Hot-wire spectra measured in pure air elliptic jet, $T_j/T_a = 0.69$. 93

Figure 5.2 Hot-wire spectra measured in pure air elliptic jet, $T_j/T_a^* = 1.2$. 94

Figure 5.3 Hot-wire spectra measured in pure air rectangular jet, $T_j/T_a = 0.69$. 96

Figure 5.4 Hot-wire spectra measured in pure air rectangular jet, $T_j/T_a^* = 1.2$. 98

Figure 5.5 Overall mass-velocity fluctuation levels in natural elliptic jet as a function of axial distance from nozzle 100

Figure 5.6 Overall mass-velocity fluctuation levels in natural rectangular jet as a function of axial distance from nozzle. 101

Figure 5.7 Fluctuation amplitudes in elliptic jet excited at St = 0.4 showing the growth rate of individual modes. 103

Figure 5.8 Axial phase distribution for elliptic jet excited at St = 0.4. 105

Figure 5.9 Axial phase distribution for elliptic jet excited at St = 0.2. 108

Figure 5.10 Phase speed as a function of Strouhal number in artificially excited elliptic jet (downstream of potential core). 111

Figure 5.11 Phase speed as a function of Strouhal number in artificially excited rectangular jet (downstream of potential core) 113

Figure 5.12 Phase distribution across elliptic jet shear layer at x/Deq = 1.8, flapping excitation. 116

Figure 5.13 Phase distribution across elliptic jet shear layer at x/Deq = 3.5, flapping excitation. 119

Figure 5.14 Schematic of vortex model. 120

Figure 5.15 Predicted phase and r.m.s distribution across the vortex row. 122

Figure 6.1 SPL directivity arcs for pure air jets, $R/D_{eq} = 25$, $T_j/T_a = 0.69$. . . . 126

Figure 6.2 SPL directivity arcs for helium jets, $R/D_{eq} = 25$, $T_j/T_a^* = 1.2$. 128

Figure 6.3 Far-field microphone spectra from pure air elliptic jet, $R/D_{eq} = 25$, $T_j/T_a = 0.69$. 130

Figure 6.4 Far-field microphone spectra from helium elliptic jet, R/Deq = 25, $T_j/T_a^* = 1.2$. 132

Figure 6.5 Far-field microphone spectra from pure air rectangular jet, R/Deq = 25, $T_j/T_a = 0.69$. 135

Figure 6.6 Far-field microphone spectra from pure air rectangular jet showing the full range of screech tones, $R/D_{eq} = 25$, $T_j/T_a = 0.69$, $\beta = 25^o$. 136

Figure 6.7 Measured and predicted (Tam, 1988) screech frequencies of pure air rectangular jet, $T_j/T_a = 0.69$. 139

Figure 6.8 Far-field microphone spectra from helium rectangular jet, R/Deq = 25, $T_j/T_a^* = 1.2$. 141

Figure 6.9 Bandpassed SPL directivity arcs for elliptic air jet, $R/D_{eq} = 25$ 143

Figure 6.10 Narrow bandpassed SPL directivity for elliptic jet, St = 0.33 - 0.39, $R/D_{eq} = 25$. 146

Figure 6.11 SPL contours for pure air elliptic jet, $T_j/T_a = 0.69$. 148

Figure 6.12 SPL contours for helium elliptic jet, $T_j/T_a^* = 1.2$. 150

Figure 6.13 Microphone locations for modal decomposition measurements in ECC system. 152

Figure 6.14 Modal content of pure air elliptic jet excited at St = 0.4 by the varicose mode, $T_j/T_a = 0.69$. 154

Figure 6.15 Modal content of pure air elliptic jet excited at St = 0.4 by the flapping mode, $T_j/T_a = 0.69$. 155

Figure 6.16 Modal content of natural pure air elliptic jet, $T_j/T_a = 0.69$. 157

Figure 6.17 Modal content of natural helium elliptic jet, $T_j/T_a^* = 1.2$. 158

Figure 6.18 Modal content of natural pure air rectangular jet, full scale, $T_j/T_a = 0.69$. 161

Figure 6.19 Modal content of natural pure air rectangular jet, $T_j/T_a = 0.69$. 162

Figure 6.20 Modal content of natural helium rectangular jet, full scale, $T_j/T_a^* = 1.2$. 163

Figure 6.21 Modal content of natural helium rectangular jet, $T_j/T_a^* = 1.2$. 164

Figure A.1 Elliptic cylindrical coordinate system 180

Figure A.2 Azimuthal phase distribution of lowest order Mathieu function modes 181

LIST OF TABLES

Table 2.1 Nozzle dimensions 22

Table 3.1 Properties of Mach 1.5 jet for different gases exhausting into pure air 38

Table 3.2 Experimental conditions 51

Table 5.1 Instability wave properties for elliptic jet excited at St = 0.4 107

Table 5.2 Instability wave properties for elliptic jet excited at St = 0.4 109

NOMENCLATURE

a	speed of sound
A^*	area of flow choking location
A_c	hot-wire sensitivity to helium concentration
A_m	hot-wire sensitivity to mass-velocity value
A_T	hot-wire sensitivity to total temperature
A_t	nozzle throat area
A_y	amplitude of vortex oscillation
A_v	vortex strength coefficient
AR	aspect ratio, b_j/h_j
b_j	jet exit width
c	local helium concentration
C_p	specific heat at constant pressure
C_v	specific heat a constant volume
D_{eq}	area equivalent diameter
D_v	vortex diameter
D_{12}	coefficient of binary diffusion
e'	fluctuating hot-wire anemometer output
E	mean hot-wire anemometer output
ECC	elliptical cylindrical coordinate system

f	frequency
f_c	characteristic frequency, U_j/D_{eq}
F	Fleigner's constant
h_j	jet exit width
k_{nm}	wavenumber of shock cell system
k_T	coefficient of thermal conductivity
M	Mach number
M_i	mass of individual gas constituent
$\hat{M}$	molecular weight
$\dot{m}$	mass flow rate
m'	fluctuating mass-velocity normalized by the local mean value of mass-velocity, $(\rho u)'/(\overline{\rho u})$
P, p	pressure
q	Mathieu function parameter
R	gas constant, distance from nozzle exit or vortex center
SPL	sound pressure level, 20 log (P_{rms}/P_{ref})
St	Strouhal number, fD_{eq}/U_j
T	temperature
U, u	x-component of velocity
u	"radial" coordinate in ECC system
v	y-component of velocity
x	axial direction

y	radial or transverse direction
$y_{0.5}$	half velocity point
α	instability wavenumber
β	angle from jet axis
γ	ratio of specific heats
δ	0.99 velocity thickness
δ_ω	vorticity thickness
ζ	azimuthal pressure distribution
η_i	number of moles of constituent
λ	instability wavelength
μ	viscosity
ν	angular coordinate in ECC system, kinematic viscosity
ρ	density
$(\rho u)_*$	ordinate of hot-wire fluctuation power spectra, $\left\{\frac{(\rho u)'}{(\rho u)'_{max}}\right\}^2 \Big/ \mathrm{Hz}$
ϕ_i	mass fraction of constituent
χ_i	mole fraction of constituent
ω	radian frequency

<u>Subscripts</u>

air	air jet quantity
a	ambient property

ch	anechoic chamber property
cl	local centerline property
hel	helium/air mixture jet quantity
j	jet exit quantity
mix	helium/air mixture quantity
o	stagnation quantity
rms	root mean squared quantity
ref	reference quantity

<u>Superscripts</u>

*	simulated condition of helium/air mixture
'	fluctuating quantity

ACKNOWLEDGEMENTS

This work was sponsored by NASA Langley Research Center through Grant NAG-1-1047, monitored by Dr. J.M. Seiner. The author is grateful to NASA Langley and to Dr. Seiner for their continued support of this research. He also wishes to express his gratitude to his thesis advisor, Dr. Dennis McLaughlin, for patience, guidance, advice, and for a Penn State education that will serve him well the rest of his life. Thanks also go to Dr. Philip Morris who made this a more complete work by providing much technical assistance in the area of jet noise. Committee members Dr. Cengiz Camci and Dr. Gerald Lauchle also provided valuable suggestions throughout the course of this research.

In addition, special thanks go to fellow graduate student Mr. Steve Martens for his technical assistance and who was the author's friend and colleague throughout his time at Penn State. Thanks also go to Mr. Lee Tetu for many helpful discussions regarding the topic of aeroacoustics and also for many discussions of a less technical nature. Without reserve, the author also expresses his extreme gratitude towards his wife and son, Susan and Brian, and to his parents and the rest of his family for their unfailing love, patience, and support through a long educational process. Finally, the author wishes to acknowledge that the abilities required to complete this work have been given to him by Jesus Christ, creator of all things.

CHAPTER 1

INTRODUCTION

1.1 Overview

Since Lighthill (1952) first introduced his acoustic analogy, jet noise has been a topic of interest for many researchers. The idea that the sound radiated from aerodynamic flows can be modeled as a distribution of quadrupole sources has led to many different models and theories in order to predict the noise from jet flows. While Lighthill's original theory is valid only for low speed flow, other researchers have extended the theory into the supersonic regime. In particular, Ffowcs Williams (1953) showed how turbulence convected at high speeds can be a very strong source of noise in the far-field. He showed that the noise radiated from turbulence traveling at high speeds scales with the cube of the turbulence convection velocity. When this velocity exceeds the ambient sound speed, this noise generation mechanism becomes very efficient. Ffowcs Williams referred to this type of noise generation as Mach wave emission or Mach wave radiation.

It is now well known that the dynamics of large scale vortical structures play an important role in the development of free shear flows. McLaughlin and his students (1975, 1979, 1982) showed how the large scale structures in low-to-moderate Reynolds number supersonic jets were a direct source of noise. Their work, along with the work of Seiner et al. (1982), showed that, when scaled properly, the noise radiated from the lower Reynolds number supersonic axisymmetric jets is very similar in frequency

content and directivity to the high Reynolds number jets. Analytical work by Morris and Tam (1979) and Tam and Burton (1984) modeled the large scale structures in a supersonic axisymmetric jet as instability waves. By using quasi-linear stability methods, they predicted the noise radiated by the instability waves. Using this method, Tam and Burton (1984) showed good agreement when making direct comparisons of the predicted wave properties and radiated sound with the experimental measurements of Troutt and McLaughlin (1982). As may be inferred from the analysis of Ffowcs Williams (1953), when the convection velocity of these structures is supersonic, the noise radiated as they travel downstream dominates the sound field. All of this information indicates that an understanding of supersonic jet noise requires a firm understanding of the large scale turbulent structures in the jet.

With the interest in the design of a more viable generation of supersonic transport aircraft, the topic of supersonic jet noise has received renewed attention in recent years. Improved methods of jet noise suppression must be developed in order to reduce the noise radiated from the propulsion system to acceptable levels. One of the most promising methods of noise reduction is the use of jets with noncircular exit geometries.

Noncircular exit geometries have a distinct advantage over many other noise suppression devices in that they incur very little, if any, performance loss. This is particularly important when the application relates to military missions where there is little room for compromise in aircraft performance. The asymmetry in the noncircular jet flow promotes a more rapid mixing of the jet plume with the ambient air, which

leads to a faster deceleration of the flow compared to that of a circular jet. Since the noise from supersonic jets scales exponentially with velocity, it is advantageous to reduce the jet velocity as quickly as possible. In particular, if the region over which the large scale turbulent structures possess supersonic phase speeds can be shortened, there is the possibility for significant noise reduction due to the structures' efficient noise radiation at the higher convection speed. The disadvantage of noncircular jet geometries is that they result in a more complex flowfield than round jets. As a result, theoretical analysis and experimental measurements also become more complex and difficult.

Seiner et al. (1991, 1992) performed experiments with rectangular, elliptical, and circular supersonic jets. Their findings showed that the noncircular geometries were able to provide noise reduction over the circular case, particularly when the noise generation was dominated by Mach wave radiation. Kantola (1979) made measurements in heated subsonic jets and showed that the sound power from a rectangular jet was up to 3 dB less than that from a circular jet. Even in heated subsonic flows, the turbulent structures can achieve convective Mach numbers exceeding unity resulting in Mach wave radiation. There was also a definite "loud" and "quiet" plane measured by Seiner et al. (1991, 1992) in the elliptic jet and by Kantola in the rectangular jet. This phenomenon could be exploited by directing the "quiet" plane in the direction most sensitive to noise radiation.

Morris and Bhat (1992, 1993, 1995) have extended the stability analysis procedure for axisymmetric jets to predict the noise from elliptic jets. By using an

elliptic cylindrical coordinate system, they solved an "inner" flow solution from the compressible Rayleigh equation and matched it with an "outer" acoustic solution to solve both the near and far pressure fields. As will be mentioned throughout this thesis, comparisons of their work with the experiments reported here show good agreement.

Very little work has been done on the prediction of jet mixing noise from rectangular jets. While Tam (1988) and Morris et al. (1989) have developed methods for the prediction of the shock-cell structures and associated screech tone frequencies from rectangular jets, this is a different noise generation mechanism than Mach wave emission or typical jet mixing noise. Currently, there is research underway at Penn State to develop a large eddy simulation CFD code to predict the flow and acoustic fields of a rectangular jet. Work is also being performed on a 2D finite element method to predict the instability waves or large scale structures in a confined rectangular jet flow. However, neither research project is complete.

Clearly, the progress of elliptic jet noise prediction is much further along than that of rectangular jet noise. This would be of little consequence except for the fact that the manufacture of an elliptic jet for use on aircraft has some serious practical difficulties. Both circular and rectangular jets, now in current use, employ some type of nozzle exit area alteration at some point during flight. This is especially true for rectangular jets with thrust vectoring. Such devices are extremely difficult to design into an elliptic nozzle. Therefore, while the noise resulting from the elliptic geometry can be predicted, the geometry is not implemented easily in practical situations. The opposite is true for the rectangular geometry.

However, even though there are some fundamental differences between the elliptic jet flow and the rectangular jet flow, it is not unreasonable to assume that there must be some important similarities as well. After the flow exits the nozzle of a rectangular jet, it will develop into a flow that is more elliptical in nature than circular, at least close to the jet exit. The question arises as to how the two flows differ. The rectangular jet will most likely have secondary flow induced by the corners and some shock associated noise; however it is unclear how much fundamental difference there is between rectangular and elliptic jets. When one considers the status of the prediction methods for the two geometries, this could be an important question that may aid in the development of rectangular jet noise prediction schemes.

1.2 Heated Jet Research

One problem of performing experiments with unheated jets is that even at low supersonic Mach numbers, the large scale turbulent structures may not achieve a supersonic phase speed. Morrison and McLaughlin (1979) measured the phase speed of the dominant jet Strouhal number component to be only about three-quarters of the ambient sound speed for a cold Mach 1.5 circular jet. This would mean that the radiated noise would not contain the Mach wave emission; however when a Mach 1.5 jet is heated the jet velocity, as well as the structure convection velocity, increase significantly. In most practical applications, such as turbojet engine exhausts, the jet static temperature is well above the ambient temperature.

There are relatively few experimental investigations of heated supersonic jet noise. Tanna et al. (1975) performed experiments which attempted to isolate the effect of temperature changes on jet noise (while holding the jet velocity constant). They found that at low jet efflux velocities, increasing temperature increased the radiated noise, particularly at the lower frequencies. However, at high jet velocities, increasing the temperature reduced the radiated noise over all frequencies. This was attributed to two noise sources in the jets. One is the standard turbulent mixing noise source. The second noise source is caused by density or temperature fluctuations. The latter source dominates the noise at low velocities and high temperatures while the former dominates at higher velocities. Each source has a different dependency on temperature and velocity which explains the different behavior at low and high jet velocities.

Lau (1981) has investigated the effects of Mach number and temperature on the mean flow and turbulence characteristics in round jets. He reported that the effect of heating at supersonic Mach numbers is to initially decrease the spreading rate of the jet shear layer, but to increase the spread rate as the jet temperature is increased further. He did not propose a reason for this curious phenomenon. He also measured that the potential core of the jet contracts somewhat as the jet is heated.

More recently, Seiner et al. (1992) measured the effects of temperature on supersonic jet noise emission. They found that as the jet was heated, the spectral characteristics and directivity of the radiated noise was consistent with the theory of Mach wave emission. They also observed a decrease in the growth rate of the jet shear layer with increasing temperature accompanied by a decrease in the potential core

length. Tam and Chen (1994) extended the analysis of Tam and Burton (1984) to include a stochastic model of the instability waves to predict the turbulent jet mixing noise of Seiner et al. (1992). The calculated directivities showed good agreement with the measurements.

All of this research points to the conclusion that there are significant differences in how heated moderate supersonic jets generate noise from their unheated counterparts. Therefore, in order to study jets under realistic engine operating conditions, they should be heated so that the convection velocity of the structures is supersonic and the effects of Mach wave radiation can be measured. Because the jet noise facility at Penn State is not equipped to operate heated jets, the low density and high velocity of hot jets are simulated by using a lower density gas with different properties than air; namely helium. This allows the jet properties to be compared as the operating conditions change from cold to simulated hot conditions and to observe the effects of jet heating directly. The helium simulation will be described in more detail later.

1.3 Research Objectives

There are three major objectives of the present work. They are as follows.

1) Investigate the aeroacoustics properties of an elliptic and a rectangular Mach 1.5 near-perfectly expanded supersonic jet.

2) Evaluate the use of helium/air mixture jets to simulate heated jets in aeroacoustic studies.

3) Establish an experimental data base of acoustic and flow fluctuation measurements most relevant to the dominant noise generation processes for use in current and future computational and analytical prediction methods of noncircular supersonic jets.

The first objective is the driving force behind this work. As explained earlier, noncircular jets possess beneficial properties with regard to increased mixing and reduced noise emission. The experiments focus on relatively low aspect ratio (AR = 3) elliptic and rectangular jets and their aerodynamic and acoustic properties. Experiments have been conducted in a low-to-moderate Reynolds number environment in order to focus attention on the large scale instabilities in the asymmetric jet shear layers, similar to the experiments of McLaughlin and his students (1975, 1979, 1982) with round jets. Their experiments were instrumental in establishing the noise generation characteristics of large scale structures in supersonic jets and in evaluating the stability analysis of Tam and Burton (1984). It is hoped that a similar contribution can be made in the area of noncircular supersonic jets.

This investigation has potential payoffs in several different areas. One is that it will provide additional information regarding the fundamental flow development and acoustics of these two different jet flows. While there have been studies on each of these geometries independently, there are no basic studies focused on a comparison of these flows. This information would be helpful in exploiting the advantages of noncircular jet geometry in noise suppression. Since a rectangular jet will undoubtedly transition through an elliptical region before becoming axisymmetric far downstream,

a knowledge of the elliptic jet flow may be beneficial in understanding the rectangular jet flow.

Also, information gained during this research may be able to guide the direction of rectangular jet noise predictions. Elliptic jet noise prediction is quickly becoming an available technology and it would be helpful to know how much of this methodology could be applied to rectangular jet noise prediction schemes. Since there is some commonality in the two flows, the development of rectangular jet noise prediction methods may be accelerated by incorporating appropriate elements of elliptic jet noise predictions. Determining the appropriate elements will be a priority of this research.

The second objective of the present work is to evaluate the use of helium/air jet mixtures in aeroacoustic studies to simulate actual heated jets. As mentioned earlier, by mixing helium with the jet air flow, it is possible to produce supersonic jets with similar acoustic velocity and density ratios with respect to ambient conditions as actual heated jets. It is thus reasonable to assume that the helium simulation would produce noise in a manner similar to the actual heated jets, at least as far as the Mach wave mechanism is concerned. Experimental data from the present work and of other researchers show that heated jets can have significantly different acoustic properties than their unheated jet counterparts. Since aircraft engine exhaust flows are heated to very high temperatures, it is important to account for these effects when investigating the noise production from these jets.

Several other researchers at Penn State have worked on the use of helium to simulate heated jet flows (Barron, 1993; McLaughlin et al., 1991). However their work

focused primarily on the initial development of the helium simulation analysis and did not include a rigorous comparison of the pure air and helium/air mixture jet flows. This work picks up where they left off in regards to the evaluation of the helium simulation. It is important to determine if the helium simulation affects the jet aerodynamics and acoustics in the same manner that actual heating affects a supersonic jet. By testing the jets for both pure air and helium/air mixture flows, it is possible to determine if the helium changes characteristics such as jet spreading rate, hydrodynamic and acoustic pressure fluctuation spectral content, sound pressure level directivity, and modal content, in the same way that heating the jet would. If it can be shown that the helium simulation produces results similar to heated supersonic jets, it will provide a relatively easy and low cost method in which small scale jet noise experiments can be performed which have a direct bearing on heated jet noise measurements without the trouble and expense of operating a fully heated jet facility. While the helium simulation could never take the place of heated jet experiments, they could be used for preliminary investigations and as a diagnostic tool to aid conventional heated jet experiments.

Finally, the third objective of this work is to provide a data base for the evaluation of and input to analytical and computational methods. As mentioned earlier Morris and Bhat (1992, 1993, 1995) have already developed an instability wave method to predict the noise from elliptic supersonic jets. Their code requires the mean flow as an input to the calculations. They predict quantities such as individual mode phase speed and growth rate, sound pressure level directivity, and jet modal content. As will

be elaborated on shortly, the present experiments are especially helpful in evaluating this method since they are performed in a reduced Reynolds number environment which focuses attention on the large scale structures in the jet flow that are modeled as instability waves in the analysis of Morris and Bhat. Similar data provided by Troutt and McLaughlin (1982) on axisymmetric jets were invaluable in showing the success of the stability analysis of Tam and Burton (1984).

In addition to providing data for the elliptic jet predictions of Morris and Bhat, data will be generated for the comparison of rectangular jet predictions when they become available. Currently there are two rectangular jet prediction methods under development at Penn State. The first is a large eddy simulation code run on a massively parallel computer (see Chyszeskwi and Long, 1995). The second is a 2D finite element approach directed by Dr. P.J. Morris. A coordinated effort between the present experimental investigation and this computational research has proved to be invaluable up to this point and promises to pay further dividends in the future as the computational effort continues to mature.

1.4 Technical Approach

The experiments reported here were performed in the anechoic low pressure jet noise facility at Penn State. There are several benefits of operating the jets in the low-to-moderate Reynolds number regime rather than under conventional high Reynolds number conditions. Typical Reynolds numbers for the jets are 25,000 to 50,000 based on jet exit equivalent diameter, D_{eq}. Under these conditions, the large scale structures

in the jet are much easier to quantify as viscous forces reduce the small scale turbulence structure. As a result, the lower Reynolds number jets allow a good comparison to the instability wave models like that of Morris and Bhat (1992, 1993, 1995). Since these models identify such quantities as the most unstable frequency components and the individual modal content information, the lower Reynolds number jets make the evaluation of these models easier.

The reduced Reynolds number condition is achieved by exhausting the jets into the low pressure environment of the jet noise facility anechoic chamber. Chamber pressures of around 1/20th of an atmosphere are common. As a result, the low dynamic pressure of the jet flow allows standard hot-wire anemometry to be used without the typical problems of wire breakage in supersonic flow. Therefore, it is possible to use the wires to quantify the large scale structures with regard to size, growth rate, and spectral content. Again, this information is most helpful in the evaluation of the instability wave models.

A final benefit to the reduced Reynolds number environment is that the low ambient pressure allows the use of a glow discharge excitation system. As will be discussed in the next chapter, the glow discharge allows different instability modes to be excited in the jets and provides a phase reference for the microphone and hot-wire signals. This degree of active control over the jet is a significant advantage in the area of supersonic jet noise research.

1.5 Thesis Summary

The remainder of this thesis is devoted to a description of the experimental setup, data analysis and processing techniques, and measurements and interpretation of the results acquired during the course of researching the aerodynamic and acoustic properties of moderate Reynolds number supersonic elliptic, rectangular, and circular jets. Chapter 2 gives a full description of the facility and experimental apparatus used for the research. This includes a description of the high pressure air supply, the anechoic chamber, the vacuum recovery system, the glow discharge excitation system, and the nozzles used for the investigation.

Chapter 3 details the experimental procedures used to collect and analyze the data. The instruments used to measure the flowfield and acoustic quantities are described along with the analysis required to convert the raw data into physical quantities. A large part of this chapter is devoted to an explanation of the helium simulation and how the helium/air mixture gas properties are determined.

The results and discussion of the actual experiments begin in chapter 4. In this chapter, the mean flowfield measurements of the jets are reported. The mean flow is of primary importance in evaluating the accuracy of any predictive method and is required as input to others. Axial centerline Mach number and velocity distributions, radial velocity profiles, shear layer thickness parameters, and velocity contours are shown.

In chapter 5, fluctuating flow quantities measured using hot-wire anemometry are presented. Hot-wire fluctuation spectra, axial phase speed measurements, and

instability wave growth rates are measured with particular emphasis on how they effect the radiated noise. In order to understand the noise generation mechanisms in any flow, a clear understanding of the fluctuating flowfield is imperative.

Finally, the noise radiated from the jets is addressed directly in chapter 6. Microphones in the acoustic far-field give a description of the overall noise levels and directivity characteristics of each jet as the flow conditions are changed. Also, microphones placed in the acoustic field near the jet give a description of the azimuthal modal content of the radiated jet noise.

CHAPTER 2

EXPERIMENTAL APPARATUS

This chapter describes the hardware used in the jet noise facility, including the high pressure air supply, anechoic test chamber, vacuum recovery system, and supersonic nozzles. Figure 2.1 shows a schematic of the facility. Before an experiment, the two large vacuum recovery tanks and the facility shell are evacuated to around ten torr using a Kinney 5.66 m^3/min. vacuum pump. Dried, compressed air is delivered to the facility from a high pressure storage tank. When the valve from the compressed air supply is opened, the air flows from the supply tank to the test section. Upstream control valves create a pressure drop in the flow so that the total pressure of the flow is significantly reduced before entering the muffler section. The flow enters the settling chamber where it begins to accelerate through a contraction until it enters the nozzle section just upstream of the sonic throat. The flow then expands through the nozzle producing supersonic flow at the jet exit. While the jet is exhausting into the test chamber, aerodynamic and acoustic measurements can be made anywhere in the jet near or far-field by attaching measurement probes to a three-degree of freedom mechanized probe traverse. At the end of the test chamber, the jet enters a variable throat diffuser which is used to control the ambient test chamber pressure. Each of these components is described in the subsequent sections of this chapter.

2.1 High Pressure Air Supply

Even though the facility is driven primarily by the downstream vacuum tanks, an upstream high pressure air supply is still important for properly conditioned supply

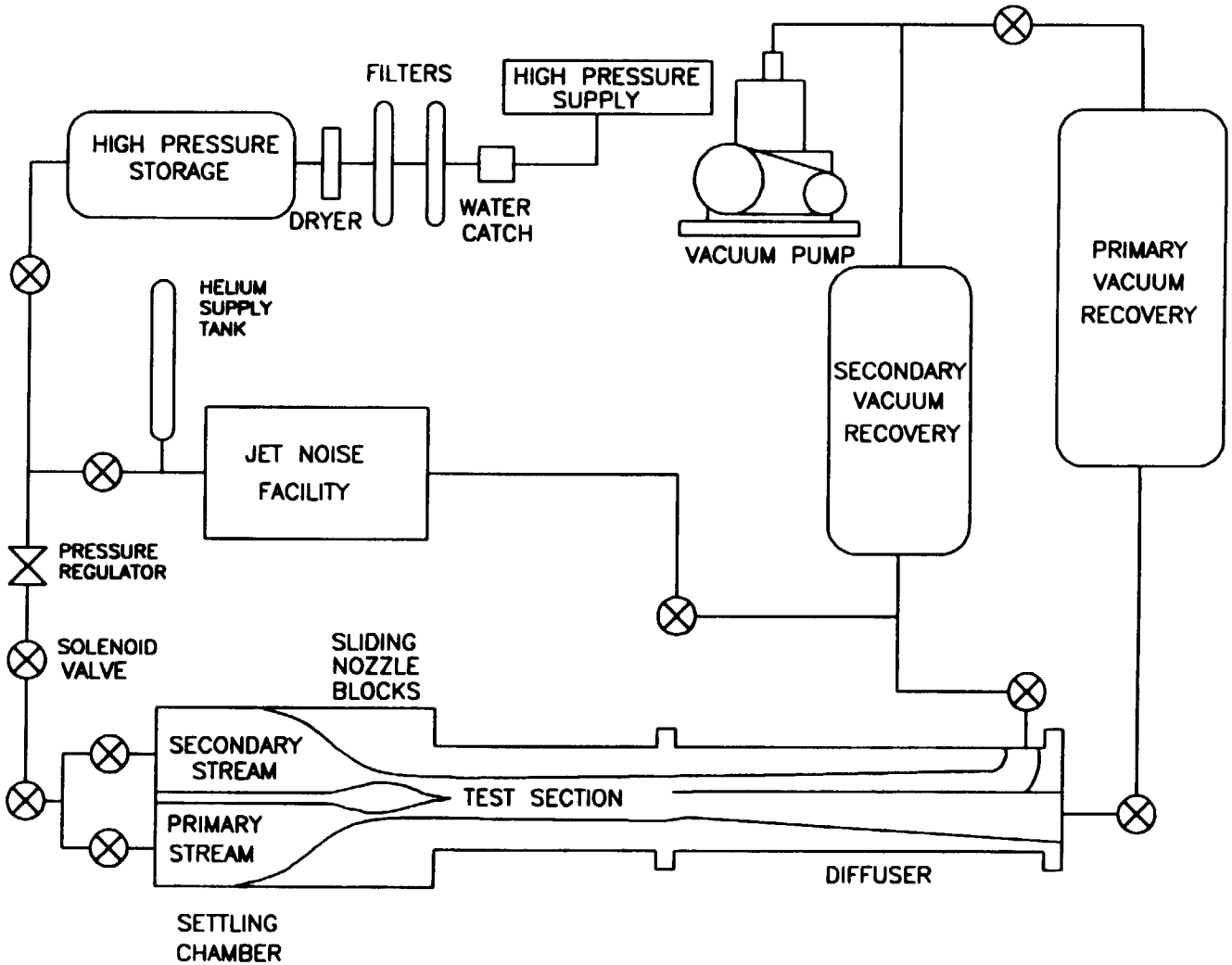

Figure 2.1 Schematic of Penn State jet noise and shear layer facilities.

air. A compressor delivers unfiltered shop air containing large amounts of water vapor. A water trap removes gross amounts of moisture before the air is filtered with two Hankinson 1 μm filters and dried with a Hankinson double pass, regenerative dryer. Drying the air is very important since the temperature of the flow drops drastically as it expands through the supersonic nozzles. With the stagnation temperature of both streams being approximately ambient temperature, the static temperature at the nozzle exit is around 180° K. Under these conditions, moisture may freeze in the flow resulting in condensation shock waves and nozzle Mach numbers that vary with the ambient humidity. Also, unfiltered particles in the flow, traveling at high velocities, may collide with measurement probes and break the fragile hot-wires, which are only 5μm in diameter.

The air is stored in a 2.83 m^3 tank at approximately 5 atmospheres until needed for an experiment. Before entering the muffler section, the air is regulated down to around 1.5 atmospheres with a high pressure regulator. Coarse and fine throttling control valves are used to precisely set the stagnation pressure of the jet. Due to the small mass flow through the nozzles, the upstream supply places no limits on the run time of the jets. However, depending on the jet Reynolds number and the resulting ambient chamber pressure, infinite run times are not possible due to the vacuum recovery system. For a pure air jet, supersonic flow may be maintained on the order of 30 minutes. The limitations of the vacuum recovery system will be discussed in a later section.

For many of the experiments, helium is mixed with the main jet air flow to produce a jet with a higher velocity and a lower density compared to a pure air jet. Standard compressed helium cylinders delivers helium at a pressure of nearly 145

atmospheres to serve this purpose. Helium passes through a regulator, reducing the pressure to around 1.5 atmospheres, before it is throttled down to the working pressure to mix with the air flow. Coarse and fine throttling valves are used to precisely control the mass flow rate of helium. The procedure to determine the concentration of helium in the jet mixture is described in the Experimental Procedure chapter. Since the helium/air mixture must pass through several pipe elbows and the baffled muffler/stilling chamber, no additional mixing procedures are considered necessary to ensure complete mixing of the two gases.

2.2 Anechoic Chamber

The anechoic chamber is the same one used in the experiments of McLaughlin and his students at Oklahoma State University (1975, 1979, 1980, 1982) and has been described extensively in the literature. The principle of operation is the same with an improved vacuum capacity having been added. Before the flow enters the anechoic chamber, it passes through a stilling chamber which contains anechoic treatment to attenuate upstream valve noise and turbulence management devices to straighten the flow and reduce the turbulence intensity at the jet exit. The stilling chamber has a diameter of 15 cm and is 50 cm long. The chamber consists of several baffled sections of 5 cm thick foam held in place by perforated plate, a 7.6 cm long honeycomb section, and 6 fine screens. Immediately following the stilling chamber is a cubic contraction section with an exit flange designed to mate with any of the nozzles used in the study.

The anechoic test chamber is 1.1 m x .66 m x .58 m and is lined with a 5 cm thick layer of Scott Pyrell acoustical foam. The foam is designed to absorb 90% of

the incident noise for frequencies above 1 kHz. A schematic of the chamber is shown in figure 2.2.

A three degree of freedom probe traverse is mounted to the floor of the facility. The traverse allows a hot-wire, pitot probe, or microphone to be accurately positioned anywhere inside the facility during an experiment. The system is controlled externally and potentiometers mounted on the traverse give a voltage output related to the position of the probe.

At the exit of the chamber, a variable-throat diffuser is used to control the chamber pressure. By increasing or decreasing the throat area, the chamber pressure is lowered or raised, respectively, and different pressure balance conditions can be achieved. Unless otherwise specified, the chamber pressure for all experiments in the present work was held to within 3% below the jet exit pressure. This produces nearly shock-free flow for all nozzles tested. A conical metal section is attached to the entrance of the diffuser to help channel the jet flow into the diffuser. In addition to the variable-throat diffuser, a diffuser bypass line connects a 3" PVC line from the chamber floor directly to the vacuum exhaust line downstream of the diffuser. This line is used when extra vacuum recovery is needed such as for an extremely low chamber pressure operating condition or to allow laboratory air to be bled into the chamber.

The chamber pressure can also be controlled by bleeding laboratory air into the chamber through the air bleed manifold shown in figure 2.2. This manifold consists of 1/2" copper pipe positioned around the endwall of the facility with small holes drilled along its length which allow air to flow into the facility. The manifold is wrapped in acoustic foam to help disperse the tiny air jets and to reduce the flow noise from the bleed. Microphone measurements with and without the bleed in operation

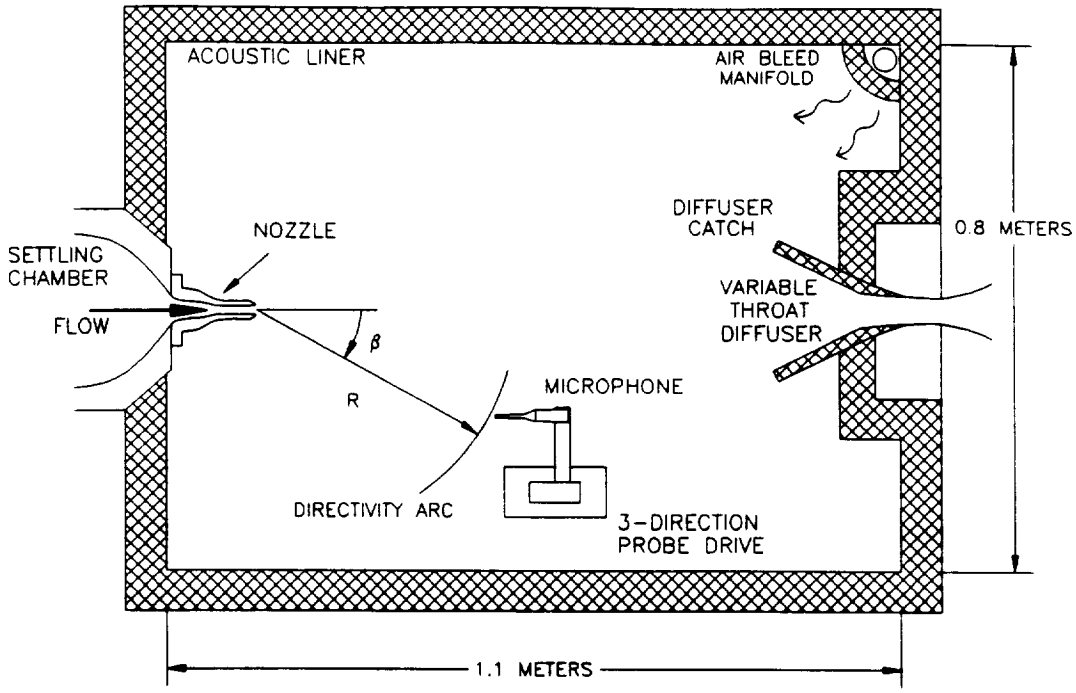

Figure 2.2 Diagram of jet noise anechoic chamber.

show no effect of the bleed on the jet noise measurements. The bleed system is primarily used to control the ambient pressure when helium is used in the jet flow. Under helium flow conditions, helium builds up in the test chamber and raises the ambient acoustic speed. As will be discussed in the next chapter, this is an undesirable situation and the bleed air dilutes the helium in the chamber and helps reduce the ambient helium concentration.

2.3 Vacuum Recovery System

The vacuum recovery system consists of three large vacuum tanks serviced by a Kinney KDH-220 5.66 m^3/min vacuum pump. Before the facility can be run, the downstream tanks must by evacuated to sufficiently low pressure. One tank has a 28.3

m^3 volume while the two other tanks each have a capacity of 3.78 m^3 giving a total capacity for the system of approximately 35.9 m^3. Since it takes about 60 minutes to pump the vacuum tanks down from atmospheric pressure, they are normally maintained well below ambient pressure, close to the necessary startup pressure.

As mentioned earlier, it is the vacuum system that places a limitation on the run time of the facility. Typical chamber pressures while the jet is operating range from around 25 torr to near 60 torr. Once the vacuum tank pressure reaches the chamber pressure, it is no longer possible to maintain a perfectly expanded jet since the chamber pressure will begin to rise above the jet static pressure. All of the Mach 1.5 pure air jets tested in the present work were able to operate perfectly expanded for at least 30 minutes before it was necessary to shut the jet down and pump the vacuum tanks to a lower pressure. Due to the large gas constant of helium compared to air, the pressure in the vacuum tanks rises much more quickly when helium jets are tested and the theoretical run times are reduced to only a few minutes. In practice, the helium jets are only operated for 15 to 20 seconds at a time in order to minimize the helium buildup in the test chamber. As will be discussed in a later section, excess helium in the chamber increases the ambient sound speed and thereby lowers the simulated temperature ratio of the jet.

2.4 Supersonic Nozzles

Figure 2.3 shows a sketch of all three nozzle exits used in this study. The elliptic and rectangular jets have identical exit areas while the circular jet has an exit area just over half that of the asymmetric jets. Some of the salient characteristics of each nozzle are listed in table 2.1.

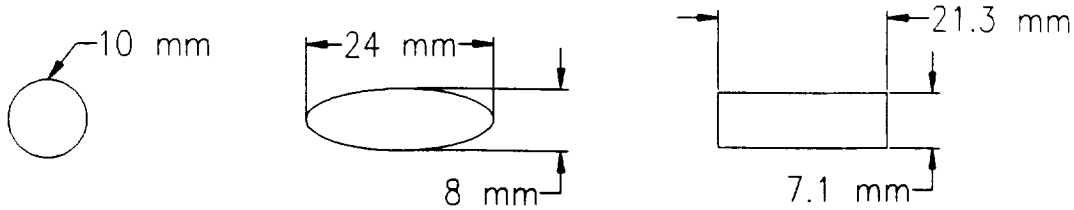

Figure 2.3 Sketches of nozzle exits.

Table 2.1 Nozzle dimensions.

Nozzle	Aspect Ratio	D_{eq} (cm)	Major Axis (cm)	Minor Axis (cm)	Exit Area (cm^2)	Mach Number
Elliptic	3	1.38	2.40	0.80	1.51	1.48
Rectangular	3	1.38	2.13	0.71	1.51	1.56
Circular	1	1.00	n/a	n/a	0.785	1.60

Figure 2.4 shows a diagram of the coordinate system and measurement plane notation used for this research. The major axis measurement plane is the plane containing the major axis. The minor axis measurement plane is the plane containing the minor axis. Since the probe drive has a wider range of motion in the y-direction than in the z-direction, the measurement probes were usually traversed in the y-x plane as shown in figure 2.4. The nozzle was then rotated 90° to obtain data in the major and minor axis planes separately. The angle β is measured from the jet axis to the measurement location. Therefore, $\beta = 0^o$ represents a point on the positive x-axis in the direction of the flow.

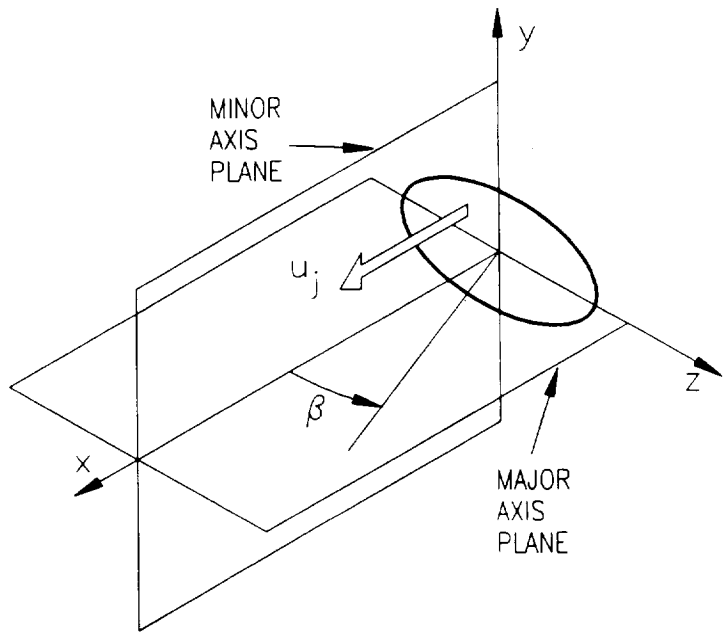

Figure 2.4 Measurement coordinate system and nomenclature.

2.4.1 Elliptic Nozzle

The elliptic nozzle used for this research has an aspect ratio of 3:1 and is designed for shock-free flow with a design exit Mach number of 1.5. Since the nozzle was scaled down from a NASA nozzle designed to operate at a much higher Reynolds number, the boundary layer correction designed for the original NASA nozzle is not enough to account for the thicker boundary layer which results when the nozzle is operated at the reduced Reynolds numbers of the present work. As a result, the actual jet exit Mach number is about 1.48.

The nozzle was manufactured at Penn State by wrapping graphite epoxy filaments around a mandrel that was machined at NASA Langley Research Center using scaled down coordinates of a NASA Mach 1.5, 3:1 aspect ratio elliptic nozzle. After the graphite epoxy filaments were cured in an autoclave, the mandrel was removed, and

a smooth inner contour was left to form the nozzle flow passage. The nozzle exit has a major axis length of 2.4 cm and a minor axis length of 0.8 cm. The exit area of the nozzle is 1.51 cm^2, which is equivalent to a circular nozzle with diameter 1.38 cm. The equivalent diameter, D_{eq}, is used as the length scale to nondimensionalize the experimental results.

2.4.2 Rectangular Nozzle

The rectangular nozzle also has an aspect ratio of 3:1 with a design Mach number of 1.5. In order to maintain an exit area of 1.51 cm^2 it has a major axis length of 2.13 cm and a minor axis length of 0.71 cm. The nozzle was machined in four pieces at the Penn State Engineering Services Machine Shop. The nozzle coordinates were also provided by NASA from a method of characteristics design. The supersonic portion of the nozzle is only contoured along the wide side of the nozzle. The narrow sidewalls are parallel. A boundary layer correction was applied to the contour which results in an actual exit Mach number of 1.54 when operated in the facility. Even though the nozzle is theoretically designed by the method of characteristics for shock free flow, the boundary layers which grow on the straight side walls cause a weak shock cell pattern to form in the jet plume.

2.4.3 Circular Nozzle

The circular nozzle was manufactured at Oklahoma State University and is the same nozzle used in the work of Morrison and McLaughlin (1979, 1980). The circular nozzle was designed by the method of characteristics with a boundary layer correction applied prior to nozzle fabrication. Since the nozzle was originally designed to operate

in the Reynolds number range of 4000 to 8000, the boundary layer correction results in an exit Mach number of 1.56 when used in the present work at higher Reynolds numbers. This also results in a weak jet plume shock cell pattern which causes the Mach number to oscillate slightly in the jet potential core. The nozzle has an exit diameter of 1.00 cm with a corresponding exit area of 0.785 cm^2.

2.5 Glow Discharge Excitation System

A desirable research aid in the study of transitional flow is a device with the ability to excite the naturally occurring instability waves in the jet. A small disturbance of a known frequency can then be introduced into the flow and tracked with respect to its size, coherency, and growth rate. The excitation source can also provide a phase reference for studies involving the phase relations of the instability waves. In a high Reynolds number supersonic flow, designing the physical mechanism for such an excitation system is very difficult. In this facility, the low pressure allows the implementation of a glow discharge excitation system.

It is a common phenomenon at higher pressures for electrical arcing to occur from one electrode to another if the voltage difference between them is high enough. At a very low ambient pressures, however, a high voltage produces a steady and much more controlled glow from one electrode to another. This is the principle behind the glow discharge system. A voltage is applied to an electrode placed close to the jet exit. If the ambient pressure in the facility is low enough, the surrounding air will be ionized and current flows through the electrode producing a steady glow when a minimum threshold voltage is reached.

Figure 2.5 shows a schematic of the glow excitation system. An oscillating signal of approximately 1.5 V_{rms} is generated by a signal generator at a specified frequency. If necessary, a second channel of the same signal may be run through a phase inverter to shift the phase of the signal 180° from the first channel. Each signal is then amplified by a 250 W stereo amplifier to boost the rms voltage to approximately 7.5 V_{rms}. The signals then enter the glow controller panel which contains transformers to boost the signal to approximately 250 V_{rms}. The controller then biases each signal with a D.C. voltage of -400V resulting in a signal to each electrode which oscillates between -750 V and -50V. The current flow is only a few amperes (depending on the ambient pressure) and therefore the power draw is relatively low considering the high voltages.

Whenever the voltage to an electrode exceeds a threshold voltage, a local glow is produced. For a pressure of 20 torr, the threshold voltage is approximately -500 V. Since the glow is a result of the ionization of the air molecules, a very high temperature is produced close to the electrode. The temperature perturbation causes small density and pressure disturbances which artificially excite the flow. Therefore, these small disturbances can be introduced at any desired frequency simply by controlling the frequency of the applied A.C. voltage. As the disturbances are convected downstream, they either grow or decay depending on the response of the jet to the excitation frequency.

Each nozzle is fitted with four glow discharge electrodes oriented as shown in figure 2.6 (for the elliptic nozzle). The electrodes consist of a solid copper rod 1.6 mm in diameter inserted into a ceramic tube with an outside diameter of 3.2 mm. The ceramic tube is then inserted into a thin walled copper sheath which is electrically

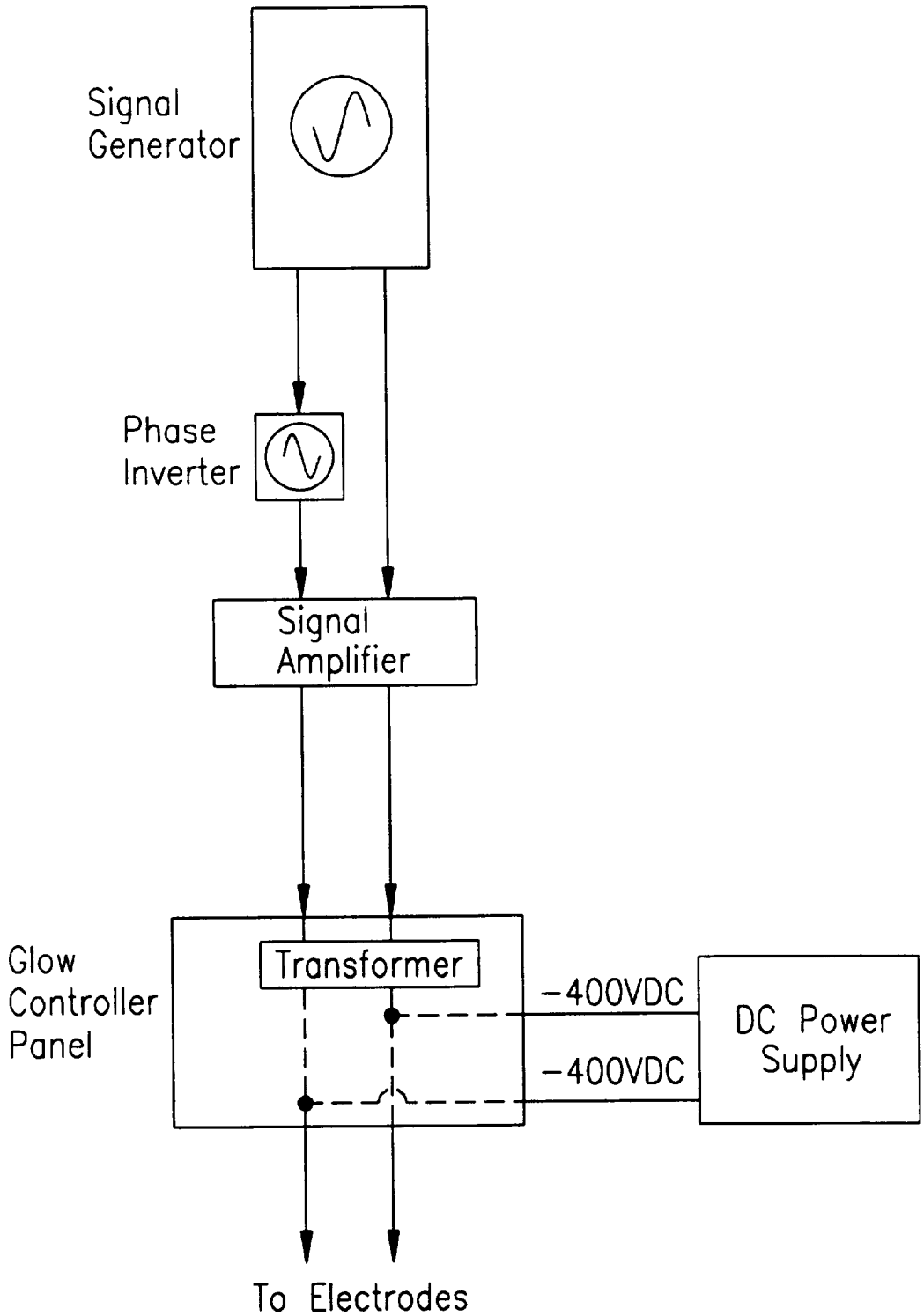

Figure 2.5 Schematic of the glow discharge system.

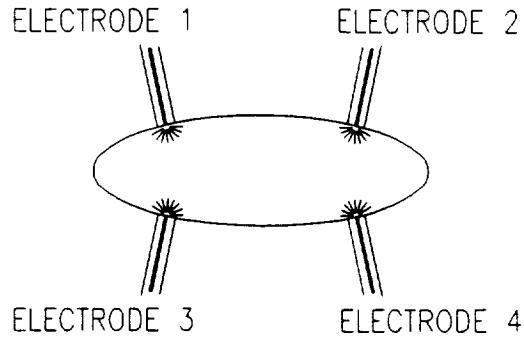

Figure 2.6 Electrode placement around nozzles.

grounded. When a large enough voltage is applied to the inner copper rod, a current flows to the outer copper sheath and a local glow is produced. This voltage can be modulated at any desired frequency. Since the electrodes are located just outside the nozzle exit, very close to the flow, the modulating local high temperature perturbs the jet at the chosen frequency.

Because each electrode can be individually controlled, different instability modes can be excited in the jet. For instance, by modulating all four electrodes in phase, a varicose instability can be excited. The varicose mode is equivalent to an axisymmetric mode in a circular jet. By exciting electrodes 1 and 2 exactly 180° out of phase from electrodes 3 and 4 (see Figure 2.6), a flapping mode about the major axis (flapping in the minor axis plane) can be excited. Other combinations will lead to the excitation of other modes in the jet. However, it should be noted that the excitation of individual modes in the elliptic jet using the four-point excitation is problematic. Though the dominant mode produced is likely to be the desired mode additional modes are certain to be excited.

CHAPTER 3

EXPERIMENTAL PROCEDURE

This chapter describes the experimental techniques and instrumentation used to investigate the jets. The primary instruments used are hot-wire anemometers, condenser microphones, and pressure transducers, with all data acquired by a fully computerized data acquisition system. This chapter also gives a detailed description of the helium simulation and how the gas properties are calculated for the helium/air mixtures. Special analysis procedures required to analyze the raw data from the helium/air mixture jets are also described.

3.1 Digital Signal Acquisition

Due to the volume of data acquired and the short duration of the experimental runs, an 80386-33 IBM-compatible personal computer (PC) is used in every phase of data processing from acquisition to final data analysis. Two types of A/D convertors are used to acquire the data. A TransEra MDAS 7002 A/D convertor (currently manufactured by Kaye Instruments) is linked with the PC to acquire mean flow data from the pressure transducers and a Metrabyte DAS-58 board is used for fluctuating pressure and hot-wire measurements.

3.1.1 TransEra System

The analog-to-digital conversion of mean pressure signals is performed by a 16 channel TransEra MDAS-7002 sample-and-hold data acquisition system with a 12 bit A/D convertor. Each channel has its own independently controlled amplifier to aid in boosting the signal-to-noise ratio of the measurement signals. The effective voltage inputs to the TransEra range from ±0.078 V to ±10 V. The TransEra has a single channel digitizing rate of 625 kHz with a 500 kbyte onboard memory buffer. However, when two channels are acquired the maximum digitizing rate drops to approximately 59 kHz. In order to prevent aliasing of high frequency signals into lower frequency components of the spectrum, it is required that each channel of fluctuating data be filtered at a frequency no higher the one-half of the digitizing rate (the Nyquist frequency). This limits the TransEra to a maximum useful frequency response of less than 30 kHz when more than one channel are acquired simultaneously. Because a large quantity of the necessary measurements involve the cross-correlation between two sensors, each measuring frequencies up to 60 kHz, the TransEra is not suited for these types of high speed measurements. Therefore, the Trans-Era is used primarily to acquire steady state pressure data.

The TransEra is controlled by the PC through a General Purpose Interface Bus (GPIB) card. Commands are sent to the GPIB through an interactive Pascal computer code developed as a part of this study. Since the TransEra has its own onboard CPU, it is capable of performing many functions such as data averaging. The majority of the pressure signals acquired by the TransEra are monitored for several seconds and only

the average value is written to the screen or to a computer file. This procedure saves both time and hard disk space since it eliminates most of the need for the post-processing of large pressure data files.

3.1.2 DAS-58 Board

Because of the relatively low acquisition rate of the TransEra, a Metrabyte DAS-58 board with sample-and-hold is used for all high speed data acquisition such as microphone and fluctuating hot-wire measurements. The DAS-58 also utilizes a 12 bit A/D convertor. The DAS-58 has a maximum signal channel digitizing rate of 1 MHz with the two channel rate dropping to 333.33 kHz. The board also has 1 MB of onboard memory and an input range of ±2.5 V to ±10 V. Typical acquisition rates for the present work are 120 kHz for hot-wire measurements and 200 kHz for microphone measurements.

The DAS-58 is controlled by a manufacturer supplied pop-up menu screen which operates simultaneously with the TransEra data acquisition code. Acquisition options such as digitizing rate and number samples are set and triggered via the computer mouse while the TransEra monitors the test section and jet pressures in the background. When the jet pressures reach their desired set point, the DAS-58 is manually triggered to begin acquisition. After the test is over, the DAS-58 downloads the contents of the onboard memory to a user specified computer file for post-processing.

3.2 Pressure Measurements

3.2.1 Mean Flow Pressure

All mean flow pressure transducers used in the facility are a differential piezoresistive type manufactured by Microswitch Corporation. During facility operation, a vacuum reference below 100 μm Hg is maintained on one side of the transducers. Care is taken as the test chamber is evacuated from atmospheric conditions to equalize the pressure differential across the low level transducers so that overpressurization will not occur. The response time of the transducers is specified to be on the order of microseconds. However, due to the small diameter and length of the tubing used to connect the transducers to the pressure taps, the actual response time is observed to be on the order of 1-2 seconds for the transducers to read a steady-state value.

Three ranges of pressure transducers are used depending on their location in the facility. Low level transducers are calibrated using a Meriam oil manometer as a standard. Medium and high level transducers are calibrated by a Heise absolute pressure gauge. The Heise gauge is also used to monitor the facility pressure during the pumpdown of the test chamber while the transducers are in the overpressurization range. Due to the low vacuum pressures encountered, a Pirani gauge is used to measure the pressure of the vacuum recovery tanks and the vacuum reference.

3.2.2 Fluctuating Acoustic Pressure

Acoustic measurements are made with 1/8" diameter B & K condenser microphones. The microphones are calibrated before and after each experiment using an electronic acoustic calibrator. Following the work of Morrison and McLaughlin (1979, 1980) and Troutt and McLaughlin (1982), the sound pressure level (SPL) is calculated using a reference pressure scaled by the ambient chamber pressure, p_{ch}, as follows:

$$SPL = 20 \log_{10} \left[\frac{p_{rms}}{p_{ref}} \right], \qquad \text{where}$$

$$p_{ref} = \left[\frac{p_{ch}}{p_{atm}} \right] (20 \times 10^{-6}) \ N/m^2$$

The microphone signals are bandpass filtered between 1.5 kHz and 60 kHz. High-passing the signal removes a facility acoustic resonance below 1 kHz. Low-passing the signal prevents aliasing and eliminates a microphone resonance at about 80 kHz in the low pressure environment. The microphone data are typically acquired around 200 kHz. The record length normally exceeds 50,000 data points. The spectral analysis code used to process the fluctuating pressure and hot-wire data is described in Appendix B.

3.3 Hot-Wire Anemometry

Because the facility is run at such low pressures, the resulting densities produce relatively low dynamic pressures for supersonic flow. As mentioned earlier, this allows

the use of fragile hot-wire sensors without damage to the wires. Hot-wires are ideal to measure the development of the instability waves. The hot-wires can be used to obtain fluctuating and mean mass-velocity values. From the fluctuating measurements, the spectral content of the flow field can be extracted.

DISA 55M10 feedback circuitry is used and consistently provides a frequency response in excess of 45 kHz with the homemade hot-wire probes. The hot-wires use subminiature probes manufactured by Dantec Corp. and are mounted on the end of a brass probe. The leading edge of the probe is filed sharp to reduce the force on the probe in supersonic flow. When held in place, the probe is swept approximately 60° forward to reduce the effective flow deflection angle of the leading edge wedge. The probe is mounted on the probe traverse described in section 2.2 and can be placed anywhere in the jet flow.

The use of hot-wire anemometers in supersonic flow is more complicated than in low speed flow. In supersonic flow, hot-wire output voltage is sensitive to the product (ρu), referred to as mass-velocity or mass-flux, as well as changes in the total temperature, T_o. Without additional information such as the local temperature and pressure, interpreting this information can be very difficult. Following Kovasznay (1950) and Morkovin (1954), the hot-wire voltage fluctuations may be expressed as

$$\frac{e'}{\overline{E}} = A_m \frac{(\rho u)'}{\overline{\rho u}} - A_T \frac{(T_o)'}{\overline{T}_o} \qquad 3.1$$

where A_m and A_T are determined from calibration data. Troutt and McLaughlin (1982) found that for a low Reynolds number jet with flow conditions similar to the ones in

the present work, that the total temperature fluctuations accounted for less than 2% of the hot-wire voltage fluctuations. The total temperatures for their both work and the present jets are approximately ambient temperature. The same assumption regarding the total temperature fluctuations is made here and therefore the second term in equation 3.1 is neglected. Following the methods of Rose (1973) and Ko, McLaughlin, and Troutt (1978) the coefficient of the mass-velocity term may be shown to be:

$$A_m = \frac{\overline{\rho u}}{\overline{E}} \frac{\partial \overline{E}}{\partial \overline{\rho u}} \qquad 3.2$$

The problem then becomes one of calibrating the hot-wire to find the value of A_m. By placing the hot-wire at the exit of the jet and operating the jet over a range of Reynolds numbers, a calibration curve of mass-velocity versus hot-wire output voltage can be determined. A discussion of the calibration of the hot-wires in the helium flow will be delayed until more background has been provided on the use of helium/air mixtures in this research.

3.4 Heated Jet Simulation

One problem of performing experiments with unheated jets is that, even at low supersonic Mach numbers, the large scale turbulent structures may not achieve a supersonic phase speed. Morrison and McLaughlin (1979) measured the phase speed of the dominant jet Strouhal number component to be only about three-quarters of the ambient sound speed for a cold Mach 1.5 axisymmetric jet. This means that the radiated noise typically would not include the Mach wave emission process and the

noise field would not be predicted very well by the instability wave models. When a Mach 1.5 jet is heated, however, the jet velocity, as well as the structure convection velocity, increases significantly. In most practical applications, such as jet engines, the jet static temperature is well above the ambient temperature. Therefore, in order to study the Mach 1.5 jets under realistic engine conditions, they should be heated so that the convection velocity of the structures will be supersonic and the effects of Mach wave radiation can be measured. Because the jet noise facility is not equipped to operate heated jets, the low density and high velocity of a hot jet are simulated by using a lower density gas with different properties than air, namely helium.

As described in Barron (1993) and McLaughlin et al. (1992), the facility has been modified to mix helium with the main jet air flow. The jet then has a reduced density and higher acoustic speed (and jet velocity) compared to an unheated air jet. As a result, the helium/air mixture jets simulate more closely a heated jet by having a density and velocity more comparable to an actual heated jet.

Because the jets will be run under perfectly expanded conditions, the jet pressure and ambient chamber pressure will be equal and the perfect gas law and isentropic relations can be used to relate the ambient and jet density in the following manner:

$$\frac{\rho_j}{\rho_a} = \frac{T_a R_a}{T_j R_j} = \left(\frac{R_a}{R_j}\right)\left[1 + \left(\frac{\gamma_j - 1}{2}\right) M_j^2\right] \qquad 3.3$$

Equation 3.3 also requires that the stagnation temperature is equivalent to the ambient temperature ($T_a = T_o$). Both of these values are assumed to be 273° K for the jet noise

facility. Now, for an actual heated pure air jet equation 3.3 can also be written as (where no assumption is made on the value of T_o):

$$\left(\frac{\rho_j}{\rho_a}\right) = \left(\frac{T_a}{T_j}\right) \qquad 3.4$$

Therefore, it is possible that an unheated jet composed of a different gas than the ambient environment could simulate the flow of a hotter air jet, provided the density ratios of the cold jet simulation and hot air jet were similar. For example, a helium jet exhausting into an air environment has a simulated temperature ratio, based on density, which can be calculated from equation 3.3 and using equation 3.4 to determine the density ratio from an actual hot jet. This can be written as:

$$\left(\frac{T_j}{T_a}\right)_{simulated} = \left(\frac{\rho_a}{\rho_j}\right)_{helium\ jet} = \left(\frac{\rho_a}{\rho_j}\right)_{hot\ air\ jet} \qquad 3.5$$

While this analysis shows that helium/air jets can be used to simulate the density ratio of an actual hot jet, it is important that the jet velocity of the hot jet be simulated as well. Since helium has a higher acoustic speed than air, a helium/air jet operating at the same Mach number as a pure air jet will also have a higher jet velocity. This can be seen by comparing the jet exit velocities of an air jet and a helium/air mixture jet at the same Mach number.

Table 3.1 shows several important jet and gas properties for a helium/air mixture jet and for two relevant heated Mach 1.5 jets, all with the same exit velocity. The helium concentration is calculated by mass, not molar quantities. Properties of an unheated Mach 1.5 jet (case A) are also listed for comparison. The first three cases

shown are for jets exhausting into standard atmospheric temperature conditions resulting in an ambient acoustic speed of 343 m/s. The last case shown (case D) is for a heated jet exhausting into an environment with a temperature of 430°K. This last case will be shown shortly to be most comparable to the simulation reported in this work. The temperature and density ratios listed in Table 3.1 are actual values calculated from isentropic relations. The specific heat ratios for the jets are also listed.

Table 3.1 Properties of Mach 1.5 jet for different gases exhausting into pure air.

Case	T_o (°K)	Helium Concent. (by mass)	U_j (mps)	a_j (mps)	a_a (mps)	ρ_a/ρ_j	Actual T_j/T_a	γ_j
A	293	0	430	290	343	0.69	0.69	1.4
B	293	26%	690	460	343	1.5	0.61	1.55
C	760	0	690	460	343	1.8	1.8	1.4
D	760	0	690	460	415	1.2	1.2	1.4

The question of what temperature ratio the helium/air jet simulates does not have a clear cut answer. As mentioned earlier, since the simulation obviously does not match the actual temperature in a heated jet, it is desirable that the jet mixture be such that the simulation has a similar velocity and density as the actual heated jet since these quantities strongly influence both the jet development and radiated noise. However, it is seen from Table 3.1 that while the jet exit velocity is matched by the helium/air jet (case B), the jet density is not equivalent to the actual hot jet case exhausting into a similar environment (case C). Due to the gas properties of the unheated helium/air

mixture, it is not possible to exactly match both of these quantities. Therefore, the simulated jet temperature ratio can be based either on the jet velocity or jet density. In other words, the simulated temperature ratio can be equivalent to the actual hot jet temperature ratio such that the heated jet and the simulation have either matching jet velocity ratios or matching jet density ratios. Since the present work focuses primarily on the aeroacoustics of the problem, which scales strongly with velocity, the simulated jet temperature ratio is based on the actual temperature ratio that results in a heated air jet with the same exit velocity, Mach number, and ambient acoustic speed as the simulation. It is seen from Table 3.1 that even with the mismatch between the simulation and an actual heated jet, the simulation results in flow conditions much closer to those of an actual heated jet than by running the unheated pure air jet. Also, as will be discussed shortly, excess helium that builds up in the chamber during an experiment tends to lower the value of ρ_a/ρ_j such that it becomes closer to that of the actual heated jet which is being simulated.

3.4.1 Properties of Gas Mixture

In order for the helium/air mixture to be useful, it is required to know gas properties of the mixture such as the specific heat ratio and the gas constant. If these quantities are known, standard isentropic relationships can be used to determine the jet Mach number, velocity, temperature, and density. For a binary gas mixture like the one in this work, it is straightforward to calculate these quantities as long as either the mass fraction or mole fraction of each constituent is known. A complete description of this

methodology can be found in most fundamental thermodynamic books. Reynolds and Perkins (1977) is an example. The following section describes the procedure used to determine the gas properties of the helium/air mixture for any given mixture concentration.

For any gas mixture with *n* constituents, let the mass fraction, Φ_i, and the mole fraction, χ_i, of each individual constituent be defined respectively as:

$$\Phi_i = \frac{M_i}{\sum_{i=1}^{n} M_i} \qquad \chi_i = \frac{\eta_i}{\sum_{i=1}^{n} \eta_i} \tag{3.6}$$

where M_i is the mass of an individual constituent and η_i is the number of moles of an individual constituent. Since we are only concerned with a binary mixture (n = 2) of air and helium, we can specify the mass fraction of each constituent and find the number of moles per unit mass of air and helium in the mixture by the following relationships:

$$\eta_{he} = \frac{\Phi_{he}}{\hat{M}_{he}} \qquad \eta_{air} = \frac{\Phi_{air}}{\hat{M}_{air}} \tag{3.7}$$

where $\hat{M}$ indicates the molecular weight of the specified gas. The total number of moles per unit mass of the mixture is then

$$\eta_{mix} = \eta_{he} + \eta_{air} \tag{3.8}$$

Now, the mole fraction of each constituent which corresponds to the specified mass fraction is determined by

$$\chi_{he} = \frac{\eta_{he}}{\eta_{mix}} \qquad \chi_{air} = \frac{\eta_{air}}{\eta_{mix}} = (1 - \chi_{he}) \qquad 3.9$$

Figure 3.1 shows the molar fraction of helium in the mixture as a function of the mass fraction of helium in the mixture. Due to the low molecular weight of helium compared to air, small amounts of helium added by mass have a large effect on the molar content of the helium in the mixture. By the time helium comprises 50% of the total mass of the mixture, nearly 90% of the molecules in the mixture are helium. Since the gas properties of the mixture are weighted by the mole fraction of the individual constituents in the mixture, small amounts of helium added by mass can have a large effect on the thermodynamic characteristics of the mixture.

The molecular weight of the mixture is can be computed by the following

$$\hat{M}_{mix} = \frac{1}{\eta_{mix}} \qquad 3.10$$

Figure 3.2 shows the molecular weight of the mixture as a function of the mass fraction of helium contained in the mixture. It is seen once again that the effect of adding relatively small amounts of helium by mass is to quickly lower the molecular weight of the mixture

Thermodynamic gas properties are calculated by weighting the properties of each individual constituent by its mole fraction. For instance, the specific heat of the mixture at constant pressure ($C_{p,mix}$) is computed from the following equation:

$$C_{p,mix} = \frac{\chi_{he} \cdot C_{p,he} \cdot \hat{M}_{he} + \chi_{air} \cdot C_{p,air} \cdot \hat{M}_{air}}{\hat{M}_{mix}} \qquad 3.11$$

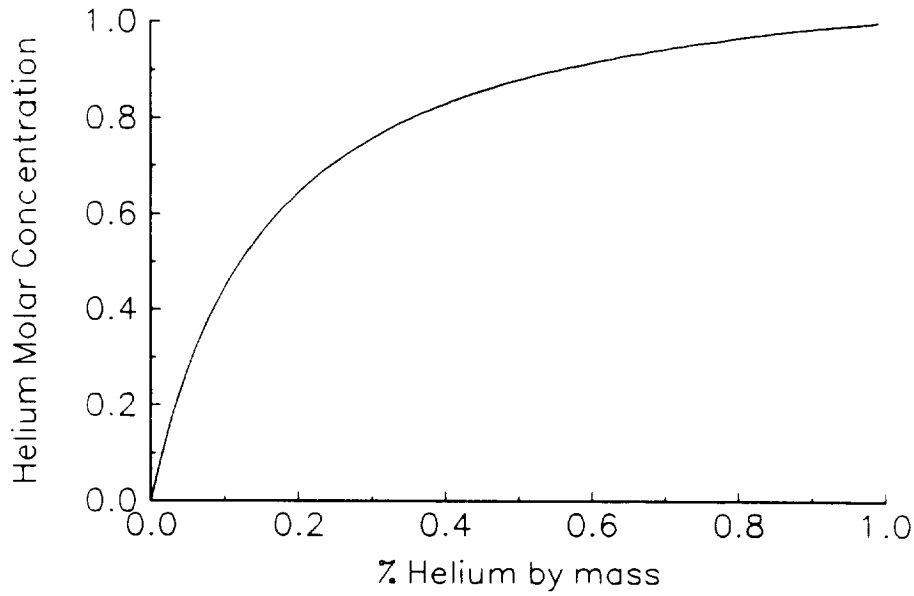

Figure 3.1 Molar concentration of helium in gas mixture as a function of helium mass concentration.

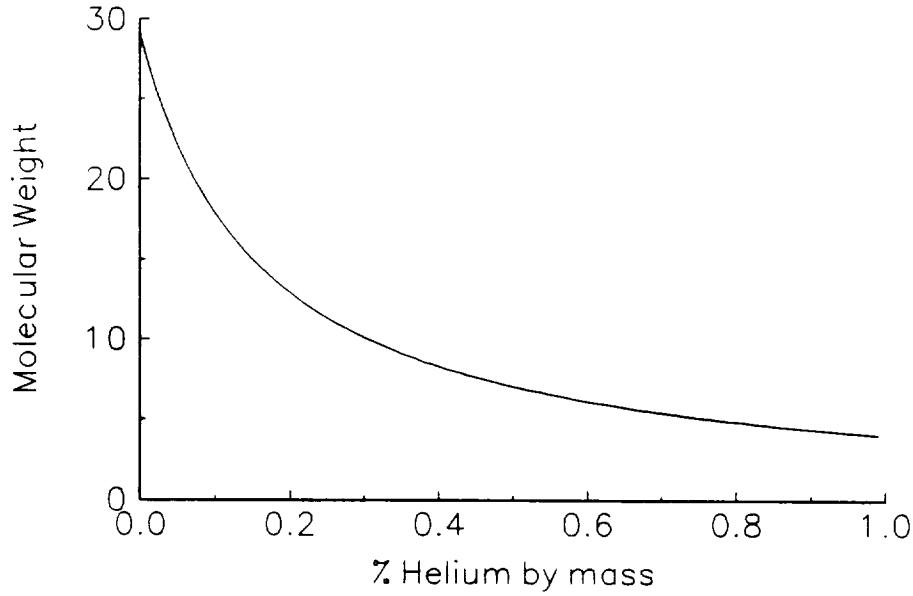

Figure 3.2 Gas mixture molecular weight as a function of helium mass concentration.

The specific heat at constant volume ($C_{v,mix}$) is found in a similar manner. The gas constant (R_{mix}) can be calculated either from the equation $C_{p,mix}$ - $C_{v,mix}$ or from dividing the universal gas constant (8.314 kJ / kg ^{o}K.) by the molecular weight of the mixture. Figures 3.3 and 3.4, respectively, show the ratio of specific heats and the gas constant as a function of mass concentration of helium in the jet mixture. Considering the strong non-linearity of the other quantities shown here, it is interesting to note that the mixture gas constant is a linear function of helium mass concentration. This results from the fact that the mixture gas constant is proportional to the number of moles per unit mass of the mixture which is a linear function of helium mass concentration.

A detailed explanation of how the mixture viscosity is calculated is provided by Barron (1993)[1]. An accurate knowledge of the mixture viscosity is important when calculating the jet Reynolds number. Because an actual hot jet has a higher viscosity than the helium/air mixture, the Reynolds number of the hot jet is not matched exactly by the simulation and is about 25% lower than the actual Reynolds number of the simulation. Because the present work is performed at reduced Reynolds numbers compared to conventional jets, this difference is not considered of significant consequence.

3.4.2 Jet Mixture Concentration

Since it is possible to determine the gas mixture properties if either the helium or air concentration of the mixture is known, it is necessary to develop a procedure to

---

[1] It should be noted that the analysis of mixture thermodynamic quantities such as C_p, C_v, and R is performed incorrectly in Barron (1993). The present analysis corrects the errors.

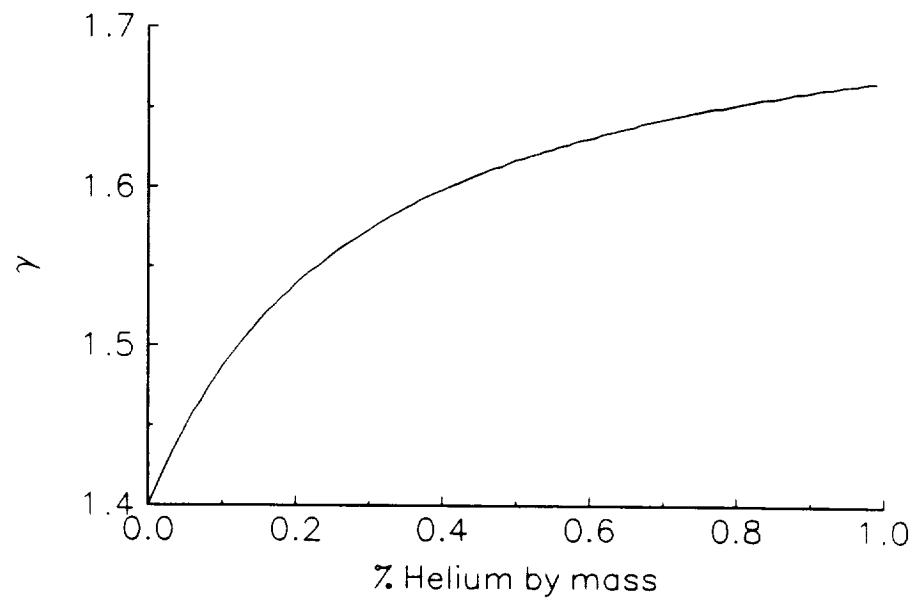

Figure 3.3 Ratio of specific heats (γ) for gas mixture as a function of helium mass concentration.

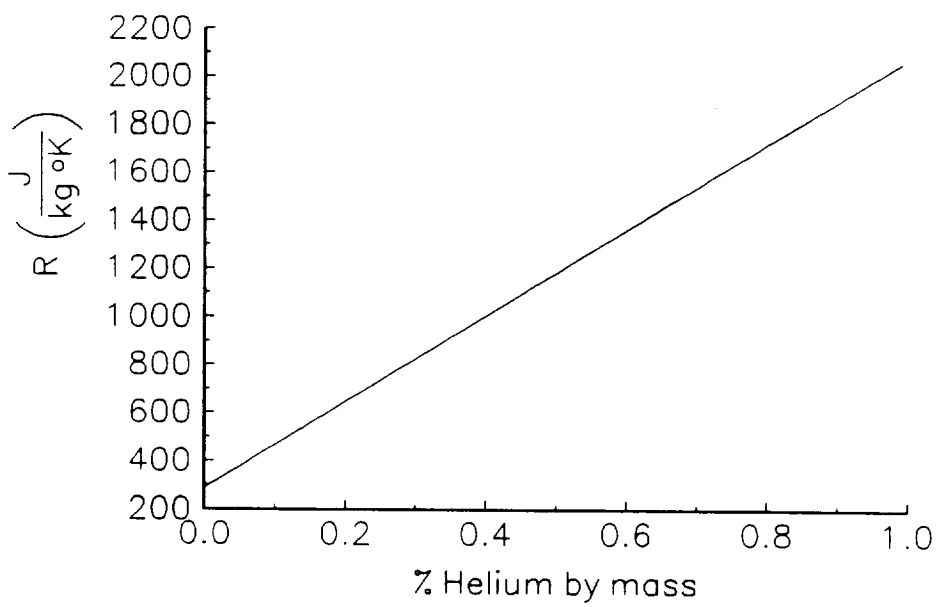

Figure 3.4 Gas constant (R) for gas mixture as a function of helium mass concentration.

mix the upstream helium and air supplies such that the mixture molar content is known and can be controlled. Figure 3.5 shows a schematic of the upstream supply lines and important choke points in the system. The key to determining the mixture concentration is to ensure that the air flow and the helium flow each pass through a choked valve before mixing. Since the mass flow through a choked orifice is constant regardless of the flow conditions downstream of the choke point, this guarantees that the mass flow of each gas into the system will not change once the upstream regulator and throttling valve are set. These choke points are shown as V1 and V2 in figure 3.5. The pressure upstream of each valve is maintained at approximately 2.5 atm while the pressure downstream of the valves is typically less than 0.5 atm thereby ensuring that the valves are choked for any operating condition within the scope of this work.

Isentropic relations show that the mass flow through a choked orifice can be described by the equation:

$$\frac{\dot{m}\sqrt{T_o}}{A^* P_o} = \sqrt{\frac{\gamma}{R}\left(\frac{2}{\gamma + 1}\right)^{\frac{\gamma+1}{\gamma-1}}} \qquad 3.12$$

Therefore, the mass flow through the orifice is dependent only on the orifice size, total temperature and total pressure upstream of the orifice, and the specific heats of the gas. The right hand side of equation 3.12 will be a constant for any given specific heat ratio and gas constant, which for the present work will be a unique function of helium concentration of the gas mixture. This constant is referred to as Fliegner's constant, F. For air (γ = 1.4, R = 287 kJ/kg ^{o}K) and helium (γ = 1.67, R = 2077 kJ/kg ^{o}K) Fliegner's constants are F_{air} = 0.0404 and F_{he} = 0.0159.

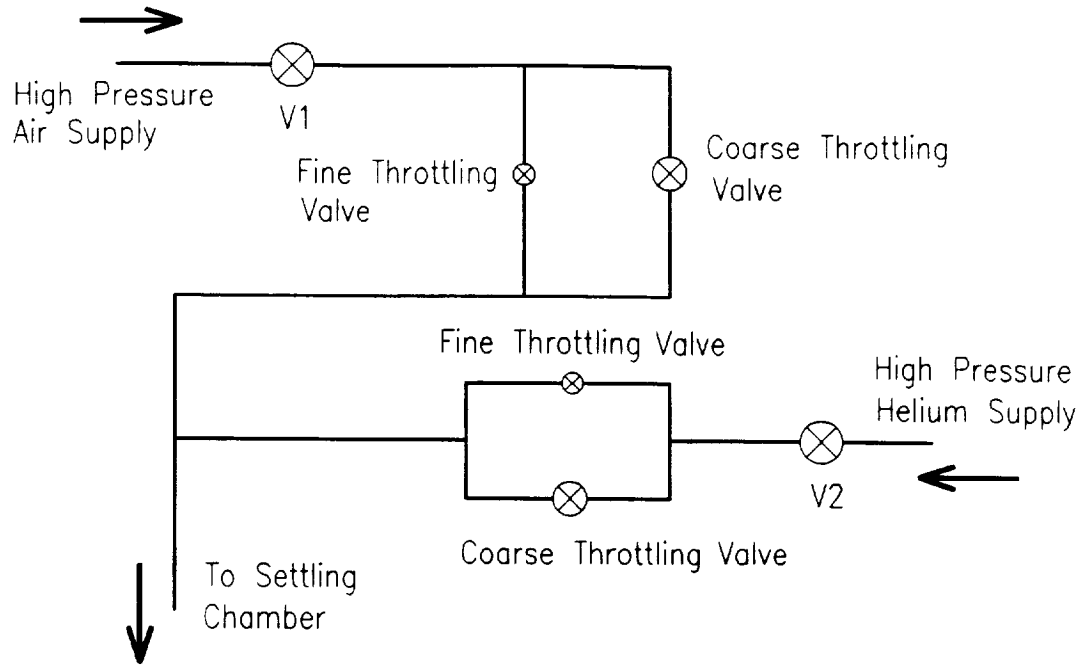

Figure 3.5 Schematic of upstream supply lines and critical choke points needed to set the helium concentration of the jet flow.

Since the nozzle throat is also a choke point where it is convenient to measure the flow conditions, we can use Fliegner's constant at that location to measure the mass flow of the entire system. When either the air or helium flow is operating individually, the mass flow of each gas can be determined from the equations

$$\dot{m}_{air} = \frac{P_o A_t}{\sqrt{T_o}} \cdot 0.0404 \qquad \dot{m}_{he} = \frac{P_o A_t}{\sqrt{T_o}} \cdot 0.0159 \qquad 3.13$$

Since the supply valves V1 and V2 remain choked when the flows are combined, the mass flows of each individual gas described by equation 3.13 will not change and the mass flow of the mixture will be

$$\dot{m}_{mix} = \dot{m}_{air} + \dot{m}_{he} = \frac{P_{o,mix} A_t}{\sqrt{T_o}} \cdot F_{mix}(\gamma, R) \qquad 3.14$$

where $F_{mix}(\gamma,R)$ is Fliegner's constant for the mixture. Fliegner's constant for the mixture, F_{mix}, is a function only of the mixture specific heat ratio and gas constant. These quantities can be determined from the helium concentration of the gas mixture. Figure 3.6 shows F_{mix} as a function of mixture helium concentration by mass.

If equations 3.13a and 3.13b are combined with equation 3.14, the following equation must be satisfied

$$\frac{P_{o,air} A_t}{\sqrt{T_o}} \cdot 0.0404 + \frac{P_{o,he} A_t}{\sqrt{T_o}} \cdot 0.0159 = \frac{P_{o,mix} A_t}{\sqrt{T_o}} \cdot F_{mix}(\gamma, R) \qquad 3.15$$

Since the reference point for the mass flow calculations is the nozzle throat, A_t is the same for each of the terms in equation 3.15. Also, since the total temperature of the flow is assumed to be ambient room temperature, T_o is also equal for each term in equation 3.15. This simplifies equation 3.15 to

$$P_{o,air} \cdot 0.0404 + P_{o,he} \cdot 0.0159 = P_{o,mix} \cdot F_{mix} \qquad 3.16$$

Therefore, the procedure to determine the helium concentration in the jet mixture is to set the upstream supply valves which control $P_{o,air}$ and $P_{o,he}$ and record each of these pressures individually in the absence of flow from the other gas. Then, $P_{o,mix}$ is recorded when the gases are combined. Once F_{mix} is known from equation 3.16, the concentration of helium in the mixture can easily be found by the calculations that lead to figure 3.6. When the helium concentration of the mixture is known, the methods of the previous section may be used to determine the gas properties of the flow.

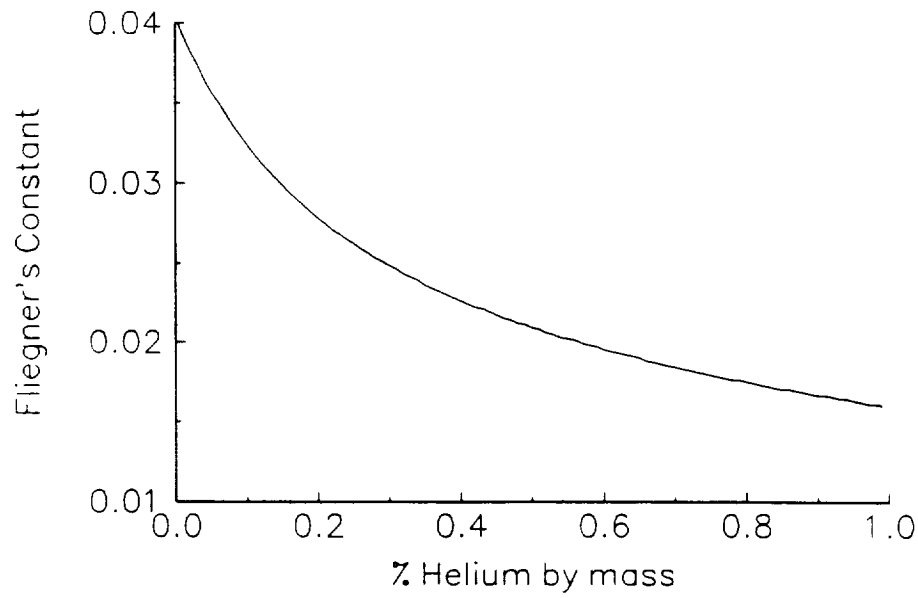

Figure 3.6 Fliegner's constant (F) as a function of helium mass concentration.

3.4.3 Helium Concentration in Test Chamber

An important parameter in this work is the amount of helium which builds up in the test chamber during a run. Hot jets are only simulated if there is a large difference in gas properties between the jet flow and ambient environment. If too much helium builds up in the chamber, the jet ceases to simulate a hot jet based on density ratio or speed ratio, and reverts to typical cold jet operating conditions with regard to Mach wave emission. When this happens, the ambient acoustic speed increases such that the structures no longer have a supersonic phase speed relative to the ambient environment and additional effects from Mach wave emission are lost.

To reduce the effect of the helium buildup, laboratory air is bled into the chamber during the run in order to dilute the helium which is present. The helium concentration in the chamber is determined from a method that measures the speed of sound in the chamber surrounding the jet. This is done by using two phase matched microphones with a known separation distance and measuring the phase difference of various spectral components of the radiated noise. By separating the microphones by a known distance and pointing them at the approximate sound source location in the jet (typically near the end of the jet potential core), the phase difference between the microphone signals allows the speed of sound in the chamber to be calculated. It is known that the sound speed in the chamber can be calculated from

$$a_{ch} = \sqrt{R_{ch}\,\gamma_{ch}\,T_{ch}} \qquad 3.17$$

In this expression, a_{ch} is measured from the dual microphone phase difference and T_{ch} is measured from a thermocouple in the test chamber. Since both R_{ch} and γ_{ch} are related uniquely to the amount of helium in the chamber, the helium concentration can be found by determining what concentration of helium results in values of R_{ch} and γ_{ch} which gives the measured sound speed. Barron (1993) and McLaughlin et al. (1992) give a detailed description of this procedure.

Once the acoustic speed in the chamber is measured (from the frequency and phase difference), the corresponding helium concentration which results in that acoustic speed can be calculated. Since it is impossible to purge all of the helium from the chamber during an experiment, small amounts of helium in the chamber result in an ambient helium concentration on the order of about 7% by mass. In terms of the

simulation, the increase in ambient sound speed due to the helium corresponds to a simulated ambient temperature higher than the standard value of 293°K. This results in a lower simulated temperature ratio than if the jet were exhausting into pure air.

Table 3.2 shows the experimental conditions reported in this paper for the pure air jets and the simulated hot jets. The helium/air jets most closely simulate case D listed in Table 3.1. Note that due to the excess helium in the chamber, which lowers the ambient gas density from pure air conditions, the ambient to jet density ratio is nearly matched with the actual heated jet conditions for these experiments. Also, due to the difficulty in applying boundary layer corrections for such small nozzles at reduced Reynolds numbers, the Mach numbers of the nozzles are not exactly equal. This leads to slight velocity differences between the nozzles for the air jet cases and small simulated temperature differences between the nozzles for the helium jet cases. When operating the helium/air mixture jets, the helium concentration is set such that all three nozzles have the same exit velocity, within experimental uncertainty. Throughout this thesis, the temperature ratio for all air jets will be nominally referred to as $T_j/T_a = 0.69$ and all helium/air mixture jet cases will be referred to nominally as $T_j/T_a^* = 1.2$. In addition, the 0% helium concentration cases will be referred to as pure air jets while the helium/air mixture jets are usually referred to as simply helium jets.

Table 3.2 Experimental Conditions.

Shape	M_j	D_{eq} (cm)	helium concent. (by mass)	T_j/T_a^*	u_j (mps)	P_o (torr)	P_j (torr)	f_c (Hz)	Reynolds Number
Elliptic	1.48	1.38	0	0.69	425	101	28	30,800	27,000
Rectangular	1.56	1.38	0	0.67	435	115	29	31,500	27,000
Circular	1.6	1.00	0	0.66	445	160	37	44,500	27,000
Elliptic	1.5	1.38	26 %	1.2	690	185	47	50,000	27,000
Rectangular	1.58	1.38	24 %	1.1	690	194	44	50,000	27,000
Circular	1.61	1.00	23 %	1.1	690	240	51	69,000	27,000

A test of the helium delivery system was made by shutting off the outside bleed supply and operating a given helium/air jet until the chamber environment had approximately equalized with the jet mixture concentration. The dual microphone system in this case measures a helium concentration in the chamber equivalent to the jet helium concentration set using the flow control valves. Since each of these methods is independent of one another, this procedure serves as a check on the accuracy of both methods. Figure 3.7 shows a graph of the measured chamber concentration as a function of the predetermined jet helium concentration for several different jet mixtures. Except for the 100% helium point, the measured values agree very well with the set values. The lower measured helium concentration for the 100% helium jet is probably due to the chamber not being entirely purged of air during the pure helium test. These results give confidence to the procedures which have been developed to calculate the jet mixture gas properties and to measure the ambient gas concentration.

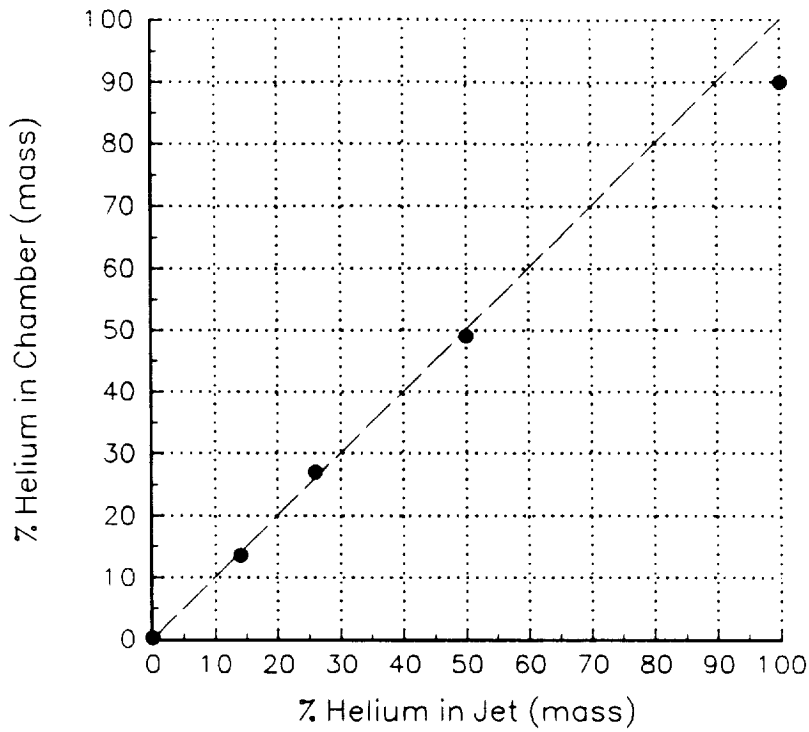

Figure 3.7 Measured helium concentration (by mass) in the chamber as a function of the jet helium concentration.

3.4.4 Calculation of Helium Jet Plume Velocity

For the pure air jets, it is straightforward to compute flow quantities such as Mach number and velocity from measured pressure values since the gas properties are uniform throughout the jet. However, for jets containing helium, this is a more difficult task. Even though the gas properties are known relatively accurately at the jet exit and in the potential core region from the methods of section 3.4.2, once the jet begins to entrain ambient air, the helium concentration (and gas properties) begins to change from these values. Therefore, the local helium concentration continually changes across the jet from the centerline value to the ambient value in the chamber. Since the

concentration can never be higher than the original jet exit value nor lower than the ambient helium concentration measured by the dual microphone method of section 3.4.3, an upper and lower bound on the concentration value are known at any point in the jet.

Since a method to measure the local helium concentration directly at a point in the jet is not available, a method of estimating this value must be determined in order to know the velocity in the plume of the helium jet. Since the molecular diffusion of helium particles through the jet is meant to simulate the thermal diffusion of heat through the jet, it is not unreasonable to treat the scalar value of concentration in a similar manner as one normally treats the scalar quantity of temperature. With that in mind, it is possible to develop an analysis where the concentration of the jet depends on velocity in much the same manner as the Crocco-Busemann relation (Schlicting, 1954) describes the temperature field in a compressible boundary layer as a function only of velocity.

The momentum equation for a gas mixture is the same as for a single gas and is written as:

$$\rho\left(u\frac{\partial u}{\partial y} + v\frac{\partial u}{\partial y}\right) = -\frac{dP}{dx} + \frac{\partial}{\partial y}\left(\mu\frac{\partial u}{\partial y}\right) \qquad 3.18$$

Schlichting (1954) derives an equation which relates the concentration of a binary gas mixture to the spatial velocity field and temperature field of the flow:

$$\rho\left(u\frac{\partial \phi}{\partial y} + v\frac{\partial \phi}{\partial y}\right) = \frac{\partial}{\partial y}\left[\rho D_{12}\left(\frac{\partial \phi}{\partial y} + k_T\frac{\partial \ln T}{\partial y}\right)\right] \qquad 3.19$$

In equation 3.19, ϕ is the mass concentration of one gas, D_{12} denotes the coefficient of binary diffusion, and k_T is the thermal diffusion ratio. As in the Crocco-Busemann derivation, we can assume ϕ depends only on velocity such that:

$$\phi = \phi(u)$$

Using the chain rule for partial derivatives, equations 3.18 and 3.19 can be combined such that they result in a single equation:

$$\phi_u \frac{\partial^2 u}{\partial y^2} = \frac{\partial}{\partial y}\left(\frac{D_{12}}{\nu}\phi_u \frac{\partial u}{\partial y}\right) + \frac{\partial}{\partial y}\left(\frac{D_{12}}{\nu} k_T \frac{\partial \ln T}{\partial y}\right) \qquad 3.20$$

If the Schmidt number for the problem is assumed to be unity, then equation 3.20 becomes:

$$\phi_{uu}\left(\frac{\partial u}{\partial y}\right)^2 = \frac{\partial}{\partial y}\left(k_T \frac{\partial \ln T}{\partial y}\right) \qquad 3.21$$

Also, since the jet is unheated, it is reasonable to neglect the thermal diffusion term on the right-hand side of equation 3.21. Schlicting (1954) also proposes neglecting this term in certain situations. The concentration equation then reduces to simply:

$$\phi_{uu} = 0 \qquad 3.22$$

Equation 3.22 can be integrated twice to obtain:

$$\phi = k_1 u + k_2 \qquad 3.23$$

The helium concentration value is known at the jet exit where the jet velocity is also known and in the ambient environment where the jet velocity is zero. By applying these boundary conditions to equation 3.23, an equation for the concentration as a function of velocity is written as:

$$\phi = \left(\frac{\phi_j - \phi_a}{u_j}\right) u + \phi_a \qquad 3.24$$

Equation 3.24 can be used anywhere in the jet to estimate the helium concentration as long as the velocity at that location is known. It seems somewhat simplistic that the concentration varies linearly with velocity, particularly since the Crocco-Busemann equation shows that temperature varies with the square of velocity. However, for lack of a better estimate, equation 3.24 is used to determine the jet concentration. Comparisons between actual hot jets and the simulated hot jets of the present work will show similar trends and lead to the conclusion that equation 3.24 is an adequate approximation for the present work.

In order to actually use equation 3.24, an iterative process must be used. First, a local velocity is assumed and a corresponding concentration is determined from equation 3.24. Then, using the gas properties from that concentration value, the measured pitot and static pressures are used to calculate a local Mach number and velocity. If the assumed velocity does not agree with calculated velocity from the pressure measurements, a different velocity is assumed until the two values agree. The converged velocity then leads to the best estimate for the local helium concentration. This process is used in subsequent sections whenever velocity values for the helium jets are shown.

3.4.5 Helium/Air Mixture Hot-Wire Calibration

When the hot-wires are used in the helium/air mixture jets, the calibration becomes especially difficult since the anemometer output then becomes a function of gas concentration as well as the other terms in equation 3.1. The problem is complicated by the fact that the helium concentration changes across the jet shear layer. Efforts to obtain a precise calibration in the helium/air mixtures in the manner of Way and Libby (1970) were unsuccessful, but they do suggest that a less rigorous approach to the determination of the influence coefficients of the relative parameters may lead to a calibration that has acceptable engineering accuracy.

In order to learn how helium concentration affects the anemometer output, calibrations were performed as described for the pure air case at different values of helium concentration in the jet mixture. Figure 3.8 shows this calibration at several different values of helium concentration, including the pure air case. It is seen that for a given value of mass flux, the addition of helium tends to increase the anemometer output voltage. Since helium has a higher value of thermal conductivity than pure air, it convects more heat away from the constant temperature wire and therefore draws more voltage from the anemometer (for comparable levels of ρu). It is seen that for each value of concentration, the calibration curve is deterministic and follows a regular polynomial type curve. In fact, if each of the calibration curves in figure 3.1 is plotted in a King's law type formulation where

$$E^2 = A(\rho u)^{0.5} + B$$

then each data sets fits on a straight line with the slope increasing as helium is added.

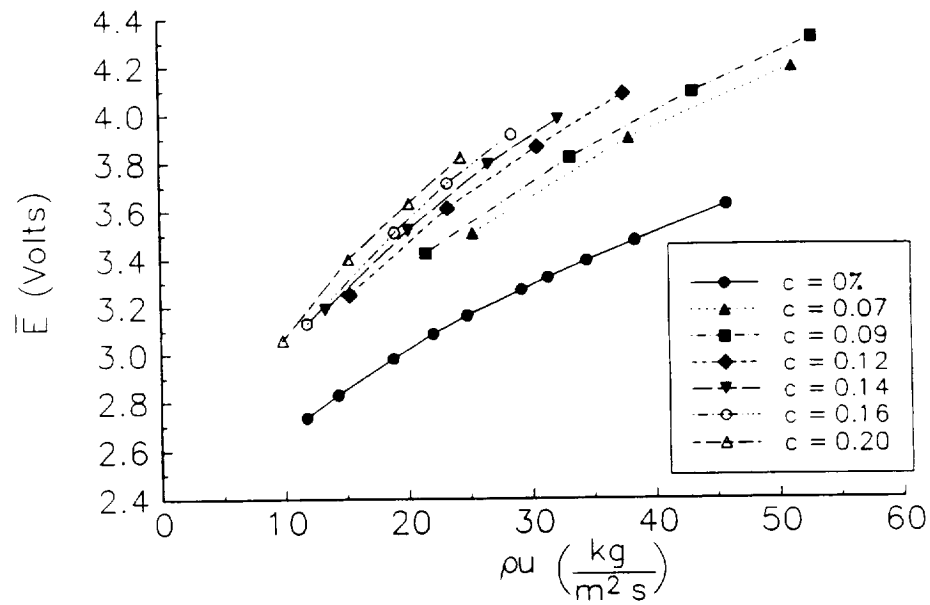

Figure 3.8 Hot-wire calibration for varying helium concentrations (by mass).

Therefore, if the helium concentration at the measurement point is known and is a constant, the appropriate calibration curve can be determined and equations 3.1 and 3.2 can be used for the helium mixture. However, the helium concentration is not constant outside the potential core region and changes continuously across the jet shear layer. It is seen from figure 3.8 that the addition of helium concentration fluctuations will serve to increase the voltage fluctuation output from the anemometer. Experience does show that voltage fluctuation levels measured in the helium/air mixture jets are significantly higher than those in the pure air jets.

It is valid to say that, neglecting the stagnation temperature sensitivity, equation 3.1 can be written to include the helium concentration sensitivity as:

$$\frac{e'}{\overline{E}} = A \cdot \frac{(\rho u)'}{\overline{\rho u}} - A_c \frac{c'}{\overline{c}} \qquad 3.25$$

The variable c represents the local value of helium concentration which has a mean and fluctuating component just like any other flow variable. The problem then becomes one of the determination of the relative contributions of the mass flux term and the concentration term to the measured voltage fluctuation from the anemometer. These contributions can be estimated from the data of figure 3.8.

It is known from the present work and of other supersonic mixing layer researchers (Morrison and McLaughlin, 1980; Kistler, 1959; Kosvaszny, 1950) that the mass-velocity fluctuation levels normalized by the local mean value are typically around 0.25 in the type of free shear flows considered here. Also, these previous researchers have shown that the covariance of the density and velocity terms in the measured mass-velocity fluctuation is close to unity with approximately half of the measured fluctuation level due to density fluctuations and half due to the velocity fluctuations (in the Mach 1.5 range). Also, recall that it was shown in section 3.4.4 that the helium concentration in the jet scales approximately linearly with velocity (following a Crocco-Busemann-like relationship). Therefore, if the mass-velocity fluctuation level is 0.25, then the concentration fluctuation level normalized by the mean value of concentration would be around 0.12.

For all measurements shown in the present work, the local mean value of the mass-velocity term on the lipline of the jet is around 30 kg/($m^2 \cdot s$). Also, from mean velocity measurements and the analysis of section 3.4.4, it is known that the helium

concentration at most hot-wire measurement locations (on the lipline) through the potential core region is typically around 20% to 23% helium by mass. It is slightly lower downstream of the potential core. Now, by considering the 20% helium curve shown in figure 3.8, a 25% mass-velocity fluctuation at 30 kg/($m^2 \cdot$ s) gives a voltage fluctuation of approximately 0.21 V. If the mass-velocity value is held constant, a 12% fluctuation in helium concentration around the 20% helium curve gives a voltage fluctuation of approximately 0.082 V. Therefore, this would suggest that of a total voltage fluctuation measured by the hot-wire for these conditions, approximately 30% of the fluctuations would be due to helium concentration fluctuations and approximately 70% of the fluctuations would be due to mass-velocity fluctuation.

This conclusion is further supported by a consideration of the ratio of typical voltage fluctuations from pure air jets compared to those from the helium/air mixture jets. Figure 3.9 shows the ratio of $(e'/E)_{air}$ to $(e'/E)_{hel}$ for the major and minor axes of the elliptic and rectangular jets as a function of downstream distance. Assuming that the mass-velocity fluctuation levels are approximately the same for the two jet gas cases, this ratio helps isolate the influence of helium concentration on the voltage fluctuations. It is seen that except for early locations in the jet and the rectangular jet major axis measurements, this ratio is between 0.6 and 0.7 over the entire measurement range. This also is evidence that the mass-velocity fluctuations are only about 70% of the total fluctuations in a helium/air mixture hot-wire measurement.

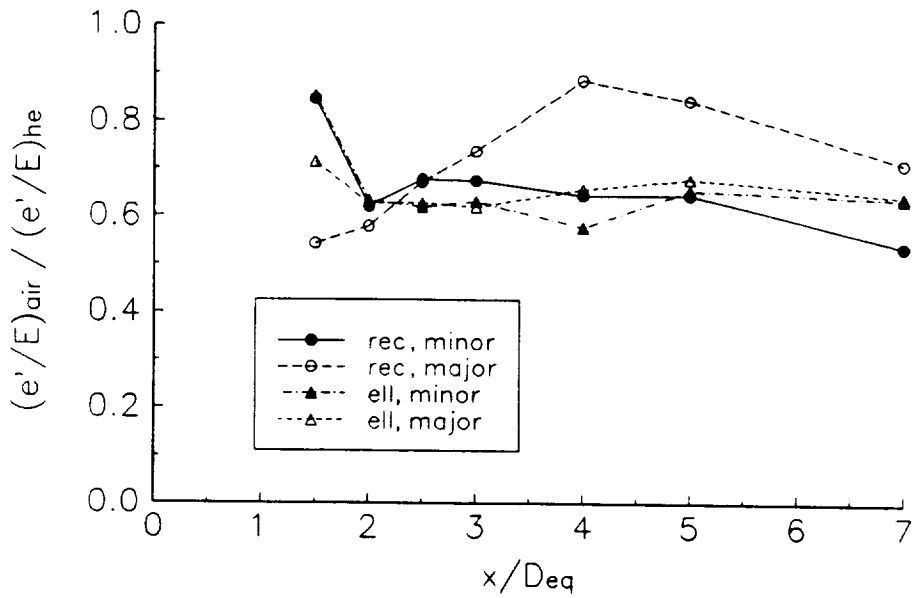

Figure 3.9 Ratio of air jet anemometer output to helium jet anemometer output as a function of axial location.

Therefore, the procedure to calibrate the hot-wire anemometer output in helium flow is to first determine an estimate of the local helium concentration at the measurement location. This is done using the mean velocity profiles and the analysis of section 3.4.4. Then, the calibration data of figure 3.8 are used to obtain a value for the mass-velocity fluctuation level without correcting for additional fluctuations due to changes in helium concentration. From the above analysis, it is then estimated that the actual mass-velocity fluctuation level is about 65% of that obtained from applying the calibration of figure 3.8. This methodology is applied wherever hot-wire fluctuation levels are presented for helium/air mixture jets.

CHAPTER 4

MEAN FLOWFIELD MEASUREMENTS

Since the radiated noise from a supersonic jet is related directly to the turbulent flow structure of the jet, a clear understanding of the noise generation process is not possible without a knowledge of some basic aerodynamic quantities of the flow. All analytical and computational models depend on a knowledge of the near-field mean and/or fluctuation flow quantities in order to predict the far-field sound. These quantities must either be known *a priori* or are calculated as a part of the prediction method. With analytical models such as the one developed by Morris and Bhat (1992, 1993), the jet mean flow is required as an input to the code. Methods using conventional CFD codes typically calculate mean velocities via the Reynolds-averaged Navier-Stokes equations as a precursor to making far-field noise predictions. Also, initial hydrodynamic pressure and flow fluctuation quantities close to the nozzle exit must be specified by most prediction schemes in order to predict far-field acoustic pressure quantities.

Given the importance of the aerodynamic flow quantities on the radiated sound field, the next two chapters focus on mean and fluctuating flow measurements which will aid in interpreting the acoustic data presented in Chapter 6. The experimental data presented can also be used to evaluate analytical and computational techniques as well as provide a data base for certain information which is required for input to such work.

Basic measurements such as velocity profiles from pitot pressure data are presented for all three jet geometries under investigation.

The pressure measurements described in this chapter were performed with either a single pitot tube probe or with a five-hole pitot probe rake. A schematic of each of these probes is shown in Figure 4.1. Since the jets were operated close to perfectly expanded conditions, the static pressure throughout the jet was assumed to be equal to the ambient chamber pressure. By knowing the jet static pressure and pitot pressure, the local Mach number at the measurement location can be calculated. If the pressure ratio is below the critical pressure ratio value for supersonic flow ($P_o/P_j < 1.89$, for $\gamma = 1.4$), the Mach number is subsonic and the velocity is computed using standard isentropic relations. If the pressure ratio is above the critical value for supersonic flow ($P_o/P_j > 1.89$, for $\gamma = 1.4$), then the Mach number is supersonic and the velocity is computed using the Rayleigh pitot formula which corrects for the normal shock in front of the pitot tube. For all velocity calculations, the total temperature is assumed to be equal to the ambient room temperature. The velocity in the helium jets was calculated using the technique described in section 3.4.4.

4.1 Helium/Air Jet Mixtures

Since the amount of data from actual heated jets available in the open literature are relatively scarce, particularly for asymmetric jets and for the exact conditions of the present simulation, the evaluation of the validity of the helium simulation on the flowfield is difficult. Seiner et. al (1993) and Lau (1981) provide mean flow data

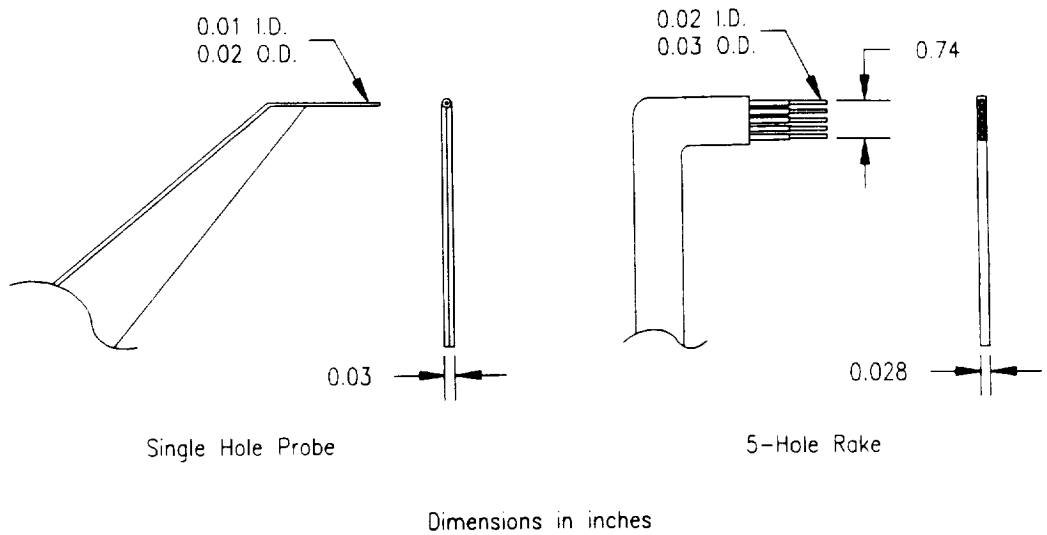

Figure 4.1 Pitot probes used to measure mean jet velocity.

from heated circular jets which can be used to interpret data from the present work. In general, both of these references show a decrease in the spreading rate of the jet shear layer and a shortening of the potential core as the jet temperature increases. Lau (1981) speculates that since the shear layers grow slower in a heated jet, they may curve inward in order to account for the shortened potential core. This section reports the limited mean flow measurements performed in the helium jets.

4.1.1 Centerline Mach Number and Velocity Distributions -- Helium Jets

The centerline Mach number distribution from the pure air elliptic jet is compared to that of the helium/air mixture jet ($T_j/T_a^* = 1.2$) in Figure 4.2a. As expected in the potential core region, the Mach number of the helium jet is slightly

(a)

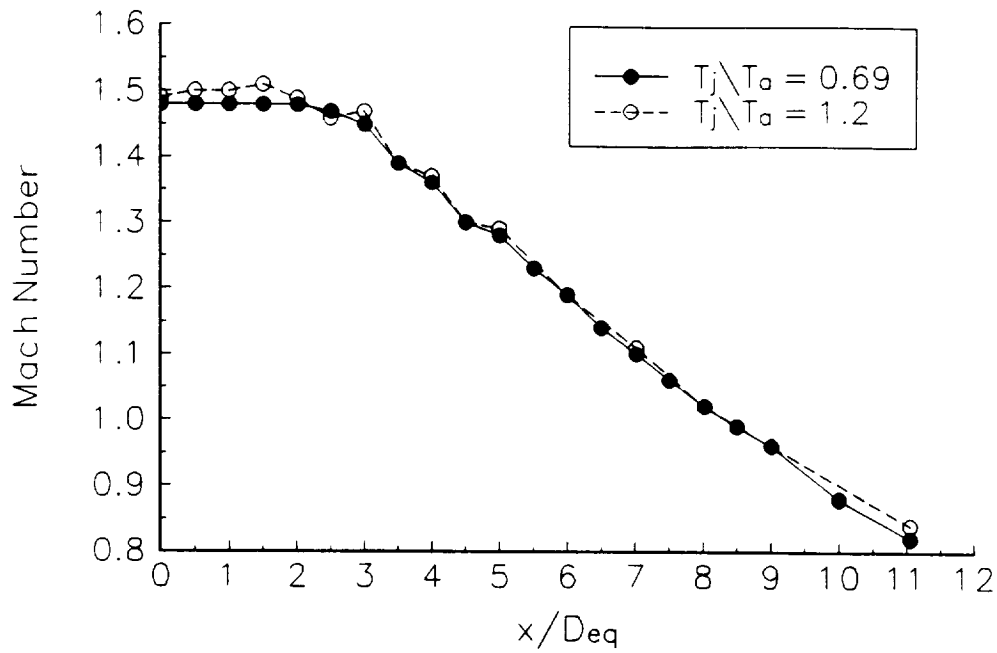

(b)

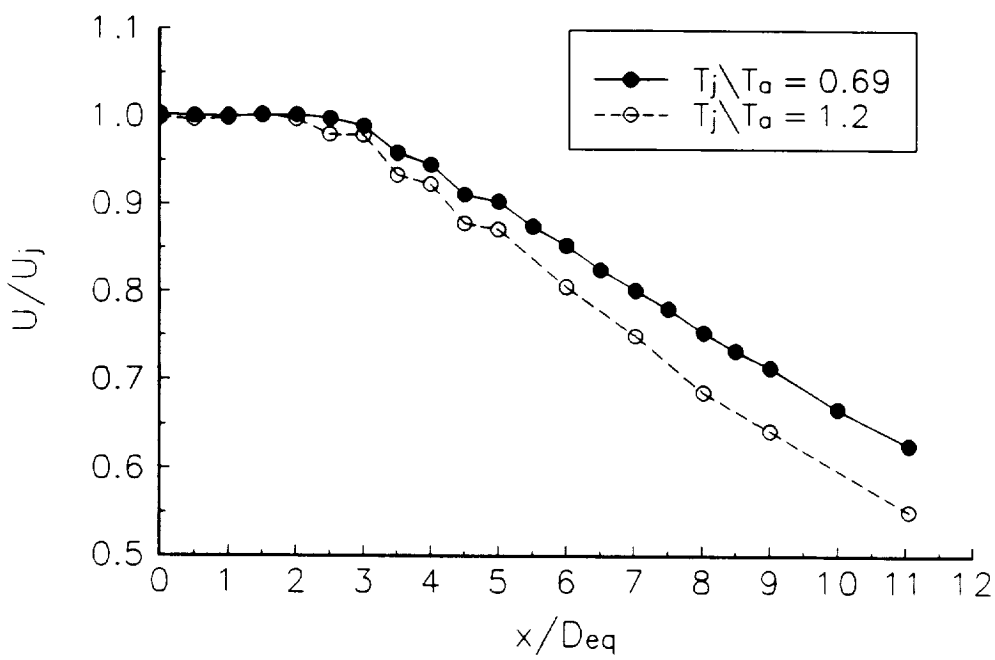

Figure 4.2 Helium and air centerline Mach number and velocity distributions for the elliptic jet. (a) Mach number (b) velocity.

higher than that of the pure air jet. Recall that this is due to the increase in γ for the helium jet. After the potential core region, however, the Mach number and decay rate from both jets are virtually identical.

Figure 4.2b shows the centerline velocity distribution of the two jets normalized by the jet exit velocity. The helium jet shows an increased decay rate compared to the air jet with a very slight decrease in potential core length. According to the work of Lau (1981) on axisymmetric jets, the potential core region generally contracts as the jet is heated accompanied by a corresponding faster decay of the centerline velocity. For a Mach number of 1.4, Lau shows a decrease in potential core length from approximately 6 to 4.5 diameters as the jet temperature is increased from isothermal to $T_j/T_a = 2.32$. Since the elliptic jet already has a shorter potential core than the circular jet (as will shown shortly) and the simulated temperature ratio in the present work is not large, the data of figure 4.2 appear to agree with the conclusions drawn from the work of Lau (1981) in actual heated jets. This evidence supports the use of helium to simulate a heated jet and the approximations of section 3.4.4 to estimate the local helium concentration in the jet.

4.1.2 Circular Jet Velocity Profiles

Figure 4.3 shows radial velocity profiles at four different axial locations for the air and helium circular jets. The profiles are shown for both dimensional and nondimensional values normalized by the jet exit velocity. Lau (1981) shows that the effect of temperature on unnormalized velocity profiles is to raise the velocity in the

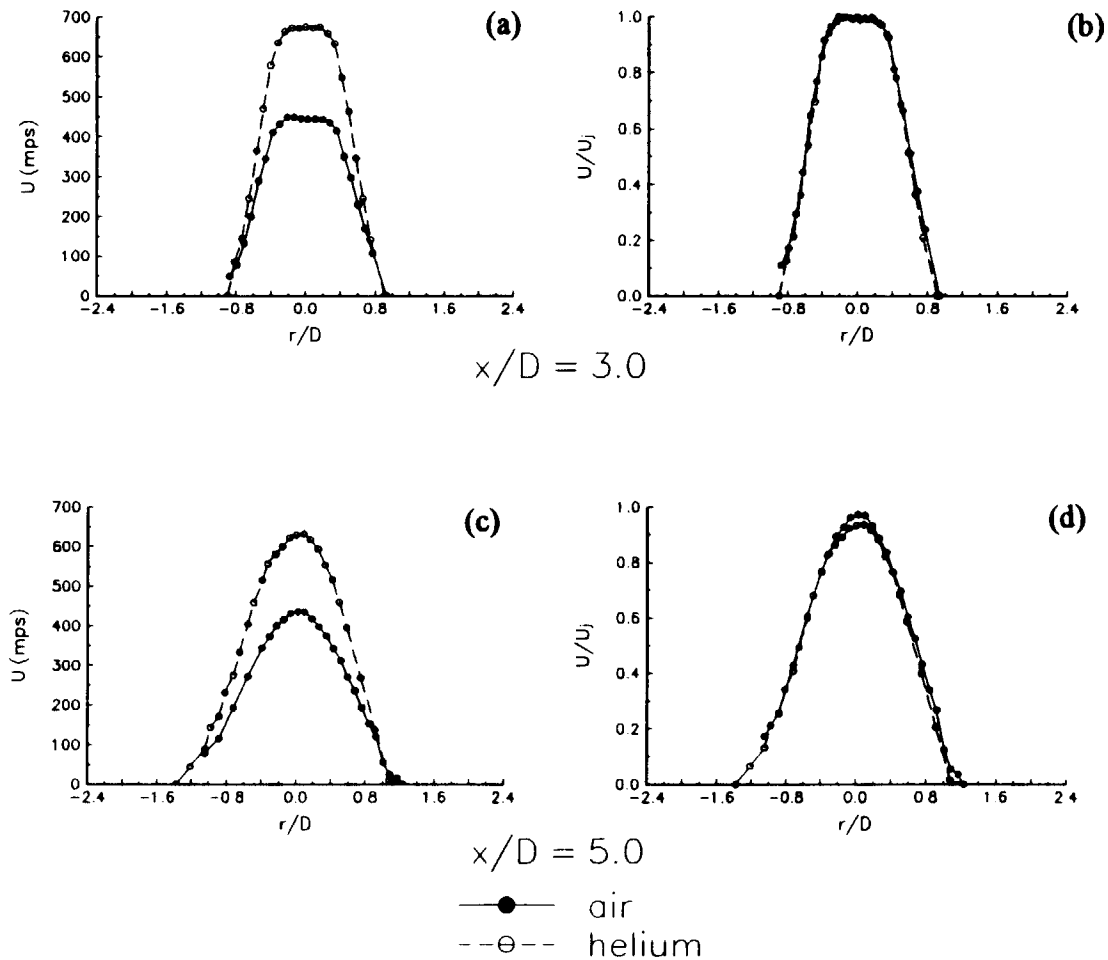

Figure 4.3 Dimensional and nondimensional velocity profiles for air and helium axisymmetric jet. (a) x/D = 3, dimensional, (b) x/D = 3, nondimensional, (c) x/D = 5, dimensional, (d) x/D = 5, nondimensional.

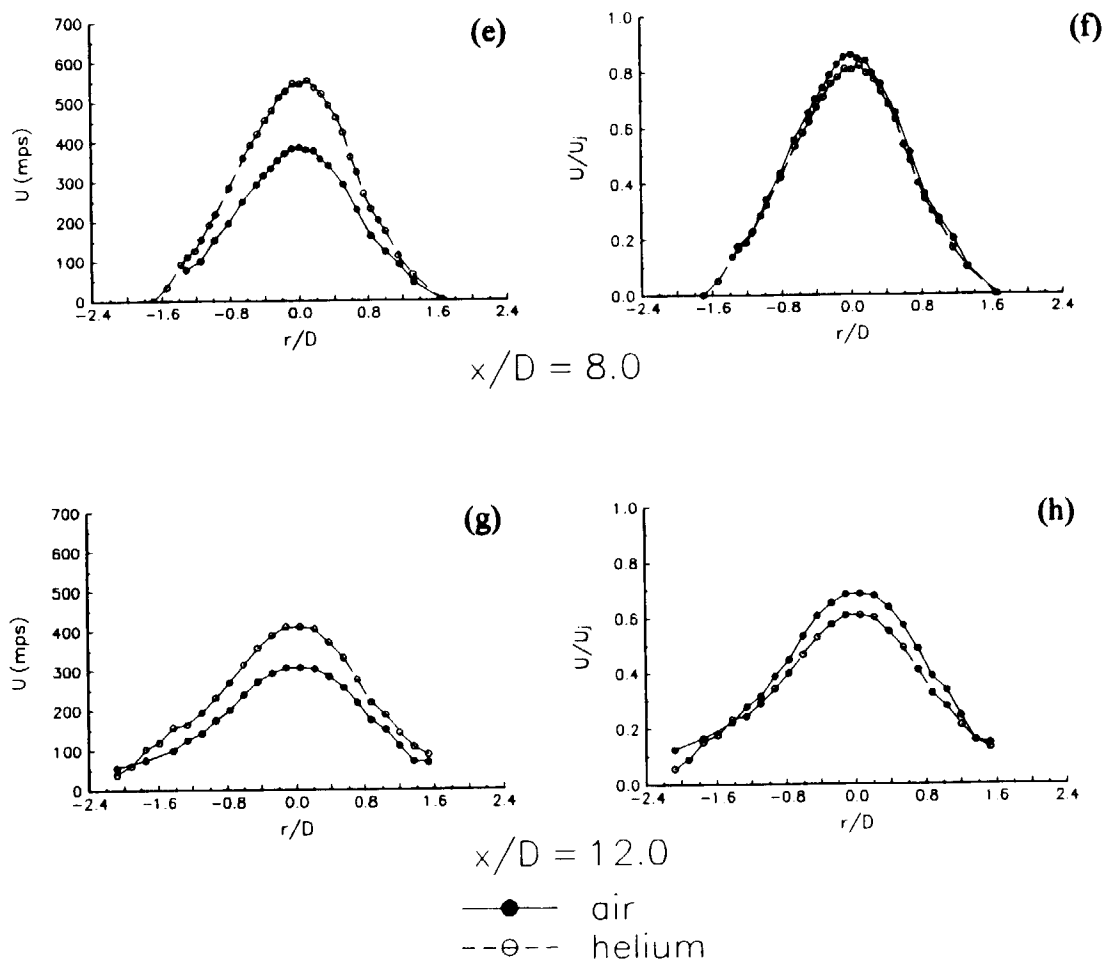

Figure 4.3 (cont.) Dimensional and nondimensional velocity profiles for air and helium axisymmetric jet. (e) x/D = 8, dimensional, (f) x/D = 8, nondimensional, (g) x/D = 12, dimensional, (h) x/D = 12, nondimensional.

center of the jet while leaving the outer region of the jet mostly unaffected. The same observation can be made from the data of figure 4.3 which show that helium increases the velocity in the inner region of the jet, but has less effect at the outer edges. As expected, the dimensional velocity profile of the simulated hot jet approaches that of the cold jet at farther downstream locations.

The normalized velocity profiles are nearly identical in the potential core region of the jet, which extends to approximately x/D = 5. As the jet develops, the faster decay of the centerline velocity with respect to the jet exit velocity is seen in the helium jet. Recall that this was also observed in the centerline velocity distribution of the air and helium elliptic jet shown in figure 4.2 and agrees with the trends measured by Lau (1981) and Seiner et al. (1993) in actual heated jets. However, even though the centerline velocity decay trend agrees with these researchers, the spread rate of the shear layers in the helium jets did not show any measurable difference over the air jet case. It is generally accepted that heating tends to decrease the spread rate of compressible mixing layers. This apparent anomaly may be understandable, however, given the difficulty in the measurement of the shear layer spreading rates in the helium jets and the only moderate simulated temperature ratio of the present work. It will be shown later that even though the helium does not appear to affect the mean flow of the jet in terms of jet spreading, it has a substantial effect on the fluctuation flowfield and radiated acoustics.

Because of the difficulty in obtaining measurable differences in the mean flow between the air jet and helium jet in the round case, detailed velocity profile

measurements were not performed for the asymmetric jet cases. The velocity profiles were checked at several downstream locations for the air and helium elliptic jet and, as with the round jet, no measurable difference was observed. It was reasoned that further measurements in the asymmetric jets would not yield any more fruitful results than the circular jet. Therefore, the remainder of the this chapter deals exclusively with measurements of the pure air jet flow fields.

4.2 Pure Air Jets

4.2.1 Centerline Mach Number and Velocity Distributions -- Pure Air Jets

Since the radiated noise is such a strong function of jet velocity, the axial centerline velocity distribution can give a rough indication of the axial region over which large amounts of noise are likely to be produced. A large region of high velocity fluid implies that more noise would be produced from that region than from other portions of the jet which have a lower velocity. The Mach wave emission process described in Chapter 1 is only present in regions of the jet where the large-scale structures convect supersonically with respect to the ambient medium. This limits the region of the jet flow where this type of noise can be generated to those where the jet velocity is high enough to induce supersonically travelling structures. Axial centerline velocity distributions can aid in the determination of this region.

Figure 4.4 shows the centerline Mach number and velocity distributions for all three jet geometries under investigation. The axial distance is normalized by the jet equivalent diameter. Note that the rectangular and round jets contain a slight shock cell structure due to the nozzle imperfections described in section 2.4.

Both of the asymmetric jets have shorter potential core lengths than the circular jet. This shortening of the potential core agrees with the measurements of Seiner et al. (1992) in high Reynolds number noncircular jets. The length of the potential core may be a relative indicator of the mixing which takes place in the jet over that region. For a jet with a higher mixing rate, the annular shear layer around the jet will grow faster and merge on the jet centerline faster than in a jet with a lower mixing rate. Therefore, the shorter potential core of the asymmetric jets suggests a higher mixing rate in these jets.

The elliptic and rectangular jet profiles are similar. They both show a potential core length of approximately 2.5 D_{eq}. The decay rate of the elliptic jet is somewhat higher than the rectangular jet. This is likely a result of the slightly higher Mach number from the rectangular jet.

The conclusion of higher mixing rates based on the nondimensional potential core length alone can be misleading since the choice of length scales in the asymmetric jets is somewhat arbitrary. For instance, if the jets were nondimensionalized by the minor axis height, the nondimensional potential core lengths would be much longer than when the equivalent diameter is used. Also, as in the case of the heated round jets measured by Lau (1981), a shortened potential core was observed even as the shear

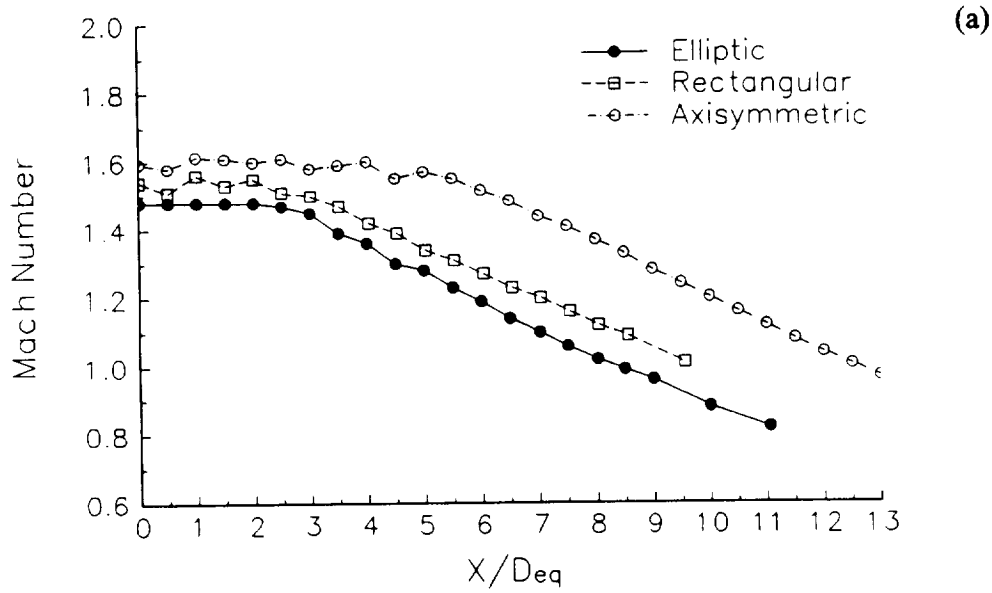

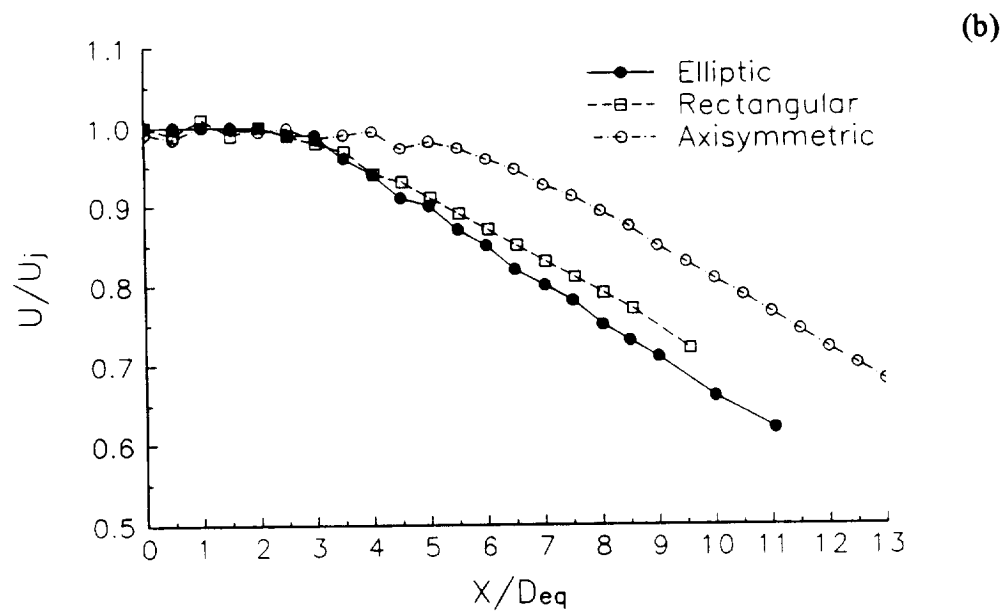

Figure 4.4 Centerline Mach number and velocity distributions for pure air jets, $T_j/T_a = 0.69$. (a) Mach number, (b) velocity.

layer growth rate decreased. However, in this case, other evidence of increased mixing is available. Zaman (1994) showed from axial mass flux measurements that asymmetric supersonic jets entrain higher amounts of fluid than similar circular jets.

The nondimensionalization by the equivalent area diameter allows the three jets to be compared based on equal thrust. The shortening of the potential core from the asymmetric nozzles indicates that if all three jets had the same exit area producing the same thrust, the circular jet would have a potential core longer than the asymmetric jets. As a result, the round jet would have a larger high velocity noise producing region than the nonround jets. As a result, the axial extent of supersonically convecting turbulence generating Mach wave emission present in the asymmetric jets should be reduced relative to a round nozzle.

4.2.2 Asymmetric Jet Velocity Profiles

As mentioned earlier, the mean flow development is very important to many analytical and computational methods. Therefore, measurements were performed to assess the radial development as well as the axial development of the jet mean flows. This was done by traversing a pitot probe across the jet shear layer at different axial locations.

Figures 4.5 (a-h) shows radial velocity profiles for the elliptic jet at a Reynolds number of 27,000. These measurements were made with the five-hole pitot rake and are normalized by the jet exit velocity. The centerline velocity for both axes does not begin to decay until an axial location of nearly $x/D_{eq} = 3.0$. This is consistent with the

centerline velocity measurements of section 4.2.1. At the end of the potential core, the minor axis profile takes on a Gaussian type distribution across the jet, while the major axis maintains a radial region of constant velocity up to an axial distance beyond $x/D_{eq} = 5$. This would result in the jet having a "wedge-like" shape between the axial locations of $x/D_{eq} = 3$ to just after $x/D_{eq} = 5$. By $x/D_{eq} = 8$, the major axis also displays a Gaussian-like shape across the jet and the jet has become nearly axisymmetric. By $x/D_{eq} = 12$, profiles on both the major and minor axis are practically identical indicating that the jet has developed to an axisymmetric shape. This axisymmetry extends through the remaining measurement range to $x/D_{eq} = 17$.

It is interesting to note that through the measurement range of $x/D_{eq} = 17$, there is no evidence of axis switching. This phenomenon is common in low-speed elliptic jets and in underexpanded elliptic jets. Hussain and Husain (1981), Zaman (1994), Schadow et al. (1989), and others have documented axis switching in elliptic jets for both the low-speed case and underexpanded case. However, measurements by Seiner et al. (1992) also show no evidence of axis switching in a perfectly expanded Mach 2, AR = 3:1 elliptic jet through an axial distance of $x/D_{eq} = 30$. Data to be presented from the rectangular jet suggest that shocks in the jet plume may play a role in the axis switching of supersonic jets.

Figures 4.6 (a-h) show radial velocity profiles from the rectangular jet at a Reynolds number of 27,000. The basic profiles are very similar to those from the elliptic jet. The "wedge-like" shape has disappeared by $x/D_{eq} = 8$. At $x/D_{eq} = 8$, the major and minor axis profiles overlay one another indicating a transition to an

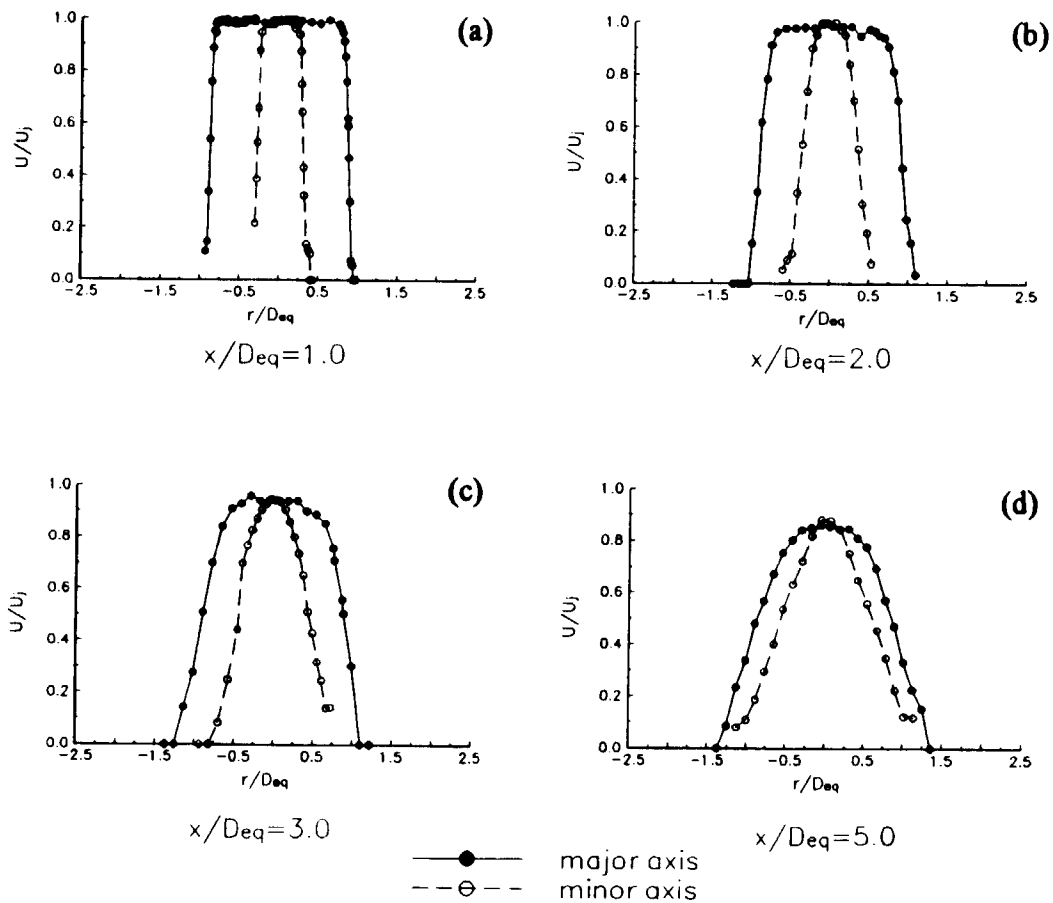

Figure 4.5 Velocity profiles for pure air elliptic jet, $T_j/T_a = 0.69$. (a) $x/D_{eq} = 1$, (b) $x/D_{eq} = 2$, (c) $x/D_{eq} = 3$, (d) $x/D_{eq} = 5$.

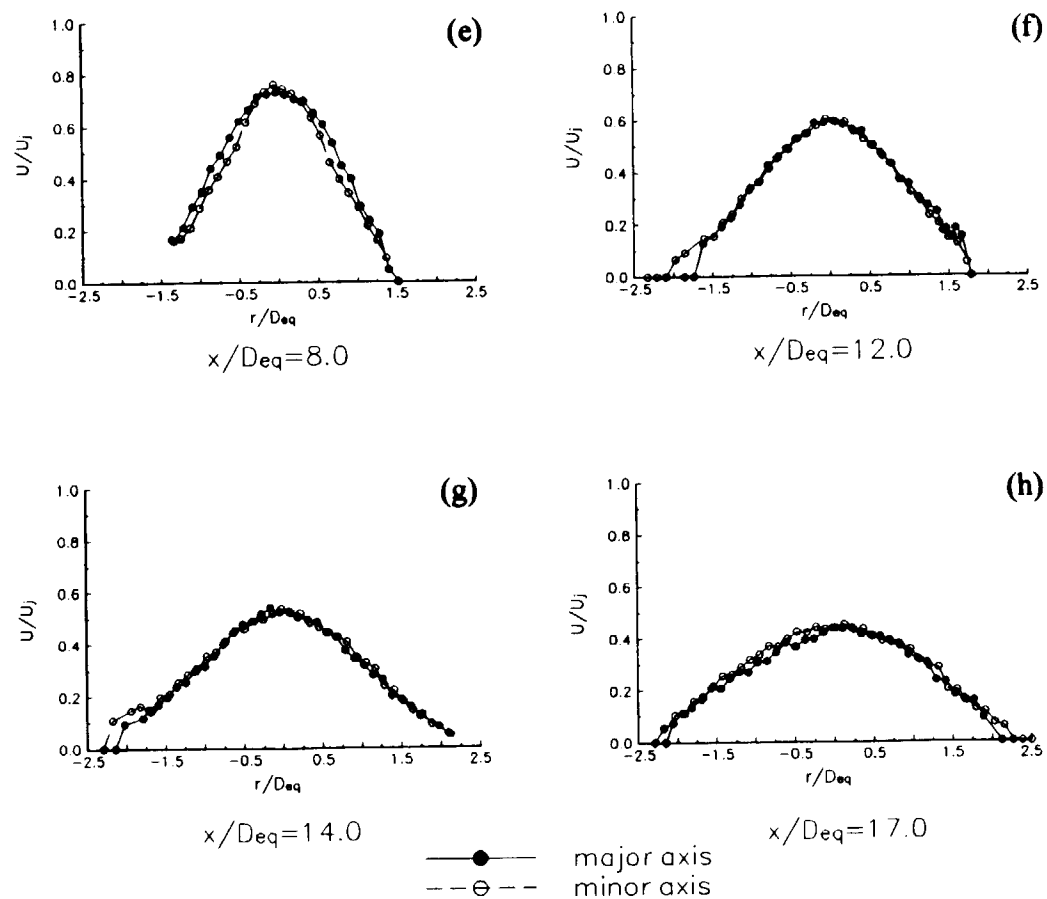

Figure 4.5 (cont.) Velocity profiles for pure air elliptic jet, $T_j/T_a = 0.69$. (e) $x/D_{eq} = 8$, (f) $x/D_{eq} = 12$, (g) $x/D_{eq} = 14$, (h) $x/D_{eq} = 17$.

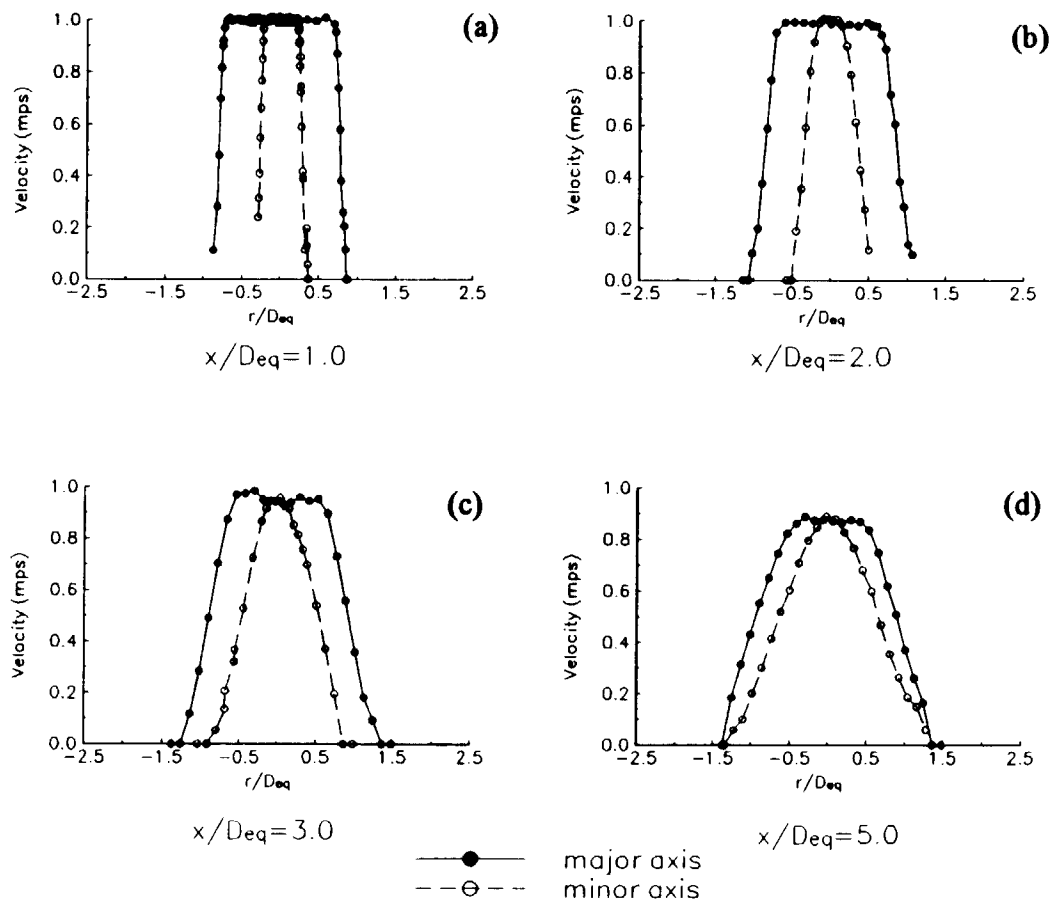

Figure 4.6 Velocity profiles for pure air rectangular jet, $T_j/T_a = 0.69$. (a) $x/D_{eq} = 1$, (b) $x/D_{eq} = 2$, (c) $x/D_{eq} = 3$, (d) $x/D_{eq} = 5$.

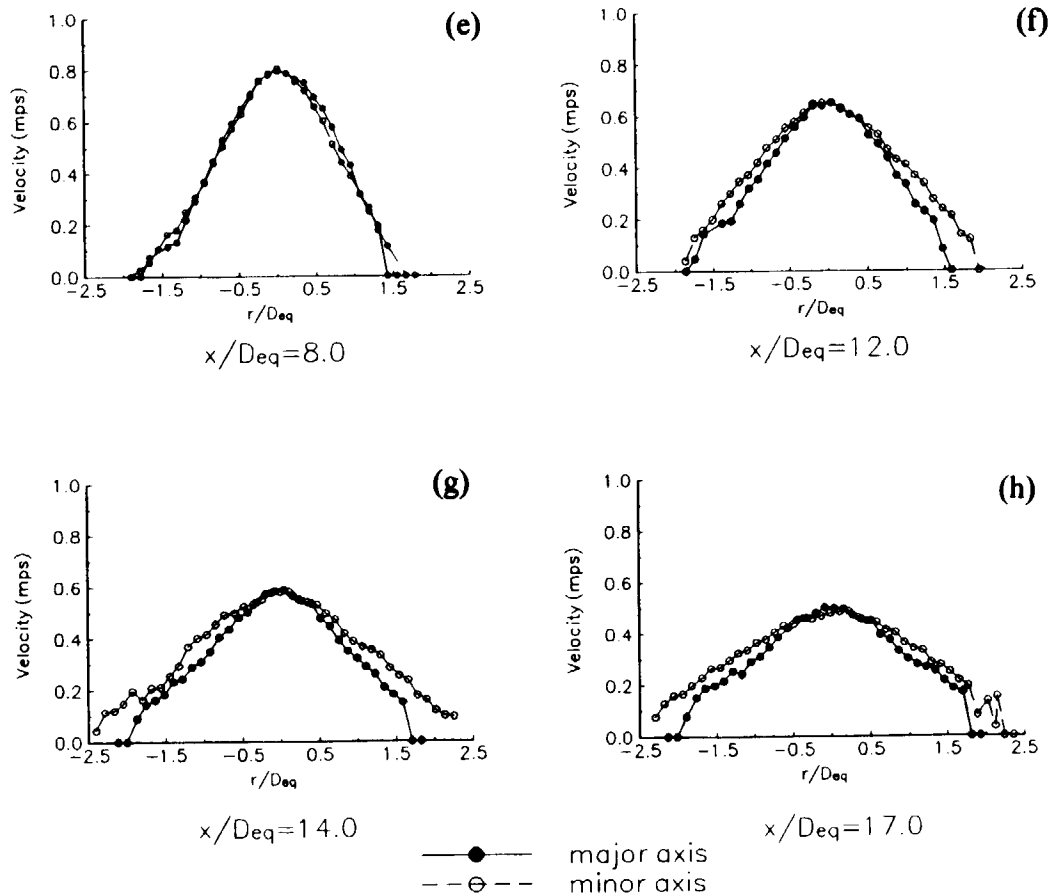

Figure 4.6 (cont.) Velocity profiles for pure air rectangular jet, $T_j/T_a = 0.69$. (e) $x/D_{eq} = 8$, (f) $x/D_{eq} = 12$, (g) $x/D_{eq} = 14$, (h) $x/D_{eq} = 17$.

axisymmetric shape. However, by $x/D_{eq} = 12$, the minor axis becomes slightly larger than the major axis indicating an axis switch. Even at $x/D_{eq} = 17$, the minor axis still appears slightly larger than the major axis.

Given the very similar initial development of the elliptic and rectangular jets, the axis switch present in the rectangular case indicates a fundamental difference between the two jets. As seen in the centerline velocity distributions, the elliptic jet shows no evidence of a shock cell structure while the rectangular does indicate a relatively weak shock cell structure. Since the author is not aware of any studies showing axis switching from supersonic perfectly expanded asymmetric jets, it is hypothesized that the shocks contained in the rectangular jet have an impact on the axis switching. Also, as measured by Zaman (1995), the vorticity dynamics present in the corners of the rectangular jet likely affect the shape of the jet cross section differently than that in the elliptic jet. The influence of shocks on axis switching is seen further by observing that the axis switch in the rectangular jet can be made much more prominent by operating the jet in a highly underexpanded condition, producing stronger shock cells. Since the focus of this work is on perfectly expanded jets, this phenomenon has not been investigated in detail.

4.2.3 Vorticity Thickness and Normalized Velocity Profiles

Figure 4.7 shows shear layer vorticity thickness as a function of axial distance on the major and minor axis for the pure air elliptic and rectangular jets. The vorticity thickness is found graphically using the method shown in figure 4.8. It is defined as:

$$\delta_{\omega} = \frac{U_{cl}}{|dU/dx|_{max}}$$

Although most researchers of supersonic jets use the momentum thickness to characterize the shear layer thickness, since the shear layers of the jets in the present work are only on the order of few millimeters, the calculation of momentum thickness by integrating the velocity profile is a time consuming process and prone to errors. Therefore, the vorticity thickness is used because it can be calculated directly from the velocity profiles as shown in figure 4.8.

In general, the vorticity thicknesses and growth rates of the major and minor axis are similar for both jets. The rectangular jet does show a slight increase in the minor axis vorticity thickness over the major axis thickness by $x/D_{eq} = 12$ where the axis switch is noticeable in the velocity profiles. It is also interesting to note that except for the axis switch in the rectangular jet, the growth rates in both planes of the jets are nearly identical. It will be shown shortly that, if a spread rate is defined using the half velocity points of the jet, the minor axis grows faster than the major axis.

In order to develop a better understanding of the asymmetric jet mean flow, the velocity profiles of figures 4.5 and 4.6 were normalized in the manner of Troutt and McLaughlin (1982). Rather than normalizing the local velocity by the jet exit velocity, the velocity is normalized by the jet velocity on the centerline at the axial measurement location. The radial distance from the jet centerline, η, is defined as:

$$\eta = \frac{(y - y_{0.5})}{\delta}$$

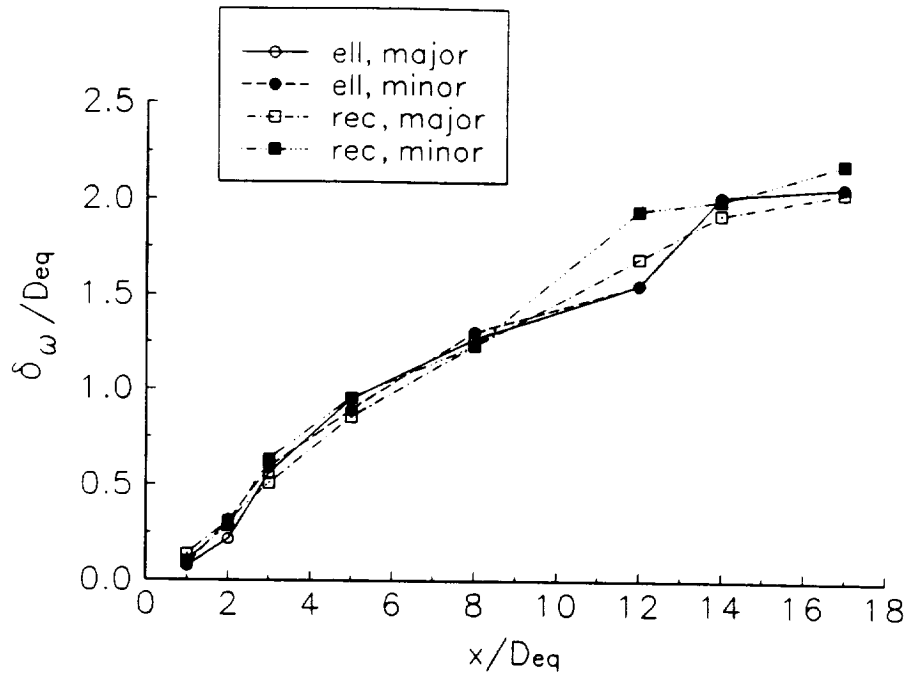

Figure 4.7 Vorticity thickness distribution for pure air jets, $T_j/T_a = 0.69$.

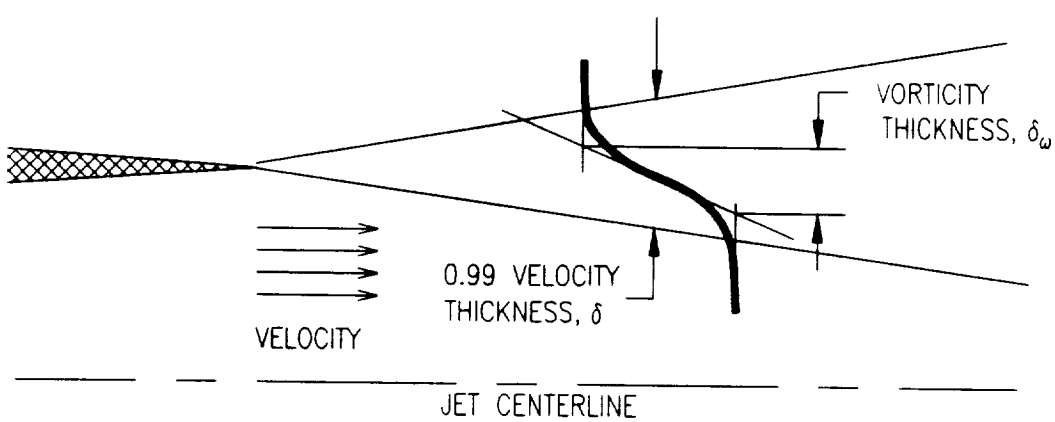

Figure 4.8 Graphical definition of vorticity thickness, δ_ω, and 0.99 velocity thickness, δ.

where $y_{0.5}$ is the distance from the jet centerline to the radial location where the velocity is half that on the centerline and δ is jet shear layer thickness between 0.99 and 0.01 times the centerline velocity. This type of normalization has been shown by Troutt and McLaughlin (1982), Lau (1986), and others to collapse the velocity profiles of axisymmetric jets over a wide axial range onto a single universal curve.

Figure 4.9 shows the normalized velocity profiles for both the major and minor axes of the pure air elliptic jet. Considering the asymmetric nature of the jet, it is surprising how well this method collapses the data, particularly since the half velocity point used as a normalization parameter is a somewhat artificial characteristic of the jet thickness due the aspect ratio of the jet differing from unity. The major axis appears to fit the universal curve better than the minor axis. Despite the asymmetry, the jet does appears to have an element of self similarity throughout the measurement range.

Figure 4.10 shows the same normalized velocity profiles on the major and minor axis for the pure air rectangular jet. The data do not collapse onto a singe curve as well as the elliptic jet. The profiles on the major axis at x/D_{eq} = 5 and 8 are particularly scattered from the rest of the data. It has already been speculated that the mild shock cell structure in the rectangular jet influences the mean flow by inducing an axis switch at x/D_{eq} = 8. This would undoubtedly have an effect on this type of normalization technique and hinder the development of the jet in a self similar manner.

Figure 4.11 shows the thickness parameters used to normalize the data of figures 4.9 and 4.10. As seen with the vorticity thickness (δ_ω) measurements, the shear layer thicknesses (δ) of both jets on each axis are similar. The axis switch is apparent in the

(a)

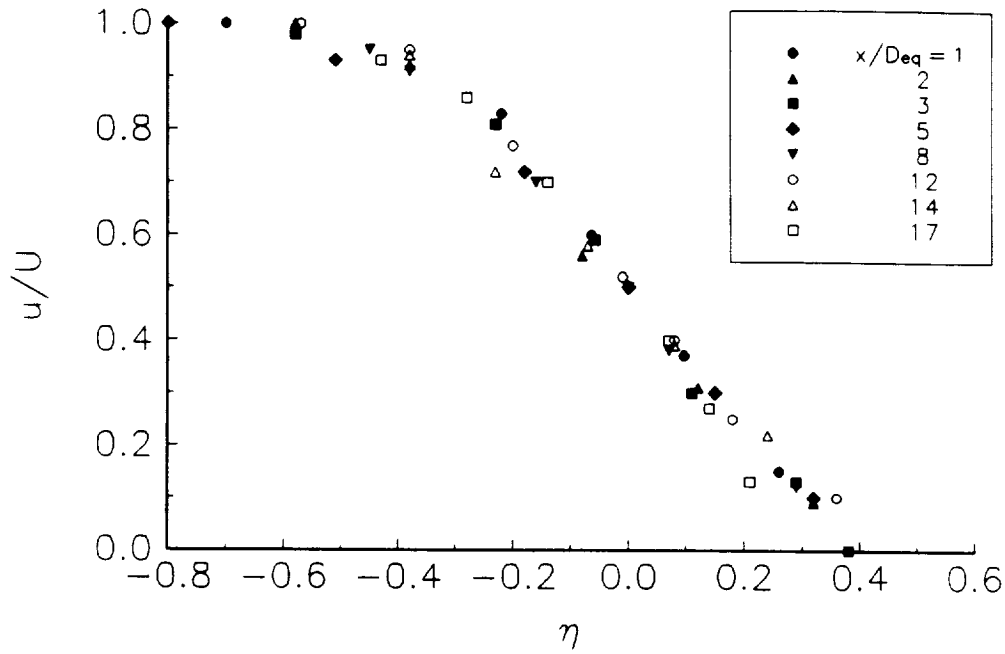

(b)

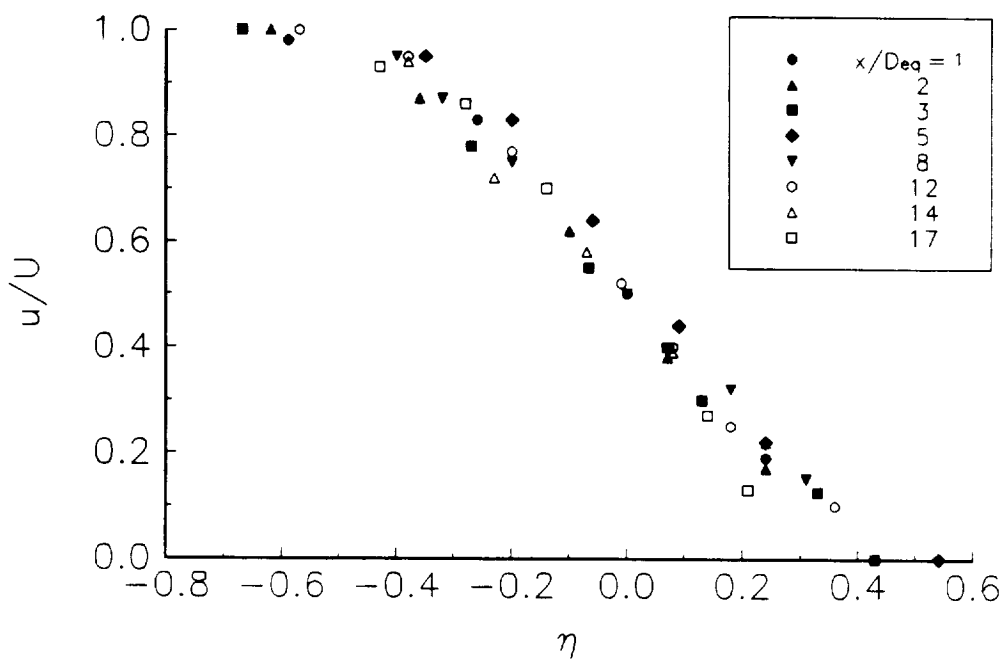

Figure 4.9 Normalized velocity profiles of the pure air elliptic jet, T_j/T_a = 0.69. (a) major axis (b) minor axis.

(a)

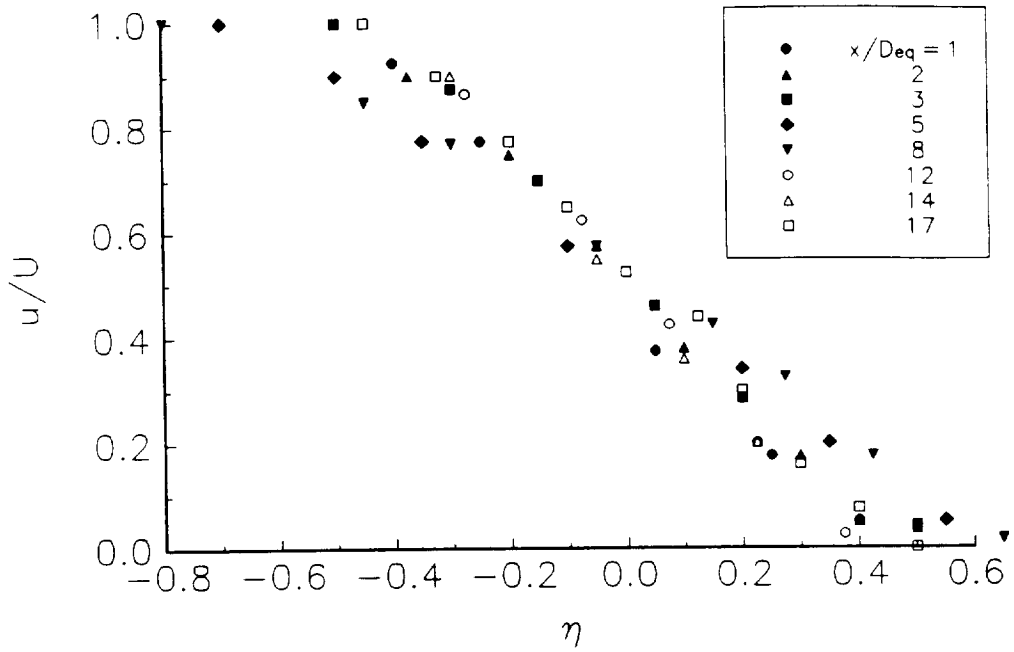

(b)

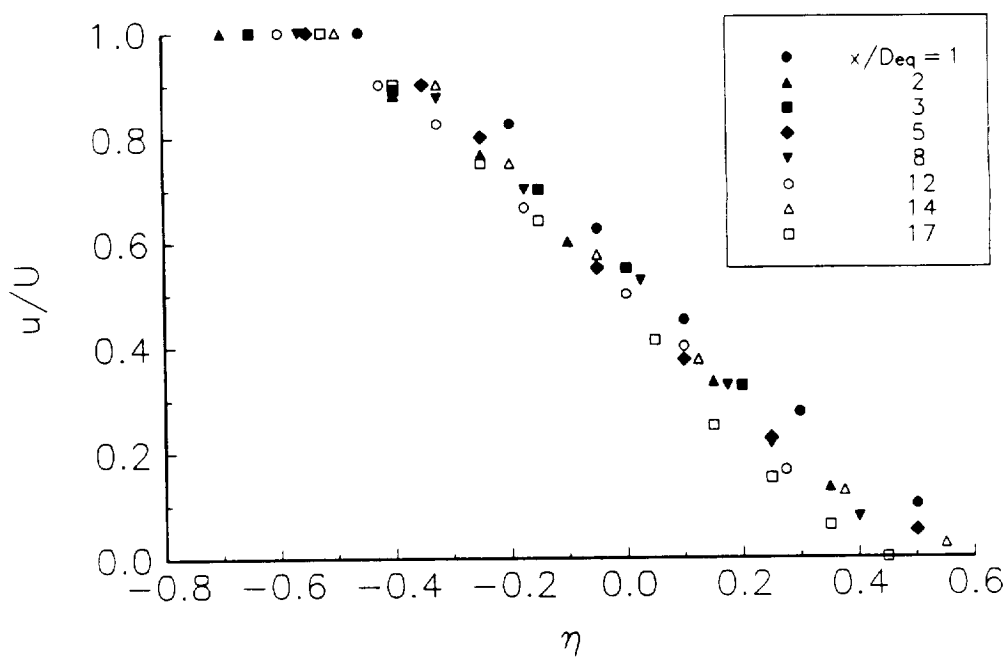

Figure 4.10 Normalized velocity profiles of the pure air rectangular jet. (a) major axis (b) minor axis.

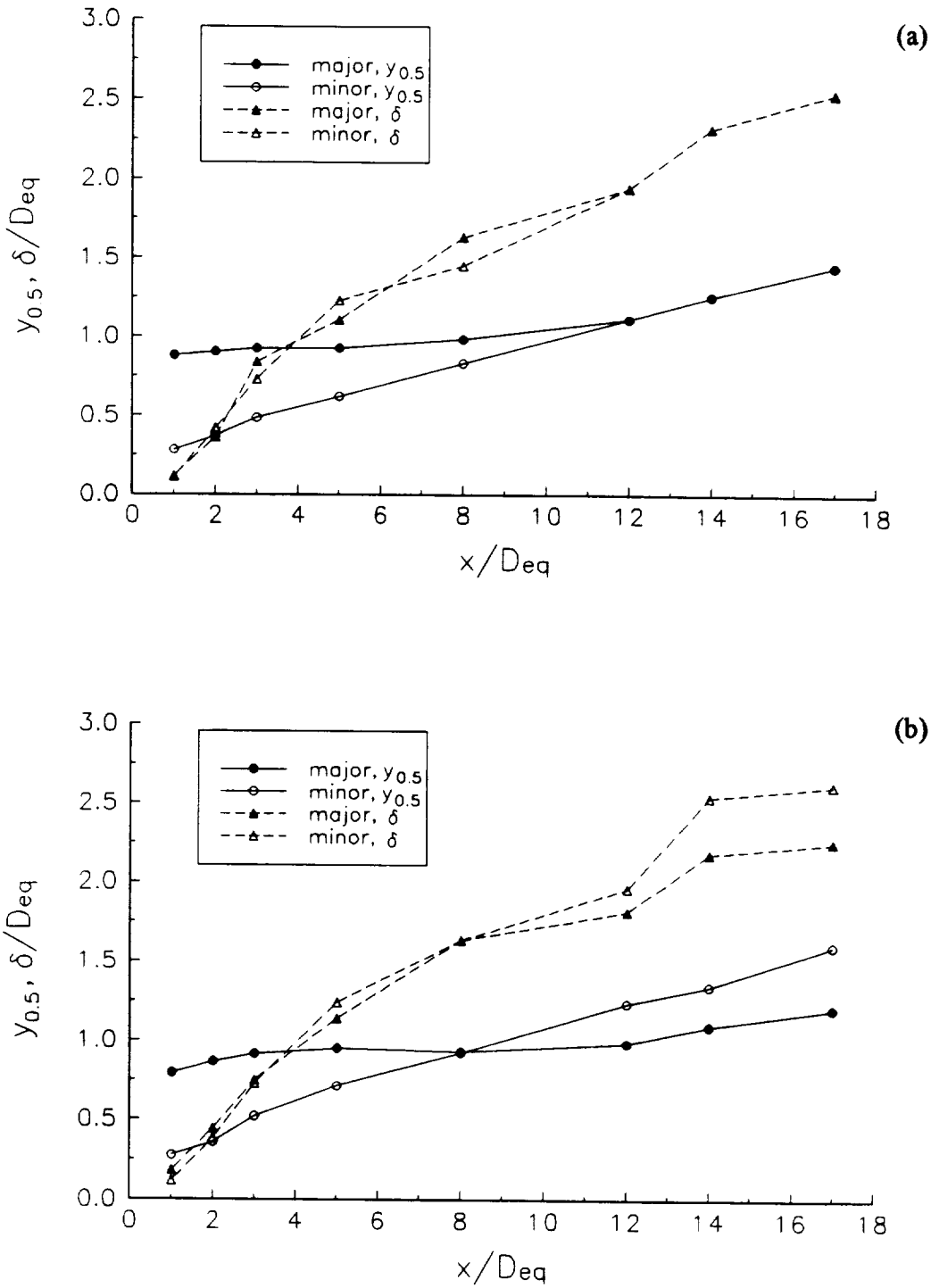

Figure 4.11 Thickness parameters used to normalize the jet velocity profiles of figures 4.9 and 4.10, $T_j/T_a = 0.69$. (a) elliptic jet (b) rectangular jet.

rectangular jet in both the shear layer thickness and the half velocity points. In both jets, the growth rate on the minor axis is higher than that on the major axis as defined by the half velocity points. However, as with the vorticity thickness growth rates shown in figure 4.7, the shear layer thickness growth rates defined by the 0.99 and 0.01 velocity points are approximately equal on both axes. Obviously, when discussing the spread rate of asymmetric jets, it is important to know exactly how the spread rate is defined.

It should be mentioned that the jet development as defined by these thickness parameters does not appear to be completely Reynolds number independent. Figure 4.12 shows the half-velocity point growth rates for the pure air elliptic jet at Reynolds numbers of 27,000 and 50,000. Through the potential core region, there is little difference between the two cases. However, as the jet develops downstream of the potential core, the higher Reynolds number jet holds its elliptic shape for a longer distance. The major axis grows at a somewhat higher rate in the higher Reynolds number case while the minor axis grows slightly slower resulting in an elliptical shape further downstream. From the velocity data of Troutt and McLaughlin (1982) in circular jets, it is seen that the reduction of Reynolds number tends to stretch out the development early in the jet because of the transitional state of the shear layers. This could explain why the major axis grows faster when the Reynolds number is increased, but it is somewhat puzzling that the minor axis growth appears to decrease. A comparison of the vorticity thickness of the high and low Reynolds number cases is shown in figure 4.13. Again, the potential core region is similar for both cases, but the

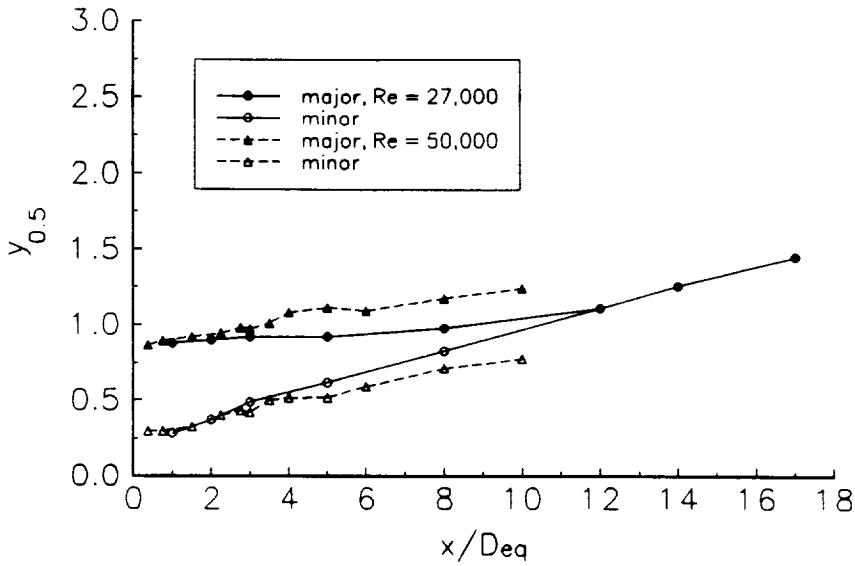

Figure 4.12 Half-velocity points of the pure air elliptic jet for Reynolds numbers of 27,000 and 50,000, T_j/T_a = 0.69.

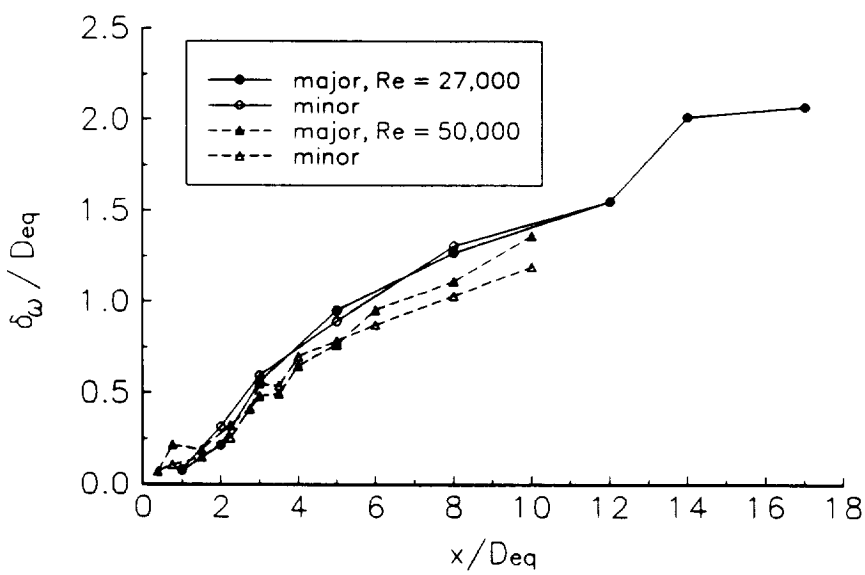

Figure 4.13 Vorticity thickness of the pure air elliptic jet for Reynolds numbers of 27,000 and 50,000, T_j/T_a = 0.69.

higher Reynolds number jet has slightly smaller vorticity thickness values farther downstream. The half-velocity point is affected much more by the change in Reynolds number.

4.2.4 Velocity Contour Measurements

Since the radial velocity profiles described in section 4.2.2 only describe the jet shape on the major and minor axis centerline planes, more detailed pressure measurements were made in off-centerline planes in order to form velocity contour distributions over a given jet cross-section. These measurements were made by traversing the five-hole rake systematically over the cross-section of the jets at various downstream locations. These measurements were made in an effort to assess differences in the mean flow development between the elliptic and rectangular jet. One would expect the rectangular jet to transition through an elliptical region before becoming axisymmetric far downstream. The question arises as to how similar is this elliptical transition region to the actual elliptic jet case.

Figure 4.14 shows side by side comparisons of the contours for each jet. From the jet exit through a downstream distance of $x/D_{eq} = 2$, it is possible to identify the shape of the nozzle as either elliptical or rectangular. Note that in the rectangular jet, there is a region of high velocity in the corners of the jet close to the jet exit. This is most likely due to corner vortices that develop inside the rectangular jet. However, by $x/D_{eq} = 3$, both jets have nearly identical shapes and are nearly indistinguishable from one another. By $x/D_{eq} = 8$, both jets are nearly axisymmetric. At $x/D_{eq} = 12$, close

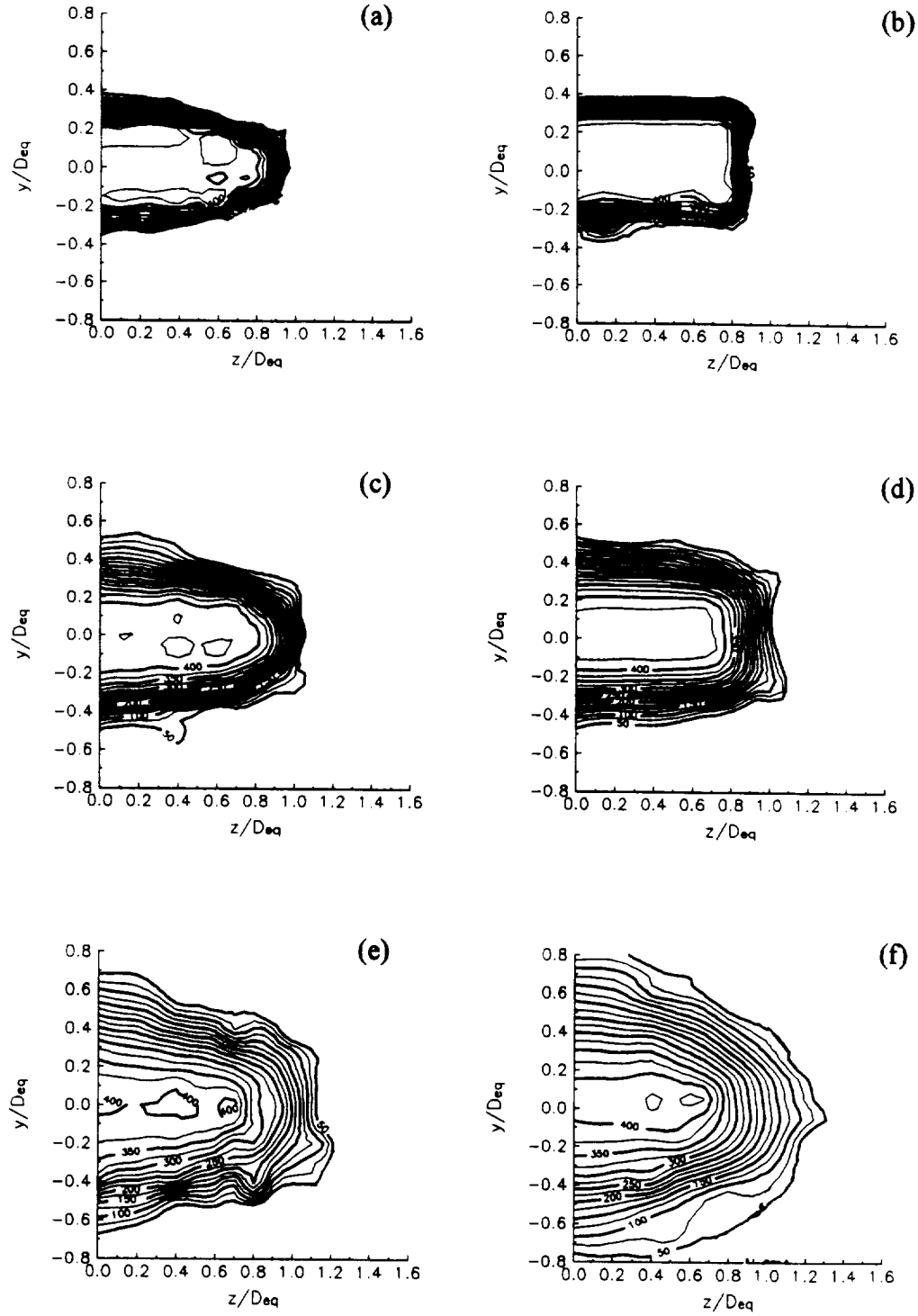

Figure 4.14 Velocity contours from pure air elliptic and rectangular jets, T_j/T_a = 0.69. (a) x/D_{eq} = 1, elliptic, (b) x/D_{eq} = 1, rectangular, (c) x/D_{eq} = 2, elliptic, (d) x/D_{eq} = 2, rectangular, (e) x/D_{eq} = 3, elliptic, (f) x/D_{eq} = 3, rectangular.

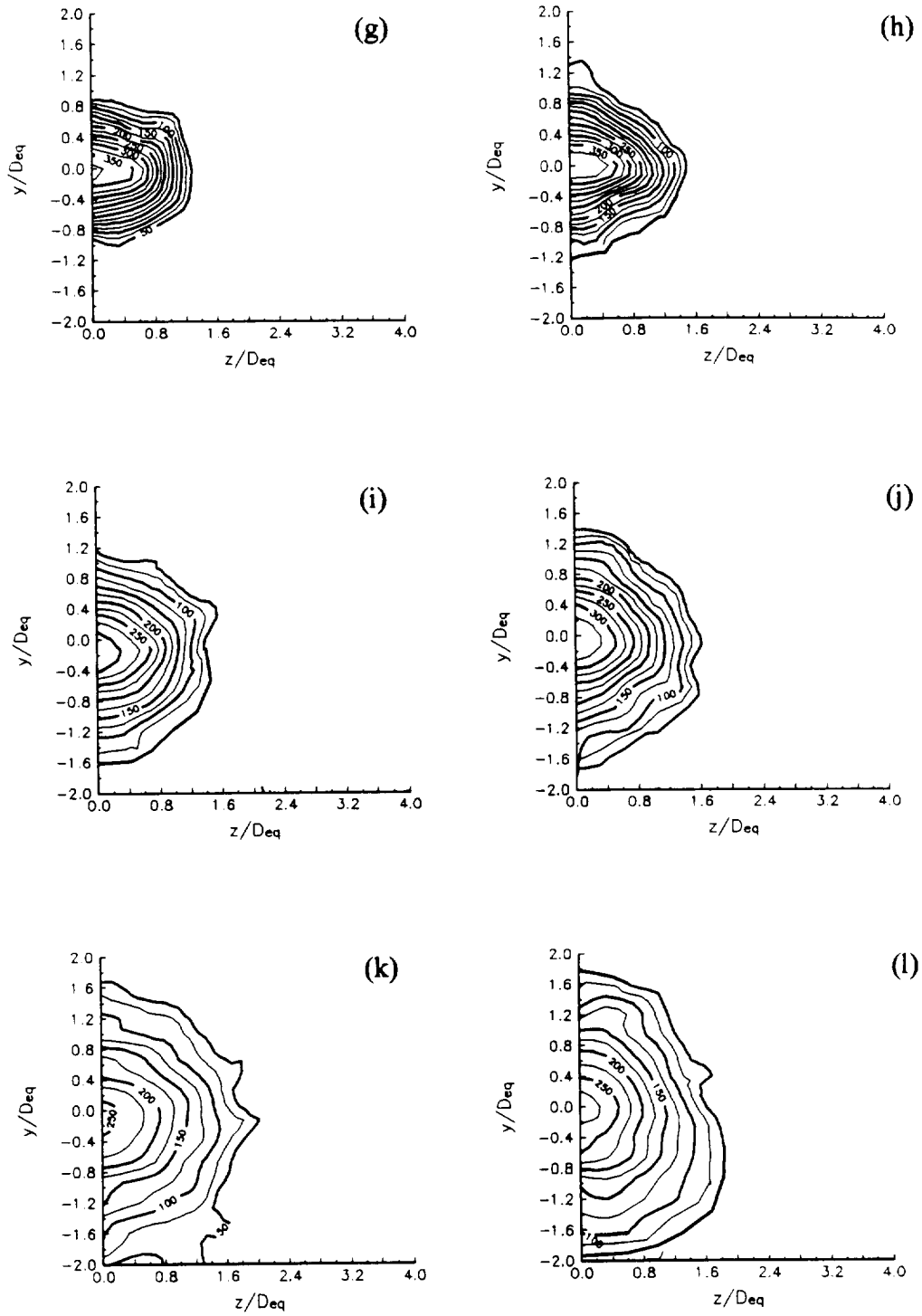

Figure 4.14 (cont.) Velocity contours from pure air elliptic and rectangular jets, $T_j/T_a = 0.69$. (g) $x/D_{eq} = 5$, elliptic, (h) $x/D_{eq} = 5$, rectangular, (i) $x/D_{eq} = 8$, elliptic, (j) $x/D_{eq} = 8$, rectangular, (k) $x/D_{eq} = 12$, elliptic, (l) $x/D_{eq} = 12$, rectangular.

examination of the rectangular jet contour does show evidence of the small axis switch as seen in the velocity profiles of figure 4.6.

Although there have been some differences, the similarity of the mean flow between the elliptic and rectangular jets is quite apparent. As will be shown later, these similarities also extend to the fluctuating velocity and far-field pressure fields. The present data suggest that, in situations where the specific elliptic or rectangular flow field is unknown, it would be a reasonable assumption to use one geometry's mean flow as an approximation to the other so long as the data are for similar operating conditions. This may occur where experimental data from only one geometry are known while analytical or computation efforts require mean flow data from the other geometry. It must be remembered, however, that the present data are for nearly perfectly expanded jets. As seen with the rectangular jet, the introduction of shock cells into the mean flow can have a potentially drastic effect on the mean flow development. The present work does not attempt to draw any conclusions concerning a comparison of the flow between two asymmetric jets operating in off-design conditions.

CHAPTER 5

FLUCTUATING FLOWFIELD MEASUREMENTS

In an effort to characterize the flow fluctuations that have a direct bearing on the radiated noise field, detailed hot-wire measurements of the asymmetric jets were made for both the pure air and helium cases. A knowledge of quantities such as root mean squared (r.m.s.) fluctuation amplitudes, spectral content measurements, and relative phase distributions can help to determine the contribution of the various modes to the radiated sound as well as allow calculation of the instability wave phase velocities.

5.1 Hot-wire Fluctuation Amplitudes

Figure 5.1 shows hot-wire spectra measured at several axial locations in the shear layer of the pure air elliptic jet. For comparison, both the major and minor axis plane fluctuations are shown on the same graphs. For these measurements and all other similar hot-wire fluctuation measurements, the hot-wire is placed at the approximate location of maximum r.m.s. amplitude. This is close to the jet lip throughout the potential core region and then moves to the jet centerline downstream of the potential core. The amplitudes are normalized by the maximum mean squared fluctuation level over all measurement locations. Therefore, the value of the ordinate of figure 5.1 is defined as:

$$(\rho u)_* = \left\{\frac{(\rho u)'}{(\rho u)'_{max}}\right\}^2 \Big/ \mathrm{Hz}$$

Early fluctuations in the minor axis plane are characterized by peaks that appear and disappear in the spectra. By $x/D_{eq} = 2.5$, energy around St = 0.4 begins to show the highest amplitude. These components grow and continue to have the highest amplitude through a location of $x/D_{eq} = 5.0$. Morris and Bhat (1995) predict the St = 0.4 component to be close to the instability wave with the highest growth rate in a Mach 1.5, AR = 3 elliptic jet. By $x/D_{eq} = 7.0$, the fluctuation levels are significantly lower with the highest levels shifting to the lower frequency components. In this regard, the spectra of figure 5.1 bear a strong resemblance to the spectral evolution measured by Troutt and McLaughlin (1982) in a round moderate Reynolds number Mach 2.0 jet.

Rather than showing sharp peaks as in the minor axis, the major axis plane spectra show a much more broad-band frequency content. In fact, the St = 0.4 component prevalent in the minor axis hardly shows any increase at all over the broad-band level of the spectra. The levels of the individual frequency components are also generally lower in the major axis plane than in the minor axis plane. As will be shown shortly, this leads to lower overall fluctuation levels in the major axis plane compared to the minor axis plane.

Figure 5.2 shows hot-wire spectra measured in the minor and major axis planes for the helium elliptic jet. Again, the spectra amplitudes have been normalized by the

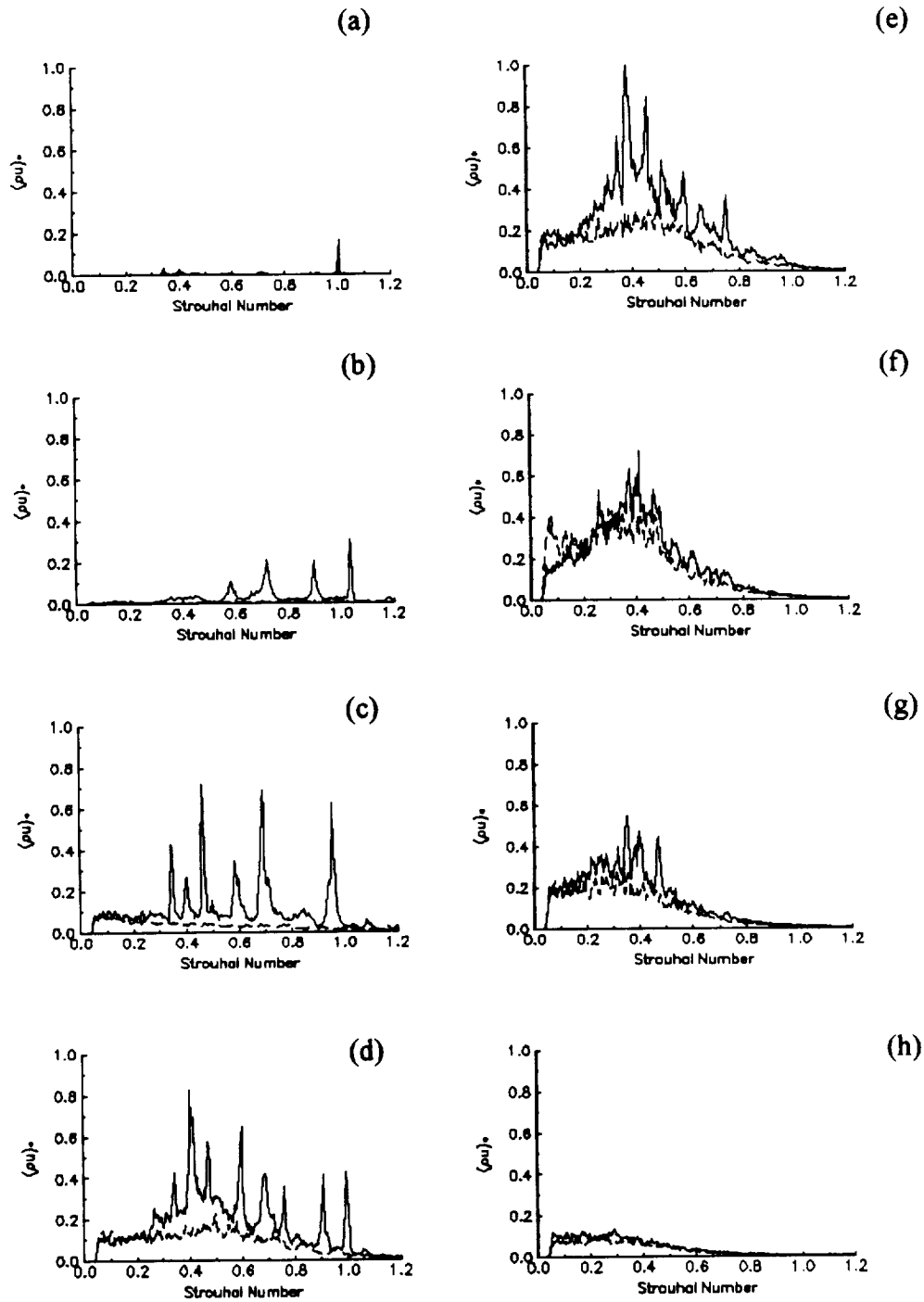

Figure 5.1 Hot-wire spectra measured in pure air elliptic jet, $T_j/T_a = 0.69$. —— minor axis; - - - - major axis. (a) $x/D_{eq} = 1.0$, (b) $x/D_{eq} = 1.5$, (c) $x/D_{eq} = 2.0$, (d) $x/D_{eq} = 2.5$, (e) $x/D_{eq} = 3.0$, (f) $x/D_{eq} = 4.0$, (g) $x/D_{eq} = 5.0$, (h) $x/D_{eq} = 7.0$.

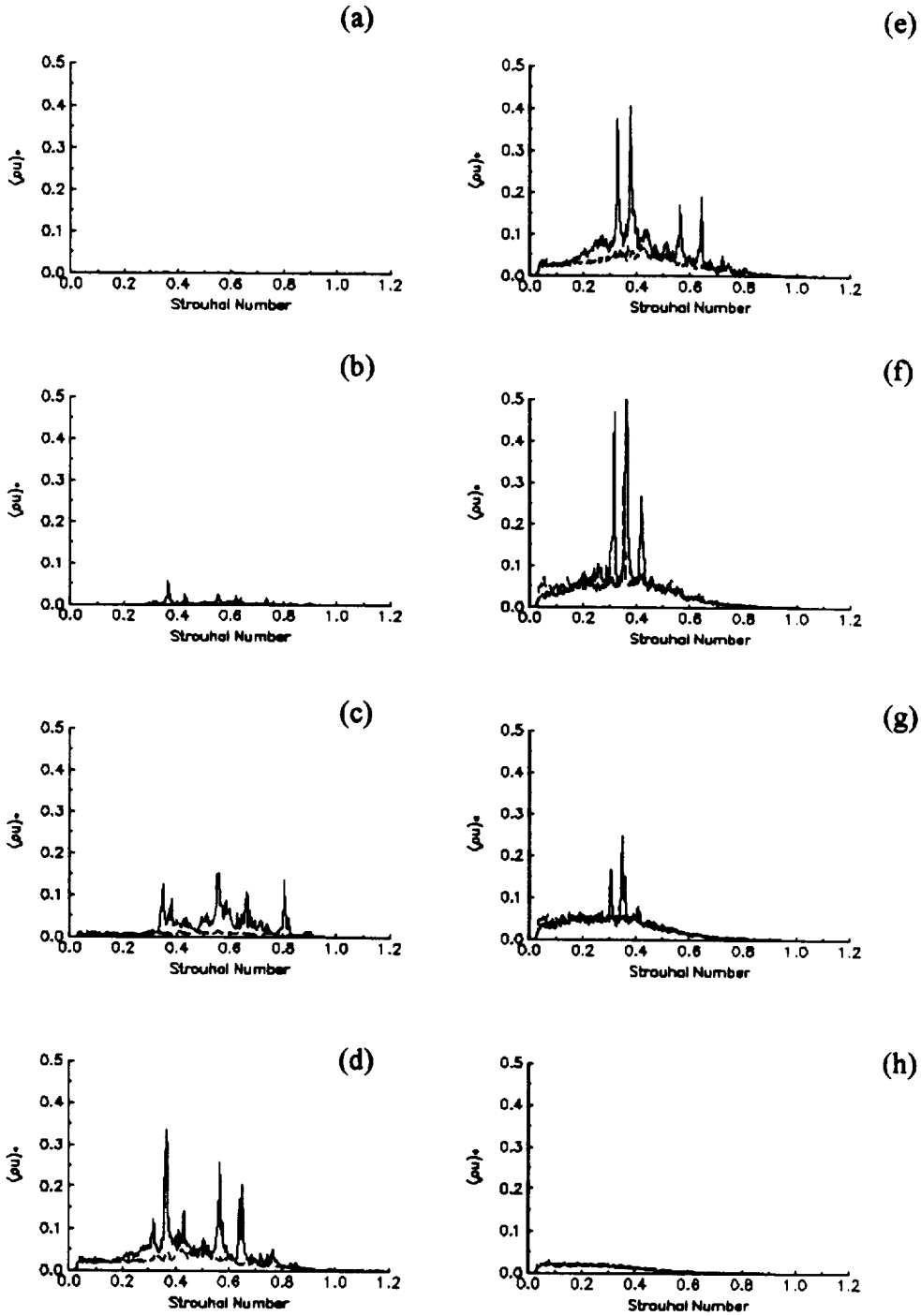

Figure 5.2 Hot-wire spectra measured in helium elliptic jet, $T_j/T_a^* = 1.2$. —— minor axis; - - - - major axis. (a) $x/D_{eq} = 1.0$, (b) $x/D_{eq} = 1.5$, (c) $x/D_{eq} = 2.0$, (d) $x/D_{eq} = 2.5$, (e) $x/D_{eq} = 3.0$, (f) $x/D_{eq} = 4.0$, (g) $x/D_{eq} = 5.0$, (h) $x/D_{eq} = 7.0$.

maximum level over all measurement locations. However, the full range of the vertical scale is not displayed in figure 5.2 in order to show the detail over the entire frequency range. This is required due to the large relative amplitude of the narrow spikes seen in the spectra. In general, the spectra show the same trends as the air jet. The minor axis plane shows narrow peaks throughout its development with the peak level located around St = 0.38. The peaks tend to be narrower and have higher relative amplitudes than those in the air jet. As with the air jet, the major axis plane spectra tend to be flatter and of lower level than the minor axis plane.

Figure 5.3 shows hot-wire spectra measured in the pure air rectangular jet. The minor axis spectra show two sharp peaks which appear in the first axial location (x/D_{eq} = 1) and are present all the way through x/D_{eq} = 5. The absence of any kind of analogous peaks in the elliptic jet and the narrow band nature of the spikes imply that these high frequency tones are related to the shock cells contained in the rectangular jet. Far-field acoustic spectra to be shown later also show dominate tones at these same frequencies. The lower frequency peak at St = 0.3 agrees well with Tam's (1988) prediction theory of fundamental screech tones from rectangular jets, even though Tam only claims his theory to be good for aspect ratios above 4. The nature of the second peak is more difficult to characterize. It has a value approximately 2.8 times that of the lower peak thus eliminating the possibility of it simply being an integer harmonic of the fundamental screech frequency. A more thorough discussion of these screech tones will be delayed until Chapter 6.

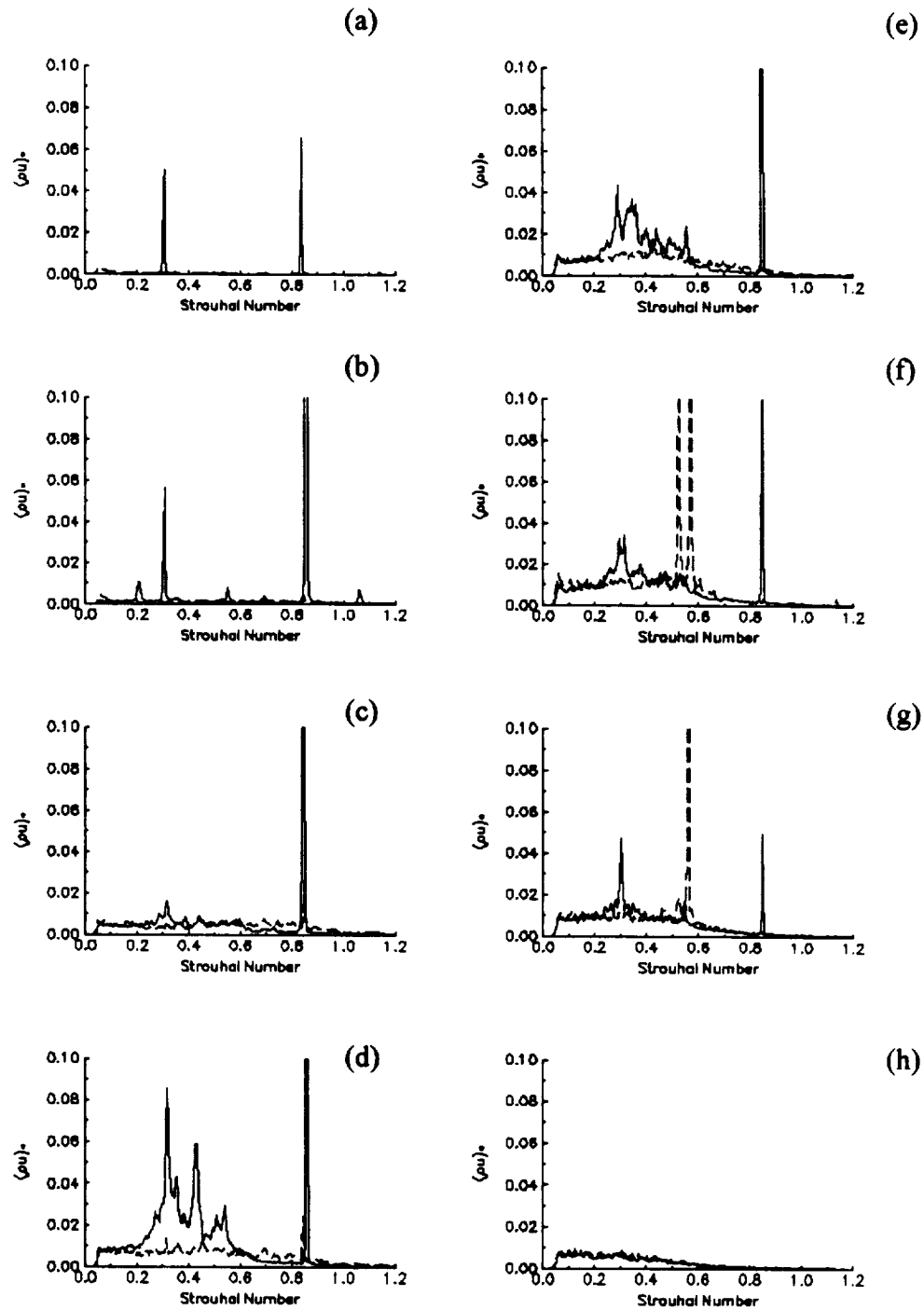

Figure 5.3 Hot-wire spectra measured in pure air rectangular jet, $T_j/T_a = 0.69$. —— minor axis; - - - - major axis. (a) $x/D_{eq} = 1.0$, (b) $x/D_{eq} = 1.5$, (c) $x/D_{eq} = 2.0$, (d) $x/D_{eq} = 2.5$, (e) $x/D_{eq} = 3.0$, (f) $x/D_{eq} = 4.0$, (g) $x/D_{eq} = 5.0$, (h) $x/D_{eq} = 7.0$.

Aside from the two dominate narrow band tones, the rectangular jet minor axis spectra bear a strong resemblance to the elliptic jet minor axis spectra. The peak in the broad-band hump of the rectangular jet is close to St = 0.3, a little lower than that found in the elliptic jet. This is likely due in part to the fundamental screech frequency also occurring at approximately St = 0.3 and the slightly higher Mach number of the rectangular jet.

As with the elliptic jet, the major axis plane fluctuations show lower levels than the minor axis plane. They show little evidence of the St = 0.83 tone found in the minor axis plane. What does stand out in these spectra, however, are tones around a Strouhal number of 0.55. At $x/D_{eq} = 4.0$ there are two closely spaced tones while at $x/D_{eq} = 5$ there is only one. It is interesting that these tones do not appear in the minor axis plane. Raman and Rice (1994) recently observed that the fundamental screech mechanism in a high aspect ratio rectangular jet appears as an antisymmetric mode while the second harmonic of the screech tone appears as a symmetric mode. This could explain why the St = 0.55 tone is measured only in the major axis plane. This phenomenon will be discussed further in the rectangular jet acoustic section.

Hot-wire spectra in the minor and major axis planes of the rectangular helium jet are shown in figure 5.4. Tam's (1988) fundamental screech frequency is prominent only at $x/D_{eq} = 4.0$ for these jet conditions. The large high frequency tone is present at a slightly lower Strouhal number, St = 0.68. Once again, it is approximately 2.8 times the fundamental screech tone frequency. Again, tones close to the second harmonic of the fundamental screech frequency appear in the major axis spectra. The

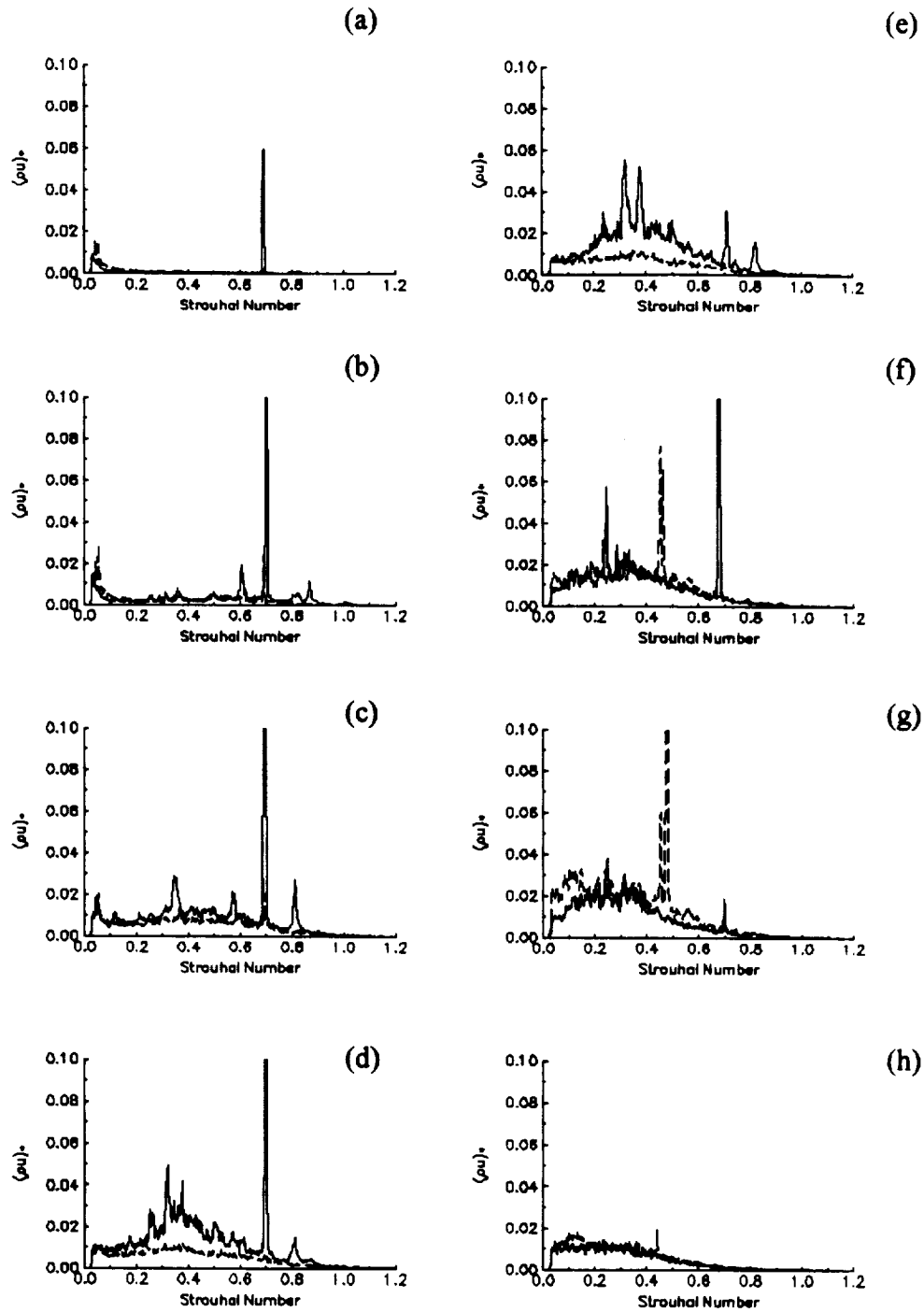

Figure 5.4 Hot-wire spectra measured in helium rectangular jet, $T_j/T_a^* = 1.2$. —— minor axis; - - - - major axis. (a) $x/D_{eq} = 1.0$, (b) $x/D_{eq} = 1.5$, (c) $x/D_{eq} = 2.0$, (d) $x/D_{eq} = 2.5$, (e) $x/D_{eq} = 3.0$, (f) $x/D_{eq} = 4.0$, (g) $x/D_{eq} = 5.0$, (h) $x/D_{eq} = 7.0$.

minor axis spectra are comparable in frequency content to those measured in the minor axis of the elliptic helium jet.

The maximum mass-velocity fluctuation levels for the unexcited pure air elliptic jet as a function of downstream distance are shown in figure 5.5a. As implied by the individual spectra, the overall levels measured in the minor axis plane are higher than those measured in the major axis plane. The minor axis plane shows higher fluctuation levels throughout the potential core region and then begins to approach the major axis fluctuation levels further downstream. Measurements for the helium jet case are shown in figure 5.5b. The hot-wires were calibrated as described in section 3.4.5 to obtain these overall levels. A higher uncertainty level is associated with these measurements due to the assumptions required for the calibration. The helium jet case shows the same trend as the air jet case with the minor axis plane having higher fluctuation levels as the major axis plane through the potential core region.

Figures 5.6a and 5.6b show the same measurements for the rectangular jet. The results in the air jet are very similar to those in the pure air elliptic jet case. The fluctuation levels for the helium jet case, however, appear to have very irregular trends and are likely in error. It appears from all jet cases that the minor axis fluctuation levels grow at a faster rate and peak slightly farther upstream than the those on the major axis. This will be related shortly to a higher growth rate measured for the flapping mode compared to the varicose mode. It is likely that the difference in fluctuation levels between the two axes in the asymmetric jets is directly related to the

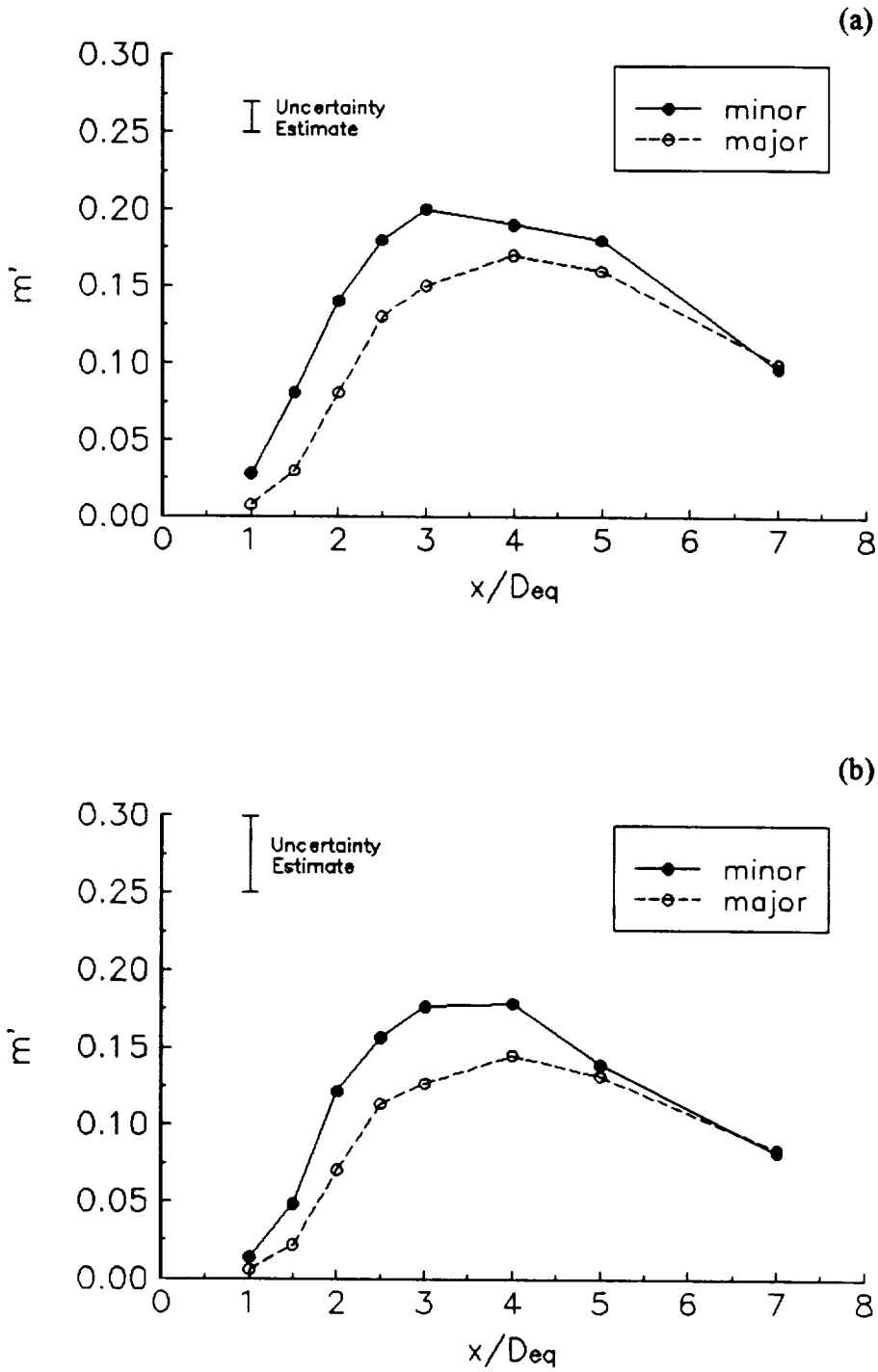

Figure 5.5 Overall mass-velocity fluctuation levels in natural elliptic jet as a function of axial distance from nozzle. (a) pure air jet, $T_j/T_a = 0.69$, (b) helium jet, $T_j/T_a^* = 1.2$.

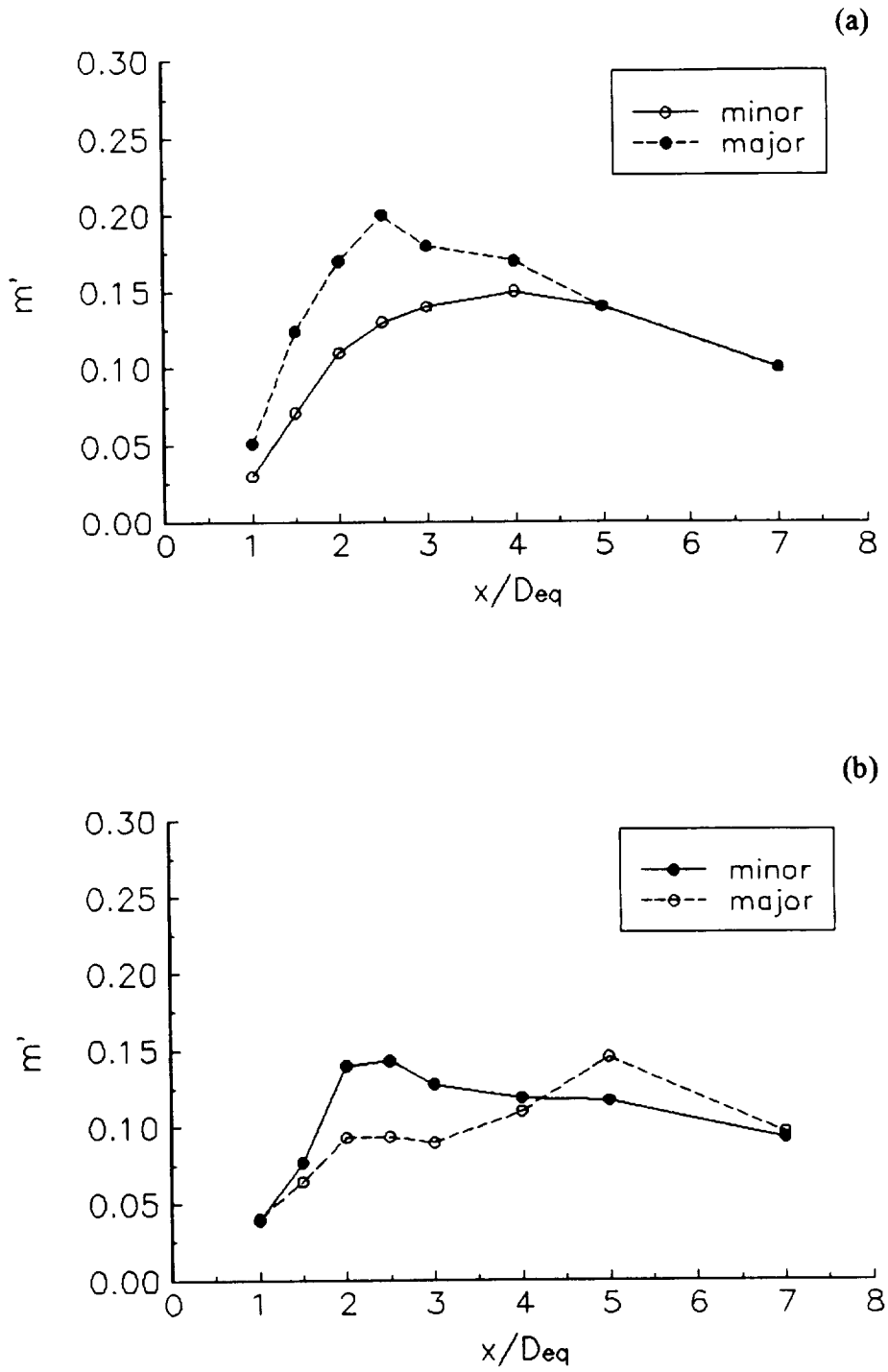

Figure 5.6 Overall mass-velocity fluctuation levels in natural rectangular jet as a function of axial distance from nozzle. (a) pure air jet, $T_j/T_a = 0.69$, (b) helium jet, $T_j/T_a^* = 1.2$.

lower noise levels measured in the major axis plane. These acoustic measurements will be presented in the next chapter.

5.2 Instability Mode Growth Rates

Tam and Morris (1980) showed that the radiated noise from a compressible mixing layer is strongly dependant on the growth and decay of individual frequency components in the shear layer. The frequency components with the highest axial growth rates, or most unstable components, are normally the ones that radiate the most noise to the far-field. Morris and Bhat (1992, 1993) predict the flapping mode to have a higher growth rate than the varicose mode in a Mach 1.5, AR = 3 elliptic jet. Therefore, they also predict the flapping mode to radiate more strongly to the far-field.

By exciting the jet in either a varicose mode or flapping mode and measuring the fluctuation amplitude as a function of axial distance, it is possible to determine the relative axial growth rate of each mode at a specific frequency. Figure 5.7a shows the fluctuation levels as a function of downstream distance for the pure air elliptic jet excited at a Strouhal number of 0.4. Figure 5.7b shows the same data for the helium elliptic jet. The slope of the curves give an indication of the growth rate of each mode. The initial exponential growth region noted by Troutt and McLaughlin (1982) in a Mach 2 round jet is less apparent in the present measurements. The flapping mode does show a higher growth rate than the varicose mode for both jet conditions.

From these data, it might be expected that the flapping mode will radiate more noise than the varicose mode for both the air and helium jets. However, it will be

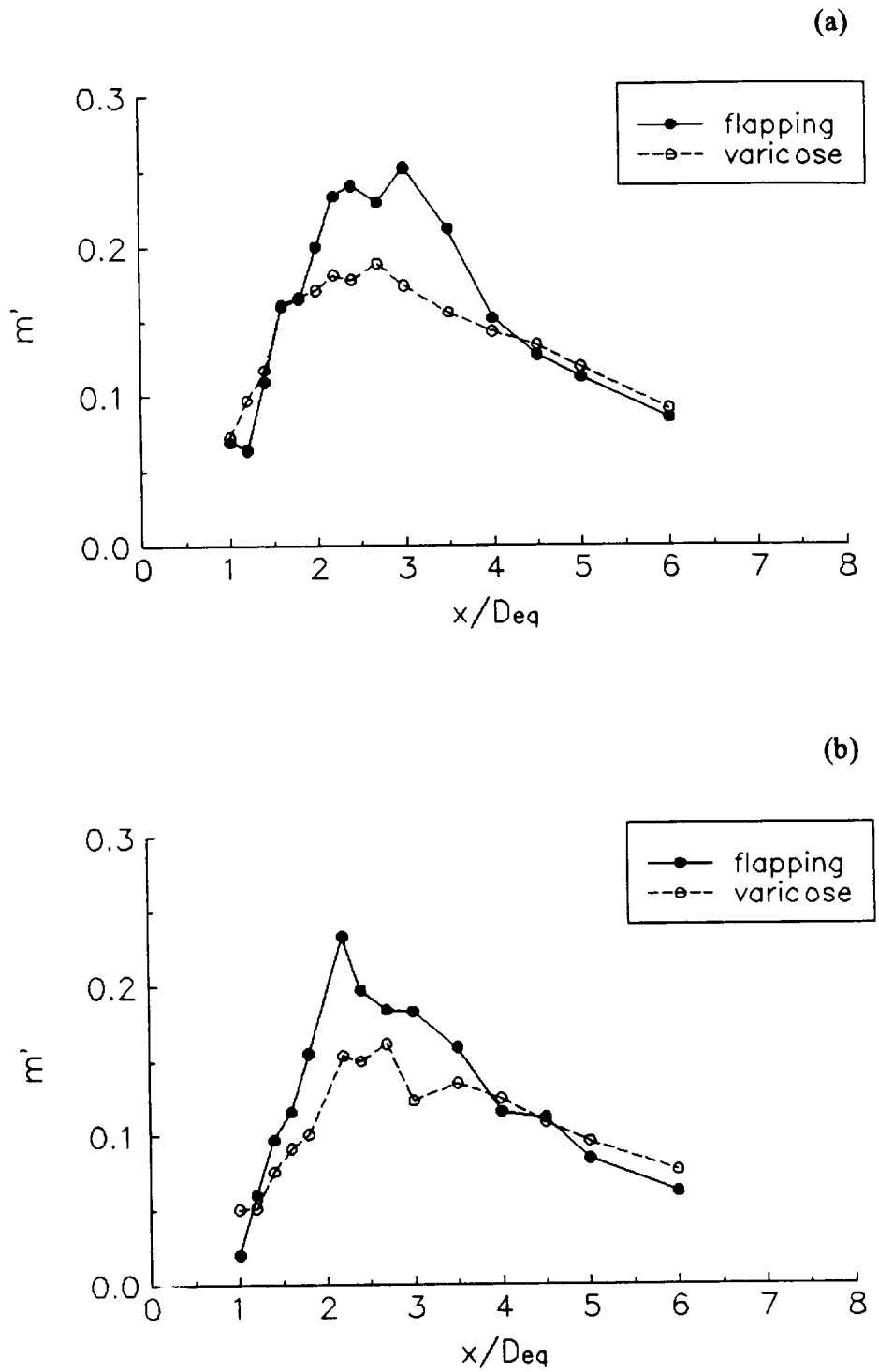

Figure 5.7 Fluctuation amplitudes in elliptic jet excited at St = 0.4 showing the growth rate of individual modes. (a) pure air jet, $T_j/T_a = 0.69$, (b) helium jet, $T_j/T_a^* = 1.2$.

demonstrated that the phase speed of each mode plays a significant role in how efficiently each mode radiates to the far-field. Additionally, since the flapping mode radiates primarily in the minor axis plane, one might expect to measure higher noise levels in that plane due to the flapping. This is in fact the case as will be shown by the acoustic measurements in the next chapter.

5.3 Axial Phase Speed

Since the convection velocity of the large-scale structures is such an important parameter relative to Mach wave emission, an effort has been made to measure the convection speed of the structures quantitatively. By cross-correlation of the excitation signal with the hot-wire signal and calculation of the phase difference as a function of axial position of the hot-wire, the phase velocity of the large-scale structures can be determined. Figure 5.8a shows the axial phase distribution for the pure air elliptic jet excited at a Strouhal number of 0.44. For the regions where the phase distribution is a linear function of axial distance, the slope of the line can be used to calculate the wavelength of the instability wave. The wave length, λ, is equal to $360^{\circ}/m$ where m is the slope of the line as shown in figure 5.8. Since the excitation frequency is known, the convection velocity of the wave can be calculated ($U_c = f\lambda$). Note that convection velocity is inversely proportional to the slope of the phase plot.

It is apparent from the change in slope of the lines at the end of the potential core region in figure 5.8a that the convection velocity of the structures change at this location in the jet. In the potential core region, the data of figure 5.8a show the

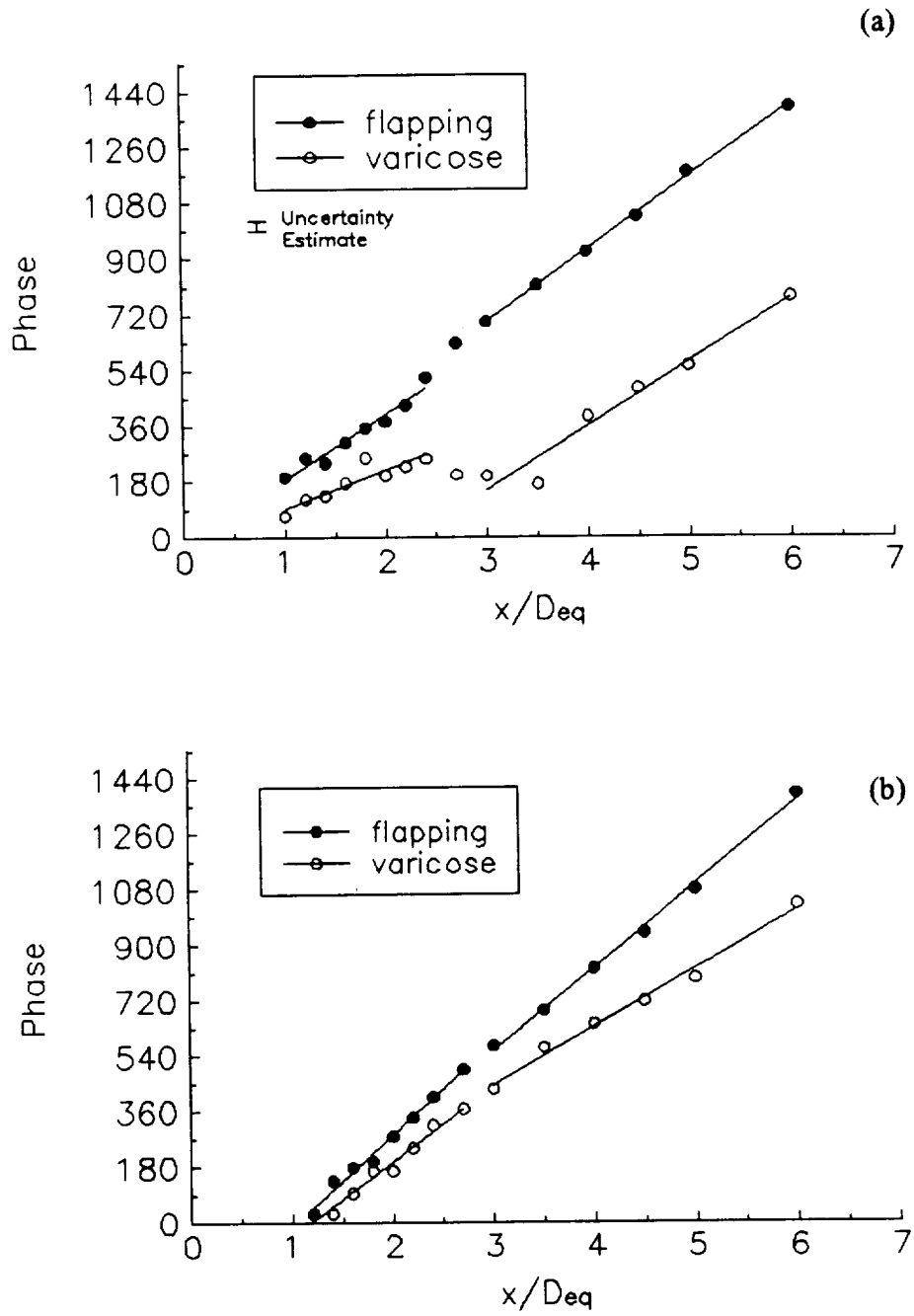

Figure 5.8 Axial phase distribution for elliptic jet excited at St = 0.4. (a) pure air jet, $T_j/T_a = 0.69$, (b) helium jet, $T_j/T_a^* = 1.2$.

varicose mode to have a phase velocity relative to the jet exit velocity of 1.26 while the flapping mode has a phase velocity relative to the jet exit velocity of 0.75. Obviously, this method gives a nonphysical value of phase velocity for the varicose mode since the convection velocity of the structures cannot be faster than the jet exit velocity. However, as seen from figure 5.8, even though the actual phase measurements are believed to be relatively accurate and repeatable, fitting a straight line to the phase data leads to a relatively high uncertainty estimate on the phase speed values, particularly in the potential core region. For reasons to be discussed later, it is especially difficult to perform these measurements accurately in the potential core region of the jet. Downstream of the potential core, the varicose mode has a phase velocity of 0.77 times the jet exit velocity and the flapping mode has a phase velocity of 0.68 times the jet exit velocity.

Figure 5.8b shows the same data for the elliptic helium jet excited at a Strouhal number of St = 0.4. Again, there is a change in the slope of each line at the axial location corresponding to the end of the potential core indicating a change in phase velocity as the structures convect out of the potential core. In the potential core region, the varicose mode has a phase velocity of 0.59 with respect to the jet exit velocity and the flapping mode has a phase speed of 0.49 with respect to the jet exit velocity. Downstream of the potential core, the varicose mode has a phase velocity of 0.77 and the flapping mode has a phase velocity of 0.51, both with respect to the jet exit velocity. The trend for the helium jet appears to differ from the air jet in that the structures actually accelerate after leaving the potential core region. Due to the high

uncertainty of the measurements in the potential core region, it is highly likely that this trend is in error. However, a possible explanation for this phenomenon will be provided shortly. Table 5.1 summarizes the wavelengths and convection velocities for the elliptic jets excited at St = 0.4.

Table 5.1 Instability wave properties for elliptic jet excited at St = 0.4

	Varicose Excitation				Flapping Excitation			
	Potential Core		Downstream Region		Potential Core		Downstream Region	
T_j/T_a^*	0.69	1.2	0.69	1.2	0.69	1.2	0.69	1.2
λ, cm	3.94	2.07	2.40	2.70	2.35	1.72	2.12	1.79
f, Hz	13,600	19,700	13,600	19,700	13,600	19,700	13,600	14,700
U_c, mps	536	407	327	531	319	338	289	352
U_c/U_j	1.26	0.59	0.77	0.77	0.75	0.49	0.68	0.51
U_c/a_{ch}	1.29	0.98	0.79	1.28	0.77	0.81	0.70	0.85

The axial phase distribution for the air and helium elliptic jets excited at a Strouhal number of 0.2 is shown in figures 5.9a and 5.9b. The difficulties mentioned earlier about the measurement of the phase velocity in the potential core become more apparent at this Strouhal number. For the air jet, there is no linear region of phase in the shear layer surrounding the potential core that gives a realistic value of convection velocity. For the helium jet, both modes have four points near the end of the potential core that could be used to determine the phase velocity of the travelling waves. Table 5.2 summarizes the measured wavelength and convection velocities at an excitation

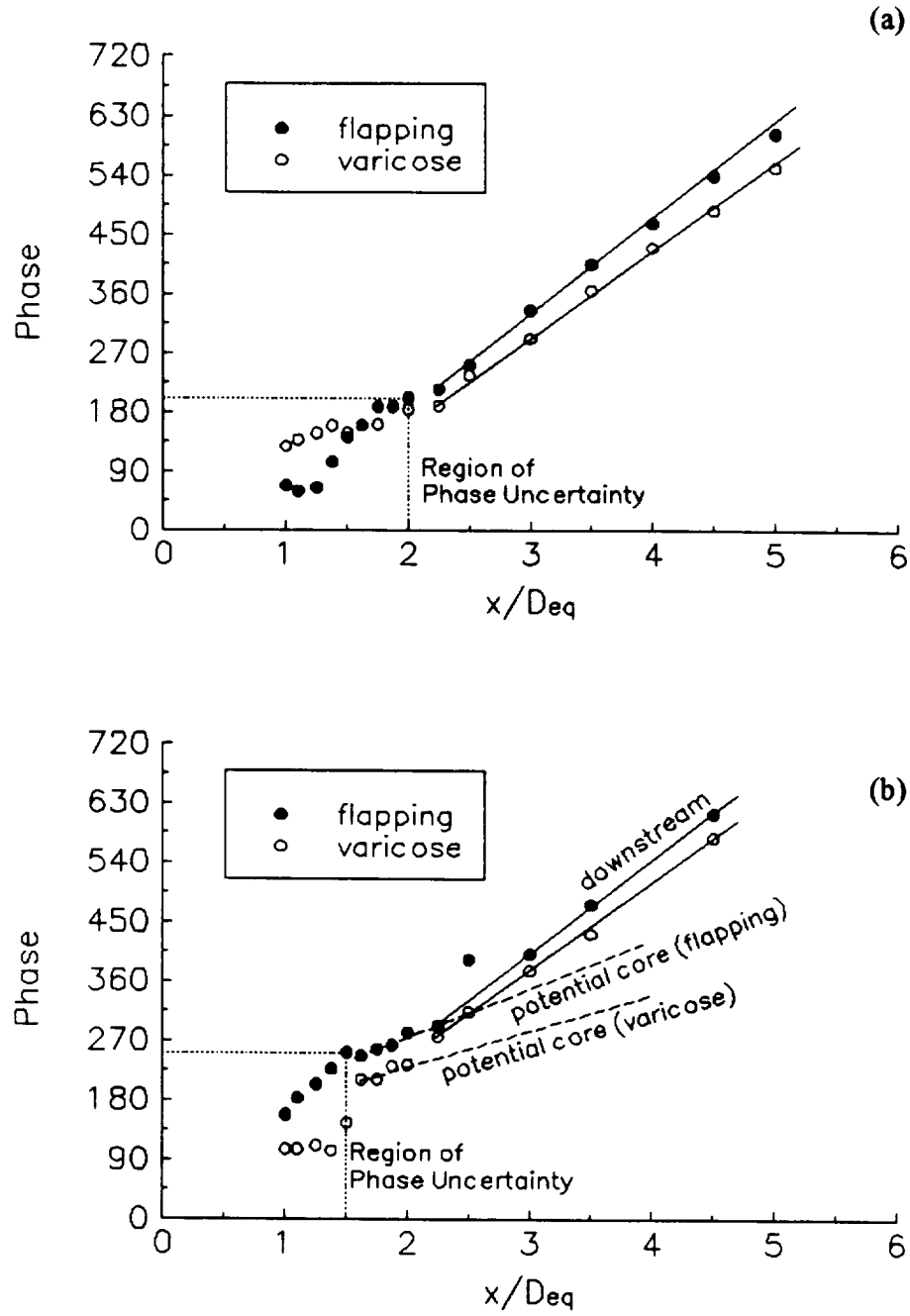

Figure 5.9 Axial phase distribution for elliptic jet excited at St = 0.2. (a) pure air jet, $T_j/T_a = 0.69$, (b) helium jet, $T_j/T_a^* = 1.2$.

Table 5.2 Instability wave properties for elliptic jet excited at 0.2

	Varicose Excitation				Flapping Excitation			
	Potential Core		Downstream Region		Potential Core		Downstream Region	
T_j/T_a^*	0.69	1.2	0.69	1.2	0.69	1.2	0.69	1.2
λ, cm	--	7.00	3.76	4.42	--	5.60	3.41	3.31
f, Hz	--	9,370	5,860	9,370	--	9,370	5,860	9,370
U_c, mps	--	654	220	414	--	524	200	310
U_c/U_j	--	1.58	0.52	0.60	--	1.26	0.47	0.45
U_c/a_{ch}	--	0.95	0.64	1.00	--	0.76	0.58	0.75

Strouhal number of 0.2. Note that for this Strouhal number, the structures do not show a phase speed increase downstream of the potential core for the helium jet case as for St = 0.4. It is not known if this difference reflects the actual physics of the flow or if one of the two cases is in error due to the difficulties in the measurement of the phase speed in this region.

It is believed that sharp changes in phase across the shear layer surrounding the jet potential core are the cause of the difficulty in measuring the phase velocity in this portion of the jet. The shear layer in this region is very thin and experiences a large change in phase distribution from one side of the layer to the other making the measurements of axial phase speed difficult. The radial phase distribution across the shear layer and its impact on the axial phase speed measurements will be discussed in detail in the next section. Also, as mentioned in Chapter 2 and as will be shown in the modal decomposition measurements of Chapter 6, the point electrodes excite higher order modes in addition to the desired fundamental mode. This multi-mode mix will

undoubtedly complicate the phase distribution in the jet, particularly in the potential core region before these higher order modes are damped farther downstream.

Measurements like those shown in figures 5.8 and 5.9 were made over a range of Strouhal numbers in order to obtain a better understanding of the jet instability waves. In the potential core region, it was not possible to obtain a linear phase relation as seen in figure 5.8 for a wide Strouhal number range. As a result, only measurements in the region just downstream of the potential core are reported here.

Figure 5.10a shows the phase velocity of the instability waves as a function of Strouhal number for the pure air elliptic jet. In general, the varicose mode has a higher velocity than the flapping mode and the phase velocity increases with increasing Strouhal number, except at the highest frequencies. The horizontal line represents the phase velocity which is equivalent to the ambient speed of sound normalized by the jet exit velocity. Therefore, structures with phase velocities above this value may radiate noise through Mach wave emission. Except for the varicose mode at St = 0.4, no Strouhal number component exceeds this value for the air jet case.

Figure 5.10b shows the same measurements for the helium/air elliptic jet. Again, the varicose mode shows a higher velocity compared to the flapping mode. It should be pointed out that the stability analysis of Morris and Bhat (1993) also predicts the varicose mode to have a higher phase velocity than the flapping mode for both the cold and heated jet conditions. They also predict the phase velocity of both modes relative to the jet exit velocity to decrease as the jet is heated. In general, the present measurements also show these trends, although the varicose mode does show a slight

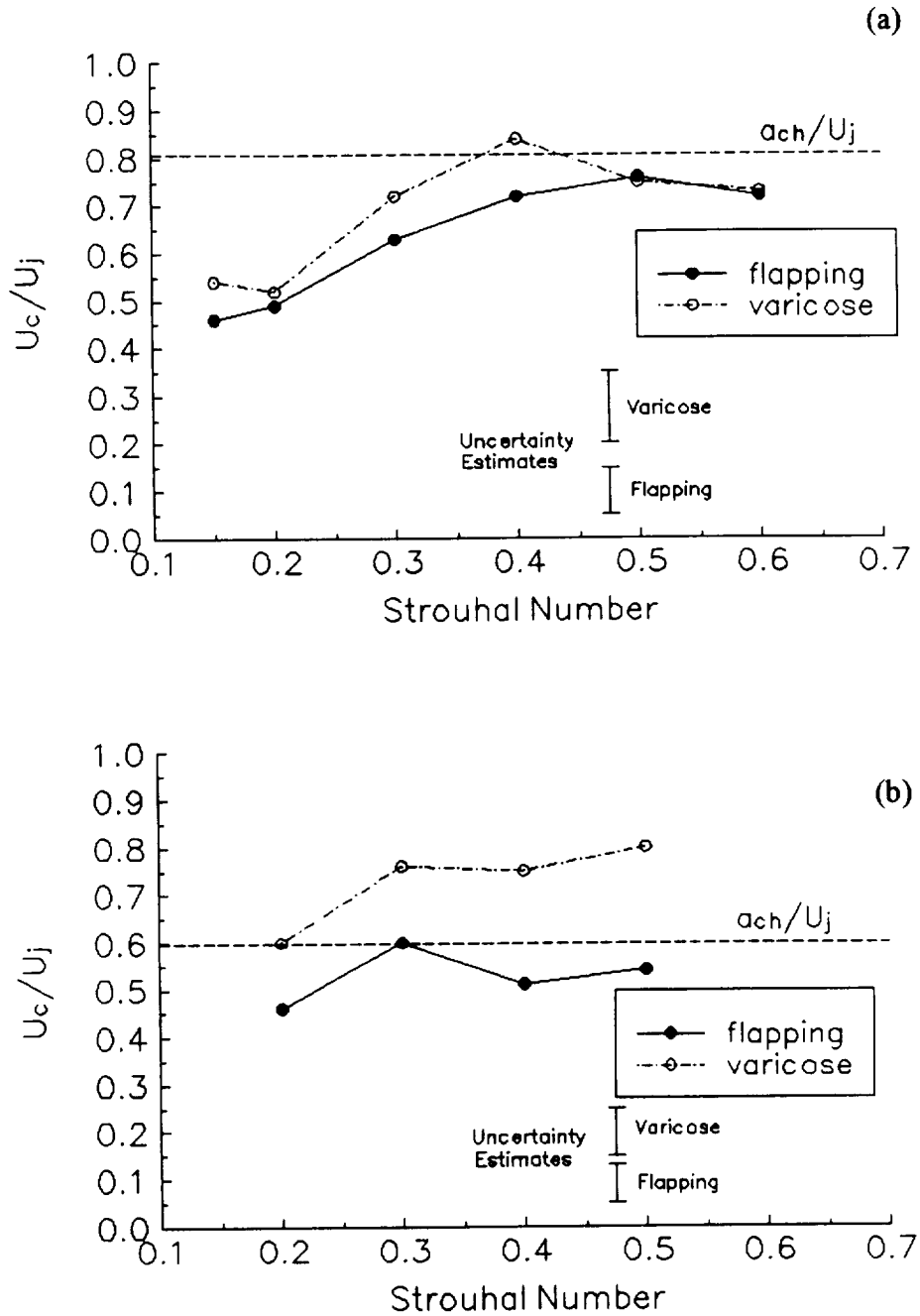

Figure 5.10 Phase speed as a function of Strouhal number in artificially excited elliptic jet (downstream of potential core). (a) pure air jet, T_j/T_a = 0.69, (b) helium jet, T_j/T_a^* = 1.2.

velocity increase for some frequencies when helium is added. Therefore, our results agree with the predictions of Morris and Bhat (1993) that jet heating causes the instability wave phase velocity to increase with respect to the ambient sound speed, but decrease with respect the jet exit velocity.

As mentioned earlier, fitting a straight line through the axial phase data leads to a relatively high uncertainty estimate for the phase speed measurements. In general, the flapping mode phase data had less scatter from the linear fit than the varicose mode which is why there are separate uncertainty estimates for each mode. Also, both modes appeared to be more easily excited in the helium jets than in the pure air jets. The effectiveness of the excitation can evaluated through the coherence level between the excitation and hot-wire signals as well as by observing an oscilloscope during a test. When a mode is effectively excited at a given frequency, the coherence level between the excitation and hot-wire signals is typically higher than 0.98. Also, there is a visual phase locking between the two signals simultaneously displayed on an oscilloscope. The varicose mode excitation would occasionally have a coherence level close to 0.90 which is why there tends to be more scatter in those data. Also, it likely that rather than exciting purely one mode or the other, some type of multi-mode mix may be introduced into the jet shear layer by the quadruple electrode system. Since each mode has a different phase velocity, any kind of modal mixture would complicate the axial phase speed measurements and lead to difficulties like those encountered here.

Figure 5.11 shows the phase speed as a function of Strouhal number for the air and helium rectangular jets. In general, they show the same trends as the elliptic jet.

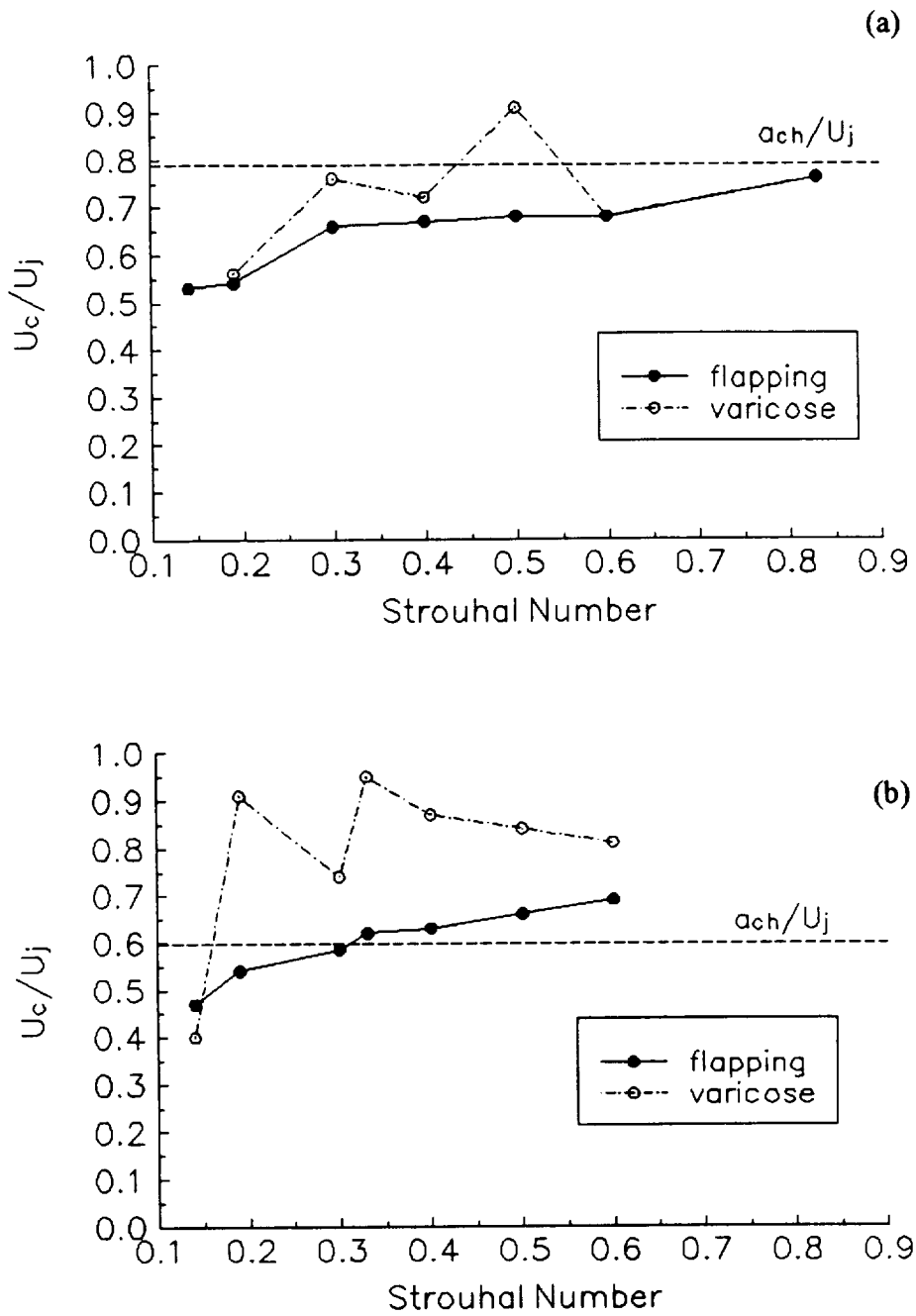

Figure 5.11 Phase speed as a function of Strouhal number in artificially excited rectangular jet (downstream of potential core). (a) pure air jet, T_j/T_a = 0.69, (b) helium jet, T_j/T_a^* = 1.2.

The flapping mode phase velocity shows a clear tendency to increase as the frequency is increased. As just mentioned, the irregularities seen in the varicose mode result from difficulties in exciting the rectangular jet in a symmetric mode. Certain excitation frequencies produce higher levels of coherence in the hot-wire signal which can have an effect on the phase measurements that lead to the irregular data shown in figure 5.11.

There is a possible reason why the phase velocity of the St = 0.4 components shows an increase in velocity downstream of the potential core in the helium jet case. As the jet begins to mix and become closer to the cold jet conditions, the instability wave characteristics should approach those of the cold jet. Since the cold jet instability waves tend to have a higher phase velocity relative to the jet exit velocity than the heated jet case, it is plausible that as the hot jet begins to approach the cold jet conditions, the relative velocity of the instability waves may increase with respect to the jet exit velocity. However, the centerline jet velocity begins to decrease at the end of the potential core and therefore has less energy to drive the structures. Intuitively, it is not physical think that the structures would accelerate under these conditions. Even though the axial phase distribution measurements in the potential core region shown in figure 5.8 appear to be reasonably linear, it is likely that they result in the misleading conclusion that the flapping mode has subsonic phase speed in this region and that the structures actually accelerate downstream of the potential core. Acoustic data to be presented in Chapter 6 shows evidence of Mach wave emission from the flapping mode which requires a supersonic phase velocity at some point in the jet. Therefore, it seems

more reasonable to assume that for the helium jet case, the structures travel supersonically through the potential core and then decelerate upon entering the mixing region of the jet.

It should also be noted that for the helium case, the phase speed of the varicose mode exceeds the ambient speed of sound over nearly the entire Strouhal number range while the flapping mode is close to, but just below, the sonic value. Tam and Morris (1980) showed that near sonic instability waves can have supersonic wavenumber components which will radiate to the far-field. Evidence of the stronger coupling of the hydrodynamic pressure field to the acoustic field at the higher jet velocity will be seen in the modal decomposition measurements of the helium elliptic jet. Also, far-field acoustic data to be presented later show evidence that this increase in instability wave phase velocity compared to the ambient sound speed corresponds to an increase in acoustic radiation consistent with Mach wave emission.

5.4 Radial Hot-wire Measurements

As discussed in section 5.3, it is very difficult to obtain consistent phase measurements in the potential core region of the jet such that an instability wave convection speed can be determined reliably. This section addresses this issue and attempts to provide an explanation for the difficulty in the measurement of the relative phase distributions in the jet shear layer. Figure 5.12 shows the relative phase between the hot-wire signal and the glow excitation signal (flapping mode) as the hot-wire is traversed radially across the pure air elliptic jet shear layer with the axial measurement

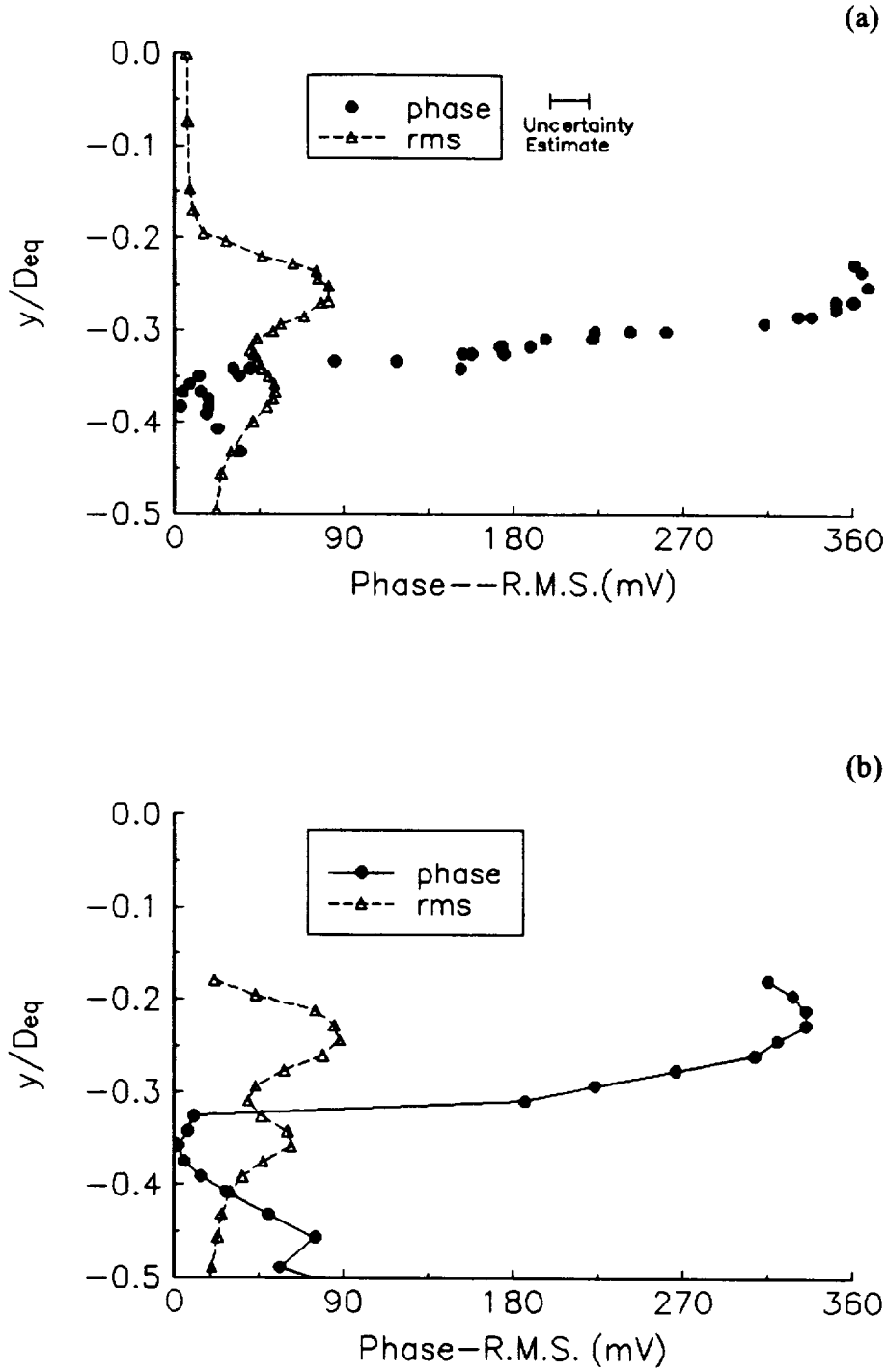

Figure 5.12 Phase distribution across elliptic jet shear layer at $x/D_{eq} = 1.8$, flapping excitation. (a) pure air jet, $T_j/T_a = 0.69$, St = 0.2, (b) pure air jet, $T_j/T_a = 0.69$, St = 0.4.

location held constant. The axial location is $x/D_{eq} = 1.8$, about midway through the potential core region, and two different excitation frequencies are shown. Figure 5.12a corresponds to an excitation frequency of St = 0.2 and figure 5.12b corresponds to a frequency of St = 0.4. The r.m.s fluctuation amplitude for each position is also shown on the graphs. For both excitation frequencies, there is approximately a 360° phase shift across the shear layer and two peaks in the r.m.s. fluctuation distribution. For most of the hot-wire measurements discussed until now, the hot-wire has been located at the point of maximum r.m.s. fluctuations seen in figure 5.12.

It is seen from the phase distribution that there is a relatively narrow plateau of constant phase both on the inner and outer edge of the shear layer. Between these plateaus is a region where the phase changes rapidly across the shear layer. The whole shear layer is located within the two r.m.s. humps with a thickness of approximately 0.2 D_{eq}. This is a very thin region and is less than 3 mm thick. Therefore, it is not surprising that the measurement of consistent axial phase distributions is difficult when there is such a large phase change occurring over such a narrow measurement range. Ideally, as the hot-wire is traversed axially to obtain the phase distributions of figures 5.8 and 5.9, it should be located on the phase plateau on the inner side of the shear layer as seen in figure 5.12. However, since the shear layer is so thin and the variation in phase across the layer is so large, the slightest error in placement of the hot-wire can lead to an irregular axial phase distribution such as seen in some of the data in section 5.3.

Figure 5.13a shows the radial phase measurements across the pure air elliptic jet shear layer excited at a Strouhal number of 0.2 at an axial location of $x/D_{eq} = 3.5$, just downstream of the potential core end. Figure 5.13b shows the same measurements at the same axial location for the helium elliptic jet excited (flapping mode) at St = 0.4. This time, there is approximately a 270° phase change across the shear layer. However, the shear layer is much thicker and therefore the change is more gradual. This type of phase distribution is more conducive to the estimation of axial phase distributions than those in the relatively thin shear layer surrounding the jet potential core.

The general trend of the present work, therefore, is that the phase distribution across the shear layer shows approximately a 360° change in the potential core region and then a somewhat lower phase change farther downstream in the jet. However, there are some discrepancies to this trend over the test matrix of the present work. A totally consistent and unifying description of the phase changes and conditions under which they are produced is not possible from the present data. It is hoped that the work presented here will contribute to such a theory in the future.

The radial phase distributions seen in figure 5.12 and 5.13 show similar trends to those predicted and measured in a low-speed planar shear layer by Gaster et al. (1985). At a moderate axial distance downstream, they show an approximately 270° phase shift across the mixing layer. Farther downstream, their phase change is lower and is approximately 200° across the shear layer. As in the present work, they also show a double peak in their r.m.s. profiles at early axial locations. These similarities

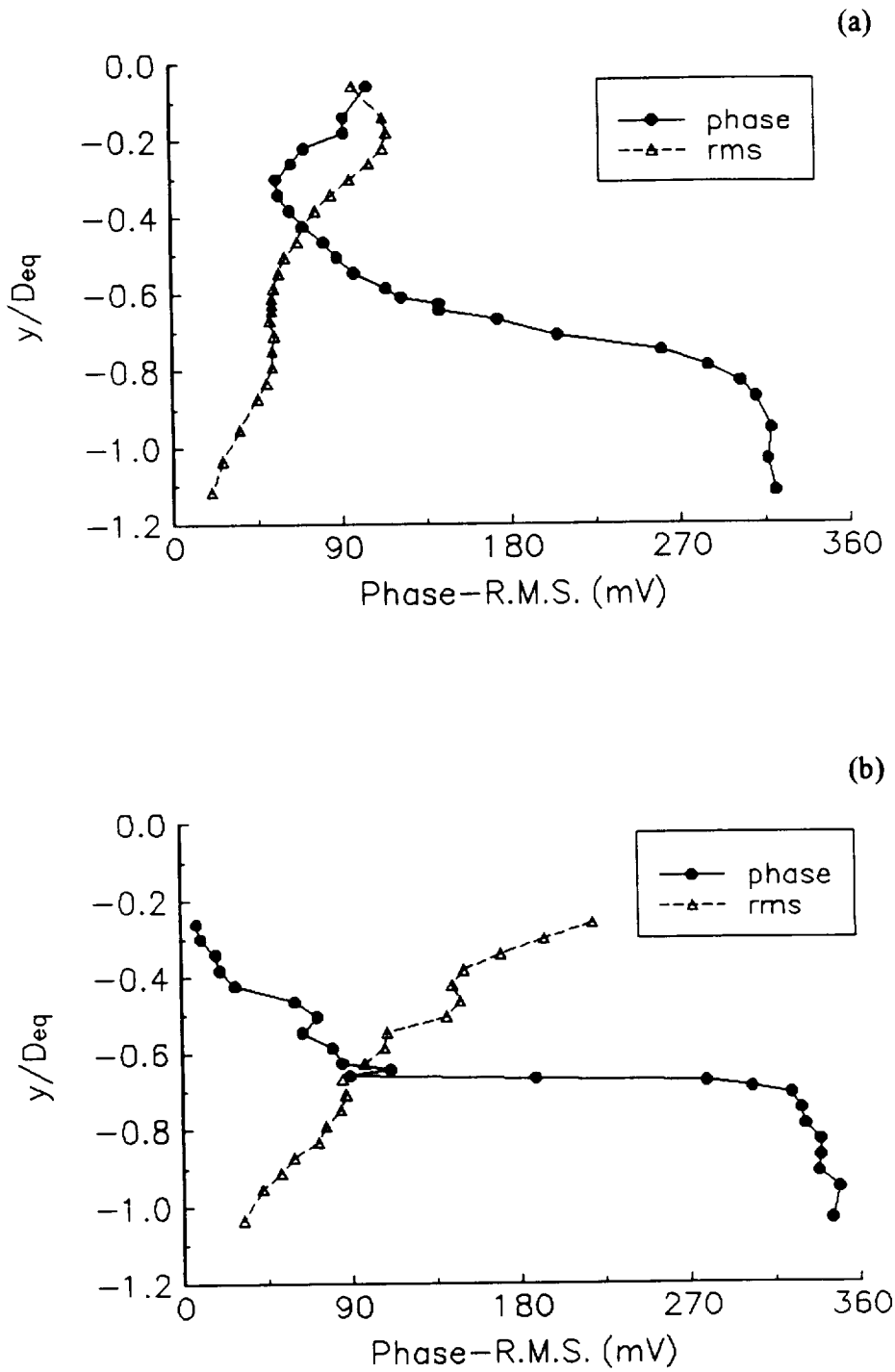

Figure 5.13 Phase distribution across elliptic jet shear layer at $x/D_{eq} = 3.5$, flapping excitation. (a) pure air jet, $T_j/T_a = 0.69$, St = 0.2, (b) helium jet, $T_j/T_a = 1.2$, St = 0.4.

suggest that the dynamics of mixing in both high and low speed shear layers share some fundamental qualities.

In an effort to learn more about the basic structure of mixing layers, a simple analytical model has been developed based on the principle of traveling vortices. Flow visualization from both high and low speed mixing layers show that shear layers are indeed composed of vortical like structures which grow in size as the layer develops (Martens et al., 1994; Winant and Browand, 1974). The present model assumes that the large scale structures in a mixing layer can be thought of as vortices which convect downstream while at the same time oscillating in the transverse direction to simulate additional "waviness" of the mixing layer. This is shown schematically in figure 5.14. The model is similar to one used by Winant and Browand (1974) to describe vortex pairing in a low speed shear layer.

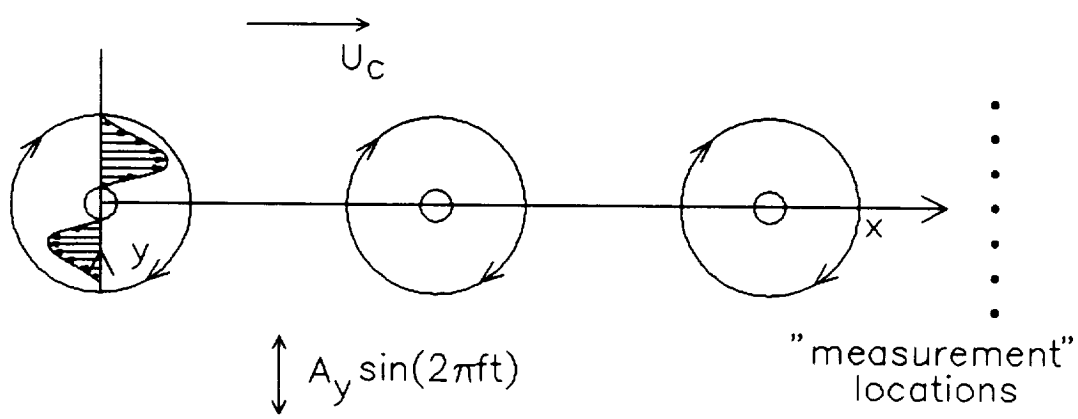

Figure 5.14 Schematic of vortex model.

The velocity components of the vortex are written as:

$$u = -A_v y e^{-R} \qquad v = A_v x e^{-R} \tag{5.1}$$

where A_v is a scaling factor and R is the distance from the center of the vortex. Note that there is a region of near-irrotational flow in the center of each vortex. The u-component of velocity on the high speed side of the simulated shear layer is increased by a specified amount over the u-component of velocity on the low-speed side to conform approximately to the mean velocity profile. Also, in addition to a convection speed in the x-direction, a small oscillation in the y-direction is added to the vortex motion. The center of the vortex therefore traces out a sine wave of specified amplitude and frequency. The model then simulates a train of vortices which travel in the x-direction at a chosen velocity while "bouncing" up and down with a chosen amplitude and frequency. It is then possible to predict the velocity at any location as the vortices travel past that point. Cross-correlation of the velocity signal with the y-oscillation trace is then analogous to a cross-correlation of a hot-wire signal with an excitation signal forcing the mixing layer of the jet artificially. The relative phase and r.m.s. amplitude can then be calculated using the same methods described for the supersonic jets of the present work. Appendix C gives a listing of the code used to generate the velocity traces used in the vortex simulation.

Figure 5.15 shows the phase and r.m.s. amplitude distribution across the vortex train as the amplitude of the y-oscillation is changed from $A_y = 0.2$ to $A_y = 0.013$. The vertical position across the vortex train and the y-oscillation amplitude are

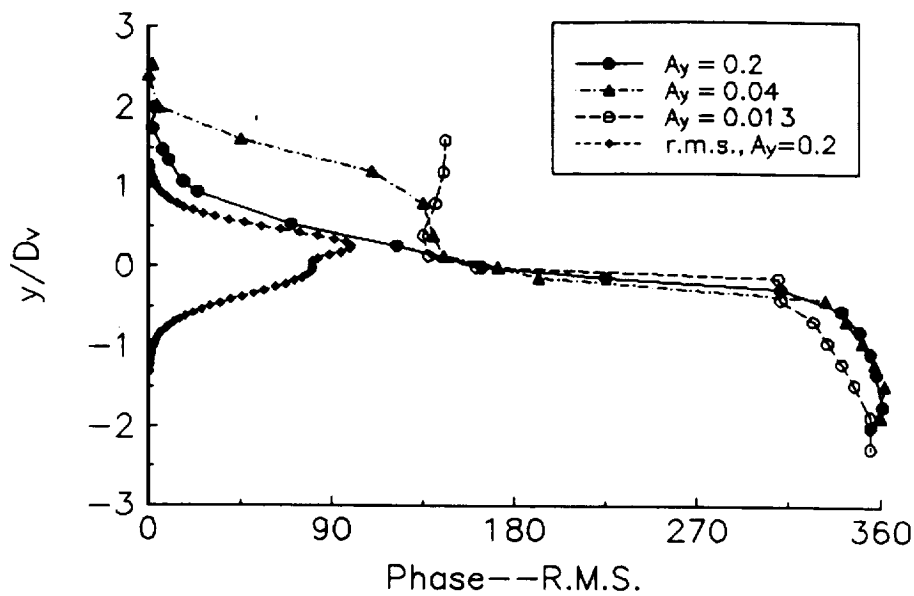

Figure 5.15 Predicted phase and r.m.s distribution across the vortex row.

its maximum value. The r.m.s. amplitude distribution is also shown for the case where $A_y = 0.2$. It is obvious that the oscillation amplitude has a large effect on the measured phase distribution across the vortex train.

There is approximately a 360° phase change across the vortex row when the amplitude of vortex oscillation with respect to the vortex size is high ($A_y = 0.2$). This is the same phase change observed in the early stages of the mixing layers investigated in the present work. At the lowest amplitude of vortex oscillation ($A_y = 0.013$), there is only a 180° phase change across the vortex row. The intermediate oscillation amplitude ($A_y = 0.04$) shows a somewhat irregular distribution as it makes a 360° phase change across the vortex train.

While the physics described by this simple model is not yet completely understood, it appears to offer some insight into the radial phase distribution across a shear layer. Early in the actual shear layer development, it is hypothesized that the mixing layer can be modeled by vortices that oscillate with a relatively high amplitude with respect to their size. As seen by the model prediction, this produces a near 360° phase change across layer and is in agreement with the measurements of the present work at axial locations close to the initial formation of the jet shear layer. As the vortices grow and the shear layer thickens, the relative amplitude of their excursion from some mean value is lower compared to earlier in the shear layer development. For these conditions, the model then predicts the phase difference across the layer to be approximately 180°. The present experiments show approximately a 270° phase shift across the jet shear layer and Gaster et al. (1985) show a near 200° phase change across the layer at the farthest downstream measurement locations. The trend of the model is for the phase difference across the vortex row to decrease from 360° to 180° as the amplitude of the vortex oscillation is decreased. This trends appears to be in agreement with the available experimental data of relative phase distribution across a mixing layer.

In addition to a reasonably good prediction of the phase distribution across the shear layer, the model also qualitatively predicts the double peak in the r.m.s. distribution. As in the present work, this double peak is often observed in the r.m.s fluctuation distribution across both high and low speed free shear layers (see Winant and Browand, 1974; Demetriades and Brower, 1982; Oster and Wygnanski, 1982;

Martens, 1995). From velocity measurements in a low speed shear layer, Oster and Wygnanski (1982) conclude that the double peak arises from the passage of "vortex lumps" past a measurement plane with high velocity regions surrounding a quiescent core region. Their conclusion is supported by the present model. The higher peak is always seen to be next to the high speed side of the shear layer. The higher fluctuation level next to the high speed side of the shear layer apparently arises from the asymmetry of the vortex which is skewed toward the high speed side.

Even though there are still questions to be answered, the proposed vortex model appears to provide a rational description of both high and low speed free shear flows. Qualitatively, the r.m.s. and phase distributions predicted by the model are in reasonable agreement with experimental observations. The fact that the present measurements do not show exactly a 180° phase shift at the farthest downstream measurement location or that Gaster et al. (1985) do not show exactly a 360° phase shift at their farthest upstream location is not necessarily in conflict with the proposed vortex model. In its current form, the model is only a qualitative predictor of the shear layer behavior. The model has several different parameters that would need to be optimized in order to accurately represent a specific free shear flow. Some of these parameters include vortex size, excursion amplitude, convection speed, passage frequency, and strength. For the present time however, it provides a plausible explanation for the somewhat unexpected hot-wire measurements across the jet shear layer, as well as a description of the detailed motions of the large scale velocity fluctuations in the shear layer.

CHAPTER 6

ACOUSTIC MEASUREMENTS

This chapter presents a discussion of the acoustic properties measured in the model jets. Up to this point, the results and discussion have focused on the aerodynamic characteristics of the jets. Because the jet flowfield has such a direct bearing on how the noise is produced and radiated in supersonic jets, it is important to establish a firm understanding of the mean and fluctuating flow field properties. Now, as data are presented from microphones in the jet acoustic field, the previously discussed flow data are available to aid in the interpretation of the acoustic results.

6.1 Sound Pressure Level Directivity

SPL directivity distributions along arcs of $R/D_{eq} = 25$, centered at the nozzle exits, are shown in figure 6.1 for the pure air elliptic, rectangular, and circular jets. This radius ranges from 3 to 30 times the acoustic wavelength over the Strouhal number range of 0.1 to 1.0, which makes these measurements representative of the acoustic far-field. Because of the limited size of the anechoic chamber, full arcs at $R/D_{eq} = 25$ are not possible. The major noise producing region is accessible, however. The peak noise directions are between 25° and 30° for all cases. The minor axis planes of the asymmetric jets are louder than the major axis planes. As speculated from the hot-wire data, this relative noise difference most likely results from the higher fluctuation levels in the minor axis plane compared to the major axis plane and the higher growth rate

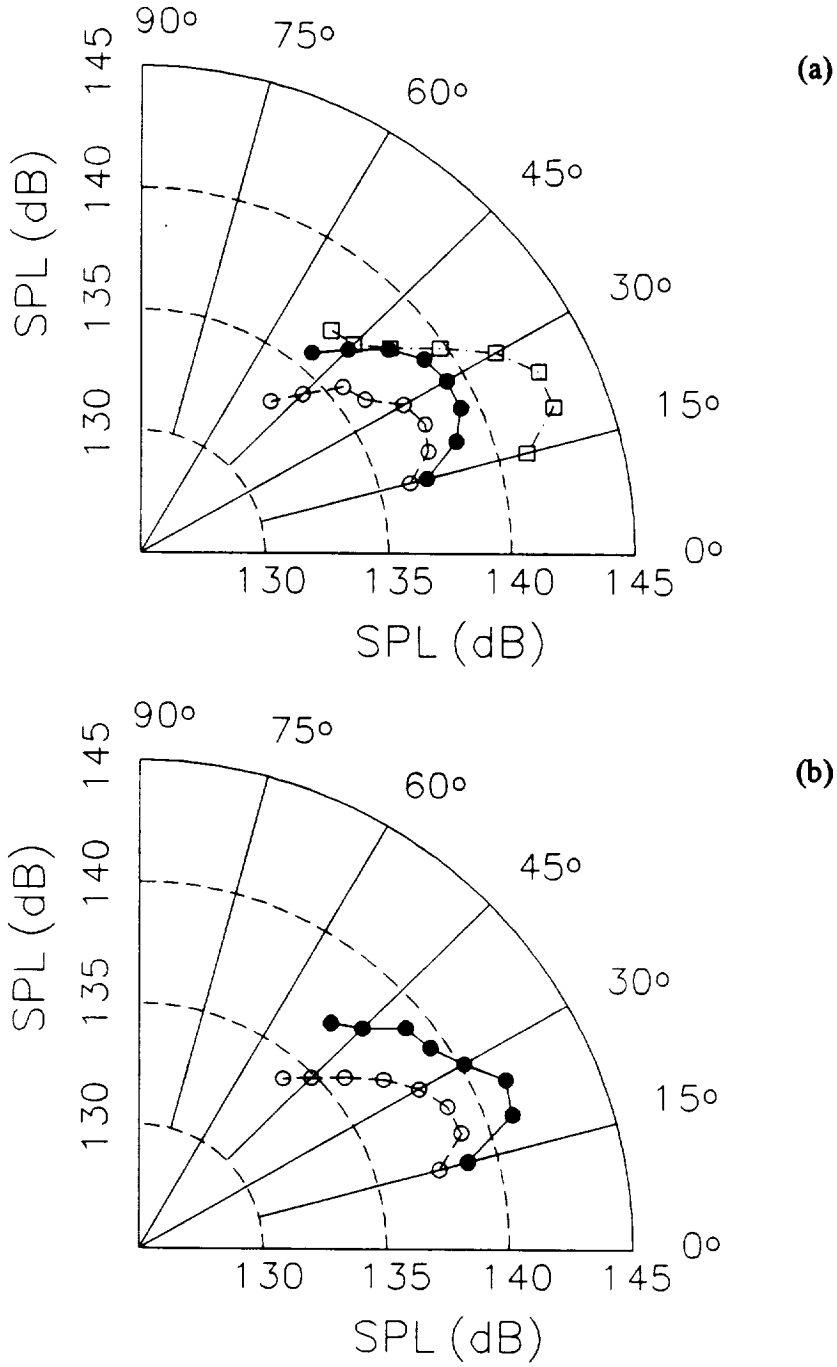

Figure 6.1 SPL directivity arcs for pure air jets, $R/D_{eq} = 25$, $T_j/T_a = 0.69$. ● minor axis, ○ major axis, □ axisymmetric jet, (a) elliptic and axisymmetric jets, (b) rectangular jet.

of the flapping mode, which will radiate predominately in the minor axis plane. The non-circular jets also emit less total noise than the round jet.

Figure 6.2 shows the same measurements for the helium jets. It is clear that the helium jets radiate more noise at a higher angle to the jet axis compared to the pure air jets. The peak noise angles for the helium jet cases have increased to between 30° and 35°. The major axis planes of both asymmetric jets are 4 - 5 dB quieter than the circular jet. Also, the relative difference between the major and minor axis planes of the asymmetric jets has increased making the major axis plane of the asymmetric jets even quieter compared to the minor axis plane. A similar phenomenon was also observed by Seiner et al. (1992) in measurements of a heated Mach 1.5 elliptic jet. The increased relative noise suppression at higher velocities is attributed to the ability of the non-circular jets to mix faster compared to the axisymmetric jet. As a result, Mach wave emission, which becomes more powerful as the jet velocity increases, is suppressed more by the increased mixing characteristics of the non-circular jets at the higher jet velocity compared to the lower velocity conditions. This characteristic could be exploited in an aircraft engine design by directing the quieter plane toward a direction creating less impact on community noise.

It can also been seen from figures 6.1 and 6.2 that the overall noise levels from the elliptic and rectangular jets are very similar. For the helium jet case, the levels match at most polar angles within approximately 1 dB. Therefore, we see that the similarities observed in the aerodynamic data of chapters 4 and 5 also extend to the overall sound pressure levels radiated from the jets. Similarities in the microphone

(a)

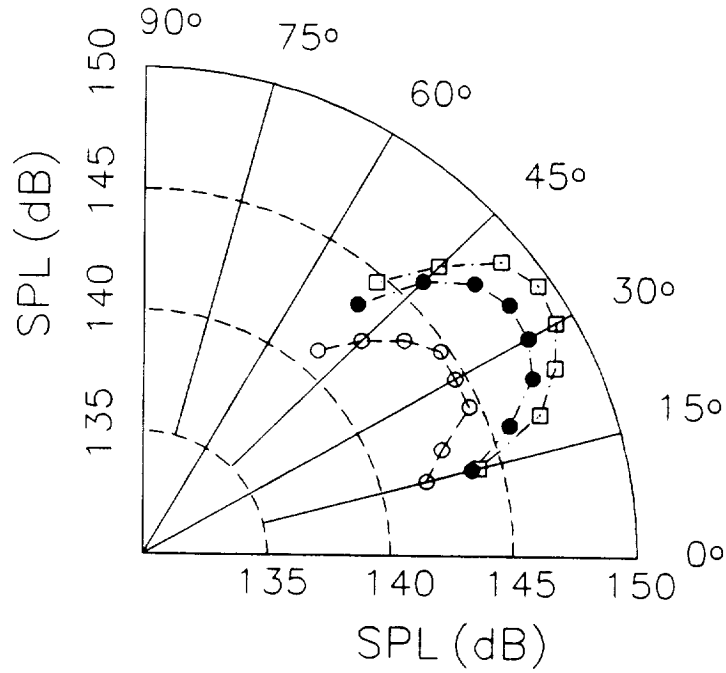

(b)

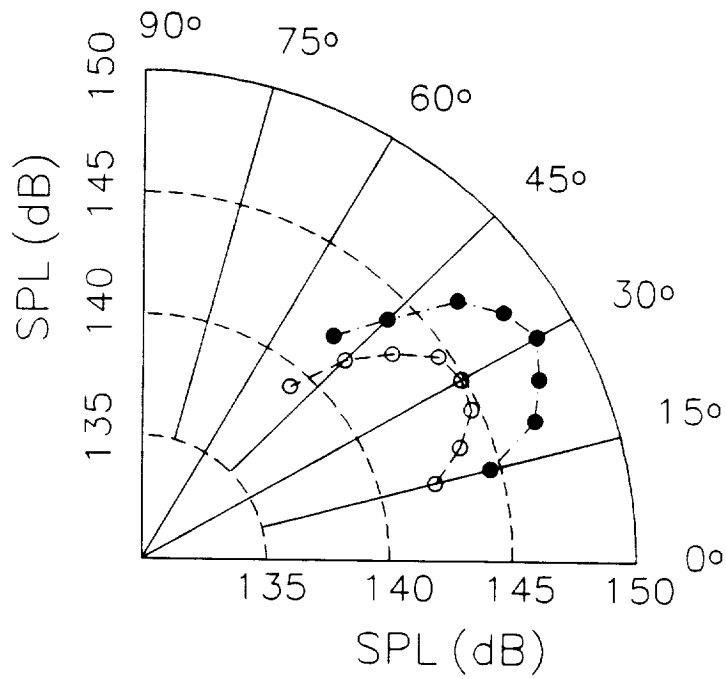

Figure 6.2 SPL directivity arcs for helium jets, $R/D_{eq} = 25$, $T_j/T_a^* = 1.2$. ● minor axis, ○ major axis, □ axisymmetric jet, (a) elliptic and axisymmetric jets, (b) rectangular jet.

power spectra will be shown in the next section. It should be reiterated that since both jets are close to perfectly expanded, it is not all that surprising that the elliptic and rectangular have so much in common.

6.2 Acoustic Spectra

Acoustic spectra corresponding to each of the SPL locations shown in figures 6.1 and 6.2 have also been recorded. Figure 6.3 shows the spectra at each polar angle measured at $R/D_{eq} = 25$ for the pure air elliptic jet. In order to more easily compare the spectral content of the major and minor axis planes, the spectra from each plane are overlaid. At angles below $\beta = 35^{o}$, the peak noise levels are around St = 0.25 in both axis planes. For Strouhal numbers less than approximately 0.4, the levels in both planes are nearly equal. The increased overall noise levels measured in the minor axis plane are apparently due to spectral components above St = 0.4. The broad humps observed in the spectra at the highest polar locations are believed to be due to facility resonances with high amplitudes close to the chamber walls. At these locations, the microphones are within only a few jet diameters of the chamber walls and thus are not considered to be particularly good free field measurement locations, even with the anechoic treatment. These resonances quickly diminish as the microphones are moved away from the facility walls.

It is interesting to note the peak acoustic frequencies for the air case tend to be lower than those of the peak fluid dynamic fluctuations measured by the hot-wires (see figure 5.1). The measurements of Troutt and McLaughlin (1982) and Morrison and

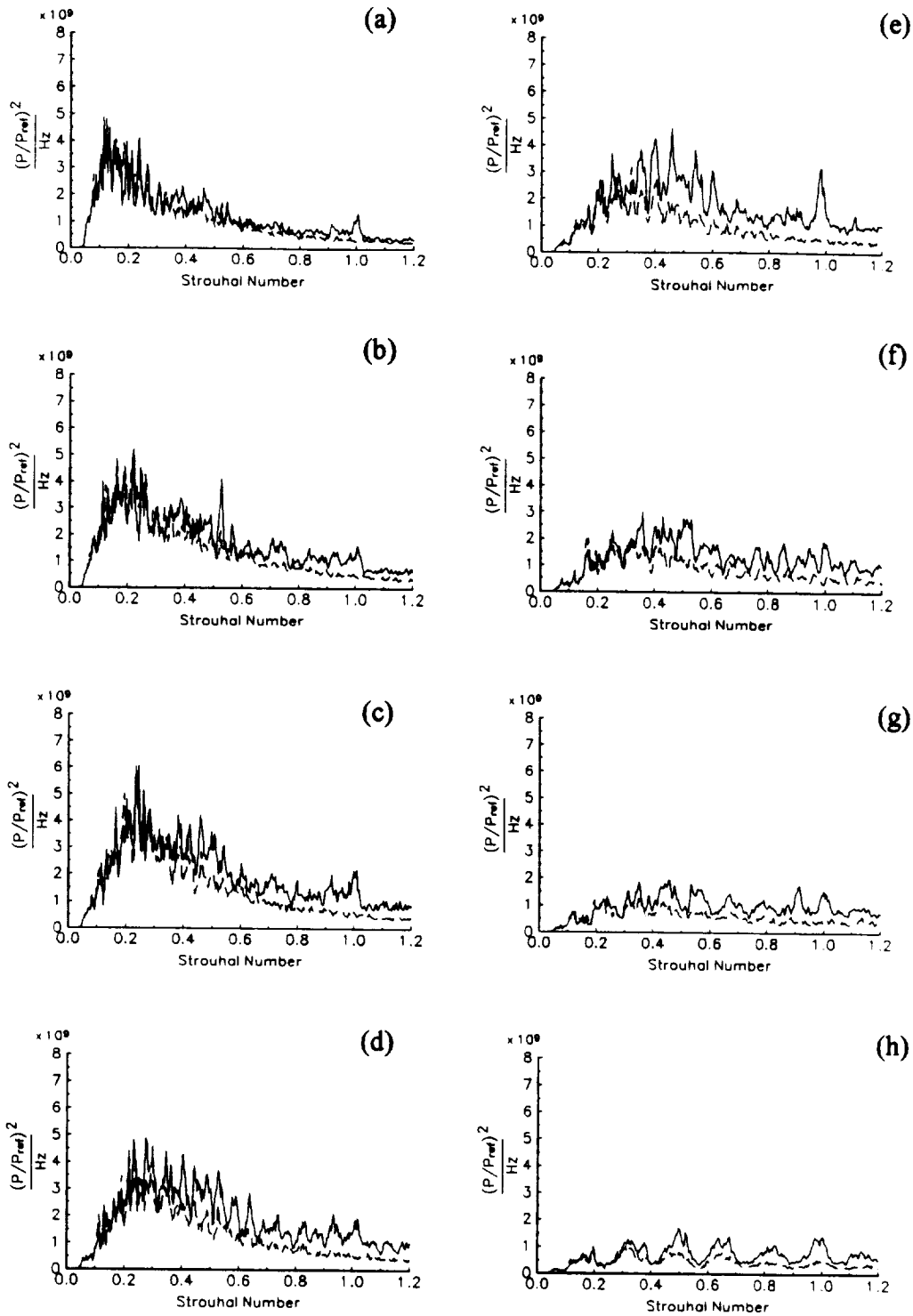

Figure 6.3 Far-field microphone spectra from pure air elliptic jet, $R/D_{eq} = 25$, $T_j/T_a = 0.69$. ——— minor axis, - - - - major axis, (a) $\beta = 15^o$, (b) $\beta = 20^o$, (c) $\beta = 25^o$, (d) $\beta = 30^o$, (e) $\beta = 35^o$, (f) $\beta = 40^o$, (g) $\beta = 45^o$, (h) $\beta = 50^o$.

McLaughlin (1979) showed hot-wire spectra and acoustic spectra to have similar spectral content for reduced Reynolds number Mach 1.5 and Mach 2.0 axisymmetric jets. However, as in the present work, Stromberg et al. (1980) observed the radiated acoustic spectra to have lower frequency content than the hot-wire spectra in a Mach 0.9 low Reynolds number round jet. This phenomenon will be discussed again after the helium jet spectra are presented.

Figure 6.4 shows the acoustic spectra measured for the helium elliptic jet at the locations shown in figure 6.2. As in the pure air case, the major and minor axis planes show similar levels for the low frequency range. However, above a Strouhal number of approximately 0.3, the minor axis plane shows significantly higher fluctuation levels compared to those in the major axis plane. This accounts for the larger relative noise difference between the two planes observed in the overall SPL distributions of the helium jets compared to the air jets, as seen in figure 6.2.

The acoustic spectra on the minor axis plane also are very similar to those measured by the hot-wire in the jet shear layer (figure 5.2). Because of their increased phase velocity relative to the ambient environment, it is believed that these Strouhal number components now radiate directly to the acoustic field for the helium jet case. Tam et al. (1992) discuss that for the Mach wave emission process, the Strouhal number of the peak radiated noise should be the same as the most amplified instability wave. The present work agrees with this theory. Recall that the data of figures 5.5 showed higher hot-wire fluctuation levels in the minor axis plane and that the data of figure 5.7 showed the flapping mode to have a higher growth rate than the varicose

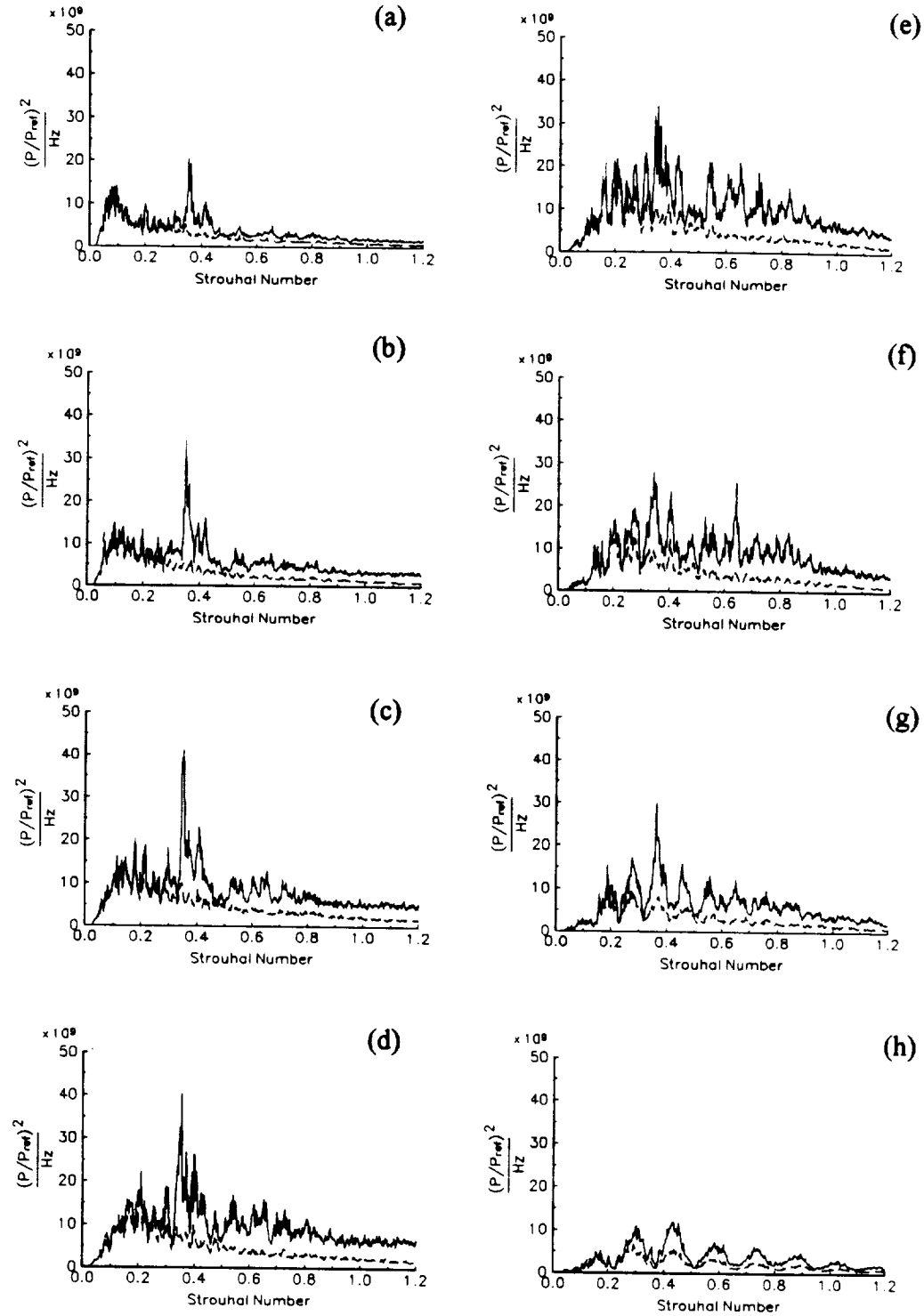

Figure 6.4 Far-field microphone spectra from helium elliptic jet, $R/D_{eq} = 25$, $T_j/T_a^* = 1.2$. ——— minor axis, - - - - major axis, (a) $\beta = 15^o$, (b) $\beta = 20^o$, (c) $\beta = 25^o$, (d) $\beta = 30^o$, (e) $\beta = 35^o$, (f) $\beta = 40^o$, (g) $\beta = 45^o$, (h) $\beta = 50^o$.

mode. Since the flapping mode will obviously radiate more sound in the direction of the flapping motion, all of this evidence leads one to expect higher noise levels in the minor axis plane, as seen in the SPL measurements and acoustic spectra. Also, the azimuthal modal decomposition to be presented shortly show that the peak spectral components of figure 6.4 are composed mostly of the flapping mode.

The comparisons of the acoustic and flow spectra of the air and helium jets suggest that the pure air asymmetric jets produce noise in a fashion more consistent with subsonic jets in terms of displaying a more nonlinear relationships between the flow fluctuations and the radiated noise. This is in contrast to the helium jet case where there is more direct correspondence between the measured flow fluctuations and the acoustic field pressure fluctuations. The observations in the helium jet case are consistent with the theory of Mach wave radiation from high speed jets (Morris and Tam, 1979; Tam et al., 1992; Tam and Chen, 1994).

Even though many of these phenomena have been observed previously in circular jets, the Mach 1.5 measurements of Morrison and McLaughlin (1979) indicate that the round jets in this speed range are closely related to higher Mach number jets with regard to noise generation. The present work, however, suggests that the Mach 1.5 asymmetric jets may have more in common with similar lower Mach number jets. This may be attributed to the increased mixing of the asymmetric jets compared to the axisymmetric jets. Seiner (1992) showed that the normalized centerline velocity distribution from a Mach 1.52 elliptic jet was nearly identical to that from a Mach 0.86

round jet with regard to potential core length and decay rate. As a result, it may be possible that the noise generation processes hold similarities as well.

Figure 6.5 shows the acoustic spectra measured for the pure air rectangular jet. The effects of the weak shock cell structure in the rectangular jet are immediately seen in the form of discrete screech tones. In order to see the detail over the entire frequency range, the peaks of many of these tones have been truncated and the frequency range has been confined to St = 1.2. The full amplitudes and frequency range of the spectral components for $\beta = 25^{\circ}$ are shown on a logarithmic scale in figure 6.6 as a representative example of all other pure air rectangular jet spectra. Other than certain screech frequencies, the fluctuation levels in the major and minor axis planes are fairly close over most of the frequency range. The fundamental screech tone at St = 0.3 is significant only at polar angles lower than $\beta = 35^{\circ}$ and only in the minor axis plane. This frequency agrees well with the predicted fundamental screech frequency of Tam (1988) for rectangular jets.

Other than the screech frequencies, the acoustic spectra and the hot-wire fluctuations do not show particularly good correlation with respect to frequency content. Recall that this was also observed in the pure air elliptic jet case. The broad-band type noise in the acoustics is generally of lower frequency content than the flow fluctuations measured by the hot-wire. This is the same trend measured in the elliptic jet case.

There are several interesting observations to be made regarding the screech tones in the rectangular jet spectra. First, as mentioned in Chapter 5, the tones seen in figure 6.6 are not simply pure harmonics of the fundamental. This is in contrast to the

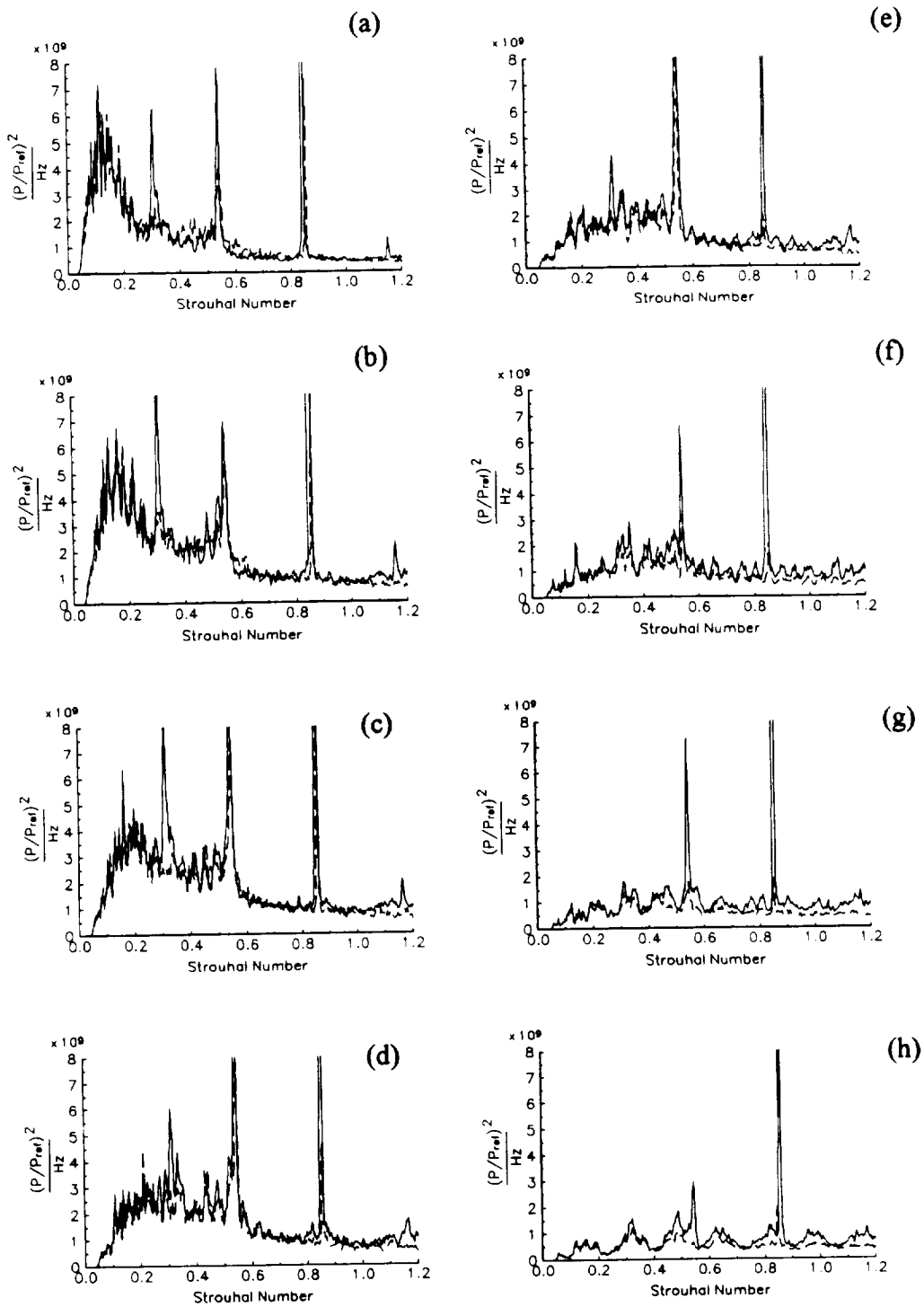

Figure 6.5 Far-field microphone spectra from pure air rectangular jet, $R/D_{eq} = 25$, $T_j/T_a = 0.69$. ——— minor axis, - - - - major axis, (a) $\beta = 15^o$, (b) $\beta = 20^o$, (c) $\beta = 25^o$, (d) $\beta = 30^o$, (e) $\beta = 35^o$, (f) $\beta = 40^o$, (g) $\beta = 45^o$, (h) $\beta = 50^o$.

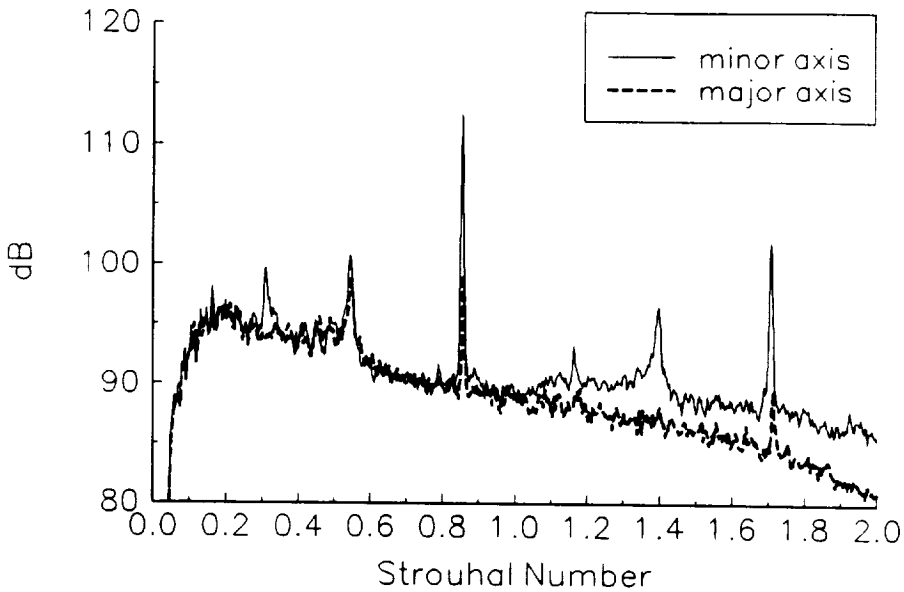

Figure 6.6 Far-field microphone spectra from pure air rectangular jet showing the full range of screech tones. $R/D_{eq} = 25$, $T_j/T_a = 0.69$, $\beta = 25°$.

measurements of most other supersonic rectangular jet researchers such as Shih et al. (1992), Gutmark et al. (1988), and Raman and Rice (1994) that all show higher frequency tones to be exact integer multiples of the fundamental frequency. The frequency ratios of the first three tones in figure 6.6 have values of $f_2\backslash f_1 = 1.8$, $f_3\backslash f_1 = 2.75$, $f_3\backslash f_2 = 1.57$. For pure harmonics these ratios would be 2, 3, and 1.5, respectively. The screech tone research of Hu and McLaughlin (1990) in low Reynolds number circular jets also showed higher frequency tones which were not integer multiples of the fundamental. In fact, the ratios of the first three frequencies for their M = 1.4 jet were all within 5% of those from the rectangular jet of the present work.

The cause of these additional tones can be found from a closer analysis of Tam's (1988) theory of the shock cell structure and screech tones of rectangular supersonic jets. In an earlier paper by Tam et al. (1986) the authors show that the approximate fundamental screech tone frequency from a supersonic jet can be given by the following expression:

$$f_1 = \frac{U_c k_{11}}{2\pi\left(1 + \frac{U_c}{a_\infty}\right)} \qquad 6.1$$

where k_{11} is the fundamental (the smallest) wavenumber of the shock cell system. Using appropriate values for U_c and k_{11}, equation 6.1 has been shown by many researchers to predict the fundamental screech frequency in both circular and rectangular jets accurately (Krothapalli, 1986; Tam et al., 1986). In a later paper, Tam (1988) provides a mathematical description of the shock cell structure in a rectangular jet based on a vortex sheet model of the jet and derives a numerical expression for the wavenumber of the shock cell system. The wavenumber is given by:

$$k_{nm} = \left(\frac{n^2}{b_j^2} + \frac{m^2}{h_j^2}\right)\frac{\pi}{\left(M_j^2 - 1\right)^{1/2}} \qquad n,\ m = 1,\ 2,\ 3,\ldots \qquad 6.2$$

where b_j/h_j is the aspect ratio of the jet. The smallest wavenumber ($n = 1$, $m = 1$) combined with equation 6.1 gives good agreement with the experimentally observed fundamental screech frequency in rectangular jets. However, in most other rectangular jet screech tone research, the fundamental is accompanied by several higher frequency harmonics which are exact integer multiples of the fundamental frequency predicted by

equation 6.1. In the present work, however, even though the fundamental frequency is accurately predicted by equation 6.1 and using k_{11} from equation 6.2, the higher frequency tones are not integer multiples of the fundamental.

However, if the higher modes of k_{nm} are considered instead of just the smallest value, it is possible to predict the higher screech frequency tones of figure 6.6 accurately. Figure 6.7 shows the measured frequency of each tone along with the corresponding prediction using the theory of Tam (1988) as summarized in equations 6.1 and 6.2. The mode numbers refer to the index *m* in equation 6.2 while *n* is held constant at a value of unity. The index *m* is associated with the narrow dimension of the jet in the eigenvalue problem. There is good agreement with between the experimental and predicted values. Even though it was not a goal of the present work, figure 6.7 provides a further validation of the theory of Tam (1988) beyond just the ability to accurately predict the fundamental screech frequency in supersonic jets.

The question arises as to why the higher order screech modes are so prevalent in the present rectangular jet, but not in the jets of other researchers. It is likely that the higher order modes are damped out in the high Reynolds number jets while the reduced Reynolds number jet allows these modes to more fully develop as described by the vortex model of Tam (1988). Recall that evidence of these higher screech modes were also observed in the low Reynolds number round jets of Hu and McLaughlin (1990). Since it is the small dimension of the jet which appears to have the most influence on the screech frequency, the higher wavenumbers associated with the higher frequency screech modes tend to result in short wavelengths that could easily

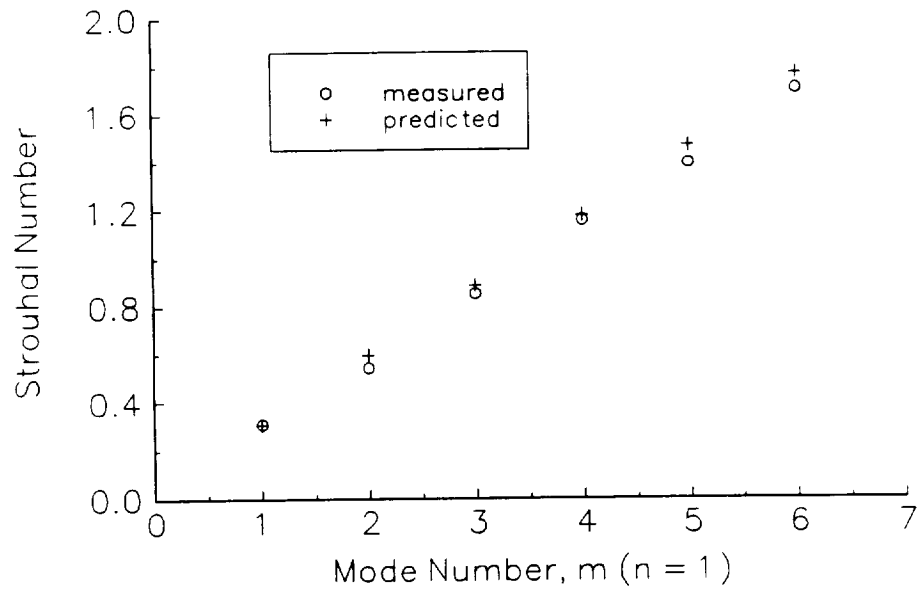

Figure 6.7 Measured and predicted (Tam, 1988) screech frequencies of pure air rectangular jet as a function of minor axis mode number, m, and major axis mode number n = 1, T_j/T_a = 0.69.

be damped by the small scale turbulence of similar wavelength. By reducing the small scale turbulence, the low-to-moderate Reynolds number jets do not break down the shock cell structure of the jet plume as quickly as in the high Reynolds number case.

It is also interesting that only certain screech tones are measured in the major axis plane. This is also consistent with the hot-wire measurements made in the jet shear layer. Typically, screech has been thought to be a process associated with the flapping motion in rectangular jets. However, recent observations by Rice and Raman (1994) show that while the fundamental screech tone is antisymmetric in nature, the second screech harmonic is symmetric around the jet. They showed this by placing

microphones opposite each other in the minor axis plane of a rectangular jet. The fundamental screech frequency was measured to 180° out of phase above and below the jet while the second harmonic was in phase above and below the jet. Even though the tones present in figure 6.6 are not pure harmonics as measured by Raman and Rice, the present measurements do support the findings of Raman and Rice by showing increased levels of screech in the major axis plane at the second screech frequency. Since a symmetric (varicose) mode may be detected more easily in the major axis plane than an antisymmetric (flapping) mode, this is evidence that the screech tones measured in the major axis plane contain symmetric pressure fluctuations while those appearing only in the minor axis plane are likely antisymmetric fluctuations. Azimuthal modal content measurements to be presented later support this conclusion.

The rectangular helium jet acoustic spectra are shown in figure 6.8. Except for the large spike close to St = 0.7, the screech tones so prevalent in the air jet case are absent in the helium jet. Massey et al. (1994) report that the intensity of screech tones tends to decrease as the jet is heated which may be why the lower order screech tones appear to be suppressed in the simulated hot jet. As in the elliptic jet case, the minor axis plane shows increased energy at Strouhal number components around 0.4. This agrees with the hot-wire fluctuation frequency content in the minor axis plane.

Except for the screech tones in the pure air rectangular jet, the acoustic properties of the elliptic and rectangular jets show many similarities. In the major noise producing region ($\beta < 35°$), both the spectra level and the frequency content of the two

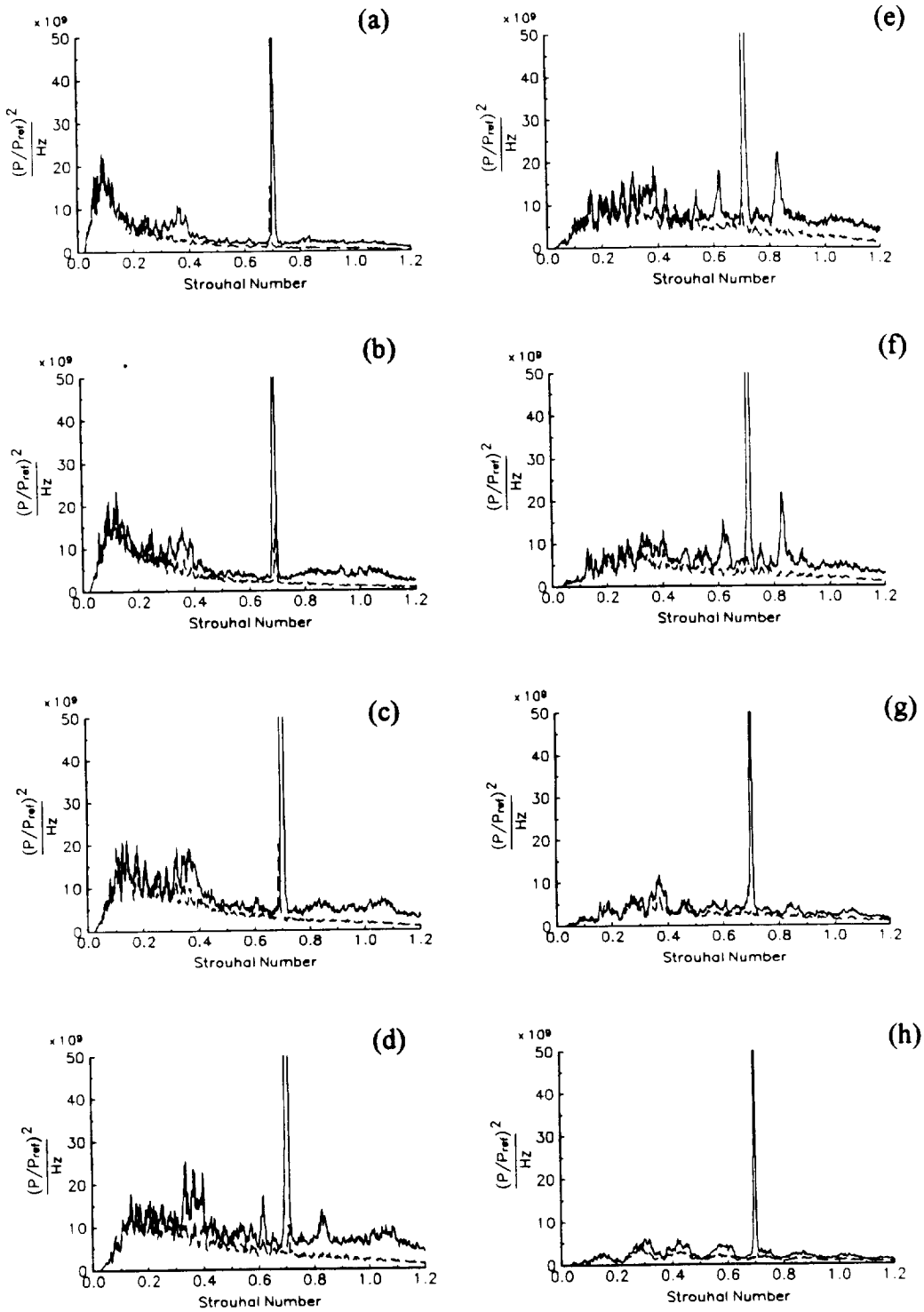

Figure 6.8 Far-field microphone spectra from helium rectangular jet, $R/D_{eq} = 25$, $T_j/T_a^* = 1.2$. ——— minor axis, - - - - major axis, (a) $\beta = 15^o$, (b) $\beta = 20^o$, (c) $\beta = 25^o$, (d) $\beta = 30^o$, (e) $\beta = 35^o$, (f) $\beta = 40^o$, (g) $\beta = 45^o$, (h) $\beta = 50^o$.

jets are very similar. Again, given the previously discussed similarities in the mean and fluctuating flow field, this is not a particularly surprising observation.

6.2.1 Bandpassed Acoustic Spectra

In order to investigate the contribution of specific frequency components to the radiated noise field, the acoustic spectra of figures 6.3 and 6.4 were digitally filtered to calculate the SPL contained only in certain frequency bands. This type of analysis is helpful in the evaluation of instability wave prediction methods which typically only calculate the noise from specific frequency components and do not produce broadband frequency spectra as an output. Therefore, the procedure was applied only to the elliptic jet results since comparisons with the instability wave analysis of Morris and Bhat (1992, 1993, 1995) are desirable.

Figure 6.9 shows the bandpassed SPL directivity arcs for both the pure air and helium elliptic jets. Due to the "peakiness" of the spectra, relatively wide frequency bands were chosen. Three equal bandwidths are shown; the first ranges from St = 0.1 to 0.3, the second ranges from St = 0.3 to 0.5, and the third ranges from St = 0.5 to 0.7. It is seen that over the lowest frequency band the directivity and levels for both the major and minor axis planes are similar for both pure air and helium conditions. As the center frequency increases, the difference between the major and minor axis planes become more pronounced. It is predicted from the stability analysis of Morris and Bhat (1992, 1993, 1995) that as the Mach emission process becomes stronger, the flapping mode becomes the dominant noise source and radiates a proportionally higher

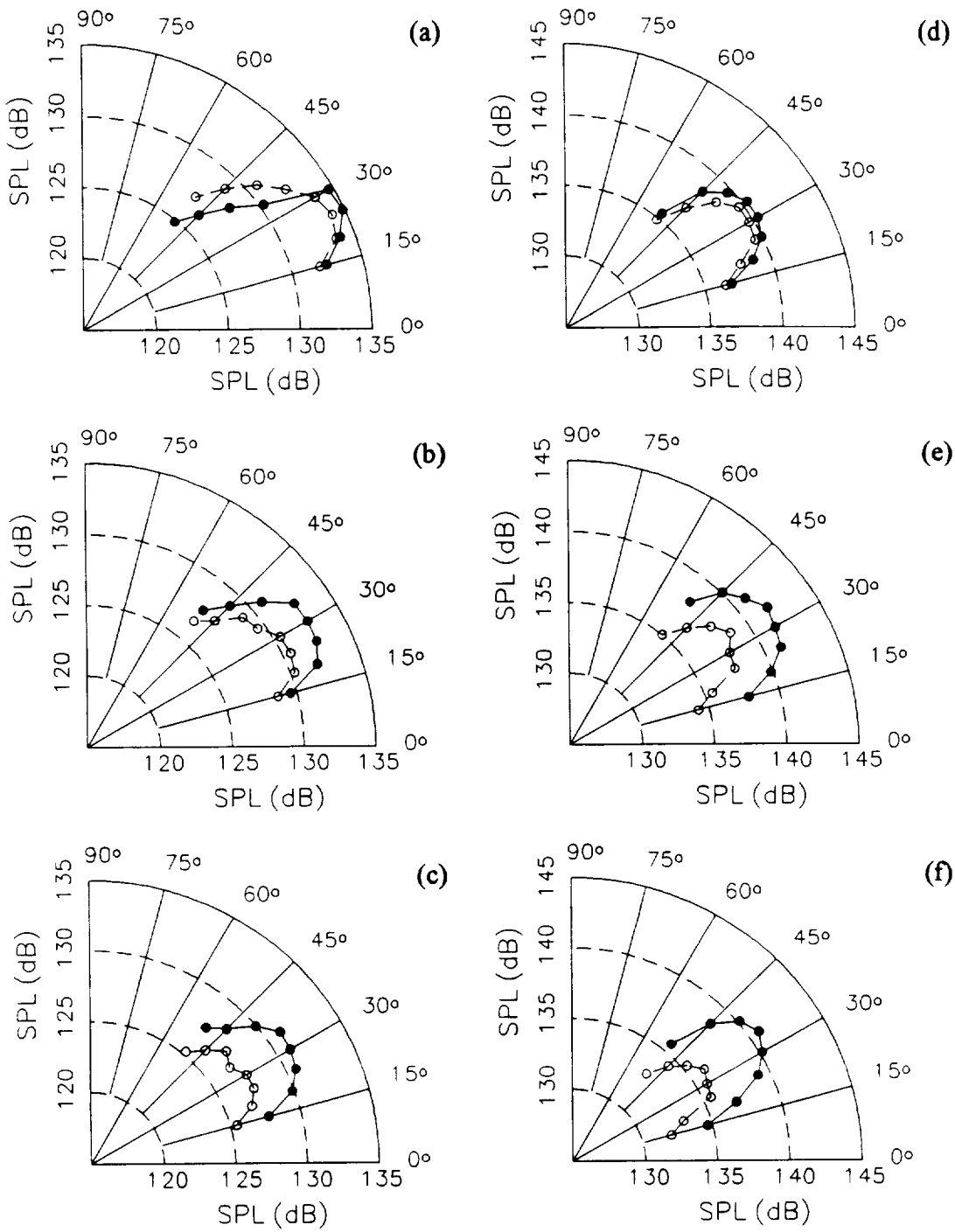

Figure 6.9 Bandpassed SPL directivity arcs for elliptic jet, $R/D_{eq} = 25$. ● minor axis, ○ major axis. (a) $T_j/T_a = 0.69$, St = 0.1 - 0.3, (b) $T_j/T_a = 0.69$, St = 0.3 - 0.5, (c) $T_j/T_a = 0.69$, St = 0.5 - 0.7, (d) $T_j/T_a^* = 1.2$, St = 0.1 - 0.3, (e) $T_j/T_a^* = 1.2$, St = 0.3 - 0.5, (f) $T_j/T_a^* = 1.2$, St = 0.5 - 0.7.

amount of noise in the minor axis plane. Therefore, the present experiments support the predictions of Morris and Bhat by showing an increased difference between the major and minor axis planes as the center frequency of the bands increases from 0.2 to 0.4 and by showing that the relative difference between the two planes also increases as the simulated jet temperature increases.

Ideally, these changes would be more pronounced than those observed in figure 6.9 for a strong case of Mach wave emission. However, because the temperature ratio of the present experiments is relatively low, the changes are not particularly distinct. If a higher Mach number jet or a higher simulated temperature ratio were compared to the lower velocity jet, it is expected that the relative difference between the two axis planes would increase for those frequency components dominating the Mach wave emission process (due to the flapping mode) and that the angle of peak noise emission would increase relative to that of the lower speed jet. Also, the predictions of Morris and Bhat do not directly account for the differences between the two axis planes seen in figure 6.9 at the highest frequency band. It is apparent from all of the acoustic spectra (figures 6.3 to 6.8) that the minor axis fluctuations taper off to a higher broadband baseline level than those in the major axis plane all the way out to the measurement cut-off frequency. This results in higher noise levels in the minor axis plane at these frequencies. Because these frequency components represent the smallest turbulence length scales of the flows, it is likely that their effect is not captured by the stability analysis which simulates only the large scale turbulent flow fluctuations.

Since evidence of Mach wave emission is seen most clearly in the spectra for the peak just below a Strouhal number of 0.4, the SPL directivity for frequency components in this range were calculated for a narrower bandwidth than that of figure 6.9. Figure 6.10 shows the narrow bandpassed SPL directivity arcs for the frequency range St = 0.33 to 0.39 for both the pure air and helium jet cases. Over this narrow frequency range, the data provides a good comparison to Morris and Bhat (1992, 1993, 1995) for their St = 0.4 component prediction. For the helium jet, there is a more distinct difference in levels between the major and minor axis planes and the noise is radiated at an angle higher to the jet axis. It also appears that the noise in the major axis plane radiates at a slightly higher angle to the jet axis than that in the minor axis plane.

The data in figure 6.10 also shows further characteristics of Mach wave emission. Seiner et al. (1993) discuss how the peak noise angle due to Mach wave emission is equal to $\beta = \cos^{-1}(M_c^{-1})$ where M_c is the convective Mach number of the travelling turbulence. Using the measured convection speeds just downstream of the potential core from Table 5.1, the St = 0.4 varicose component should radiate at an angle of $\beta = 39^\circ$. The measured flapping component does not have a supersonic convective Mach number (downstream of the potential core) and should radiate at an angle lower than that of the varicose mode. These trends are observed in figure 6.10 if the varicose mode is assumed to radiate primarily in the major axis plane while the flapping mode is assumed to radiate primarily in the minor axis plane. The directivity from figure 6.10 shows the major axis plane to peak close to 35° and the minor axis

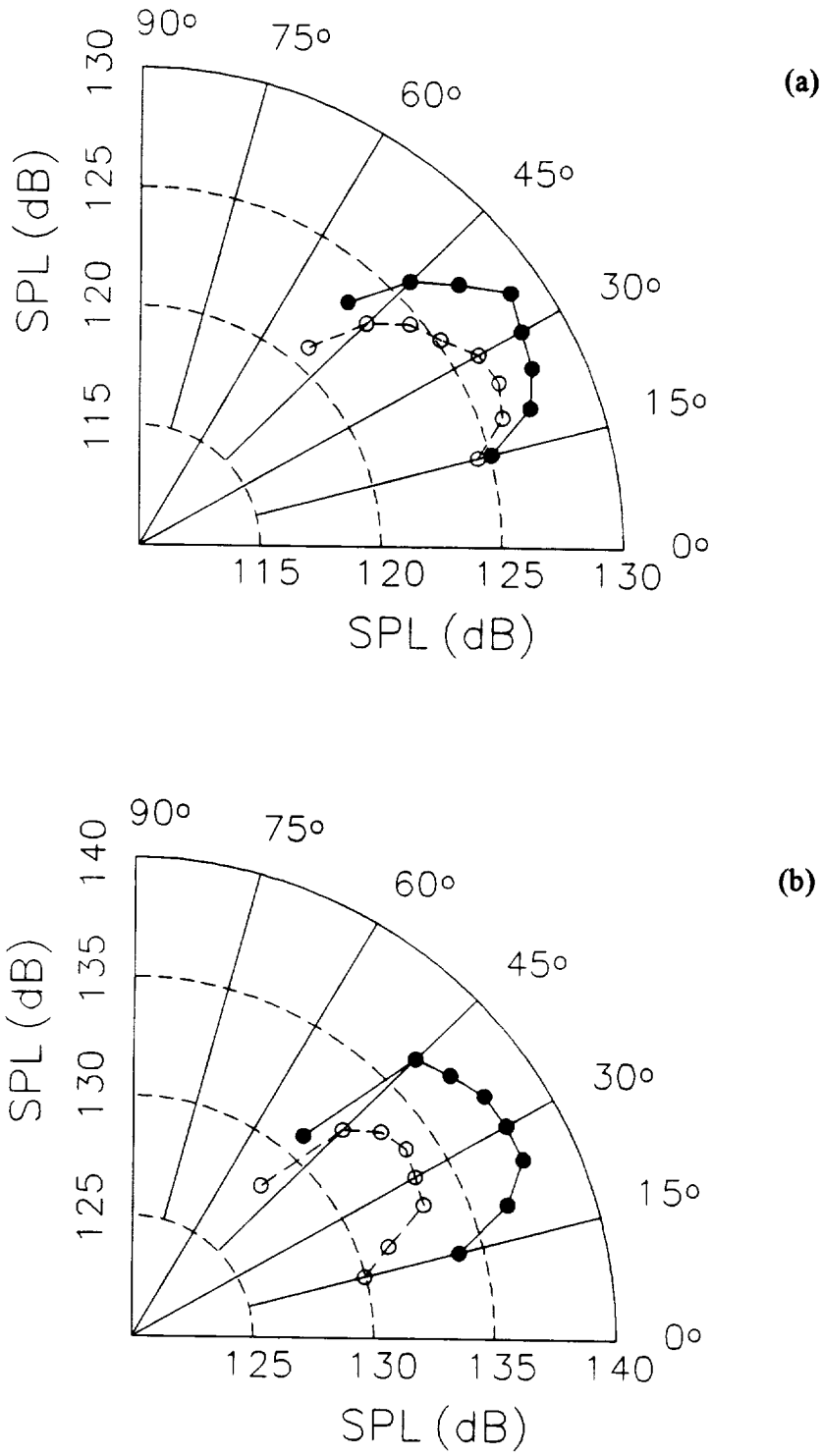

Figure 6.10 Narrow bandpassed SPL directivity for elliptic jet, St = 0.33 - 0.39, R/D_{eq} = 25. (a) T_j/T_a = 0.69, (b) T_j/T_a^* = 1.2.

plane to peak at a somewhat lower angle. It is difficult to estimate a precise angle from the data. Because the flapping mode fluctuations are primarily measured in the minor axis plane and the varicose fluctuations are measured in both planes, associating the directivity in the minor axis plane with the flapping mode and the directivity in the major axis plane with the varicose mode gives an approximation as to the directivity of each mode. For the pure air jet, both the major and minor axis planes have a similar directivity with a peak angle of nearly 30°, lower than that of for the helium jet case. (It is likely that SPL measurement in the minor axis plane at $\beta = 35^{o}$ is slightly too high and is not an indication of the true peak noise angle). Since the instability wave convection speed can not be measured directly in the potential core region, caution should be used when drawing conclusions regarding the Mach wave emission angle based on the measurements downstream of the potential core. While a higher simulated temperature ratio would likely show more distinct evidence of Mach wave emission, signs of this noise generation process are clearly present in the current data.

6.3 Sound Pressure Level Contours

Figure 6.11 shows SPL contours measured for the pure air elliptic jet. Microphone measurements were made on grid points spaced approximately $x/D_{eq} = 3$ apart. The lobed pattern is similar to SPL contours in unheated round Mach 1.5 jets measured by Morrison and McLaughlin (1979) and Yu and Dosanjh (1972). Note that away from the jet centerline, the major axis plane is quieter than the minor axis plane.

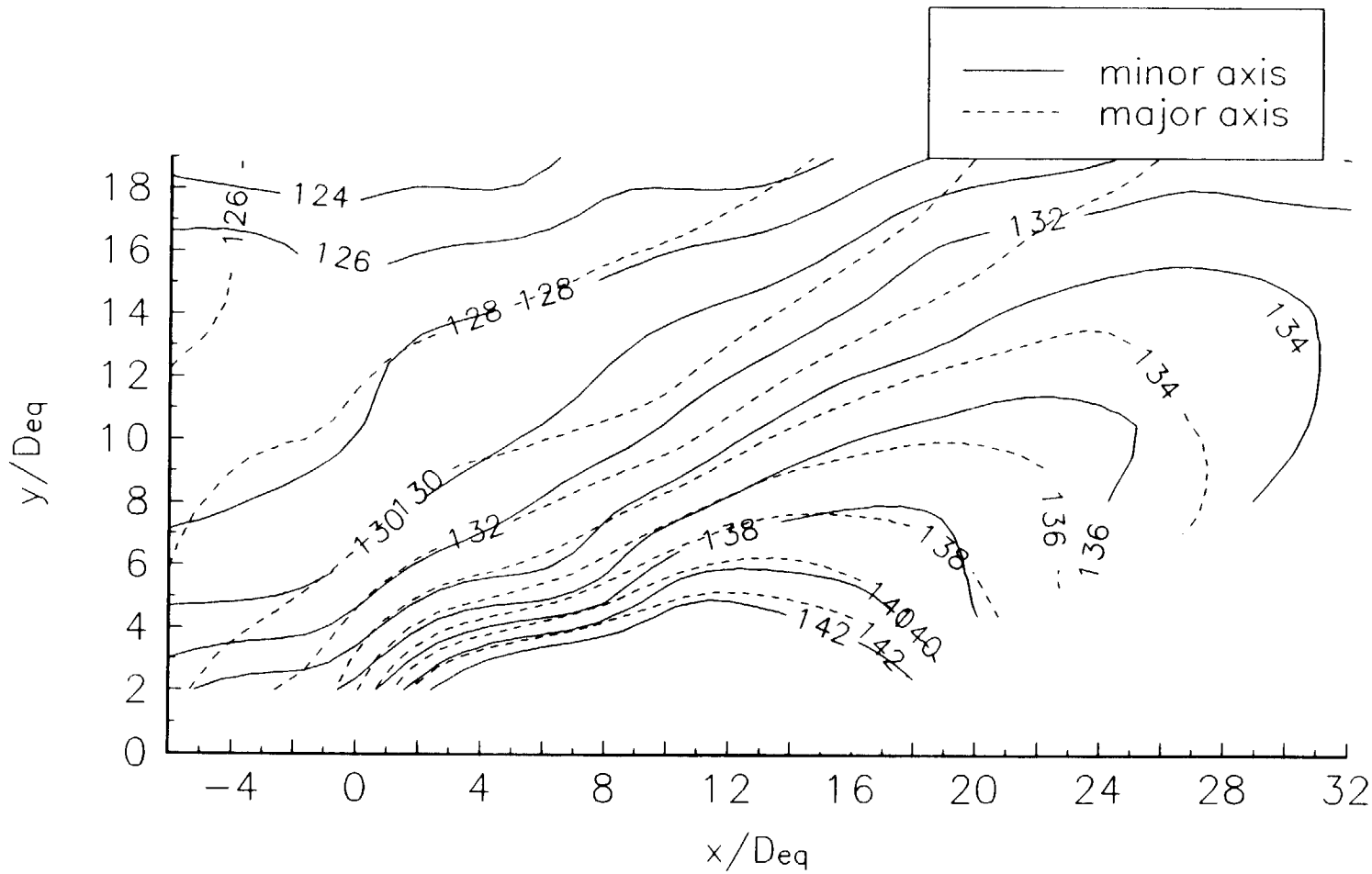

Figure 6.11 SPL contours for pure air elliptic jet, T_j/T_a=0.69.

Figure 6.12 shows SPL contours measured from the helium/air elliptic jet. Compared to the pure air jet case, the lobes are much more distinct and directed at a higher angle to the jet axis. This "directionality" is characteristic of Mach wave emission. Morris and Bhat (1993) also predict that as the actual jet temperature ratio increases from cold to heated conditions, the noise radiates at a higher angle to the jet axis and that the SPL contours show a more preferred direction of noise radiation. Recall that Morris and Bhat (1993) performed their analysis for a Mach 1.5 elliptic jet with an aspect ratio of 3:1. Since they compute the instability wave noise for both an unheated jet and a jet with $T_j/T_a = 2.0$, a reasonable comparison is available with their work.

6.4 Modal Decomposition

In an effort to determine the azimuthal modal content of the large scale turbulent fluctuations, a modal decomposition procedure similar to that performed by Troutt and McLaughlin (1982) and Hu and McLaughlin (1990) was developed for the elliptic jet. The previous authors were able to determine the modal content of supersonic jets by cross-correlating the signal from a fixed reference microphone in the acoustic field of the jet with the signal from a second microphone traversed around the azimuth of the jet. A Fourier decomposition performed on the data yielded the relative amplitude of each mode. A similar procedure is used in the present work. A detailed description of the technique is described in Appendix A and only a summary of the procedure is described this chapter.

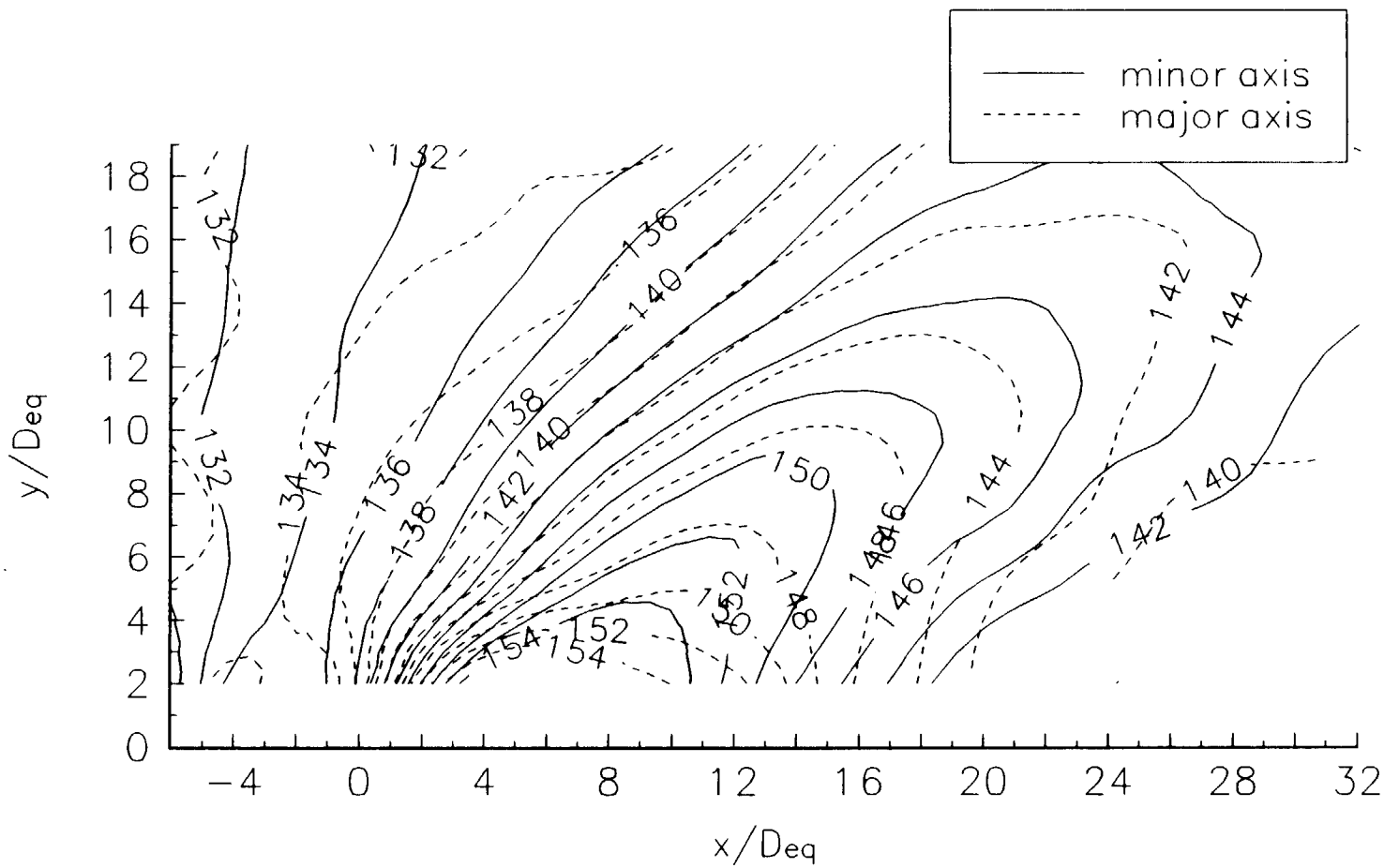

Figure 6.12 SPL contours for helium elliptic jet, $T_j/T_a^*=1.2$.

Since the modal content experiments were designed to be an aid to the analysis of Morris and Bhat (1993), the measurements were made in an elliptic cylindrical coordinate (ECC) system to be consistent with the analysis. In their analysis, Morris and Bhat describe the azimuthal pressure variation around an elliptic jet as a linear combination of Mathieu functions. Therefore, rather than analyzing the data with a typical Fourier decomposition of sines and cosines, as did Hu and McLaughlin (1990), an equivalent procedure was developed using Mathieu functions as the basis for the Fourier series. The amplitude of each Mathieu function mode can then be determined by cross-correlating a fixed reference microphone signal and a second microphone signal traversing around the jet on a contour in the ECC system.

Since Morris and Bhat (1993) predict the jet to be composed primarily of the varicose mode and the flapping mode about the major axis, these two modes are the focus for the present experiments. This simplifies the measurements and analysis since these two modes can be measured in a common plane of symmetry about the jet minor axis. Full modal decomposition measurements around the azimuth of the jet confirm that the varicose and flapping modes contain the majority of the modal content energy. In the notation of Mathieu functions consistent with Morris and Bhat, the varicose mode is described by the ce_{2n} modes where $n = 0,1,2,...$ and are referred to as even modes. The ce_0 mode specifically is occasionally referred to as the varicose mode and is equivalent to the axisymmetric mode in a circular jet where $n = 0$. The flapping mode about the major axis is described by the se_{2n+1} modes where $n = 0,1,2,...$ and are referred to as odd modes. The se_1 mode is equivalent to equal amounts of the helical

modes n = +1 and -1 in the circular jet, which also produce a flapping motion. A more complete and physical description of these modes is given in Appendix A.

Because the azimuthal measurements are made in the ECC system, the traversing microphone does not trace out an exact circle. A diagram of the measurement locations is shown in figure 6.13. The measurements were made around the azimuth, at equal angular intervals, with the traversing microphone positioned at $r/D_{eq} = 4$ when it passed by the major axis and $r/D_{eq} = 3.92$ along the minor axis. The reference microphone was held fixed at $r/D_{eq} = 3.92$ on the minor axis. The downstream distance for the measurements was $x/D_{eq} = 8$. At each azimuthal location (16 total), the cross-spectrum between the reference microphone and the traversing microphone was calculated. The complex cross-spectra then provide a description of the azimuthal pressure variation around the jet. A spatial modal decomposition is then performed on the measured data based on Mathieu functions. Since the cross-spectrum is a function of discrete frequency values, a computer code was written to perform the modal decomposition on each frequency component of the cross-spectrum.

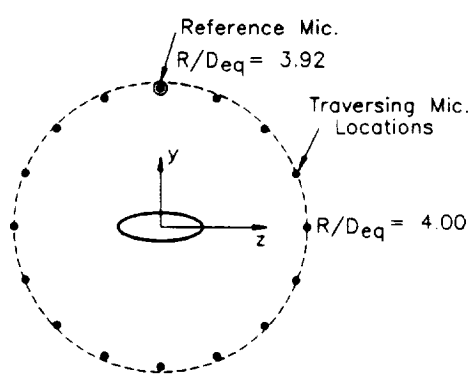

Figure 6.13 Microphone locations for modal decomposition measurements in ECC system.

Before performing the procedure on the natural jet, two test cases were tried in which the glow discharge electrodes were used to excite first the varicose mode and then the flapping mode, both for the air jet at a Strouhal number of 0.4. The modal decomposition procedure was then performed on the data to determine if the code would identify these as the dominate modes. Figure 6.14 shows the results from the varicose excitation case. The mode amplitudes are normalized by the maximum value of the ce_0 mode and only the lowest two orders of each mode are shown. Higher order modes contained negligible amounts of energy. The even modes (varicose) are clearly dominant with nearly equal amounts of the ce_0 and ce_2 present. A small amount of the odd modes (flapping) are also measured. Figure 6.15 shows the modal decomposition results when the flapping mode is excited. As expected, the se_1 (flapping) mode is dominant. There is still a significant amount of the even modes, however. This indicates that the electrodes do not excite a pure flapping mode, but introduce some varicose excitation as well. This is not particularly surprising due to the point location of the electrodes. This multi-mode mix also contributes to the difficulties discussed in chapter 5 regarding measuring the phase in the jet potential core. However, the results shown in figures 6.14 and 6.15 give confidence in the modal decomposition procedure and the glow discharge's capability to preferentially excite different modes in the jet.

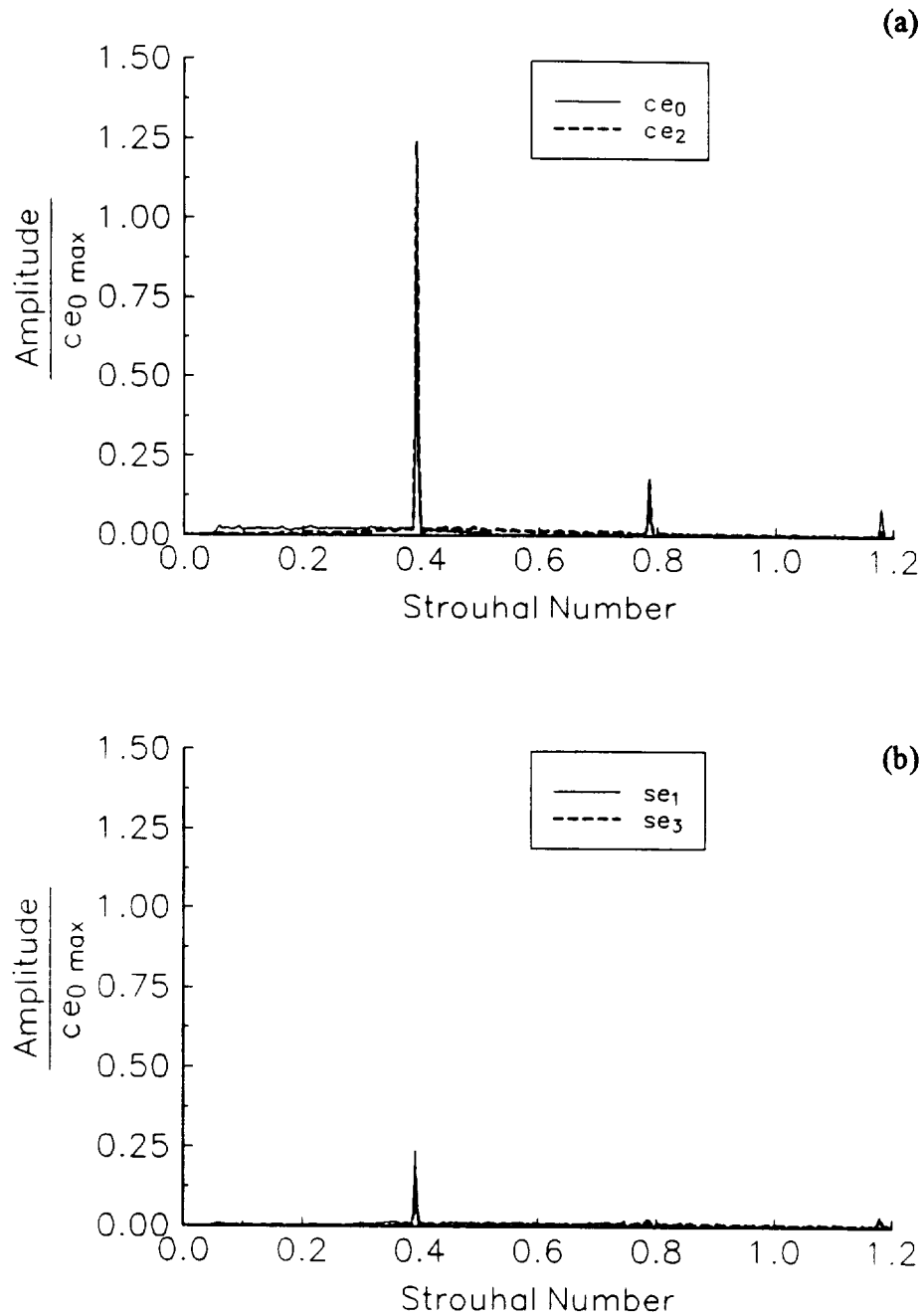

Figure 6.14 Modal content of pure air elliptic jet excited at St = 0.4 by the varicose mode, T_j/T_a = 0.69. (a) Even modes, (b) Odd modes.

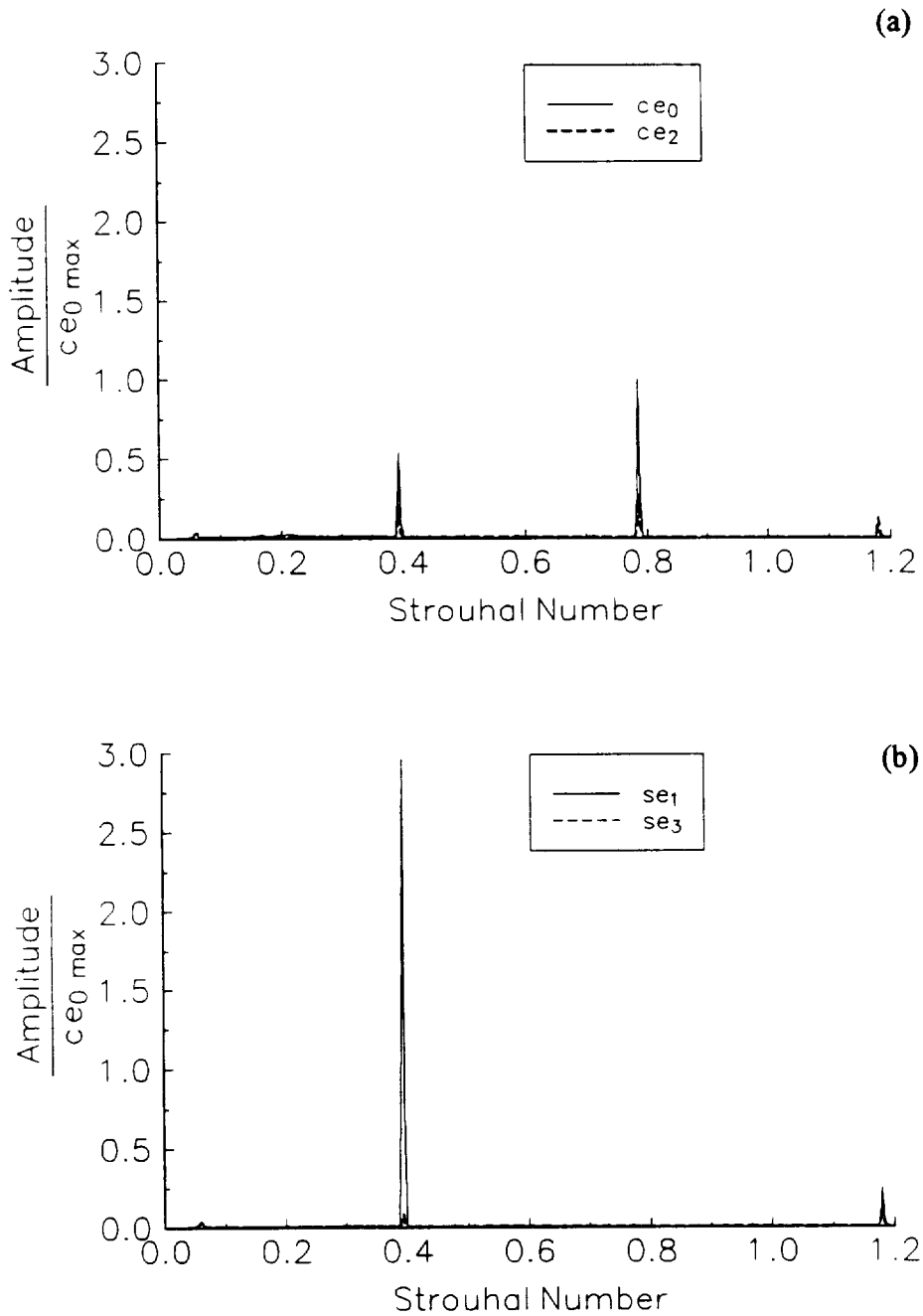

Figure 6.15 Modal content of pure air elliptic jet excited at St = 0.4 by the flapping mode. (a) Even modes, (b) Odd modes.

Figure 6.16 shows the modal decomposition results for the lowest two orders of the varicose and flapping modes for the pure air elliptic jet. Again, the amplitudes have been normalized by the maximum value of the ce_0 mode. The jet is dominated by the even modes over all frequencies. Also, the higher frequencies are seen to be composed mostly of the higher order varicose mode. There is a slight increase in the energy of the lowest order flapping mode (se_1) between the Strouhal numbers of 0.4 and 0.5. Baty and Seiner (1990) used a similar technique to measure the azimuthal modes in an unheated Mach 1.5 elliptic jet with an aspect ratio of 2 and also found the jet to be composed primarily of the varicose mode.

Figure 6.17 shows the same measurements for the helium/air jet simulating a temperature ratio of $T_j/T_a^* = 1.2$. There is a significant increase in the flapping mode compared to the pure air jet case, particularly in the midrange frequencies. Tam and Chen (1994) also predict an increase in the number of azimuthal modes present in a circular jet as the jet temperature increases. These modal decomposition measurements give additional insight into the acoustic spectra shown in figure 6.4. In the discussion of the acoustic spectra, it was shown that the minor axis fluctuation levels are higher than those in the major axis plane, particularly over the midrange frequencies. When the acoustic spectra are compared to the modal decomposition spectra shown in figure 6.17, it is seen the flapping mode shows an increased amplitude over precisely the same frequency range as the increased fluctuations measured in the acoustic field of the minor axis plane. This implies that the flapping mode radiates more efficiently to the acoustic field than the varicose mode.

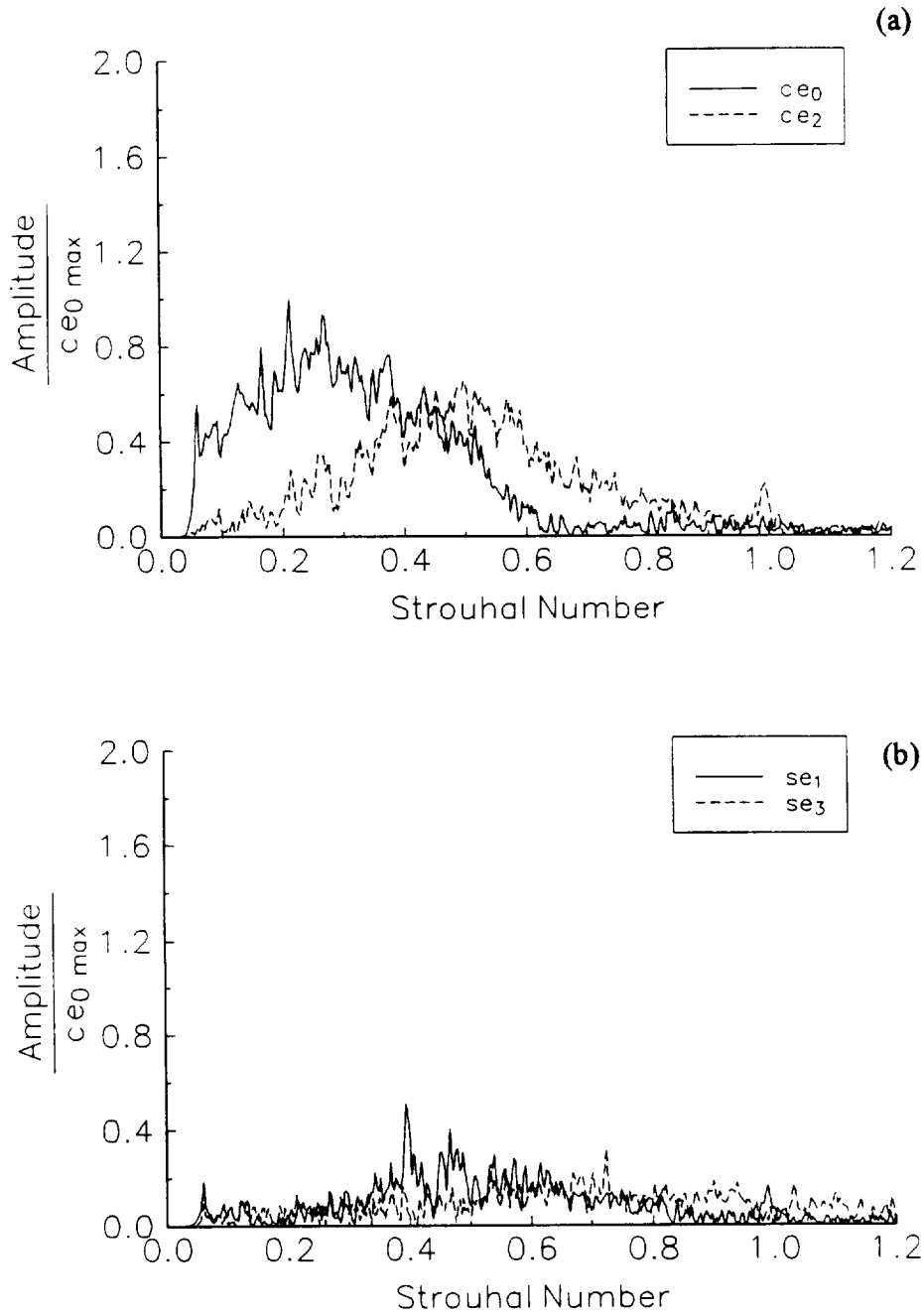

Figure 6.16 Modal content of natural pure air elliptic jet, T_j/T_a = 0.69. (a) Even modes, (b) Odd modes.

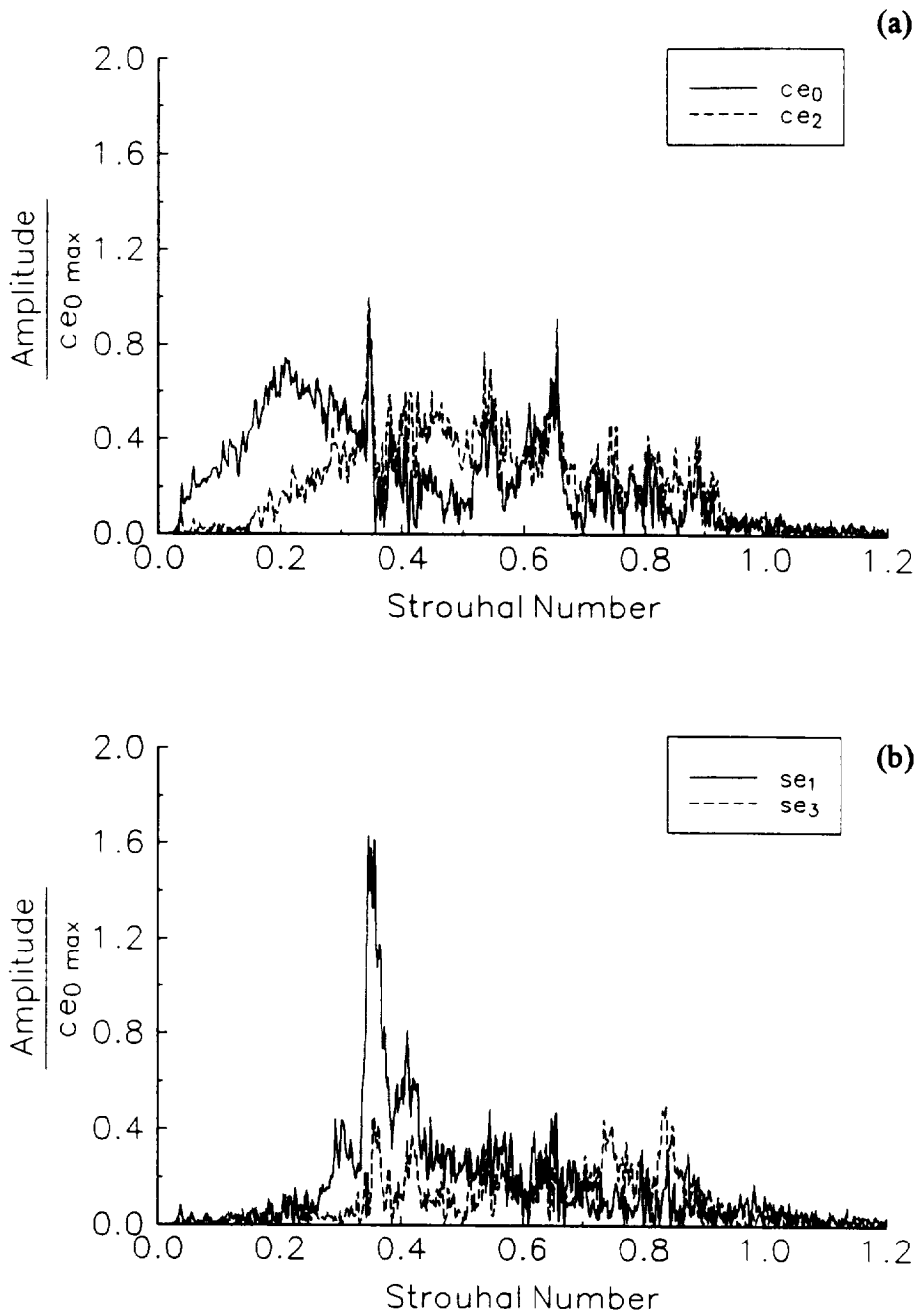

Figure 6.17 Modal content of natural helium elliptic jet, $T_j/T_a^* = 1.2$. (a) Even modes, (b) Odd modes.

The increased flapping mode in the jet acoustic field demonstrates a fundamental difference between the pure air and the helium jets and can be explained from the aerodynamic data presented earlier. Recall that as helium is added to the jet flow, the phase speed of the instability waves with respect to the ambient environment reaches supersonic values for the varicose mode and near sonic conditions for the flapping mode. These higher phase velocities compared to the air jet case will produce a stronger coupling between the hydrodynamic pressure field represented by the hot-wire measurements and the acoustic pressure field measured by the microphones. In the strictest sense, this coupling takes the form of Mach wave radiation. However, Tam and Burton (1984) and Tam and Morris (1980) showed that near sonic instability waves will also radiate to the far-field if their growth rate is sufficiently high as they will generate supersonic wavenumber components. Even though the measurements of chapter 5 showed the flapping mode phase velocities to be only near sonic just downstream of the potential core, this evidence from the modal decomposition measurements implies that the flapping waves are traveling supersonically in the potential core region. As a result, the frequency components identified with the flapping mode by the modal decomposition appear in the acoustic field with the highest energy levels.

Even though the modal decomposition technique is designed specifically for elliptic jets, an application of the method to the rectangular jet also gives insight into the azimuthal modal composition of the jet. Care should be taken when interpreting the rectangular jet modal decomposition spectra however. Because the potential core region

of the rectangular jet does not conform to the ECC system, processing the data exactly as in the elliptic jet case may lead to misleading relative amplitude levels of the individual modes. For instance, by changing the parameter q in the analysis as described in Appendix A, slightly different relative amplitude levels in the elliptic case were observed. This parameter contains the distance between the focal points of the elliptic jet, which has little meaning in the rectangular case. It is not known how this parameter affects the mode amplitudes in the rectangular jet case. At the very least, however, an application of the modal decomposition technique to the rectangular jet will give an indication of the symmetric and antisymmetric modes, even if there is some uncertainty in the exact amplitude of each mode.

Figure 6.18 shows the modal decomposition procedure applied to the pure air rectangular jet. Only the lowest orders of each mode are shown. As expected, the modal decomposition spectra bears a strong resemblance to the acoustic spectra shown in figure 6.5 being dominated by the discrete screech tones. It is interesting that the first and third tones are composed primarily of an antisymmetric (flapping) mode, while the second tone is primarily of a symmetric (varicose) nature. This supports the findings of Raman and Rice (1994) who observed the same relationships in an underexpanded rectangular jets.

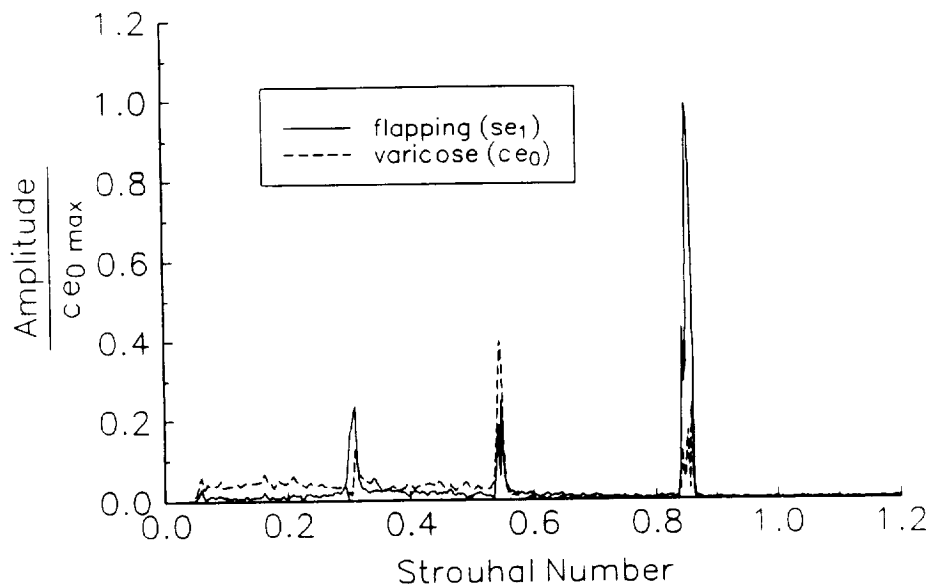

Figure 6.18 Modal content of natural pure air rectangular jet, full scale, T_j/T_a = 0.69.

In order to see the detail of the broad band spectrum, the modal decomposition results for the pure air rectangular jet are shown on a truncated scale in figure 6.19. Even though the varicose mode doesn't quite dominate the jet as in the pure air elliptic case, the varicose mode does have a significantly higher amplitude over most of the frequency range. The second order varicose mode (ce_2) also contains a significant amount of energy.

The modal decomposition results from the helium rectangular jet are shown in figure 6.20. Similar to the air case, the overall modal spectra are dominated by the discrete tone at St = 0.72. This tone is composed mostly of the flapping mode, but does contain some of the varicose mode as well. The broadband frequency content is

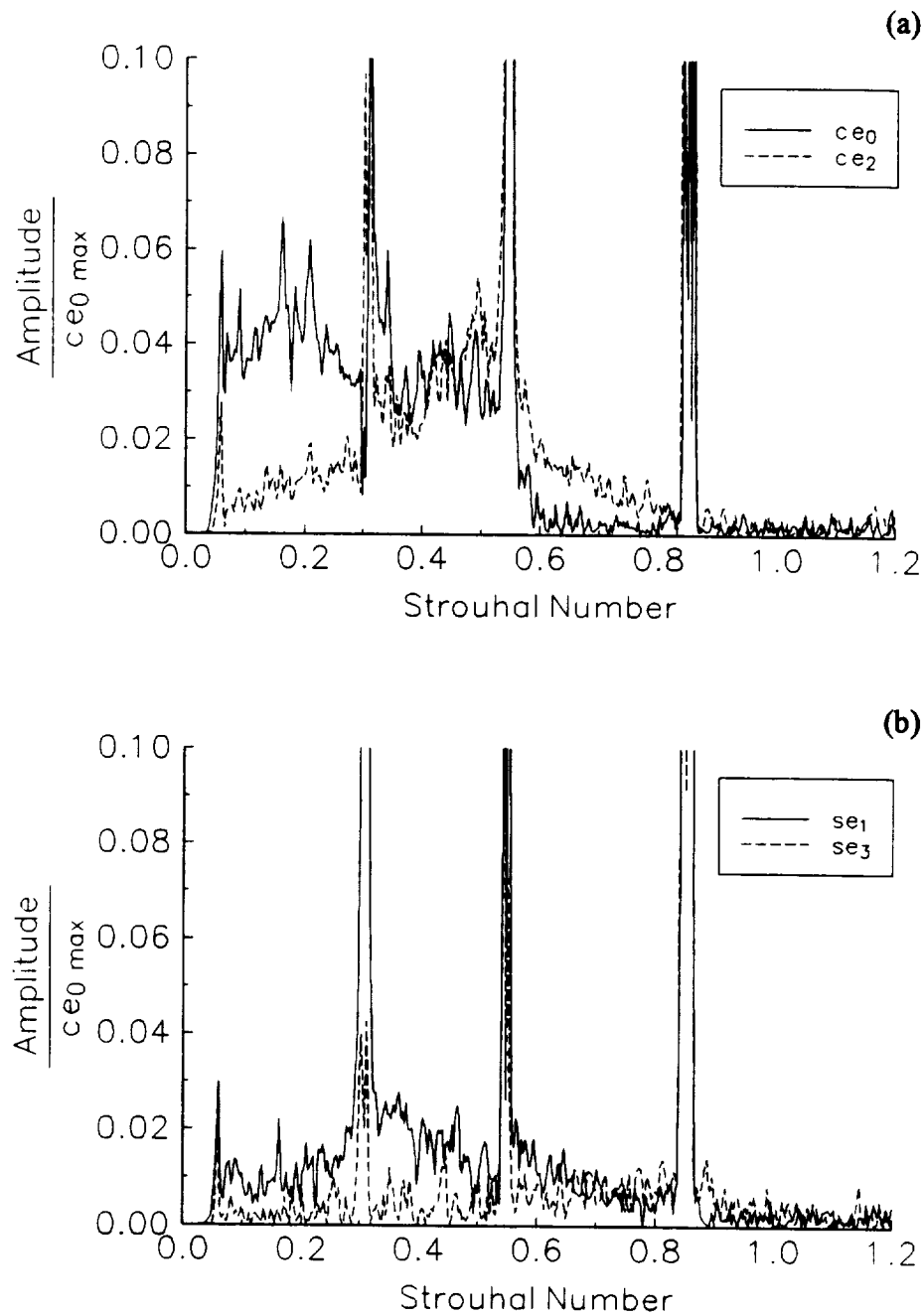

Figure 6.19 Modal content of natural pure air rectangular jet, T_j/T_a = 0.69. (a) Even modes, (b) Odd modes.

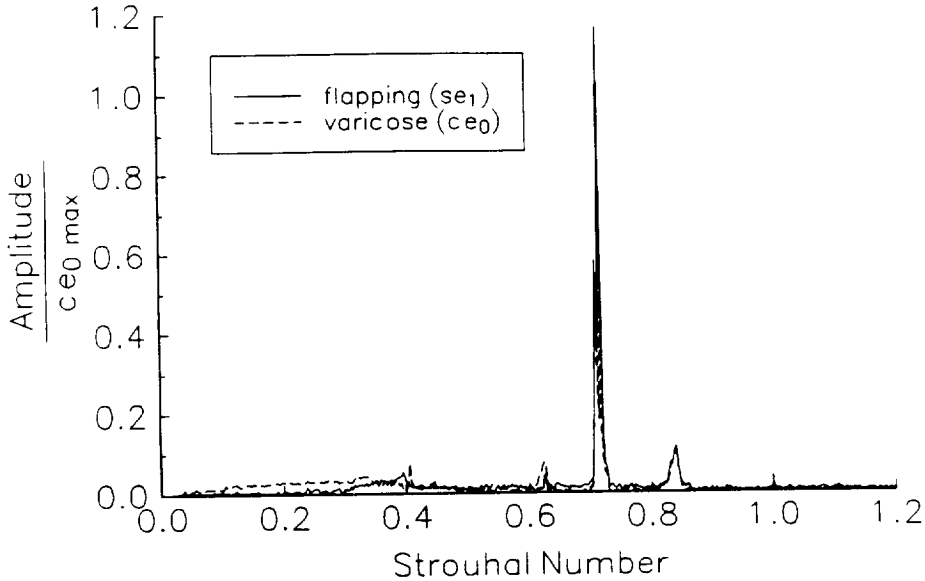

Figure 6.20 Modal content of natural helium rectangular jet, full scale, $T_j/T_a^* = 1.2$.

shown in figure 6.21, which has a truncated y-axis. Compared to the air rectangular jet, the helium jet shows an increase in flapping amplitude at Strouhal numbers above St = 0.3. Although the flapping mode does not *appear* to achieve quite the same relative amplitude over the varicose mode as in the helium elliptic jet case, there is an increase in the flapping mode compared to the pure air rectangular jet. Again, this is attributed to the higher level of coupling between the flapping hydrodynamic pressure field and the radiated noise when helium is used to increase the phase speed of the instability waves.

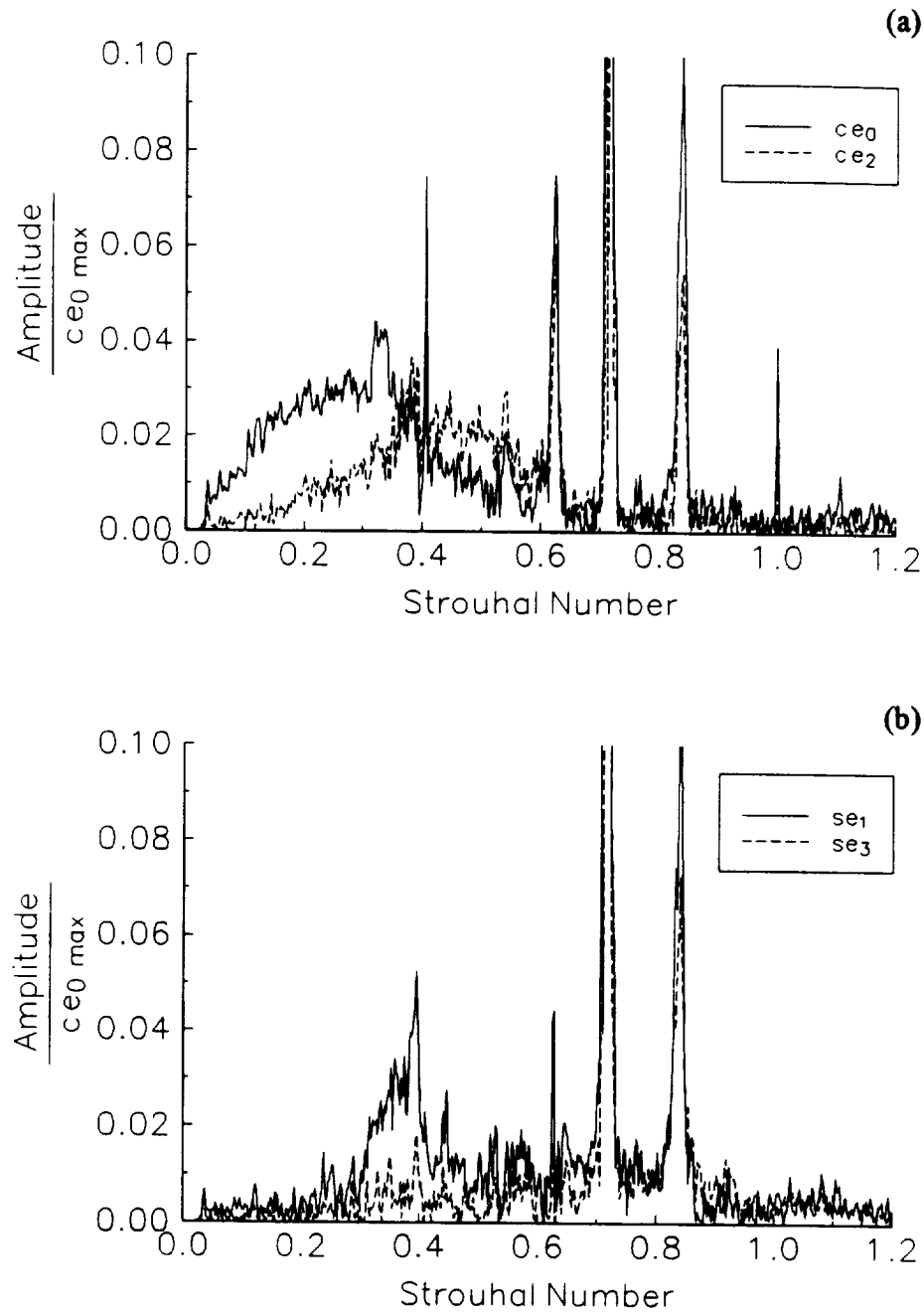

Figure 6.21 Modal content of natural helium rectangular jet, $T_j/T_a^* = 1.2$. (a) Even modes, (b) Odd modes.

CHAPTER 7

CONCLUSIONS AND FUTURE WORK

7.1 Summary

This thesis has reported aerodynamic and acoustic measurements from moderate Reynolds number elliptic, rectangular, and circular perfectly expanded supersonic jets. It has focused on the beneficial aeroacoustic effects of the asymmetric jets. Helium/air mixture jets have been used to simulate the low density and high velocity of heated jets. Recall that the three major goals of the research have been to:

1) Investigate the aeroacoustics properties of an elliptic and a rectangular Mach 1.5 near-perfectly expanded supersonic jet.
2) Evaluate the use of helium/air mixture jets to simulate heated jets in aeroacoustic studies.
3) Establish an experimental data base of acoustic and flow fluctuation measurements most relevant to the dominant noise generation processes for use in current and future computational and analytical prediction methods of noncircular supersonic jets.

The following is a list of the major results.

7.1.1 Focus on Asymmetric Jets

1) The centerline Mach number and velocity distribution of the two asymmetric jets were similar showing similar potential core lengths and

centerline velocity decay rates. Both asymmetric jets had shorter potential core lengths than the axisymmetric jet. This suggests an increased mixing rate in the asymmetric jets.

2) Radial mean velocity profiles showed minimal axis switching in the elliptic jet (as seen in many asymmetric flows) through $x/D_{eq} = 17$. The rectangular jet did show a slight axis switch by $x/D_{eq} = 12$. Since imperfections in the jet nozzle resulted in a weak shock cell structure for the rectangular jet, it is hypothesized that the shocks have an effect on the axis switching. Corner vortices in the rectangular jet may also play a role in the axis switching.

When the radial coordinate was normalized by the half-velocity point and shear layer velocity thickness, the velocity profiles collapsed reasonably well onto a single curve. The collapse for the elliptic jet was better than that for the rectangular jet. Up until the axis switch in the rectangular jet, the thickness parameters for the elliptic and rectangular jet were similar for both jets, including shear layer growth rates. Velocity contour plots of both jets showed very similar development of the mean jet flows.

3) The maximum hot-wire fluctuation levels in the minor axis plane were consistently higher than those in the major axis plane. A higher growth rate of the flapping mode was also measured compared to the varicose mode.

4) Radial hot-wire measurements showed a monotonically varying change in phase across the jet shear layer (totalling 360°) early in the jet development. Farther downstream, the phase change was closer to 270°. The r.m.s. distribution showed two peaks as the hot-wire traversed across the shear layer. A simple model simulating the shear layer by convecting vortices was proposed and agreed qualitatively with the radial hot-wire measurements of the present jet work and measurements of low-speed planar shear layers by Gaster et al. (1985).

5) Lower levels of noise were measured from the asymmetric jets in the far-field compared to the round jet, especially in the major axis plane. The major axis plane was quieter than the minor axis plane for both jets. With the exception of screech tones in the rectangular jet, the far-field noise spectral content, amplitude, and directivity for both asymmetric jets were very similar.

6) Due to the mild shock cell structure, the rectangular jet produced up to six screech tones which were not integer harmonics of one another. Excellent agreement was found for the frequency of these tones when compared to the first six modes predicted by the shock cell/screech frequency model of Tam (1988). It is believed that the appearance of these higher order modes are due to the reduced Reynolds number conditions of the present work. Similar non-

integer tones were observed in the low Reynolds number screech research of Hu and McLaughlin (1990) in axisymmetric jets.

7.1.2 Focus on Helium Simulation

1) The addition of helium to the jet flow tended to cause the potential core to contract slightly. There was no measurable difference in the development of the jet shear layers when helium was added to the flow.

2) For the helium/air mixture jets, the axial phase speed of the large scale structures approach or exceed the ambient sound speed over most frequencies. In general, the addition of helium serves to increase the structure velocity with respect to the ambient sound speed, but lower structure velocity with respect to the jet exit velocity.

3) The far-field sound pressure levels increased by 7 - 8 dB when helium was added to the jet flow. The peak radiation angle also increased for the simulated hot conditions. SPL contours also showed more distinct lobes in the radiated sound directivity pattern for the helium jets. The relative SPL difference between the major and minor axis planes of the asymmetric jets increased for the helium conditions with the major axis becoming even quieter compared to the minor axis.

4) For the air jet cases, the peak levels in the acoustic spectra occurred at lower frequencies than those observed in the hot-wire fluctuations. For the helium/air mixtures, there was good agreement between the acoustic and flow fluctuation spectra.

5) A modal decomposition technique was developed and tested for elliptic jets to measure the relative contribution of the azimuthal modes to the jet acoustic field. The air jets were observed to be dominated by the varicose mode over the entire frequency range. The helium/air mixture jets showed a significant increase in the flapping mode compared to the varicose mode over the midrange frequencies. For the simulated hot jet, the peak frequencies in the flow fluctuation spectra and the far-field acoustic spectra were the same frequencies which showed increased flapping in the modal spectra.

7.2 Concluding Remarks

From these results, it is seen that the major goals of this work have been achieved. Several beneficial aeroacoustic properties of the asymmetric jets have been demonstrated. Also, the present work has provided a clearer understanding of the nature of noncircular jet noise and how it differs from sound generated by round jets. Similarities between the near perfectly expanded elliptic and rectangular jets have also been observed. In spite of some differences, most of which can be attributed to the

weak shock cell structure of the rectangular jet, both the mean and fluctuating flowfields as well the radiated acoustics show strong likenesses.

The helium simulation of heated jets was able to reproduce successfully most of the characteristics of actual heated jets. Strong evidence of Mach wave radiation is observed only when helium is added to the jet flow. Some of the observed changes for the simulated heated conditions are an increase in the phase velocity of the large scale structures with respect to the ambient acoustic velocity, more noise produced in a more directional manner, peak instability frequencies radiating noise directly to the far-field, and an increased amplitude of the flapping mode compared to the varicose mode. All of these qualities have either been measured in actual heated jets or agree with predicted trends caused by jet heating.

This thesis has further demonstrated the necessity of performing experiments or calculations in manner which accounts for the changes which take place as a jet is heated to realistic engine exhaust operating conditions. If the Mach wave emission noise source is not reproduced properly, it is possible to draw misleading conclusions while interpreting the data. The helium simulation of heated jets is relatively easy and provides a low cost means to investigate these effects in small scale supersonic jets.

7.2.1 Future Work

While they provide a solid foundation for the investigation of reduced Reynolds number asymmetric jets, the results from the present work are far from exhaustive with respect to the possible areas of research. This is especially true with respect to the

helium/air mixture simulation of heated jets. A more rigorous evaluation of the simulation would be helpful in order to draw more quantitative conclusions from the simulation in regard to actual heated jets. This could be best accomplished by focusing attention primarily on circular jets. Because of the relatively sparse data base of actual heated asymmetric jet flow and acoustic data, drawing direct quantitative comparisons between the actual heated jet cases and the simulation is difficult for the elliptic and rectangular cases. More data is available in the literature for the circular jet case which could be used to provide a more precise evaluation of the simulation.

Further experiments for the asymmetric jet cases would provide more insight regarding how the noncircular jets produce noise and how the heated jet simulation affects the aeroacoustic properties. In particular, more detailed investigation into the artificially excited jets could provide insight regarding noise suppression through active control of the jets. Only the varicose and flapping in the minor axis plane have been investigated so far. Excitation of different modes or combination of modes may lead to enhanced jet mixing resulting in lower radiated noise. Tuning the excitation frequencies to the resonances of an external jet shroud may provide favorable cancellation effects in the shroud which may lower the radiated sound as well.

A wide range of operating conditions can also be studied using the helium simulation. Imperfectly expanded jets can easily be operated in the jet noise facility to study the effects of off-design conditions on jet noise. There is also the possibility of operating jets with higher simulated temperature ratios than those reported here. Higher simulated temperature ratios would produce stronger Mach wave radiation than what

is produced from the present jets and thereby make the phenomenon easier to study. However, higher simulated temperature ratios may require all or part of the facility anechoic chamber to be rebuilt in order to reduce the build-up of helium in the test chamber.

REFERENCES

Abramowitz, M., and Stegun, I.A., 1965, Handbook of Mathematical Functions, Dover Press, New York.

Barron, W.D., 1993, "An Experimental Study of Supersonic Helium/Air Jets at Low Reynolds Numbers," Master's Thesis, The Pennsylvania State University.

Baty, R.S., Seiner, J.M., and Ponton, M.K., 1990, "Instability of a Supersonic Shock-Free Elliptic Jet," AIAA Paper 90-3959, AIAA 13th Aeroacoustics Conference, Tallahassee, FL.

Bendat, J.S., and Piersol, A.G., 1986, Random Data Analysis and Measurement Procedures, John Wiley and Sons, New York.

Bent, P.H., 1993, "Experiments on the Aerodynamic Generation of Noise in Centrifugal Turbomachinery," Ph.D. Thesis, The Pennsylvania State University.

Choi, J.S., 1991, "Experiments on the Unsteady Flowfield Associated with Noise Generation in Centrifugal Turbomachinery," Ph.D. Thesis, The Pennsylvania State University.

Chyczewski, T.S., and Long, L.N., 1995, "Applications of an Efficient Parallel Computational Aeroacoustics Algorithm," CEAS/AIAA 95-011, 16th Aeroacoustics Conference, Munich, Germany.

Detmetriades, A, and Brower, T.L., 1982, "Experimental Study of Transition in a Compressible Free Shear Layer," AFOSR TR 83-0144.

Ffowcs Williams, J.E., 1953, "The Noise of Turbulence Travelling at High Speed," *Philosophical Transactions of the Royal Society*, A, Vol. 255, pp. 469-503.

Gaster, M., Kit, E., and Wygnanski, I., 1985, "Large-Scale Structures in a Forced Turbulent Mixing Layer," *Journal of Fluid Mechanics*, Vol. 150, pp. 23-39.

Gutmark, E., Schadow, K.C., Wilson, K.J., and Bicker, C.J., 1988, "Near-Field Pressure Radiation and Flow Characteristics in Low Supersonic Circular and Elliptic Jets," *Physics of Fluids*, Vol. 31, pp. 2524-2532.

Hu, T.F., 1985, "Flow and Acoustic Properties of Low Reynolds Number Underexpanded Supersonic Jets," Ph.D. Thesis, Oklahoma State University.

Hu, T.F, and McLaughlin, D.K., "Flow and Acoustic Properties of Low Reynolds Number Underexpanded Supersonic Jets," *Journal of Sound and Vibration*, Vol. 141, 1990, pp. 485-405.

Hussain, F., and Husain, H.S., 1989, "Elliptic Jets. Part 1. Characteristics of Unexcited and Excited Jets, " *Journal of Fluid Mechanics*, Vol. 208, pp. 257-320.

Kantola, R.A., 1970, "Noise Characteristics of Heated High Velocity Rectangular Jets," *Journal of Sound and Vibration*, Vol. 64, pp. 277-294.

Kistler, A.L., 1959, "Fluctuation Measurements in a Supersonic Turbulent Boundary Layer," *Physics of Fluids*, Vol. 2, pp. 290-296.

Ko, C.L., McLaughlin, D.K., Troutt, T.R., 1978, "Supersonic Hot-Wire Fluctuation Data Analysis With a Conduction End-Loss Correction," *Journal of Physics E: Scientific Instrumentation*, Vol. 11, pp. 488-494

Kovasznay, L.S.G., 1950, "The Hot-Wire Anemometer in Supersonic Flow, " *Journal of the Aeronautical Sciences*, Vol. 17, pp. 565-584

Krothapalli, A., Hsia, Y., Baganoff, D. , and Karamcheti, K., 1986, "The Role of Screech Tones in Mixing of An Underexpanded Rectangular Jet," *Journal of Sound and Vibration*, Vol. 106, pp. 119-143.

Lau, J., 1981, "Effects of Exit Mach Number of Temperature on Mean-Flow and Turbulence Characteristics in Round Jets," *Journal of Fluid Mechanics*, Vol. 105, pp. 193-218.

Lighthill, M.J., 1952, "On Sound Generated Aerodynamically. I. General Theory," *Proceedings of the Royal Society of London A*, Vol. 211, pp. 564-587.

Martens, S., 1995, "Experiments in a Compressible Mixing Layer," Ph.D. Thesis, The Pennsylvania State University.

Martens, S., Kinzie, K.W., and McLaughlin, D.K., 1994, "Measurements of Kelvin-Helmholtz Instabilities in a Supersonic Shear Layer," *AIAA Journal*, Vol. 32, pp. 1633-1639,

Massey, K.C., Ahuja, K.K., Jones, R.R., Tam, C.K.W. , 1994, "Screech Tones of Supersonic Heated Free Jets," AIAA Paper 93-0141, 32nd Aerospace Sciences Meeting, Reno, NV.

McLachlan, N.W., 1947, Theory and Application of Mathieu Functions, Oxford University Press, London.

McLaughlin, D.K., Morrison, G.L., and Troutt, T.R., 1975, "Experiments on the Instability Waves in a Supersonic Jet and Their Acoustic Radiation," *Journal of Fluid Mechanics*, Vol. 69, pp. 73-95.

McLaughlin, D.K., Barron, W.D., and Vaddempudi, A.R., 1992, "Acoustic Properties of Supersonic Helium/Air Jets at Low Reynolds Number," DGLR/AIAA 92-02-047, 14th Aeroacoustics Conference, Aachen, Germany.

Morris, P.J., and Tam, C.K.W., 1979, "On the Radiation of Sound by the Instability Waves of a Compressible Axisymmetric Jet," Mechanisms of Sound Generation in Flows, ed. E.A. Muller, Springer-Verlag.

Morris, P.J., Bhat, T.R.S., and Chen, G., 1989, "A Linear Shock Cell Model For Jets of Arbitrary Exit Geometry," *Journal of Sound and Vibration*, Vol. 132, pp. 199-211.

Morris, P.J., and Bhat, T.R.S., 1992, "The Noise From Supersonic Elliptic Jets," DGLR/AIAA 92-02-042, 14th Aeroacoustics Conference, Aachen, Germany.

Morris, P.J., and Bhat, T.R.S., 1993, "Supersonic Elliptic Jet Noise," AIAA Paper 93-4409, 15th Aeroacoustics Conference, Long Beach, CA.

Morris, P.J., and Bhat, T.R.S., 1995, "The Spatial Stability of Compressible Elliptic Jets, " *Physics of Fluids*, Vol. 7, pp. 185-194.

Morrison, G.L., and McLaughlin, D.K., 1979, "Noise Generation by Instabilities in Low Reynolds Number Supersonic Jets," *Journal of Sound and Vibration*, Vol. 65, pp. 177-191.

Morrison, G.L., and McLaughlin, D.K., 1980, "Instability Process in Low Reynolds Number Supersonic Jets," *AIAA Journal*, Vol. 18, pp. 793-800.

Oster, D., and Wygnanski, I., 1982, "The Forced Mixing Layer Between Parallel Streams," *Journal of Fluid Mechanics*, Vol. 123, pp. 91-130.

Press, W.H., Flannery, B.P., Teukolsky, S.A., and Vetterling, W.T., 1989, Numerical Recipes: The Art of Scientific Computing, Cambridge University Press, Cambridge.

Raman, G., and Rice, E.J., 1994, "Instability Modes Excited by Natural Screech Tones in a Supersonic Rectangular Jet," *Physics of Fluids*, Vol. 6, pp. 3999-4008.

Reynolds, W.C., and Perkins, H.C., 1977, Engineering Thermodynamics, McGraw-Hill, New York.

Rose, W.C., 1973, "The Behavior of a Compressible Turbulent Boundary Layer in a Shock Wave Induced Adverse Pressure Gradient," NASA Technical Note D-7092.

Schadow, K.C., Gutmark, E., Koshigoe, S., and Wilson, K.J., 1989, "Combustion Related Shear-Flow Dynamics in Elliptic Supersonic Jets," *AIAA Journal*, Vol. 27, pp. 1347-1353.

Schlicting, H., 1954, Boundary-Layer Theory, McGraw-Hill, New York.

Seiner, J.M., McLaughlin, D.K., and Liu, C.H., 1982, " Supersonic Jet Noise Generated by Large Scale Instabilities," NASA Technical Paper 2072.

Seiner, J.M., and Ponton, M.K., 1991, "Supersonic Acoustic Source Mechanisms for Free Jets of Various Geometries," AGARD 78thB Specialists Meeting on Combat Aircraft Noise, Bonn, Germany.

Seiner, J.M., Ponton, M.K., Jansen, B.J., and Lagen, N.T., 1992, "The Effects of Temperature on Supersonic Jet Noise Emission," DGLR/AIAA 92-02-046, 14th Aeroacoustics Conference, Aachen, Germany.

Seiner, J.M., 1992, "Fluid Dynamics and Noise Emission Associated with Supersonic Jets," Studies in Turbulence, ed. Gastski, T.B., S. Sutanu, and Speziale, C.G., Springer-Verlag, pp. 297-323.

Shih, C., Krothapalli, A., Gogineni, S., 1992, "Experimental Observations of Instability Modes in a Rectangular Jet," *AIAA Journal*, Vol. 30, pp. 2388-2394.

Stromberg, J.L., McLaughlin, D.K., and Troutt, T.R., 1980, "Flow Field and Acoustic Properties of a Mach Number 0.9 Jet at a Low Reynolds Number," *Journal of Sound and Vibration*, Vol. 72, pp. 159-176.

Tam, C.K.W., and Chen, P., 1994, "Turbulent Mixing Noise from Supersonic Jets," *AIAA Journal*, Vol. 32, pp. 1774-1780.

Tam, C.K.W., and Morris, P.J., 1980, "The Radiation of Sound by the Instability Waves of a Compressible Plane Turbulent Shear Layer," *Journal of Fluid Mechanics*, Vol. 98, pp. 349-381.

Tam, C.K.W., and Burton, 1984, "Sound Generated by Instability Waves of Supersonic Flows. Part 2. Axisymmetric Jets," *Journal of Fluid Mechanics*, Vol. 138., pp. 273-295.

Tam, C.K.W., 1988, "The Shock-Cell Structures and Screech Tone Frequencies of Rectangular and Non-Axisymmetric Supersonic Jets," *Journal of Sound and Vibration*, Vol. 121, pp. 135-147.

Tam, C.K.W., Seiner, J.M., and Yu, J.M., 1986, "Proposed Relationship Between Broadband Shock Associated Noise and Screech Tones," *Journal of Sound and Vibration*, Vol. 110, pp. 309-321.

Tanna, H.K., Dean, P.D., and Fisher, M.J., 1975, "The Influence of Temperature on Shock-Free Supersonic Jet Noise," *Journal of Sound and Vibration*, Vol. 39, pp. 429-460.

√ Troutt, T.R., and McLaughlin, D.K., 1982, "Experiments on the Flow and Acoustic Properties of a Moderate Reynolds Number Supersonic Jet," *Journal of Fluid Mechanics*, Vol. 116, pp. 123-156.

Way, J. and Libby, P.A., 1970, "Hot-Wire Probes for Measuring Velocity and Concentration in Helium-Air Mixtures," *AIAA Journal*, Vol. 8, pp. 976 - 978.

√ Winant, C.D., and Browand, F.K., 1974, "Vortex Pairing: The Mechanism of Turbulent Mixing Layer Growth at Moderate Reynolds Number," *Journal of Fluid Mechanics*, Vol. 63, part 2, pp. 237-255.

Yu, J.C., and Dosanjh, D.S., 1972, "Noise Field of A Supersonic Mach 1.5 Cold Model Jet," *Journal of the Acoustical Society of America*, Vol. 51, pp. 1400-1410.

Zaman, K.B.M.Q., 1994, "Effect of Delta Tabs on Mixing and Axis Switching in Jets From Asymmetric Nozzles," AIAA Paper 94-0186, 32nd Aerospace Sciences Meeting and Exhibit, Reno, NV.

Zaman, K.B.M.Q., 1995, "Axis Switching and Spreading of an Asymmetric Jet--ROle of Vorticity Dynamics," AIAA Paper 95-0889, 33rd Aerospace Sciences Meeting and Exhibit, Reno, NV.

APPENDIX A

MODAL DECOMPOSITION THEORY AND CODE

For a round jet, it is a relatively straightforward procedure to place microphones uniformally around the azimuth of the jet and perform a spatial Fourier decomposition on the data to obtain the relative amplitudes of the azimuthal modes. Hu (1985) and Hu and McLaughlin (1990) describe in detail a method which decomposes the azimuthal pressure variation around a circular jet into its Fourier sine and cosine modes. The resulting coefficients then give an indication as to relative amounts of each azimuthal mode in the jet.

For an elliptic jet, the same kind of procedure can be applied, except that an elliptic cylindrical coordinate (ECC) system is a more natural choice in which to resolve the modes. However, the use of sines and cosines as a basis for the Fourier series is not appropriate in the ECC system. Mathieu functions, which can be written as infinite sums of standard trigonometric functions, lend themselves to a similar Fourier decomposition technique as that used in circular jets. This appendix provides the mathematical development for the use of Mathieu functions to describe the azimuthal modal content of an elliptic jet. A detailed descriptions of Mathieu functions and their properties is not provided here, but rather only a description of their application to the modal decomposition technique of the present work. Rigorous descriptions regarding the nature and properties of Mathieu functions can be found in many mathematics

handbooks and other references such as McLachlan (1947) and Abramowitz and Stegun (1965).

A.1 General Properties of Mathieu Functions and Instability Wave Theory

For an elliptic cylindrical coordinate (ECC) system, Morris and Bhat (1993, 1995) describe the azimuthal pressure distribution around an elliptic jet using a linear combination of Mathieu functions in a series. They show that the pressure distribution around an elliptic jet can be described by the following the equations:

$$\zeta(u, v, q) = C_A(u, q) \sum_{m=0}^{\infty} A_{(2m+p)}\, ce_{(2m+p)}(v, q) \qquad p = 1 \text{ or } 2 \qquad \text{A.1a}$$

$$\zeta(u, v, q) = C_B(u, q) \sum_{m=0}^{\infty} B_{(2m+p)}\, se_{(2m+p)}(v, q) \qquad p = 1 \text{ or } 2 \qquad \text{A.1b}$$

where

$$q = -\frac{a^2}{4}\left[\alpha^2 - \rho_\infty M_j^2\, \omega^2\right]$$

In equation A.1, u and v are ECC coordinate variables described by figure A.1. They are analogous to r and θ in a circular cylindrical coordinate system. Therefore, for a constant value of u ("radius"), C_A and C_B in equation A.1 are constants depending only q, which is only a function of frequency once the jet operating conditions are specified.

Since Mathieu functions can be written as infinite sums of trigonometric functions, (see McLachlan, 1947) they also possess many of the same properties as

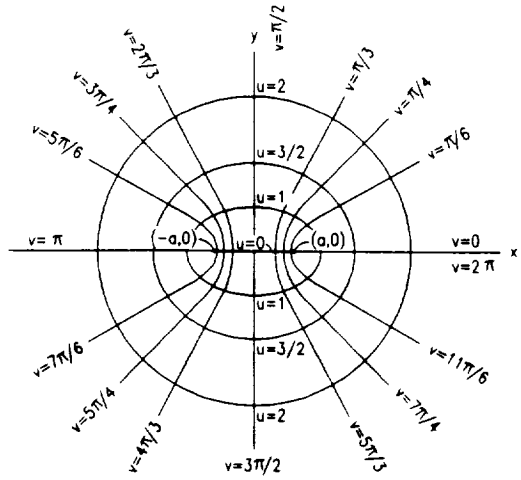

Figure A.1 Elliptic cylindrical coordinate system.

trigonometric functions. The even Mathieu functions (ce_{2m+p}) are symmetric about the horizontal axis in figure A.1 while the odd Mathieu functions (se_{2m+p}) are antisymmetric about the same axis. If $p = 0$, the solution is of period π; if $p = 1$, the solution is of period 2π. Therefore, equation A.1 represents four different equations where A_{2m}, A_{2m+1}, B_{2m}, and B_{2m+1} are the amplitudes of each of the four different Mathieu function modes.

These characteristics take on a more physical meaning when considering the modes present in an elliptic jet. Each of the four different Mathieu functions represent a different motion in the jet. The azimuthal phase distribution for the lowest order mode of each Mathieu function is shown in figure A.2. The ce_{2m} modes produce a

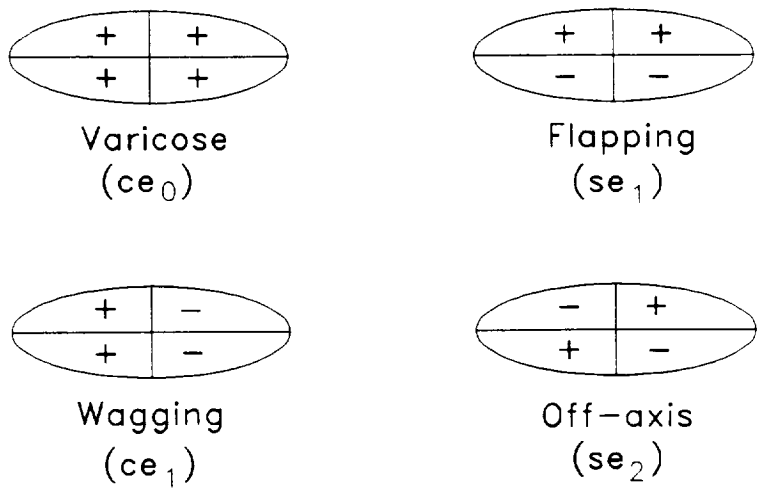

Figure A.2 Azimuthal phase distribution of lowest order Mathieu function modes.

varicose mode in the jet. This is equivalent to an axisymmetric mode in a circular jet. The ce_{2m+1} modes produce a flapping motion in the major axis plane; flapping about the minor axis. The se_{2m} modes produce off-axis instabilities while the se_{2m+1} modes produce a flapping motion in the minor axis plane; flapping about the major axis.

A.2 Fourier Decomposition of Mathieu Function Modes

By multiplying A.1a and A.1b by ce_{2n+p} and se_{2n+p}, respectively, and integrating with respect to the angular variable, ν, around the azimuth, we obtain

$$\int_0^{2\pi} \zeta(v,\ q)\, ce_{(2n+p)}(v,\ q)\, dv =$$

$$C_A(u,\ q) \int_0^{2\pi} \sum_{m=0}^{\infty} \sum_{n=0}^{\infty} A_{(2m+p)}\, ce_{(2m+p)}(v,\ q)\, ce_{(2n+p)}(v,\ q)\, dv \quad p = 1 \text{ or } 2 \qquad \text{A.2a}$$

and

$$\int_0^{2\pi} \zeta(v,\ q)\, se_{(2n+p)}(v,\ q)\, dv =$$

$$C_B(u,\ q) \int_0^{2\pi} \sum_{m=0}^{\infty} \sum_{n=0}^{\infty} A_{(2m+p)}\, se_{(2m+p)}(v,\ q)\, se_{(2n+p)}(v,\ q)\, dv \quad p = 1 \text{ or } 2 \qquad \text{A.2b}$$

Like standard trigonometric functions, Mathieu functions satisfy orthogonality conditions where

$$\int_0^{2\pi} ce_m\, ce_n\, dv = 0 \quad m \neq n$$
$$= \pi \quad m = n$$

and

$$\int_0^{2\pi} se_m\, se_n\, dv = 0 \quad m \neq n$$
$$= \pi \quad m = n$$

by applying the orthogonality integrals to equations A.2, the result is

$$\int_0^{2\pi} \zeta(v,\ q)\, ce_{2m+p}\, dv = C_A\, \pi\, A_{2m+p} \qquad \text{A.3a}$$

$$\int_0^{2\pi} \zeta(\nu,\ q)\, se_{2m+p}\, d\nu = C_B\, \pi\, B_{2m+p} \qquad \text{A.3b}$$

The relative amplitudes of each mode can then be written as

$$A_{2m+p} \sim \int_0^{2\pi} \zeta(\nu,\ q)\, ce_{2m+p}\, d\nu \qquad \text{A.4a}$$

$$B_{2m+p} \sim \int_0^{2\pi} \zeta(\nu,\ q)\, se_{2m+p}\, d\nu \qquad \text{A.4b}$$

Therefore, the since the azimuthal pressure distribution, $\zeta(\nu,\ q)$, can be measured experimentally and ce_{2m+p} and se_{2m+p} are known analytical functions, the right hand sides of equations A.4 are completely deterministic and the relative amplitudes of each azimuthal mode can be calculated.

A.3 Procedure for Modal Decomposition

The procedure to determine the relative amplitude of the azimuthal modes is as follows.

1) Measure the azimuthal pressure distribution around an ellipse of constant u in an ECC system. This is done by fixing one microphone at a given location on the ellipse and traversing a second microphone around the azimuth, measuring the cross-spectra between the two microphone signals at equal angular increments, ν (see figure 6.11). The complex cross-spectra is then used as the measured pressure value for the decomposition procedure. For the ellipse in the

ECC system, the quantities a, u, q, and aspect ratio must be specified and held constant.

Since the modal decomposition measurements are intended to provide useful information specifically for the theory of Morris and Bhat (1993, 1995), close communication with Dr. P. J. Morris was maintained while developing the modal analysis procedure. Using the experimental mean flow from the elliptic jet described in chapter 4, it was decided that the focus, a, of the ellipse over which the modal decomposition measurements should be performed had a value of $a/D_{eq} = 0.818$. This value is fairly constant through the initial portion of the jet where most of the noise is generated. The "radial" distance from the jet was chosen to be $u/D_{eq} = 1.97$. The other parameters (M_j, ρ_∞ and α) needed to evaluate the variable "q" required for equation A.1 are dependant on the jet conditions . The instability wavenumber, α, is calculated assuming a convection velocity of $U_c = 0.65U_j$ and the frequency such that $\alpha = \omega/U_c$.

2) For each mode number, m, multiply the measured pressure value, $\zeta(\nu, q)$ by the corresponding value of Mathieu function as seen in equation A.4. This produces four discrete functions which are dependant on ν (and on the specified value of q).

$$\zeta(\nu)\, ce_{2m}(\nu); \quad \zeta(\nu)\, ce_{2m+1}(\nu); \quad \zeta(\nu)\, se_{2m}(\nu); \quad \zeta(\nu)\, se_{2m+1}(\nu)$$

Recall that $\zeta(\nu)$ is a measured function while each of the Mathieu functions can be calculated analytically for each value of ν.

3) Each of these four functions is then integrated numerically over the interval 0 to 2π in order to find the coefficients A_{2m}, A_{2m+1}, B_{2m}, B_{2m+1} from equation A.4.

4) The integration is repeated for each frequency component and mode number, m, in order to determine the amplitude coefficient spectrum for each Mathieu function mode number.

A.4 Modal Decomposition FORTRAN Code

The following is a listing of the FORTRAN code used to perform the modal decomposition analysis. The actual subroutines that calculate the Mathieu functions were developed by Dr. P.J. Morris. Because of their excessive length, the Mathieu function routines are not listed here.

```
c     PROGRAM: MINTQCKH.FOR
c
c
c     This code performs a Fourier decomposition on the azimuthal cross
c     spectral density using Mathieu functions. The input is the cross-
c     spectrum between the reference mic and the traversing mic at each
c     angular position. The output is four files, each corresponding to
c     the four Mathieu functions. Only the first four modes of each
c     function are calculated.
c
c     The input file INTGRT.IN requires the characteristic frequency on
c     first line. The number of angular positions including v=0 and
c     v=360 as separate points should be on the second line. The names
c     of four output files are then listed. Finally, the input cross-
c     spectra files are listed beginning with v=0 and ending with v=360.
c
c     The code must be linked with MATHU.FOR for the Mathieu function
c     routines.
c
```

```
c
$LARGE
      implicit real*8 (a-b,d-h,o-z)
      implicit complex*16 (c)
      complex*16 func, funcnew, rc, rcoeff
      character*16 fraw,fout1,fout2,fout3,fout4
      parameter (N=11,nmodes=4, fh=620)
      dimension func(fh,18),cz(N,N), cw(N),funcnew(20)
      dimension rc(fh,nmodes),freq(fh),cq(fh)
      open (unit=11,file='intgrt.in',status='old')
      read (11,*) fch
      read (11,*) L
      read (11,*) fout1
      read (11,*) fout2
      read (11,*) fout3
      read (11,*) fout4
      open (unit=41,file=fout1,status='unknown')
      open (unit=42,file=fout2,status='unknown')
      open (unit=43,file=fout3,status='unknown')
      open (unit=44,file=fout4,status='unknown')
      L = L-1
      lhalf = L/2
      pi = dacos(-1.d0)
      pi2 = 2.d0*pi
      dv = pi2/(L)
      v = 0.d0
      rmax = 0.d0
      deq = 0.0138d0
c       ujet = 690.0d0
c       rhoinf = 1.2d0
c       rmjet = 1.58d0
c       uconv = 0.6d0*ujet
      ujet = 425.0d0
      rhoinf = 0.69d0
      rmjet = 1.48d0
      uconv = 0.65d0*ujet
      a = 1.13d0/1.38d0
c
c
c  reads in measured function
c  i corresponds to St # component, j corresponds to angular pos.
c
      j = 0
      DO 5 while (j.le.(L+1))
        read(11,*,END=999) fraw
        write(0,*)'reading next file: '
        write (0,*) fraw
        open (unit=1,file=fraw,status='old')
        j = j+1
        do 2 i = 1,fh
c           read(1,*) freq(i),gxx,gyy,gxy,rcoh,ph,func(i,j),temp1
```

```
          IF (j.eq.5) then
             read (1,*) freq(i), gxx, gyy, temp1, temp2
             func(i,j) = dcmplx(gxx,0d0)
          else
             read (1,*) freq(i),gxy,rcxy,phaxy, rgxy, rigxy
             func(i,j) = dcmplx(rgxy,rigxy)
          endif

          romega = pi2*freq(i)
          st = pi2*freq(i)*deq/ujet
          temp1 = rhoinf*(rmjet*st)**2
          alpha = (romega/uconv)*deq
          qreal = (-a**2/4d0)*(alpha**2 - temp1)
c          write (*,*) 'freq, qreal: ', freq(i),qreal
          cq(i) = qreal
2       CONTINUE
        write (0,*) 'Done reading the data file #: ',j
        close (1)
5     CONTINUE
999    CONTINUE
c
c  computes new function by multiplying measured function
c  by the appropriate Mathieu function --> ce(2n) mode
c
        DO 20 k = 1,nmodes
        write (*,*) 'ce(2n) mode: ',2*(k-1)
        DO 300 if = 1,fh
        v = 0.d0
           IF (MOD(if,100).eq.0) write (*,*) 'if: ',if
           call cofce0 (k,cq(if),cz,cw)
           DO 30 i = 0,L
             call mathce0 (k,v,cz,cval,ctemp)
              funcnew(i+1) = func(if,i+1)*(cval)
              v = v + dv
30           CONTINUE
         call simpson (0.d0,pi2,lhalf,funcnew,rcoeff)
         IF ((cabs(rcoeff/pi)).gt.rmax) rmax = cabs(rcoeff/pi)
         rc(if,k) = rcoeff/pi
300    CONTINUE
20     CONTINUE
      DO  301 if = 1,fh
301    write (41,1) freq(if),freq(if)/fch,
    +                  ((cabs(rc(if,k)/rmax)),k=1,nmodes)
c
c  computes coeffs. for -->  ce(2n + 1)
c
       DO 40 k = 1,nmodes
          write (*,*) 'ce(2n + 1) mode: ',2*k-1
          DO 400 if = 1,fh
          v = 0.d0
             IF (MOD(if,100).eq.0) write (*,*) 'if: ',if
```

```
          call cofce1 (k,cq(if),cz,cw)
          DO 50 i = 0,L
            call mathce1 (k,v,cz,cval,ctemp)
             funcnew(i+1) = func(if,i+1)*Real(cval)
             v = v + dv
50          CONTINUE
        call simpson (0.d0,pi2,lhalf,funcnew,rcoeff)
        rc(if,k) = rcoeff/pi
400    CONTINUE
40     CONTINUE
      DO  401 if = 1,fh
401    write (42,1) freq(if),freq(if)/fch,((rc(if,k)/rmax),k=1,nmodes)
c
c  computes coeffs. for -->  se(2n)
c
      DO 59 if = 1,fh
59     rc (if,1) = 0.0
      DO 60 k = 2,nmodes
        write (*,*) 'se(2n) mode: ',2*(k-1)
        DO 600 if = 1,fh
        v = 0.d0
          IF (MOD(if,100).eq.0) write (*,*) 'if: ',if
          call cofse0 (k,cq(if),cz,cw)
          DO 70 i = 0,L
            call mathse0 (k,v,cz,cval,ctemp)
             funcnew(i+1) = func(if,i+1)*Real(cval)
             v = v + dv
70          CONTINUE
        call simpson (0.d0,pi2,lhalf,funcnew,rcoeff)
        rc(if,k) = rcoeff/pi
600    CONTINUE
60     CONTINUE
      DO  601 if = 1,fh
601    write (43,1) freq(if),freq(if)/fch,((rc(if,k))/rmax,k=1,nmodes)
c
c  computes coeffs. for --> se(2n + 1)
cc

      write (*,*)
      DO 80 k = 1,nmodes
        write (*,*) 'se(2n + 1) mode: ',2*k-1
        DO 800 if = 1,fh
        v = 0.d0
          IF (MOD(if,100).eq.0) write (*,*) 'if: ',if
          call cofse1 (k,cq(if),cz,cw)
          DO 90 i = 0,L
            call mathse1 (k,v,cz,cval,ctemp)
             funcnew(i+1) = func(if,i+1)*(cval)
             v = v + dv
90          CONTINUE
        call simpson (0.d0,pi2,lhalf,funcnew,rcoeff)
```

```
        rc(if,k) = rcoeff/pi
800    CONTINUE
80     CONTINUE
      DO  801 if = 1,fh
801    write (44,1) freq(if),freq(if)/fch,
    +                  (cabs((rc(if,k)/rmax)),k=1,nmodes)
c
c
1      FORMAT(1x,f10.2,2x,f5.3,4(2x,e13.4))
      stop
      end
c
c
c  Simpson's rule integration
c
      subroutine simpson (a,b,n,func,value)
      implicit real*8 (a-h,o-z)
      complex *16 func, value
      parameter (m=150)
      dimension func (m)
c      write (*,*) ' I am in simpson'
      h = (b - a)/((2*n))
      s1 = 0.d0
      s2 = 0.d0 - func(1)
      s0 = func(1) + func(2*n)
      DO 10 i = 1,n
         s1 = s1 + func(2*i)
         s2 = s2 + func(2*i - 1)
10     CONTINUE
c      write (*,*) h,s0,s1,s2
      value = (h/3.d0)*(s0 + 4.d0*s1 + 2.d0*s2)
      return
      end
```

APPENDIX B

SPECTRAL ANALYSIS CODE

The following is a listing of the computer code used to perform the spectral analysis of the time domain data acquired by the A/D board. The fundamental form of this code was developed by Choi (1991) and Bent (1993). Modified versions of their basic routine were used througout the course of this research. The finite Fourier transform (FFT) routine was used directly from Numerical Recipes by Press et al. (1989). The procedures for computing the autospectrum, cross-spectrum, and coherence functions can be found in Bendat and Piersol (1986).

```
C-----------------------------------------------------------------------
C
C s2volt.for : Spectral analysis code with calculation of rms value
C              and overall SPL in dB ****for DAS58 2 channel data ******
C      **********  INPUT FILE MUST BE BINARY FORMAT  ********
C            Two columns of data
C            INPUT:  # of averages for FFT (K)
C                  Acquisition frequency (FREPCH)
C                  A/D board calibration constant to convert counts
C                              to volts  (SENS0)
C                  External gain applied to input signal (GAIN0)
C                  Microphone calibration from volts to Pascals
C                        (MICCAL0)
C                  Chamber pressure used to scale acoustic data (pch)
C
C-----------------------------------------------------------------------
$LARGE
    CHARACTER*30 FNAME,FRAW,FOUTS,FOUTC,FOUTN
C     character*70 header
    PARAMETER    (M=1024,MH=M/2)
    COMPLEX      FX(M),FY(M),FXY(M)
    COMPLEX      GXY
    character c1
    logical  flag
    integer*2  ich0,ich1
    INTEGER      COUNT
    REAL         MEAN0, MEAN1, MNSQ0, MNSQ1,miccal0,miccal1
    DIMENSION    FXX(M),FYY(M)
```

```
      DIMENSION    X(M),Y(M),WINDOW(M)
      DIMENSION    ICH(8),FREQ(M),XX(MH),YY(MH)
C
      HANWIN(J)    =0.5*(1-COS(2.*PI*(J-1)/(M-1)))
      DATA         IR,IW/0,0/
      DATA         PI/3.141592/
      DATA         PREF/20e-6/
      DATA         PATM/760/
C
C.... Control parameters. ......................
c      WRITE(0,'(A50)') ' File name for INPUT & OUTPUT file ?'
c      READ (0,'(A30)') FNAME
c      OPEN(UNIT=5,FILE=FNAME,STATUS='OLD')
      open (unit=5,file='spec2bin.in',status='old')
      READ (5,*) K,FREPCH
      WRITE (0,*) '# WINDOWS = ',K,'ACQ. FREQ. = ',FREPCH
C
C.... Microphone calibration constants. ...............
C
      READ(5,*) SENS0,GAIN0,miccal0,pch
      READ(5,*) SENS1,GAIN1,miccal1,pch
      WRITE (0,*) 'SENS 1 = ',SENS0,' GAIN 1 = ',GAIN0,'PCH',pch
      WRITE (0,*) 'SENS 2 = ',SENS1,' GAIN 2 = ',GAIN1
C
C.... Calculate frequency bin and overall calibration constants.......
C
      pscl = 1
      pref2 = pscl**2
      scalef = 1.0
      conver0 = sens0*gain0*miccal0
      conver1 = sens1*gain1*miccal1
      write (*,*) 'conver0',conver0,' conver1',conver1
C
      FOLD=FREPCH/2.
      DELTAF=FREPCH/REAL(M)
      DELTAT=1./FREPCH
      NTOTAL=(K+1)*MH
C
C.... Calculate window weighting factor..
C
      DO 22 J=1,M
        WINDOW(J)=HANWIN(J)
   22 CONTINUE
C
      SUMW= 0.0
      DO 30 J=1,M
        SUMW=SUMW+WINDOW(J)**2
   30 CONTINUE
      FACT=SUMW/REAL(M)
C
      DEN=K*M*M*FACT
```

```
      write (0,*) den,deltaf
C
C.... Read in raw data.........................................
C
    1 READ (5,'(A20,3A15)',END=999) FRAW,FOUTS,FOUTC,FOUTN
      WRITE(0,'(A20,3A15)') FRAW,FOUTS,FOUTC,FOUTN
      OPEN(UNIT=1,FILE=FRAW,STATUS='OLD',form='binary')
      OPEN(UNIT=2,FILE=FOUTS,STATUS='UNKNOWN')
      OPEN(UNIT=3,FILE=FOUTC,STATUS='UNKNOWN')
      OPEN(UNIT=4,FILE=FOUTN,STATUS='UNKNOWN')
C
      write(4,*) 'Names of the input and output files:'
      write (4,*) ' '
      WRITE(4,'(A20,3A15)') FRAW,FOUTS,FOUTC,FOUTN
      write (4,*) ' '
      WRITE (4,*) '# WINDOWS = ',K,'ACQ. FREQ. = ',FREPCH
      WRITE (4,*) 'SENS 1 = ',SENS0,' GAIN 1 = ',GAIN0,'PCH',pch
      WRITE (4,*) 'SENS 2 = ',SENS1,' GAIN 2 = ',GAIN1
c
      COUNT = 0
      MEAN0 = 0.
      MEAN1 = 0.
      MNSQ0 = 0.
      MNSQ1 = 0.
      FXXMAX = 0.
      FYYMAX = 0.
      FXYMAX = 0.
      rsqcop = 0.
      rsqnois = 0.
C
C Read in the data file header info and discard it before using the
C     data.  Header contains text information
C

      flag = .true.
      do 5 while (flag)
        read (1) c1
        IF (ichar(c1).eq.116) CALL strtdata (flag)
 5    continue
C
C Determine Mean value to subtract out before FFT
C
      DO 10 i = 1,NTOTAL
          READ (1) ICH0,ICH1
          IT=IT+1
          XX(J)=ich0/conver0
          YY(J)=ich1/conver1
          COUNT = COUNT + 1
          MEAN0 = XX(J) + MEAN0
          MEAN1 = YY(J) + MEAN1
10    CONTINUE
```

```
        MEAN0 = MEAN0/COUNT
        MEAN1 = MEAN1/COUNT
C
    WRITE (0,*) 'MEAN OF THE SIGNAL 1 (volts) = ',MEAN0*miccal0
    WRITE (0,*) 'MEAN OF THE SIGNAL 2 (volts) = ',MEAN1*miccal1
    REWIND(1)
c
c Again, read in the data file header info and discard it before using
c       the data.
c
    flag = .true.
    do 51 while (flag)
      read (1) c1
      IF (ichar(c1).eq.116) CALL strtdata (flag)
 51 continue
C
    DO 40 J=1,M
      FXY(J)=(0.0,0.0)
      FXX(J)=(0.0,0.0)
      FYY(J)=(0.0,0.0)
 40 CONTINUE
C
C  Read in two channels of raw data and place in XX and YY variables.
C       Each FFT overlaps by half of the block size.
C
    IT=0
    DO 50 J=1,MH
      READ (1) ICH0,ICH1
      IT=IT+1
      XX(J)=ich0/conver0 - MEAN0
      YY(J)=ich1/conver1 - MEAN1
 50 CONTINUE
C
    DO 100 IK=1,K
      DO 70 J=1,MH
        X(J)=XX(J)
        Y(J)=YY(J)
 70   CONTINUE
C

      DO 75 J=1,MH
        READ (1) ICH0,ICH1
        IT=IT+1
        XX(J)=ich0/conver0 - MEAN0
        YY(J)=ich1/conver1 - MEAN1
 75     CONTINUE
C
      DO 80 J=1,MH
        X(J+MH)=XX(J)
        Y(J+MH)=YY(J)
 80   CONTINUE
```

```
C
C  ..... Apply the window to the data..
C
      DO 90 J=1,M
        X(J)=X(J)*WINDOW(J)
        Y(J)=Y(J)*WINDOW(J)
C      WRITE (0,*) 'X(J)=',X(J),'Y(J)=',Y(J)
  90   CONTINUE
C
      WRITE(0,*) IK,IT
C
C Call TWOFFT routine from Numerical Recipes
C
      CALL TWOFFT(X,Y,FX,FY,M)
C
C Compute power spectrum and cross-spectrum by multiplying by
C   complex conjugates
C
      DO 95 J=1,M
        FXY(J)=FXY(J)+CONJG(FX(J))*FY(J)
        FXX(J)=FXX(J)+CONJG(FX(J))*FX(J)
        FYY(J)=FYY(J)+CONJG(FY(J))*FY(J)
95     CONTINUE
C
C
 100 CONTINUE
C
    DO 120 J=1,MH
C
C Correct power spectrum to proper levels to account for two-sided
C   spectrum, Hanning window, and bin width (adjust to per unit Hz)
C
      GXY=2.0*FXY(J)/DEN/DELTAF
      GXX=2.0*FXX(J)/DEN/DELTAF
      GYY=2.0*FYY(J)/DEN/DELTAF
C
C  caclulates coherence and coherent output spectra
C
     CXY=CABS(FXY(J))/SQRT(ABS(FXX(J)*FYY(J)))
     gyycop = gyy*cxy*cxy
     gyynois = gyy*(1 - cxy*cxy)
C
C  calculates phase angle
C
      PHAXY=ATAN2(AIMAG(GXY),REAL(GXY))*360./2./PI
C
C integrates the power spectrum to obtain r.m.s. values
C
      F=(J-1)*DELTAF
      MNSQ0 = DELTAF*CABS(GXX) + MNSQ0
      MNSQ1 = DELTAF*CABS(GYY) + MNSQ1
```

```
      rsqcop = deltaf*cabs(gyy)*(cxy*cxy) + rsqcop
      rsqnois = deltaf*cabs(gyy)*(1. - cxy*cxy) + rsqnois
c
      WRITE(2,310) F,cabs(GXX/pref2/scalef),cabs(GYY/pref2/scalef),
     + gyycop, gyynois
      WRITE(3,360) F,cabs(GXY/pref2/scalef),cabs(CXY),PHAXY,
     +        Real(GXY/pref2/scalef),AIMAG(GXY/pref2/scalef)
120   CONTINUE
      write (*,*) 'Mean0, Mean1', mean0*miccal0, mean1*miccal1
      RMS0 = (MNSQ0)**0.5*miccal0
      RMS1 = (MNSQ1)**0.5*miccal1
      db0 = 20*alog10(rms0/miccal0/pscl)
      db1 = 20*alog10(rms1/miccal1/pscl)
      WRITE (*,*) 'Number of Data Points:', count

      write (*,*) 'RMS0, RMS1',rms0, rms1
      write (*,*) 'rms from cop of hot-wire: ',rsqcop**0.5
      write (*,*) 'rms from hot-wire noise: ', rsqnois**0.5
      write (*,*) 'dB0, dB1',db0,db1
      WRITE (4,*) 'Number of Data Points:', count
      write (4,*) ' '
      write (4,*) 'Mean0, Mean1', mean0*miccal0, mean1*miccal1
      write (4,*) ' '
      write (4,*) 'RMS0, RMS1',rms0, rms1
      write (4,*) ' '
      write (4,*) 'rms from cop of hot-wire: ',rsqcop**0.5
      write (4,*) 'rms from hot-wire noise: ', rsqnois**0.5
      write (4,*) ' '
      write (4,*) 'dB0, dB1',db0,db1

      CLOSE(UNIT=1)
      CLOSE(UNIT=2)
      CLOSE(UNIT=3)
      CLOSE(UNIT=4)
      GOTO 1
C
 310 FORMAT(1X,f10.2,4x,e15.5,4x,e15.5,4x,e15.5,4x,e15.5)
 360 FORMAT(1X,f10.2,3X,e15.5,3X,e15.5,3X,e15.5,3x,e15.5,3x,e15.5)
C
 999 STOP
     END


C
C  This subroutine reads through the binary file header until the
C    string  't Data' is found.  This will indicate that the binary
C    data is about to start.
C
      SUBROUTINE STRTDATA (flag)
       character c1
       logical flag
```

```
read (1) c1
IF (ichar(c1).ne.32) RETURN
 read (1) c1
IF (ichar(c1).ne.68) RETURN
 read (1) c1
IF (ichar(c1).ne.97) RETURN
 read (1) c1
IF (ichar(c1).ne.116) RETURN
 read (1) c1
IF (ichar(c1).ne.97) RETURN
      read (1) c1
      read (1) c1
      flag = .false.
return
end
```

APPENDIX C

VORTEX MODEL CODE

```
C       VORTEX12.FOR
C  This code computes the velocity field from three vortices as they convect
C     in the x-direction while oscillating in the y-direction.
C   Variables:
C        dx:  spatial increment
C        dt:  time increment (dx/dt is vortex speed)
C        ay:  amplitude of sinsoidal y-oscillation
C        amp: vortex strength scaling factor
C        f:   frequency of sinsoidal y-osciallation
C
      common /one/ x01, y01, amp,ay,f,e, x02,y02,x03,y03
      dimension y(40),u1(40),yloc(40)
      open (11, file='vortexu.out',status='unknown')
      open (12, file='topfft.out',status='unknown')
      open (13, file='midfft.out',status='unknown')
      open (14, file='botfft.out',status='unknown')
c
c  These variables establish the spacing and initial location of the
c     vortices
c
      y01 = 10.
      x01 = 0.
      y02 = 10.
      x02 = 10.
      y03 = 10.
      x03 = 20
      pi = acos(-1.0)
      phi = 2.
      y0 = 10.
      x0 = 5.
      t = 0.
      xinc = 0.
      e = 2.718281828
      dx = .2
      dt = 0.05
      amp = 1.0
      ay = .3
      f = 0.416
C
C  This loop increments the spatial and temporal variables to creating
C     the vortex motion.  It computes the velocity time trace at three
C     separate values of y-location at one time.
C
      do 10 k = 1,1050
         t = t + dt
         xinc = xinc + dx
         x = 25.
```

```
        i = 1
        y(i) = 26
          call velocity (x,y(i),t,xinc,u1(i),v1,vtot1y,yloc(i))
        i = 3
        y(i) = 29
         call velocity (x,y(i),t,xinc,u1(i),v1,vtot1y,yloc(i))
        i = 2
        y(i) = 28
         call velocity (x,y(i),t,xinc,u1(i),v1,vtot1y,yloc(i))
30      continue

       write (11,120) t,yloc(2),((u1(j) + float(j/2.0)), j=1,3)
       write (12,*) yloc(2),u1(3)
       write (13,*) yloc(2),u1(2)
       write (14,*) yloc(2),u1(1)
 10   continue
100   FORMAT (1x,e15.4,2x,e15.4,2x,e15.4,2x,e15.4,2x,e15.4,2x,
    + e15.4,2x,e15.4,2x,e15.4,2x,e15.4,2x,e15.4)
120  format (1x,e15.4,2x,e15.4,9e15.4)
     stop
     end

C
C   This subroutine contains the equations for vortex motion.
C
     subroutine velocity (x,y,t,xinc,u,v,vtot,yloc)
     common /one/ x01, y01, amp,ay,f,e, x02,y02,x03,y03
       pi = acos(-1.0)
       pi2 = 2*pi
       r1 = sqrt((x- x01 - xinc)**2 + (y- y01 - ay*sin(t*f*pi2))**2)
       r2 = sqrt((x- x02 - xinc)**2 + (y- y02 - ay*sin(t*f*pi2))**2)
       r3 = sqrt((x- x03 - xinc)**2 + (y- y03- ay*sin(t*f*pi2))**2)
       ucomp = -amp*(y-y01- ay*sin(t*f*pi2))/e**r1
    +      -amp*(y-y02- ay*sin(t*f*pi2))/e**r2
    +      -amp*(y-y03- ay*sin(t*f*pi2))/e**r3
       vcomp = amp*(x - x01 -xinc)/e**r1
    +      + amp*(x - x02 -xinc)/e**r2 + amp*(x - x03 -xinc)/e**r3
       vtot = sqrt(ucomp**2 + vcomp**2)
       u = ucomp
       v = vcomp
       yloc = y - y01 - ay*sin(t*f*pi2)
c       If (yloc.lt.0) u = 1.3*ucomp
     return
     end
```

The Pennsylvania State University

The Graduate School

Departement of Aerospace Engineering

DIFFRACTION BY A HALF-PLANE USING THE DISPERSION RELATION PRESERVING SCHEME

A Thesis in

Aerospace Engineering

by Lucie Pautet

Submitted in Partial Fulfillment
of the Requirements
for the Degree of

Master of Science

August 1994

ABSTRACT

The diffraction by a half-plane is studied using a finite difference scheme, the Dispersion Relation Preserving scheme (DRP). The major problem encountered in the implementation of the scheme is the treatment of the boundary facing the half-plane and generating the incident wave. This boundary needs to be non-reflecting to let the reflected wave exit the computational domain while generating the incident wave. A decomposition of the wave into its incident and reflecting components close to the boundary is used to solve the problem. Over the rest of the computational domain and, in particular, around the half-plane, one solves for the total wave. It is to be noted that all boundary conditions considered (solid wall, non-reflecting boundary, forced boundary) are standard.

First the incident wave is considered to be a plane wave. The diffraction by a half-plane of a plane wave can be solved analytically. The agrement between the analytical solution and the DRP numerical solution is very good. The incident wave is then changed to simulate the radiation of noise produced by a jet. The diffraction by a half-plane of such a wave provides a simple model to study the noise reduction due to the diffraction effects due to the presence of a shroud around the jet. It appears that the end of the shroud should be placed at a location corresponding to the maximum of the noise radiation.

CONTENTS

LIST OF FIGURES vi

ACKNOWLEDGEMENTS vii

1 INTRODUCTION 1
- 1.1 Diffraction Problems 1
- 1.2 Theoretical Work 4
- 1.3 Previous Computational Work 6

2 NUMERICAL MODEL 8
- 2.1 Governing equations 8
- 2.2 The DRP Scheme 9
  - 2.2.1 Origin 9
  - 2.2.2 Discretization 12
  - 2.2.3 Resolution, Stability and Isotropy 13
- 2.3 Boundary Conditions 19
  - 2.3.1 Radiation Boundary 20
  - 2.3.2 Imposed Boundary 22

3 MODEL PROBLEMS 26
- 3.1 Propagation of an Oblique Wave 26
  - 3.1.1 Resolution 28
  - 3.1.2 Radiation Condition 29
- 3.2 Reflection on a Wall 32
- 3.3 Diffraction by a half-plane 42
- 3.4 Jet Noise Problem 51

4 CONCLUSION AND RECOMMENDATIONS 61
- 4.1 Conclusion 61
- 4.2 Recommendations 63

BIBLIOGRAPHY 65

Appendix. THE WIENER-HOPF TECHNIQUE 68

LIST OF FIGURES

1.1 Sketch of the diffraction problem 2

2.1 Discretized wavenumber versus real wave number 14
2.2 Polar plots of the ratio discretized velocity over exact velocity 17
2.3 Type of boundary for the diffraction problem 19
2.4 Radiation Stencil 21
2.5 Wall 24
2.6 Wall stencil 24

3.1 Oblique wave propagation problem 27
3.2 Propagation of a sinusoidal wave 29
3.3 Radiation with origin in the middle of the domain 31
3.4 propagation of a gaussian pulse 33
3.5 Reflection problem 34
3.6 Computational domains for the reflection problem 36
3.7 Wave propagation through the three domains 38
3.8 Propagation and reflection of a plane wave 41
3.9 Comparison between the exact and the numerical solutions for the reflection problem 42
3.10 Computational domains for the diffraction problem 44
3.11 Damping function 46
3.12 Diffraction of a plane wave 47
3.13 Comparison planes for the diffraction case 49
3.14 Comparaison between the Wiener-Hopf technique and the DRP numerical solution in the $S1$ plane 50
3.15 Comparaison between the Wiener-Hopf technique and the DRP numerical solution in the $S2$ plane 50
3.16 Example of incident wave for the jet noise problem 53
3.17 Propagation of the incident wave without the half-plane: $M_j = 2$, $St = 1$, cold jet 55
3.18 Propagation of the incident wave with the half-plane: $M_j = 2$, $St = 1$, cold jet 56
3.19 Observation planes for the jet noise problem 57
3.20 Diffracted waves in the half-plane plane $S1$ 58
3.21 Diffracted waves in the far-field (plane $S2$) 59

1.1 Diffraction problem 69

Chapter 1

INTRODUCTION

1.1 Diffraction Problems

According to ray theory, a large object obstructing direct rays radiating from a source should create an energy-free zone. Experimentally, it has been observed that this shadow zone does not exist. It contains some low amplitude waves. The incident wave is said to be diffracted or scattered by the object. Diffraction can exist in any kind of wave propagation problems. In optics, the light through a grating is controlled by diffraction. In electromagnetism, diffraction by antennas is a major concern. In acoustics, the quality of a highway noise barrier depends on the diffracted noise. In seismology, discontinuities are localized by their diffraction effects. An offshore station is designed to resist the additional effect of the diffracted water waves.

Unfortunately diffraction is as complicated as it is widespread. Analytical solutions are still restricted to simple problems. The classical case considered in the present thesis is that of a plane wave diffracted by a infinitely thin rigid half-plane. This problem is sketched in figure 1.1. The domains of existence of the incident wave and the reflected wave are given by the geometric theory. The shadow region (III)

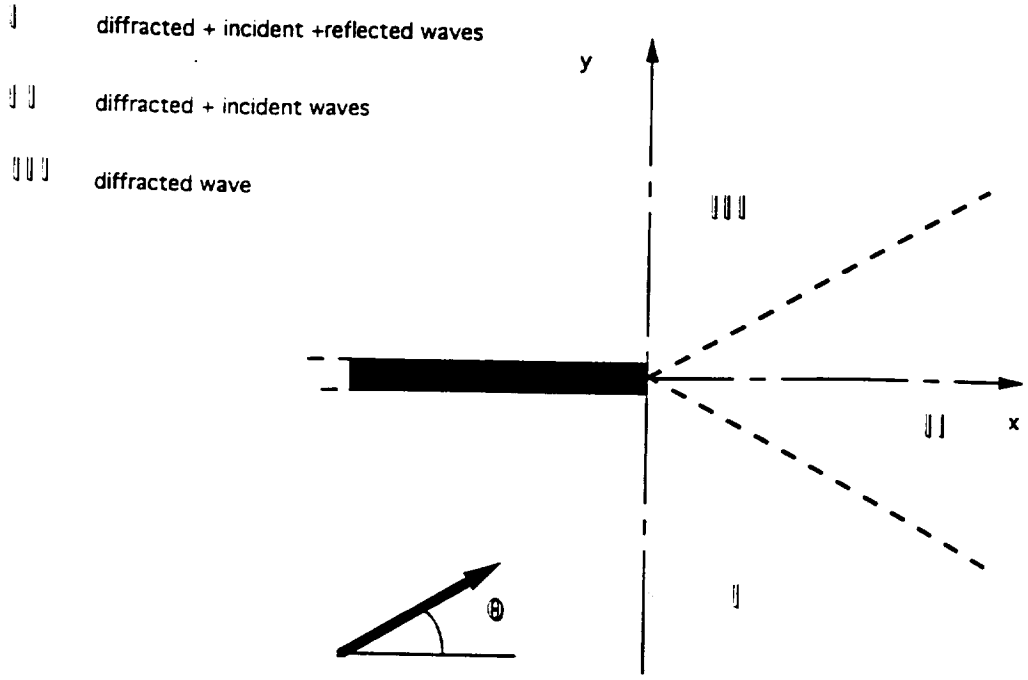

Figure 1.1: Sketch of the diffraction problem

contains only the diffracted wave.

In spite of its simplicity, this problem has been used to simulate:

- ◇ the propagation of electromagnetic waves over the boundary between land and sea [5]
- ◇ the acoustic diffraction from an open lead in the arctic ice canopy [9]
- ◇ the acoustic diffraction from highway noise barriers [16]
- ◇ the scattering of aerodynamic noise [8, 1]

An important jet noise application that involves diffraction effects concerns the radiation of noise from a supersonic jet shrouded by an ejector or shroud. Even if the dominant sources are located upstream of the shroud exit, some noise radiation may

still occur in the far-field. The diffraction of this noise by the shroud can be studied by using an incident wave that models that models that generated by the instability waves of the jet. The incident wave may no longer take a simple form. Analytical methods may have to be discarded and replaced by numerical methods.

The technique chosen in the present approach is based on a finite difference scheme. The major problem with this approach is that the boundary facing the plate which is generating the wave has to be non-reflecting to let the reflected wave exit the computational domain. One easy way to remove this difficulty is to stop the solution before the reflected wave reaches the boundary [12]. But since the steady, periodic solution is usually the one of interest, it is not practical to use such a time constraint. A more sophisticated technique is to solve the problem only in terms of the scattered field [17]. The boundary condition on the half-plane has then to be modified to take into account the fact that only the scattered field is calculated. Thus, it has to be modified each time the incident wave is changed. So, a solution for the total field provides a considerable advantage. Atkins and Casper [2] recently used a finite wave model to define their non-reflecting boundary condition. By doing so, they were able to distinguish between outgoing and incoming waves. Imposing an incoming wave while letting an outgoing wave radiate through the boundary is then possible. The main difficulty with this technique is the choice of the wave structure which defines the finite wave model. The accuracy of the model requires some knowledge of the identity and orientation of all the waves. Thus, this finite wave model is difficult to

implement in general. Considering the fact that the boundary conditions for either an incoming wave or, an outgoing wave are much easier to define, a new approach is used here. The total wave is decomposed into the incident wave and the outgoing wave on a band close to the boundary of interest. Then, three problems are solved simultaneously. The first involves an incident wave in a free domain. The second represents an outgoing wave. The third involves the total wave impinging on the half-plane.

In the following, the classical problem of diffraction of a plane wave by a half-plane is solved both analytically and computationally using a finite difference scheme. Comparisons are made between the two solutions. Then, an incoming wave, that simulates the pressure field generated by an instability wave in a supersonic jet is introduced. The results of these calculations are then used to assess the effectiveness of a shroud or ejector for shielding noise generated by a supersonic jet.

1.2 Theoretical Work

The first theory of diffraction, the Fresnel-Kirchhoff theory, dates back to the last century. It is based on Huygen's principle. Each point of the scattering surface is considered as a point source. In the case of the half-plane, the tip of the plane becomes the point source. This theory has been widely used in optics. Unfortunately its applications to acoustics are limited. Pierce ([23], 217) noted that this theory can be used only when the characteristic dimensions of the problem are large with respect

to the wavelength, and the angles considered are close to the incident angle.

New theories appeared at the beginning of this century. Each one was developed for a certain kind of problem. The Wiener-Hopf technique used here is the technique which is recommended for half-plane diffraction [22, 7]. For a rigid plane, other techniques could have been used (Sommerfeld's [21], Mc Donald's [11]). But the Wiener-Hopf is most interesting because it provides a methodology to study other types of half-planes and media. Crighton and Leppington [8] in their study of aeroacoustic scattering considered a locally reacting plane. Rawlins [24] and later Dahl and Frisk [10] used a half-plane with one side rigid, the other soft. Ashgar [1] considered the case of a finite plate in the presence of a moving fluid.

The details of the analytical solution for the rigid half-plane can be found in the appendix. Here, only a brief insight into the Wiener-Hopf technique is given. This method has been developed to solve partial differential equations using a decomposition of a function, regular and non-zero on a strip of the complex plane into two functions that are regular and non-zero on the complementary half-spaces defined by the strip. The function defined on the positive half-plane is called the $\oplus$ function, the one defined on the negative half-plane is called the $\ominus$ function. The decomposition can come either from a multiplication or a sum.

This decomposition represents the major difficulty with this technique. In particular, the process requires the sum decomposition of the Fourier transform of the derivative with respect to the distance normal to the wall of the incident wave at the

wall. In complicated cases this may not be possible analytically and may have to be performed by numerical integration of a singular function. Therefore, the use of direct computational methods is more appropriate in the general case.

1.3 Previous Computational Work

Boundary Element Methods (BEM), Finite Element Methods (FEM) or Finite Difference Methods (FDM) can be used to study diffraction effects. Boundary element and other integral methods have become very popular in the last few years [14, 18]. The major advantage they offer is that only the boundary needs to be discretized. On the other hand they require the integration of a singular Green's function and its derivative. Though this can be accomplished in most cases, the number of elements on the boundary has to be large in order to perform these integrations. Thus, these problems can overshadow the advantages of only the boundary being discretized. Furthermore BEM are recommended when only a few receiver points are considered. To map a domain, it is better to switch to FEM or FDM.

The interest in finite elements for diffraction problems comes from their ability to handle complicated geometries [13, 17]. The only difference between a simple geometry and a complicated one is the discretization. The FEM computer code itself stays the same. Finite elements have also proven popular when the wave propagation is non-linear [15, 6]. The major disadvantage in this method is that the computer memory requirements are very large. Since the scattering object here is a simple

half-plane and the wave propagates in a linear way, a finite difference scheme is a good alternative.

When considering finite difference schemes, attention has to be paid to the dissipation and dispersion errors induced by the scheme. Tam and Webb [27] developed a new scheme which minimizes these errors; the Dispersion Relation Preserving scheme (DRP). Their goal was to create a scheme for acoustics applications where accuracy in time as well as in space is mandatory. Tam and Dong [25] successfully applied this scheme to the problem of a point source being diffracted by a finite plate.

In the next chapter, we consider the numerical techniques to be used. This is followed by some sample problems including the half-plane diffraction case and the supersonic jet/ejector model. Finally, some conclusions and suggestions for future work are made.

Chapter 2

NUMERICAL MODEL

In this chapter a complete description of the numerical model that was implemented to generate the computer code is provided. The first section provides the governing equations that were used in the model. In the second section, the discretization for the Dispersion Relation Preserving (DRP) scheme is discussed. Some properties of the scheme, its resolution, stability, and anisotropy, are also examined. Finally, in the last section, the boudary conditions for a non-reflecting boundary and for an imposed boundary are reviewed. The details of the boundary treatment needed when an imposed wave and a reflected or radiating wave occur at the same boundary are given in the next chapter.

2.1 Governing equations

The linearized Euler equations in a flow at rest reduce to the wave equation. The linearized Euler equations, in the absence of sources, may be written as follows:

$$\frac{\partial U}{\partial t} + \frac{\partial E}{\partial x} + \frac{\partial F}{\partial y} = 0 \tag{2.1}$$

$$U = \begin{bmatrix} u \\ v \\ p \end{bmatrix} \quad E = c_0 \begin{bmatrix} -p \\ 0 \\ -u \end{bmatrix} \quad F = c_0 \begin{bmatrix} 0 \\ -p \\ -v \end{bmatrix}$$

where c_0 is the speed of sound

p is the pressure

u is the velocity in the x-direction

v is the velocity in the y-direction

2.2 The DRP Scheme

2.2.1 Origin

Waves can be classsified into three groups: acoustic waves, entropy waves and vorticity waves. An acoustic wave is known to be isotropic, non-dispersive, non-dissipative and travels at the speed of sound. An entropy wave as well as a vorticity wave is directional, non-dispersive, non-dissipative and is convected by the mean flow. When solving a problem numerically, one needs to preserve these properties. Unfortunately, most numerical schemes are anisotropic, dispersive and dissipative. Therefore errors induced by the scheme should be expected when evaluating the solution.

Tam and Webb [27] noted that the dispersiveness, damping rate, isotropy or anisotropy, group and phase velocities are all determined by the dispersion relation.

Preserving this relation would mean preserving all these properties. The coefficients of the expansion of a finite difference scheme are usually determined from a truncated Taylor series. Thus, the Fourier-Laplace transform of the discretized equations has no reason to be a good approximation of the transform of the partial differential equations. In other words, this kind of scheme may not in general preserve the dispersion relation. In order to preserve this relation, Tam and Webb [27] chose to calculate the coefficients of their scheme by minimizing the square of the difference between the discretized and real wavenumber and frequency. The resulting scheme is called the Dispersion Relation Preserving scheme (DRP). It ensures accuracy both in time and in space.

The spatial optimization is performed using a centered seven points stencil. The accuracy for the first derivative $\partial f/\partial x$ is of order $(\Delta x)^4$ for a uniform grid with a grid spacing Δx. The process to determine the spatial coefficients is given here. The discretized form of $\partial f/\partial x$ is written as:

$$\frac{\partial f}{\partial x}(x) \simeq \frac{1}{\Delta x} \sum_{j=-3}^{3} a_j f(x + j\Delta x) \tag{2.2}$$

A Fourier transform is then performed on both sides of the equation. By comparing the two Fourier transforms, the wave number of the Fourier transform of the scheme can be defined. The relationship between the physical wavenumber α and the

discretized wavenumber $\overline{\alpha}$ is given by:

$$\overline{\alpha} = -\frac{i}{\Delta x} \sum_{j=-3}^{3} a_j e^{i\alpha j \Delta x} \tag{2.3}$$

So $\overline{\alpha}\Delta x$ is a periodic function of $\alpha\Delta x$ with period 2π. The waves of interest are selected to have a wave length longer than 4 Δx, or in terms of wavenumber, $|\alpha\Delta x| < \pi/2$. The coefficients a_j are chosen to minimize the error function:

$$E = \int_{-\pi/2}^{\pi/2} |\alpha\Delta x - \overline{\alpha}\Delta x|^2 d(\alpha\Delta x) \tag{2.4}$$

To limit the number of operations, the traditional truncated Taylor series approximation can be combined with this approach. All but one coefficient is then calculated using the Taylor approximation, the last coefficent is determined using the optimization process. It should be noted that the optimization scheme cannot reproduce the dispersion relation for waves with wavelength less than 4 Δx or 5 points per wavelength.

The time optimization scheme is a four-level scheme. The accuracy for the first derivative $\partial f/\partial t$ is of order $(\Delta t)^2$ for a constant time step Δt. The coefficients are determined in a similar manner as for the spatial case.

2.2.2 Discretization

If the x-y plane is represented by a uniform grid with a grid spacing Δx in the x-direction and Δy in the y-direction, the discretized form of the wave equation 2.1 is given by:

$$K_{i,j}^{(n)} = -\frac{1}{\Delta x}\sum_{k=-3}^{3} a_k\ E_{i+k,j}^{(n)} - \frac{1}{\Delta y}\sum_{k=-3}^{3} a_k\ F_{i,j+k}^{(n)} \tag{2.5}$$

$$U_{i,j}^{(n+1)} = U_{i,j}^{(n)} + \Delta t \sum_{k=0}^{3} b_k\ K_{i,j}^{(n-k)} \tag{2.6}$$

where $X_{i,j}^{(n)}$ represents the vector X at the node (i,j) after n time steps.

a_k and b_k are the optimized coefficients:

$a_0 = 0$	$b_0 = 2.30255809$
$a_1 = -a_{-1} = 0.770882380518$	$b_1 = -2.49100760$
$a_2 = -a_{-2} = -0.166705904415$	$b_2 = 1.57434093$
$a_3 = -a_{-3} = 0.026843142770$	$b_3 = -0.38589142$

Under certain conditions on the grid spacing Δx, Δy, and the time step Δt, the solution given by this scheme will be accurate both in time and in space. These conditions are determined by the resolution, stability and isotropy properties of the scheme.

2.2.3 Resolution, Stability and Isotropy

The resolution of the scheme is determined by the relationship between the discretized wavenumber $\overline{\alpha}$ and the real wavenumber α:

$$\overline{\alpha} = \frac{-i}{\Delta x} \sum_{k=-N}^{M} a_j e^{ik\alpha\Delta x}$$

where M, N and a_j depends on the scheme used

In figure 2.1, the straight line represents the ideal case where $\overline{\alpha} = \alpha$. In reality this equality is satisfied only for a certain range depending on the scheme. The curve for the DRP scheme departs from the straight line at about $\alpha\Delta x = 1.45$. In other words the wavelength of the disturbances λ must be such that:

$$\lambda \geq \sup\{\, 4.5\Delta x,\ 4.5\Delta y \,\} \tag{2.7}$$

For the sixth order difference scheme which uses the same stencil as the DRP, the wavelength must be longer than 6.5 mesh spacings. For the fourth order scheme, it must be longer than 8. The DRP scheme clearly represents a net gain compared to the standard difference schemes with no additional costs. It is noted that the compact difference scheme developed by Lele [19] requires the wavelength to be only longer than 2.5 mesh spacings. But the CPU time required is much larger. Furthermore it is associated with a Runge-Kutta integration in time, in which case the discretized

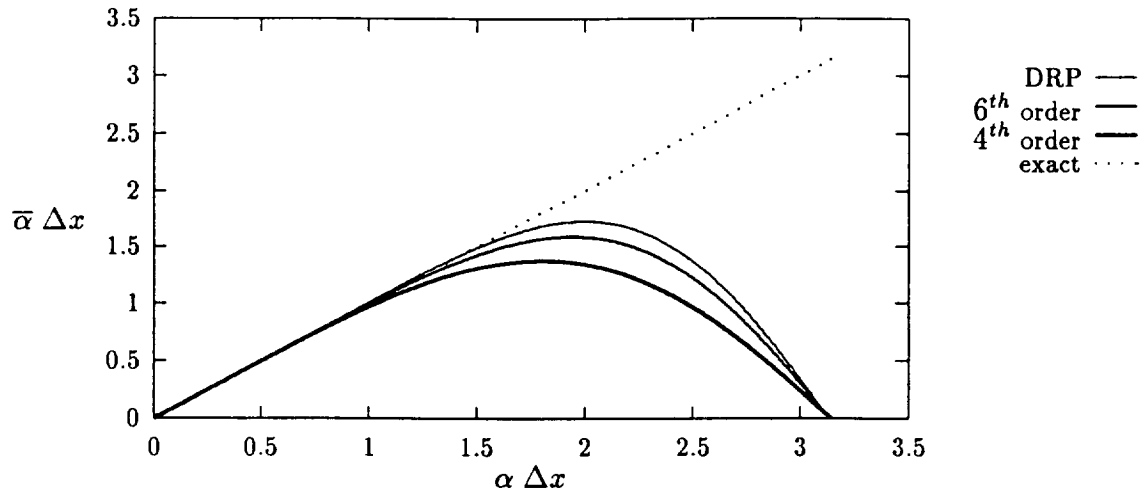

Figure 2.1: Discretized wavenumber versus real wave number

frequency does not match the physical frequency as well as it does with the DRP scheme.

Similarly, the condition on Δt is obtained by considering the relationship between the real radian frequency ω and the discretized ferquency $\overline{\omega}$. This relationship is given by:

$$\overline{\omega} = \frac{i\left(e^{-i\omega\Delta t} - 1\right)}{\Delta t \sum_{k=0}^{3} b_k e^{ij\omega\Delta t}} \tag{2.8}$$

Unfortunately this relation is not one to one, but for each ω four complex $\overline{\omega}$ can be defined. These roots must have a negative imaginary part so that their corresponding wave solutions will be damped. Otherwise numerical instability will occur. This

condition is met for $\omega\Delta t < 0.4$. So the time step Δt must satisfy:

$$\Delta t \leq \frac{0.4}{1.75\left[1+\left(\frac{\Delta x}{\Delta y}\right)^2\right]^{1/2}} \frac{\Delta x}{c_0} \tag{2.9}$$

The isotropy of the scheme may be analyzed using the technique described by Zingg and Lomax [31]. This study is based on the fact that the discretized phase speed is different from the real one. The propagation of a plane wave represented by the scalar $u(x, y, t)$ at the speed c with an angle of incidence θ is governed by the following equation:

$$\frac{\partial u}{\partial t} + c\cos\theta\frac{\partial u}{\partial x} + c\sin\theta\frac{\partial u}{\partial y} = 0 \tag{2.10}$$

This equation may be discretized on a uniform square grid such that the grid spacings are equal ($\Delta x = \Delta y = L$). Denoting the value of u at the node (i, j) by $u_{i,j}$, the discretized derivative $\partial u/\partial x$ is given by:

$$\frac{\partial u_{i,j}}{\partial x} = \frac{1}{L}\sum_{l=1}^{3} a_j(u_{i+l,j} - u_{i-l,j}) \tag{2.11}$$

Introducing the new variable $\xi = x\cos\theta + y\sin\theta$ and, k the wavenumber, the solution may be decomposed as follows:

$$u_{i,j} = \overline{u}(t)e^{ik\xi_{i,j}} \tag{2.12}$$

The wave equation is rewritten in terms of $\overline{u}$. It becomes:

$$\frac{d\overline{u}}{dt} = -\frac{ick\overline{u}\cos\theta}{L}\sum_{l=1}^{3} a_l \left(e^{iklL\cos\theta} - e^{-iklL\cos\theta}\right) \tag{2.13}$$

$$-\frac{ick\overline{u}\sin\theta}{L}\sum_{l=1}^{3} a_l \left(e^{iklL\sin\theta} - e^{-iklL\sin\theta}\right)$$

Since the exact solution is given by $u(x,y,t) = e^{ik(\xi-ct)}$, $d\overline{u}/dt$ should be equal to $-ick\overline{u}$. The discretized phase speed $\overline{c}$ is then defined such that $d\overline{u}/dt = -i\overline{c}k\overline{u}$. The ratio between the discretized phase speed and the physical phase speed on a uniform square grid is then given by:

$$\frac{\overline{c}_{squ}}{c} = \frac{2}{kL}\left(\cos\theta\sum_{l=1}^{3} a_l \sin(klL\cos\theta) + \sin\theta\sum_{l=1}^{3} a_l \sin(klL\sin\theta)\right) \tag{2.14}$$

This ratio depends on the number of points per wavelength and on the angle of incidence. Figure 2.2 shows that the DRP scheme is almost isotropic for as few as 4 points per wavelength. This is a little better than the standard 6th order difference scheme which needs at least 5 points per wavelength. It is interesting to see that under these low limits, the discretized phase speeds are highly anisotropic. If the incident wave contains low frequencies, anisotropy will occur. Zingg and Lomax [31] therefore recommended the use of regular triangular meshes rather than square meshes.

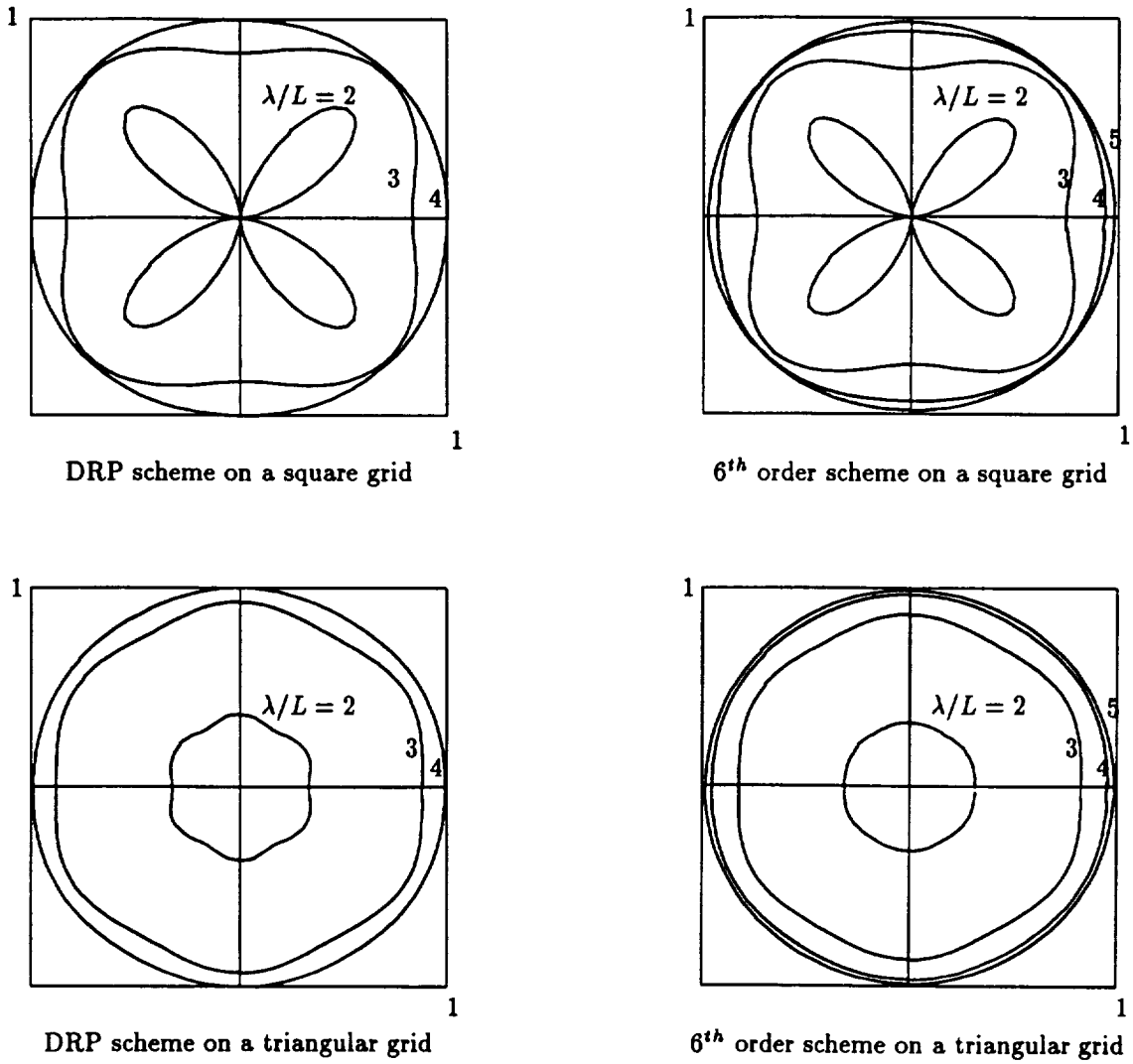

Figure 2.2: Polar plots of the ratio discretized velocity over exact velocity

On a grid constituted of regular triangles with a sides of length L, the ratio is given by:

$$\frac{\overline{c}_{tri}}{c} = \frac{4}{3kL}\cos\theta\sum_{l=1}^{3} a_l \left[\cos\left(\frac{\sqrt{3}klL\sin\theta}{2}\right)\sin\left(\frac{klL\cos\theta}{2}\right) + \sin(klL\cos\theta)\right] \quad (2.15)$$

$$+\frac{4}{\sqrt{3}kL}\sin\theta\sum_{l=1}^{3} a_l \cos\left(\frac{klL\cos\theta}{2}\right)\sin\left(\frac{\sqrt{3}klL\sin\theta}{2}\right)$$

This expression is plotted for both the DRP scheme and the 6th order finite difference scheme (figure 2.2). As expected, the DRP does a little better than the other scheme. In both cases, the plots are fairly isotropic for as few as 2 points per wavelength. It is to be noted that this isotropy is obtained by losing some accuracy at angles close to $\pi/4$.

The choice of the type of grid should be based on the type of problem. If the problem contains high frequencies then the triangular grid is the only one that might provide isotropy. But it requires much more computational time than the square grid. Therefore the square grid is preferred in most cases.

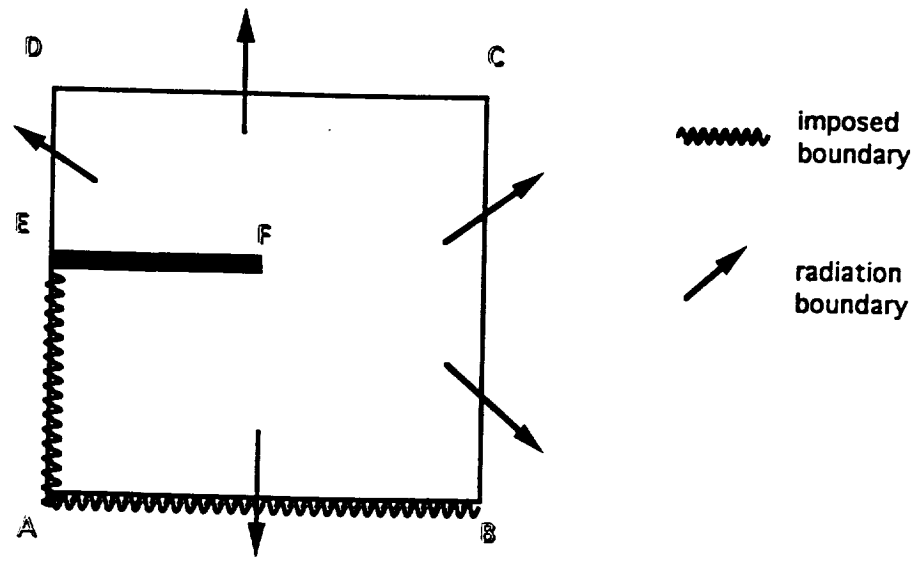

Figure 2.3: Type of boundary for the diffraction problem

2.3 Boundary Conditions

The diffraction problem was sketched in figure 1.1. The corresponding computational domain is represented in the figure 2.3. Two types of boundaries are present. The first type of boundary is the radiation boundary which is designed to let the wave exit the domain without any reflections. This type of boundary is essential because it allows an unbounded problem to be computed in a finite computational domain. The other type of boundary is the imposed boundary. This boundary condition can correspond to a wall or to an imposed wave.

2.3.1 Radiation Boundary

To conserve the same stencil over the whole domain, ghost points have to be created. Depending on the direction of the radiation condition, three rows or columns are added to the original computational domain. This added part is called the boundary region as opposed to the inner region. It is assumed that only outgoing disturbances are present in the boundary region. Tam and Webb [27] developed a system of equations to be satisfied by the disturbance by using a far-field asymptotic solution of the linearized Euler equations. This represents a slight modification from the radiation condition given by Bayliss and Turkel [4, 3] who used a far-field asymptotic solution of the wave equation. In our case, there is no mean flow so the linearized Euler equations reduce to the wave equation. Then, the two boundary conditions are equivalent.

The system of equations to be satisfied in the boundary region is given by:

$$\left(\frac{1}{c_0}\frac{\partial}{\partial t} + \frac{\partial}{\partial r} + \frac{1}{2\,r}\right)\begin{bmatrix} \rho \\ u \\ v \\ p \end{bmatrix} = 0 \tag{2.16}$$

where r is the distance between the considered point and an arbitrary origin

This system is discretized using backward and forward stencils (figure 2.4). The

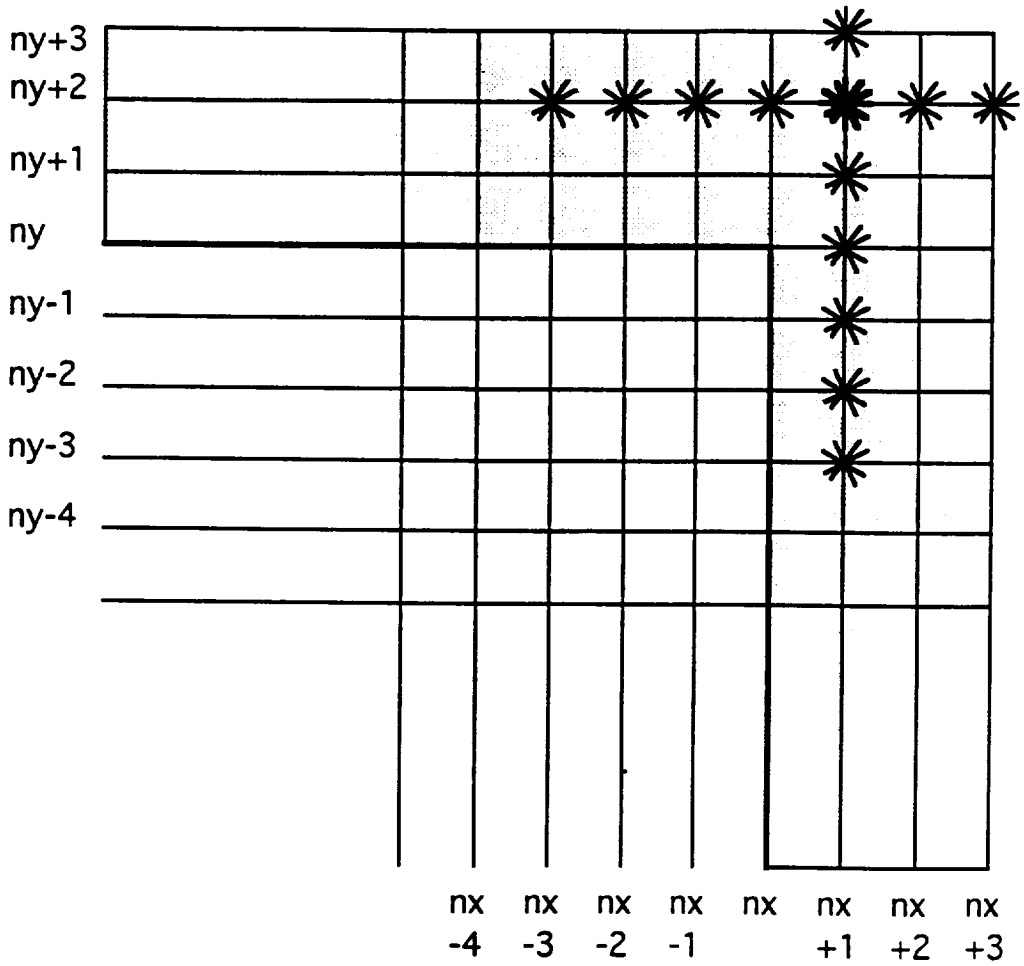

Figure 2.4: Radiation Stencil

centered coefficients a_k have to be replaced by new optimized coefficients $a_k^{l,m}$. In the case of a forward differencing in the x-direction, the indices l and m represent the number of nodes respectively on the right and on the left of the node in question. The coefficients are given by:

$$
\begin{array}{lll}
a_4^{4,2} = -0.026369431 & a_5^{5,1} = 0.048230454 & a_6^{6,0} = -0.203876371 \\
a_3^{4,2} = 0.166138533 & a_4^{5,1} = -0.28181465 & a_5^{6,0} = 1.128328861 \\
a_2^{4,2} = -0.518484526 & a_3^{5,1} = 0.768949766 & a_4^{6,0} = -2.833498741 \\
a_1^{4,2} = 1.273274737 & a_2^{5,1} = -1.388928322 & a_3^{6,0} = 4.461567104 \\
a_0^{4,2} = -0.474760914 & a_1^{5,1} = 2.147776050 & a_2^{6,0} = -5.108851915 \\
a_{-1}^{4,2} = -0.468840357 & a_0^{5,1} = -1.084875676 & a_1^{6,0} = 4.748611401 \\
a_{-2}^{4,2} = 0.049041958 & a_{-1}^{5,1} = -0.209337622 & a_0^{6,0} = -2.192280339
\end{array}
$$

For a backward difference the coefficients are the opposite of the ones above. For example, $a_4^{4,2} = 0.026369431$.

2.3.2 Imposed Boundary

Tam and Dong [25] stated that, when using a high-order scheme, it is impossible to impose in a straightforward manner the value of a variable at a boundary. Their logic is that in the discretized system of equations, the number of equations should exactly equal the number of unknowns. Therefore, imposing a value at a boundary, where both the equations and the boundary conditions are valid, would mean having

more equations than unknowns. To satisfy the extra condition, a ghost value has to be introduced. The minimum number of ghost values is equal to the number of boundary conditions. In the following calculations, a rigid wall condition is applied (figure 2.5). The same technique is applied when generating a wave by imposing a pressure or a velocity at the boundary.

Looking at the equation (2.1), it is easy to see that to impose a rigid wall condition a ghost value in p, the pressure, has to be added. Physically it means that the wall exerts a pressure on the medium such that the normal velocity component on the wall equal to zero. The calculation of the ghost value is made by rewriting the discretized equation for the normal velocity component:

$$v_{i,ny}^{(n+1)} = v_{i,ny}^{(n)} + \Delta t \sum_{k=0,3}^{3} b_k K_{i,ny}^{(n-k)}$$

$$K_{i,ny}^{(n)} = \frac{1}{\Delta x} \sum_{k=-3}^{3} a_k p_{i+k,ny}^{(n)} + \frac{1}{\Delta y} \sum_{k=-1}^{5} a_k^{51} p_{i,ny-k}^{(n)}$$

Since $v_{i,ny}^{(n)} = 0$ for any n, the only unknown is the ghost value $p_{i,ny+1}^{(n)}$. There is no ghost value for u or v, so the stencils used for p, u and v are slightly different (figure 2.6).

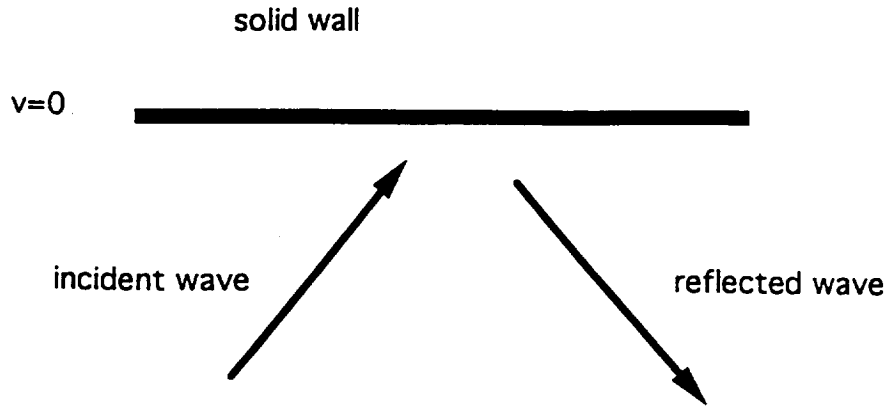

Figure 2.5: Wall

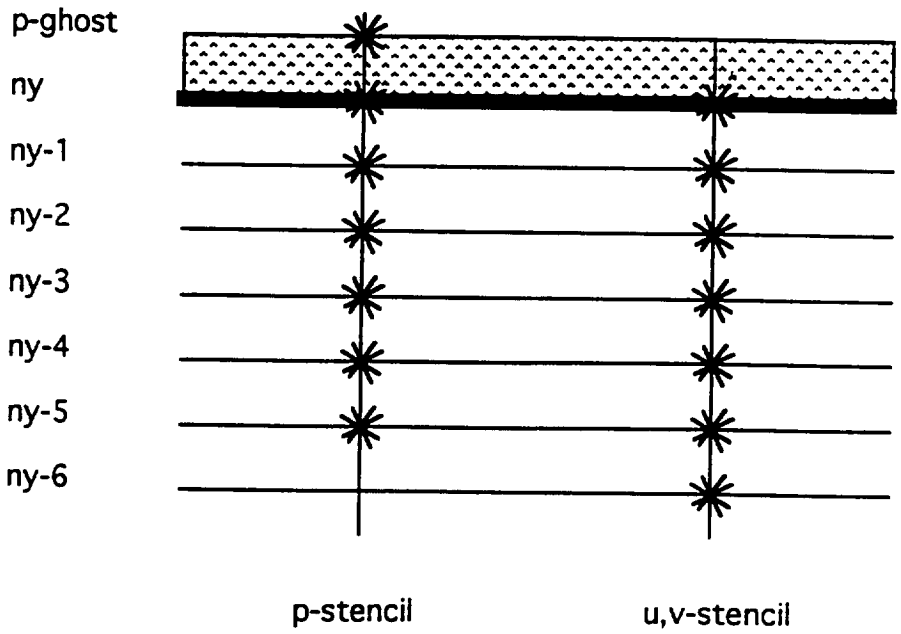

Figure 2.6: Wall stencil

In the last two sections, the governing equations have been discretized and the boundary conditions have been defined. The stability and resolution limits of the scheme have been explored. In the next chapter, this scheme will be used to solve a number of model problems. The first problem to be solved is the propagation of an oblique wave in an unbounded domain. Then, the reflection by a wall of this wave is considered. Finally, the diffraction problem will be solved. These different stages allow for the identification and solution of the many problems encountered in the diffraction problem.

Chapter 3

MODEL PROBLEMS

The diffraction of a plane wave by a half-plane is now considered. In order to isolate the different problems encountered, some preliminary model problems are considered first. These are the propagation of an oblique wave in an unbounded domain and, the reflection of a wave by a rigid wall. In the first section, the propagation problem of an oblique wave is solved to test the effectiveness of the scheme and the boundary conditions. In the second section, the reflection problem provides a way to study the problem of a boundary being non-reflecting while generating a wave without the effects of diffraction. In the third section, the diffraction problem of a plane wave by a rigid half-plane is solved. The results are compared with the analytical solution. In the last section, the incident wave is changed to model the waves generated by a supersonic jet. The diffraction effects due to a shroud surrounding a jet can then be studied.

3.1 Propagation of an Oblique Wave

In order to test the accuracy and effectiveness of the scheme and the boundary conditions, the problem of the propagation of an oblique wave in an unbounded

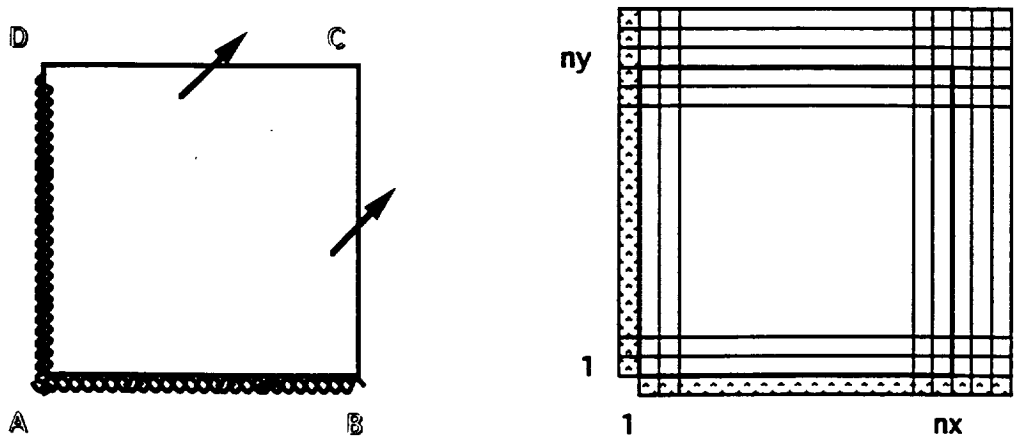

Figure 3.1: Oblique wave propagation problem

domain is considered. The computational domain is represented in figure 3.1. Two boundaries generate the wave (AB and AD) through the imposed boundary condition defined in section 2.3. At the boundary AB, the pressure and the vertical velocity component are imposed by using respectively a ghost point for the vertical velocity component and the pressure. At the boundary AD, the pressure and the horizontal velocity component are imposed by using respectively a ghost point for the horizontal velocity component and the pressure. The two remaining boundaries let the wave exit the domain by using the non-reflecting condition defined in section 2.3. This boundary condition requires the use of three ghost points.

3.1.1 Resolution

In the last chapter, the minimum number of points per wavelength was determined. It was found that the wavelength must be longer than 4.5 mesh spacings. It is noted again that a sixth order difference scheme using exactly the same stencil requires the wavelength to be longer than 6.5 spacings.

Since 5 points are necessary to define a sinusoidal wave, Tam and Webb [27] recommend the use of 5 points per wavelength instead of the possible 4.5.

To test this condition, the propagation of a plane wave resolved with 5 points per wavelength is considered. The boundary conditions for the pressure (AB and AD) is given by:

$$p\,(x, y, t) = 0.1\ \cos\,(k\cos\theta x + k\sin\theta y - \omega t)$$

where k is the wavenumber

ω is the radial frequency

θ is the angle of incidence

The velocity of the wave is defined by $c_0 = \omega/k$.

The timestep is given by the formula (2.9).

$$\Delta t \leq \frac{0.4}{1.75\left[1 + \left(\frac{\Delta x}{\Delta y}\right)^2\right]^{1/2}}\,\frac{\Delta x}{c_0}$$

The solution after 500 timesteps is compared with the exact solution at a location

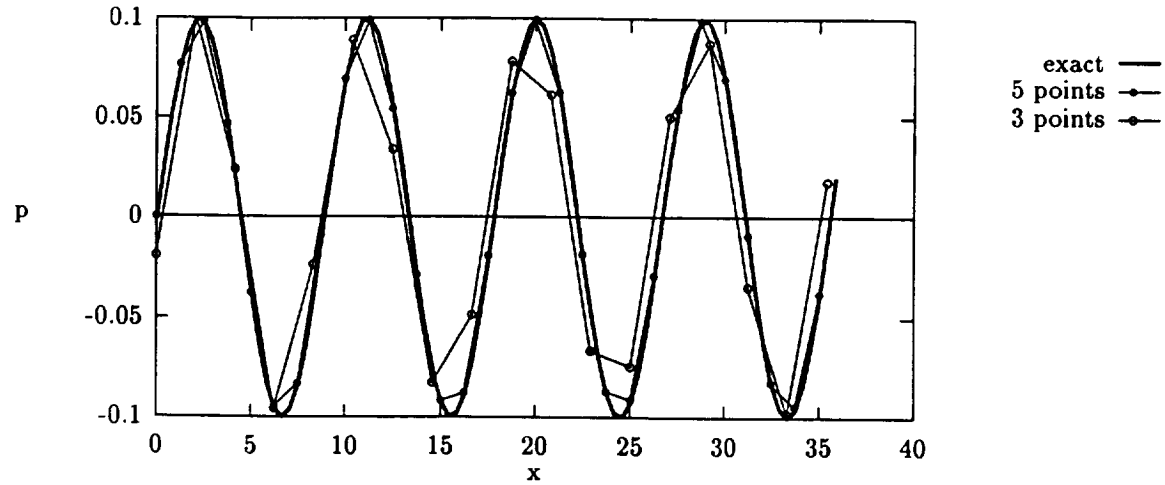

Figure 3.2: Propagation of a sinusoidal wave: $\theta = \pi/4$, $c_0 = 1$, 500 time steps

in y corresponding approximately to the middle of the computational domain (figure 3.2). The agreement obtained using 5 points per wavelength is very good. When using less points, a phase error appears.

3.1.2 Radiation Condition

To test the effectiveness of the radiation condition, a plane Gaussian pulse is imposed at the AB and AD boundaries. The expression of the Gaussian pulse in terms of pressure is given by:

$$p(x, y, t) = exp\left[-\frac{(t - t_0)^2}{b}\right]$$

where $t_0 = x cos\theta + y \sin\theta$+constant

The constant represents the time the peak of the Gaussain pulse enters the computational domain.

The origin for the calculation of r and α contained in the radiation condition has generally been taken to be in the middle of the computational domain. Tam and Webb [27] found that the radiation condition in the case of a point source gives less than 1% reflection. As can be seen in figure 3.3, this radiation condition does not work well in the case of the plane Gaussian pulse. Calculations show that most of the problems seem to occur at small x and small y as the wave is supposed to radiate right after being generated. This problem was brought to the fore by Tam and Webb [27]. They noted that when a source is located close to the boundary, strong reflections occur.

One way to improve the results is to increase the size of the domain. Nevertheless the grid needs to be huge (over 300 $\times$ 300 in this case) to get acceptable results. Therefore a modification of the position of the origin for the radiation condition is proposed. In order to determine the position of this origin, the following considerations have to be made. When the origin of the radiation condition is placed in the middle of the domain, the radiation condition is generally not satisfied by the plane pulse. This holds in particular at the corner points B and D. In order to modify the radiation condition so that they are satisfied by the plane wave, the origin of the

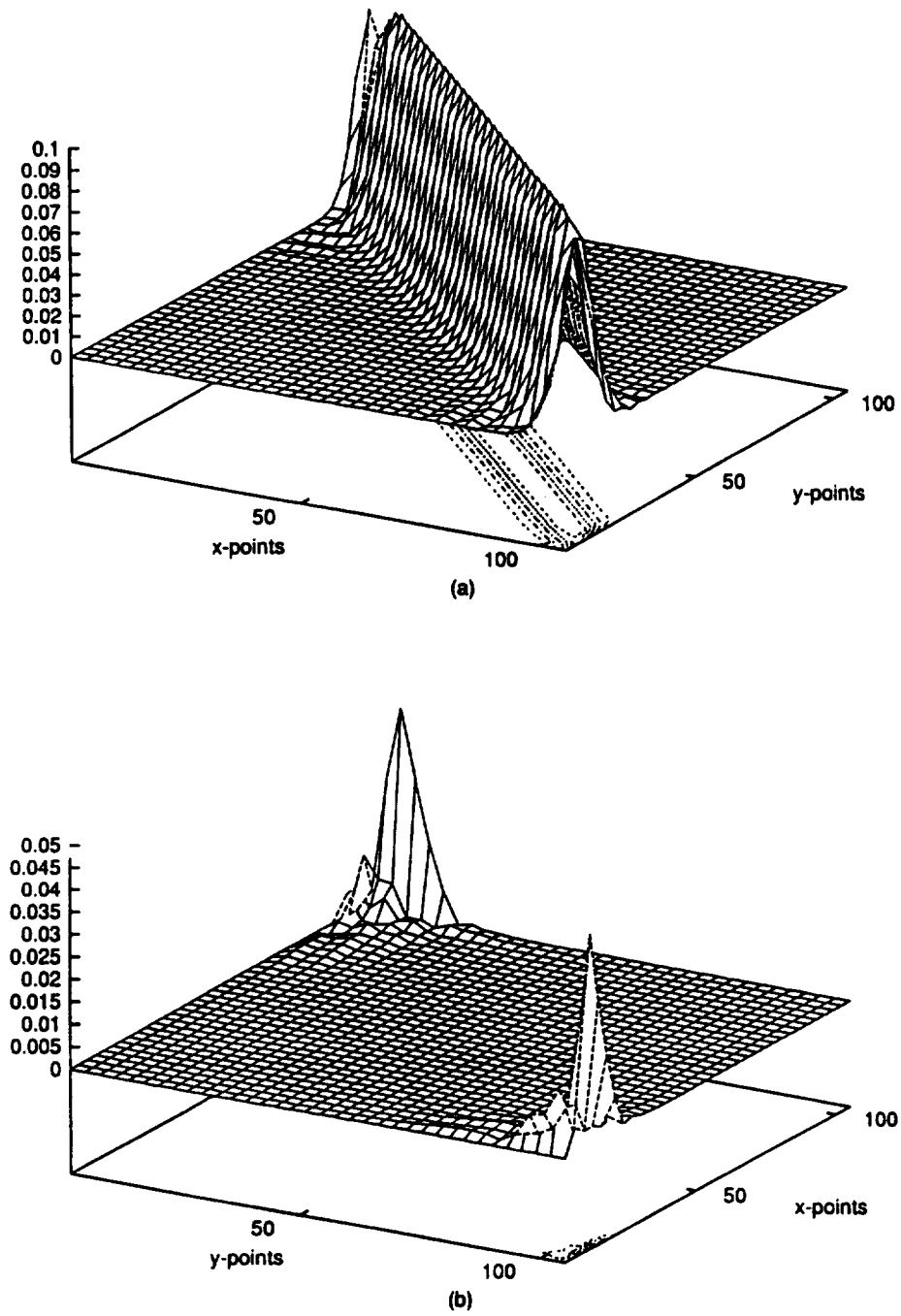

Figure 3.3: Radiation with origin in the middle of the domain: $\theta = \pi/4$, 5 points per wavelength, $c_0 = 1$, 500 time steps (a) Gaussian pulse (b) error

radiation condition needs to be such that the radiation angle is equal to the incident wave angle. Since any plane pulse can be considered as a spherical pulse with an infinite radius, the origin of the radiation condition should be placed at the source point of this spherical wave. The radiation condition would then be perfectly non-reflecting for the plane wave. But the imposition of the pulse ususally generates spurious waves. These spurious waves may not satisfy such a radiation condition. The radiation condition needs to be slightly relaxed to allow the spurious wave to radiate. That is why the plane wave is considered as a spherical pulse with a large but finite radius. The origin of the radiation condition is put at the source point of this spherical pulse.

In the case of a Gaussian pulse, the spurious waves are negligible. Therefore the origin can be located very far away (radius of the spherical wave about 1000). The pulse can then propagate without any problem even over a small domain (figures 3.4).

3.2 Reflection on a Wall

The problem of an oblique plane wave impinging on a plane wall is considered next. It is used to validate the wall boundary condition described in the preceding chapter and to study the problem of a boundary that is both non-reflecting and generates a wave (boundary AB on figure 3.2). This last boundary should both generate the incident wave and be non-reflecting for the reflected wave. Four solutions can be considered.

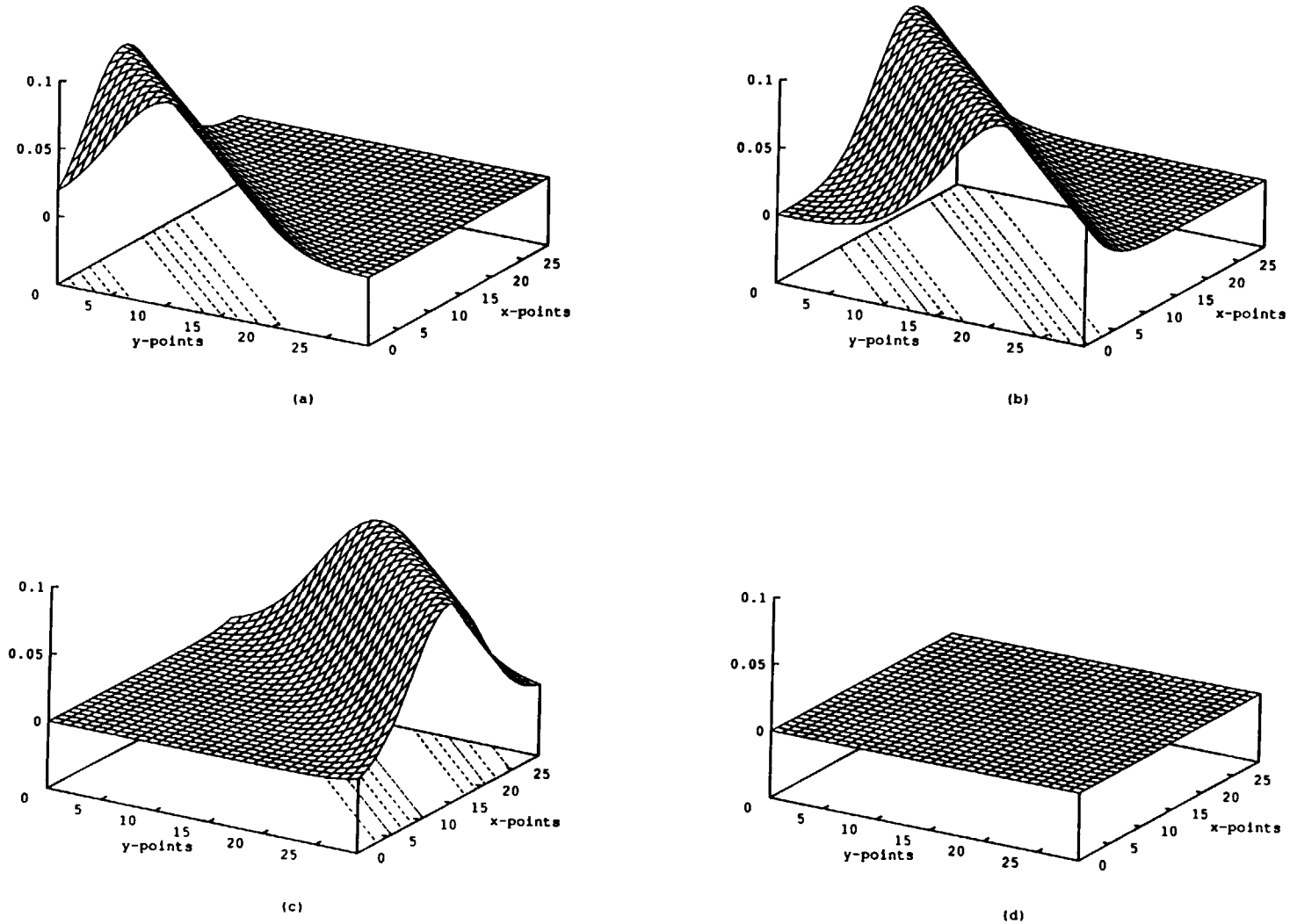

Figure 3.4: propagation of a gaussian gulse: $\theta = \pi/4$, 10 points per wavelength, $c_0 = 1$, number of time steps (a):50, (b):100, (c):150, (d):200

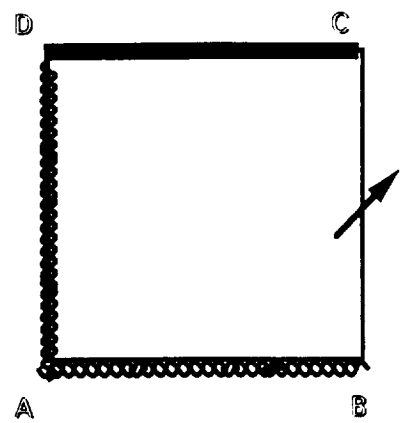

Figure 3.5: Reflection problem

The first and simplest method is to stop the calculation when the reflected wave is about to reach the boundary [12].

To avoid this time limiting factor, one can solve for the reflected wave only instead of solving for the total field. All boundaries become radiating boundaries, but the wall-condition is changed to include the effects of the incident wave [17]. The major drawback of this technique is that this wall-condition needs to be changed each time the incident wave is modified. Furthermore we can imagine that if the incident wave is not simple, its value at the wall might be difficult to determine.

A third method is described by Atkins and Casper [2]. They used a finite wave model to write their non-reflecting conditions. The advantage of this method is that, like a characteristic method, the incoming and outgoing waves can be represented by different variables. Therefore it becomes possible to impose an incoming wave

and let the outgoing wave radiate. Howewer the accuracy depends on the wave structure chosen. Some information about the direction and identities of the waves are necessary in order to choose this wave structure. Unfortunately one can imagine that this information would be difficult to obtain for waves that are not plane or simple waves.

The last method is to solve for the total field on the upper part of the domain particularly close to the wall. The wall boundary condition is then the classical one; the normal velocity is equal to zero. Close to the boundary AB, the total wave is decomposed into the incident wave which is incoming through AB and, the reflected wave which exits through AB. The advantage of this method is that the incident wave can be changed without having to change the wall boundary. The radiation boundary condition as well as the imposed boundary condition are standard. This last method is the one chosen here.

The decomposition of the total wave into the incident wave and the reflected wave is illustrated by the three computational sub-domains given in figure 3.6. The idea is that the total wave is the sum of the incident wave, incoming trough AB, and the reflected wave, exiting through AB. Thus, the total wave problem can be replaced by the incident wave problem and the reflected wave problem. This holds, in particular, close to the boundary AB. Another way of looking at the problem is to consider the reflected wave as the difference between the total wave and the incident wave. This

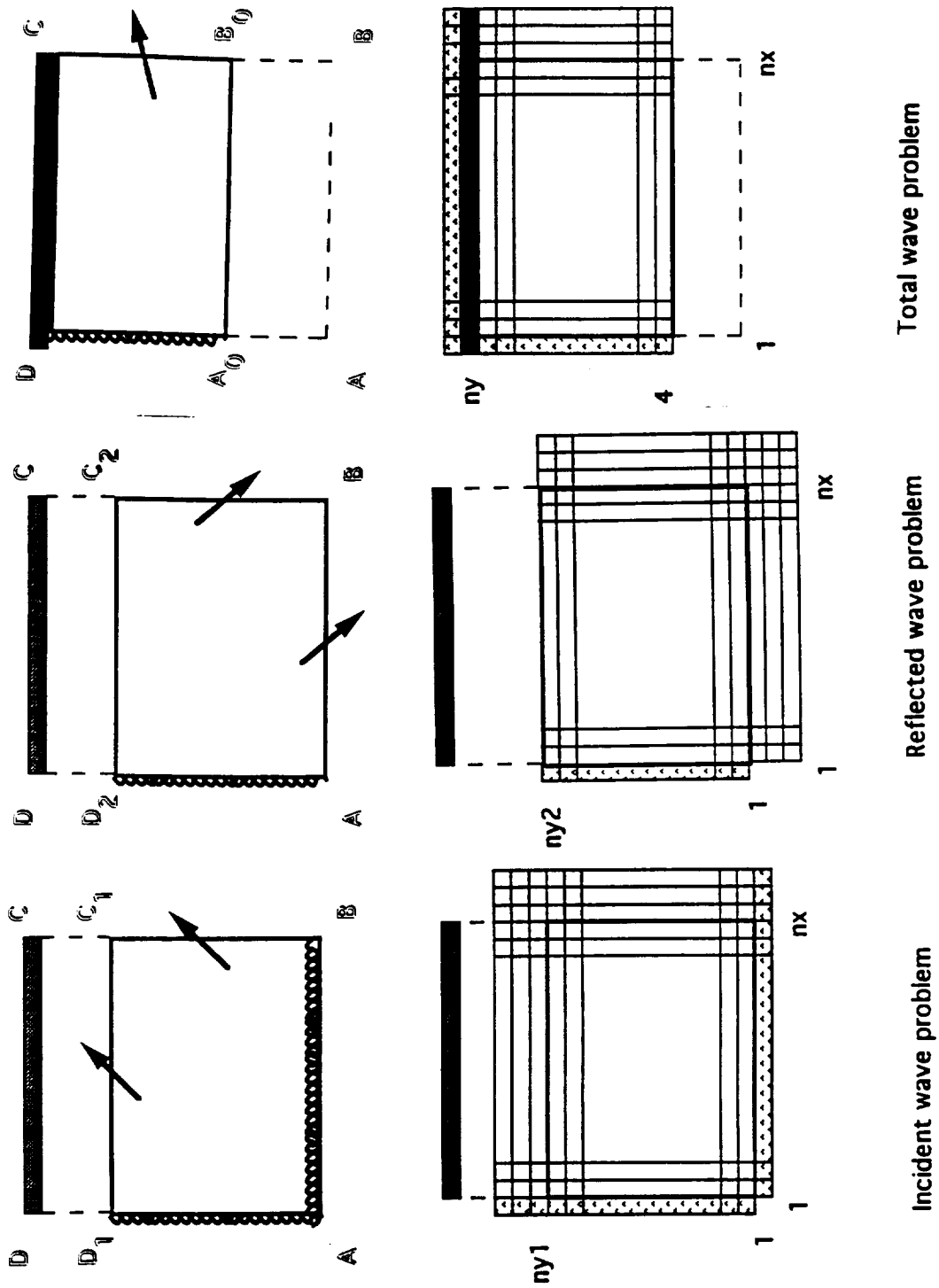

Figure 3.6: Computational domains for the reflection problem

holds, in particular, close to the wall. By using the two complementary views on complementary domains, the three components can be solved over the whole domain. The definition of the three domains then becomes straightforward. The incident wave problem is the classical oblique wave propagation problem studied in the last section. The reflected wave problem is also an oblique wave propagation problem. But the boundary C_2D_2 is not imposed as in the classical case. The boundary C_2D_2 is defined through matching. Finally, the total wave problem is the one of a wave reflecting on the wall. As for the reflected wave case, the boundary A_0B_0 is not imposed by a function but through the matching.

To show how the three problems are interconnected, the hypothetical propagation of a sinusoidal wave is shown in figure 3.7.

- first stage: the incident wave begins to propagate. It stays within the zone where the decomposition is performed. The reflected wave is evidently equal to zero. The total wave is equal to the incident wave.

- second stage: the incident covers a larger domain. In particular, it goes over A_0B_0. The reflected wave is still equal to zero. Below A_0B_0, the total wave is obtained by matching. Above A_0B_0, it is calculated.

- third stage: the incident wave begins reflecting. The reflected wave stays above C_2D_2. The reflected wave is obtained by differencing the incident wave from the total wave. The total wave is obtained in the same way as in the second

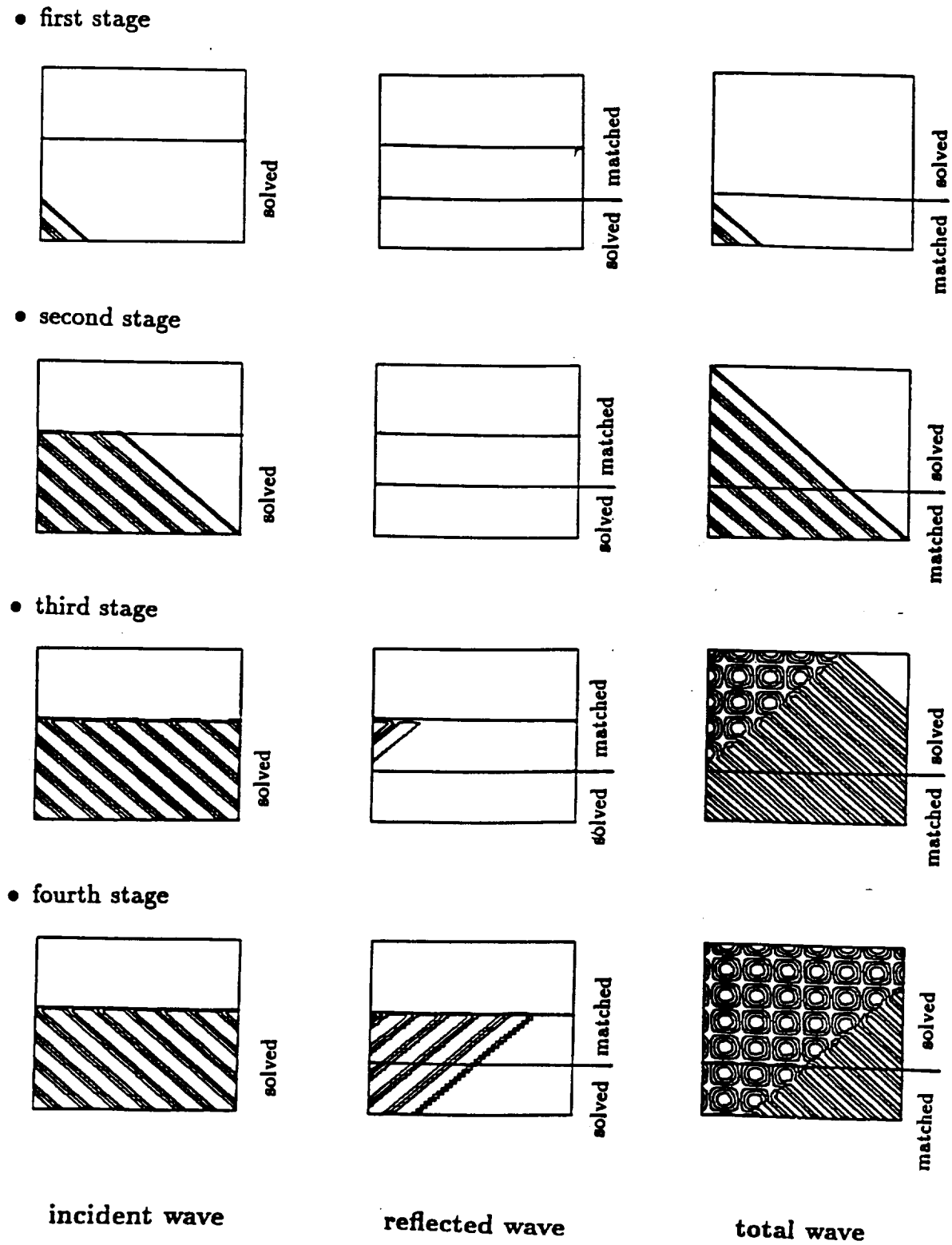

Figure 3.7: Wave propagation through the three domains

stage.

- fourth stage: the reflected wave covers most of the domain. Above C_2D_2, the reflected wave is obtained by matching. Under this line, it is calculated. The total wave is obtained in the same way as in the second stage. The difference is that the reflected wave is now non-zero under A_0B_0.

The location of the matched boundaries depends on the scheme. The computational domain for the total wave must be such that the stencil for the points on the line A_0B_0 is centered. Since the stencil is a seven point centered stencil, the number of the row representing A_0B_0 needs to be 4. The domains for the reflected wave and the total wave need to be complementary. So the number of the row representing D_2C_2 is 3. The y-stencil for a point on the line D_2C_2 will extend up to the 6th row. The reflected wave needs to be known up to this row. Thus, the incident wave needs to be solved at least for the first 6 rows. In the last section, it has been seen that the domain for an oblique wave propagation problem needs to be much larger than six rows. The number of the row representing D_1C_1 is called ny_1.

The procedure to advance one time step of the reflection problem is listed here:

◇ solve for the incident wave $\quad i = 1..ny_1$

◇ solve for the total wave $\quad i = 4..ny$

◇ solve for the reflected wave $\quad i = -2..3$

◇ calculate the reflected wave $\quad i = 4..6$

◇ calculate the total wave $\quad i = 1..3$

It should be noted that the stability of the scheme seems to be influenced by the introduction of the wall. There is no simple explanation for this phenomena. It is observed that the solution tends to blow up along the wall when the time step prescribed by equation (2.9) is used. This has not been observed for waves issuing from a point source. By dividing the time step by two, stability is retrieved.

The figures 3.8 shows the propagation of the wave. The wave is generated, then gets reflected, and then the reflected wave leaves the domain. The decomposition of the total wave seems to be quite suitable.

It is to be noted that the radiation boundary for the total field (boundary BC) seems to generate reflections. A 50×50 grid is used to calculate the results shown in figure 3.9. At i=35, in the domain, the agreement between the exact and the numerical solutions is very good. At i=45, close to the boundary BC, the numerical solution is different from the exact solution. When considering the propagation of an oblique wave over a free-domain, it was observed that the radiation condition is not very efficient for plane waves (section 3.1). A change of the origin for the radiation boundary condition was used to improve the results. In this case, the boundary should be non-reflecting to two plane waves with very different angles of incidence. Moving the origin is not an option anymore. Only an increase of the domain can improve the results. A grid of 100×100 is sufficient in most cases to obtain acceptable results.

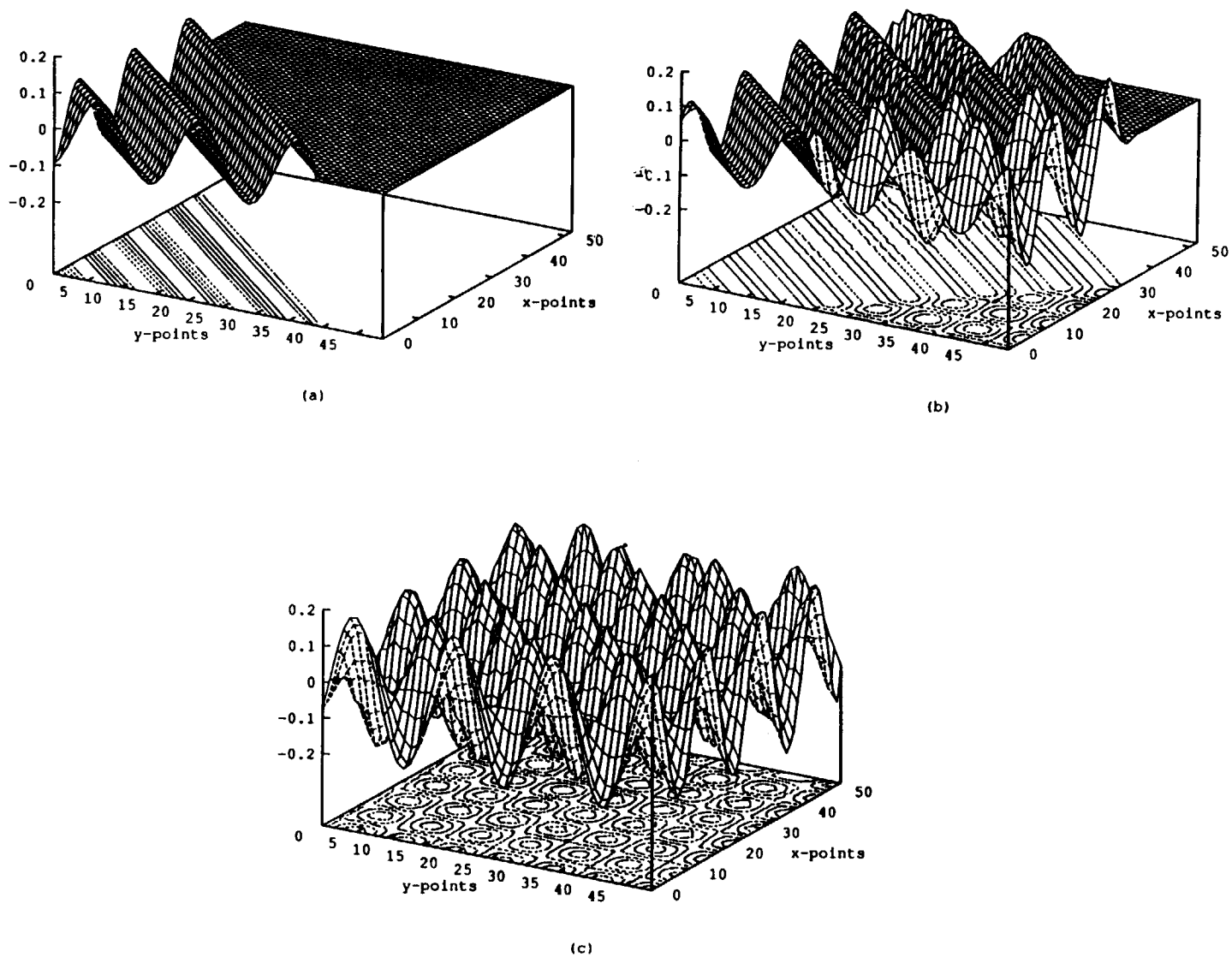

Figure 3.8: Propagation and reflection of a plane wave: $\theta = \pi/4$, 10 points per wavelength, $c_0 = 1$, number of time steps (a) 350, (b) 700, (c) 1500

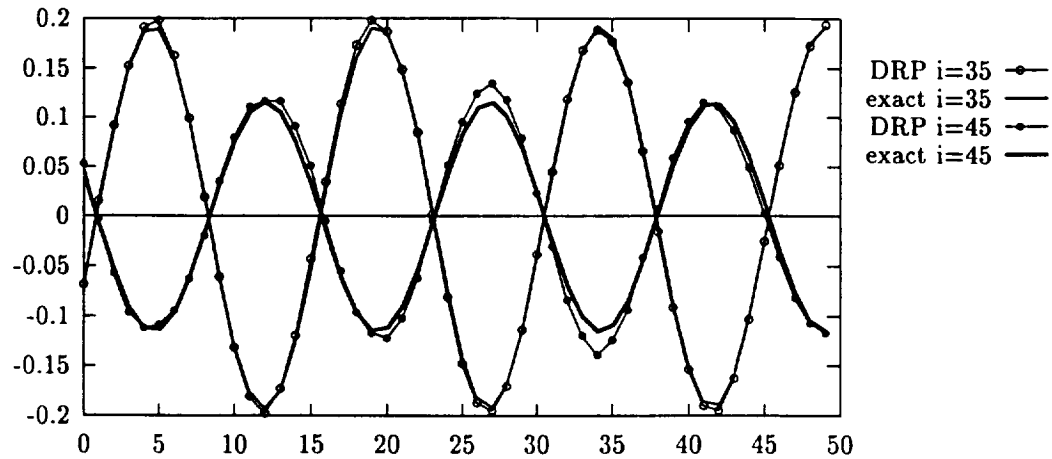

Figure 3.9: Comparison between the exact and the numerical solutions for the reflection problem: $\theta = \pi/4$, 10 points per wavelength, $c_0 = 1$, 1500 time steps, 50 points in x-direction

3.3 Diffraction by a half-plane

In the above sections, the validity of the scheme and the boundary conditions have been tested. Now the reflecting plane is replaced by a semi-infinite plane. The incident wave is not only reflected, but is diffracted. The same decomposition as for the reflection problem is used here to solve the problem of the boundary AB. So three problems (incident wave, reflected wave, total wave) are solved. The only difference between the diffraction case and the reflection case is in the total wave problem. Instead of containing a full plane as in the reflection problem, it contains a half-plane. Thus, the principle of the decomposition stays the same and will not be repeated. The three computational domains relative to the incident wave, reflected

wave and total wave are given in figure 3.10.

In these domains, the boundary AE is purely an imposed boundary, although the diffracted wave could be passing through it. In fact this boundary should be treated as the boundary AB. To do so, the total field should be decomposed into three fields (incident, reflected, diffracted) instead of two (incident, outgoing). This would make the computer code less efficient and quiet complicated. Since the amplitude of the scattered field at this location is much lower than the amplitude of the total field, it is assumed that it can be neglected. As long as the tip of the plane is far from the point E, this assumption is valid.

To calculate the gradients in x at the three grid points on the x-axis closest to the plate, it is assumed that the average of the values below and above the plane can be used.

The diffraction problem is now ready to be computed. When coded this way, the solution diverges at the radiation boundaries. Tam and Dong [25] noted that, along with the diffracted wave, some spurious waves are created. In order to have a valid and stable solution, these spurious waves have to be eliminated. Tam and Dong [25] proposed to add some dissipation to the scheme. Tam, Webb and Dong [28] noticed that the parasite and dispersive waves have a shorter wavelength than the initial waves. Therefore they designed an artificial damping which selectively damps out the short waves but has a minimal effect on the long waves. This is achieved by optimizing the dissipation coefficients such that, in the one-dimensional case, the

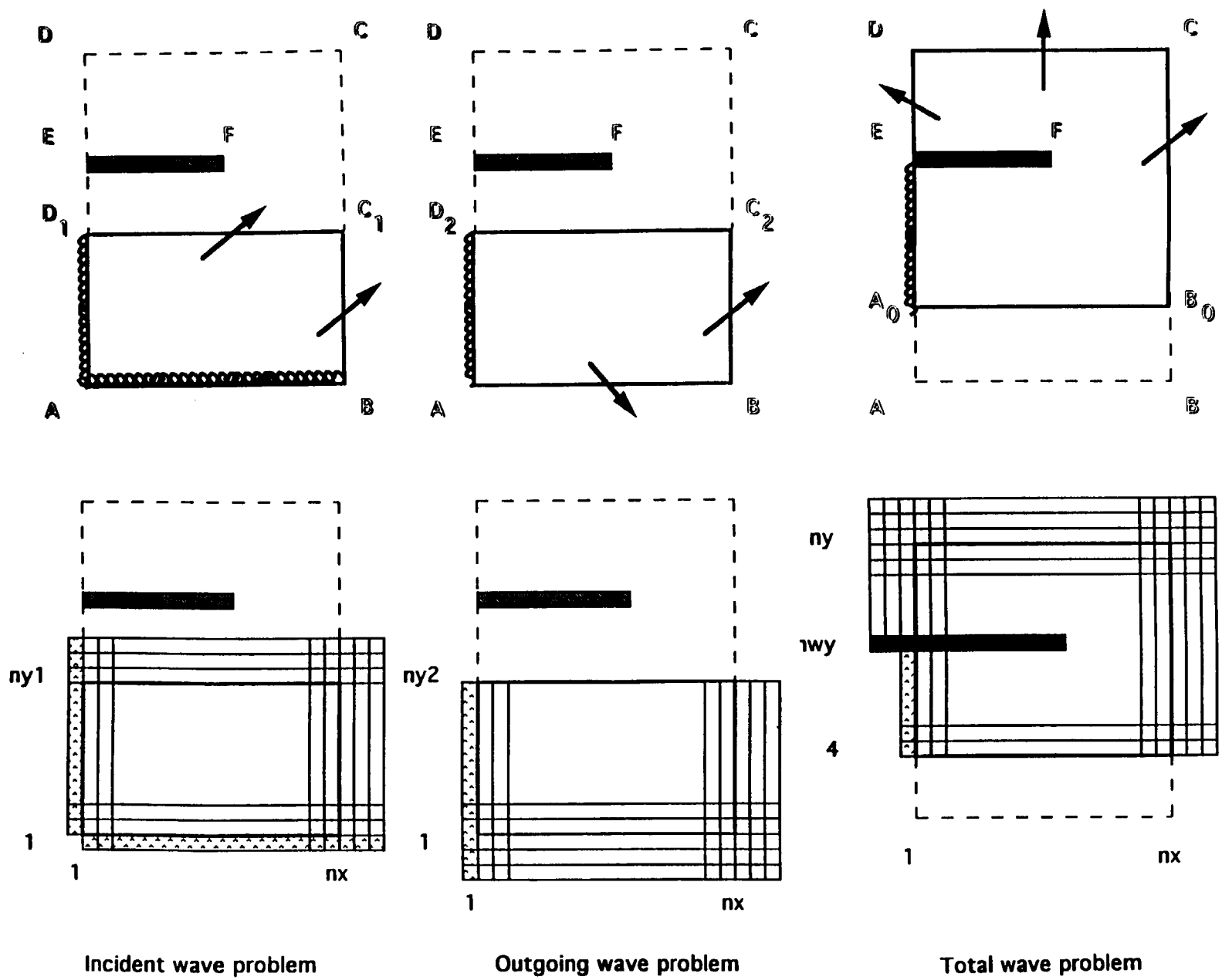

Figure 3.10: Computational domains for the diffraction problem

Fourier transform of the artificial damping is a good approximation over the interval $[0, \beta]$ to the function:

$$exp\left[-\ln 2\left(\frac{\alpha\Delta x - \pi}{\sigma}\right)\right]$$

where α is the wavenumber

Δx is the grid spacing in x

σ is a constant

The damping term is given by:

$$D_i^{(n)} = \mu\frac{1}{\Delta x^2}\sum_{k=-3}^{3} c_k\, U_{i+k}^{(n)} \tag{3.1}$$

where μ is a constant ($\mu = 0.3$)

The coefficients c_k depends on the value of the parameters σ, β. For $\sigma = 0.2\pi$, $\beta = 0.33327\pi$ (ref. [26]), they are given by:

$$\begin{aligned} c_0 &= 0.3030588 \\ c_1 = c_{-1} &= -0.231695528614 \\ c_2 = c_{-2} &= 0.09840572424 \\ c_3 = c_{-3} &= -0.018304471386 \end{aligned} \tag{3.2}$$

Figure 3.11 represents $\overline{D}(\alpha\ \Delta x)$, the damping constant for a wavenumber α. The function peaks at $\alpha\ \Delta x = \pi$ and decays quickly towards the long wave number range. These are the desirable properties of a selective damping function.

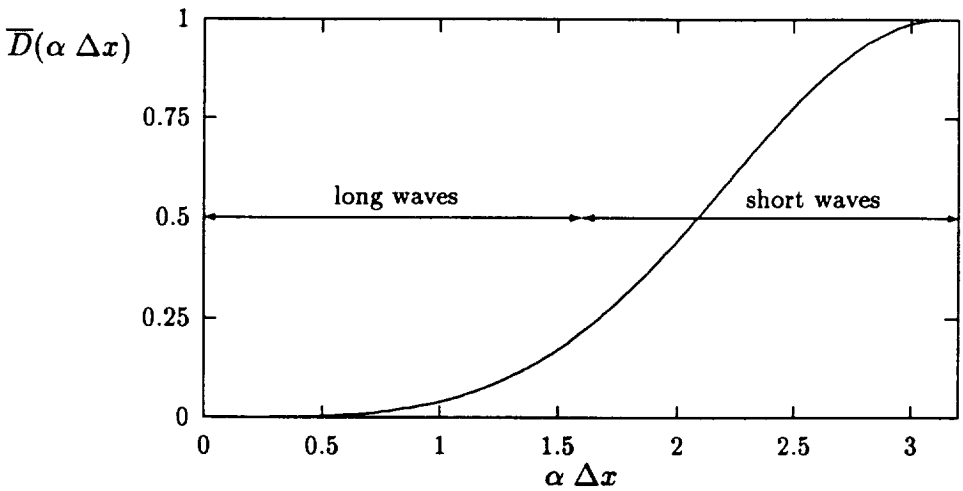

Figure 3.11: Damping function

The expression for $U_{i,j}^{(n+1)}$ given by (2.6)

$$U_{i,j}^{(n+1)} = U_{i,j}^{(n)} + \Delta t \sum_{k=0}^{3} b_k\ K_{i,j}^{(n-k)}$$

has to be changed to:

$$U_{i,j}^{(n+1)} = U_{i,j}^{(n)} + \Delta t \sum_{k=0}^{3} b_k\ \left(K_{i,j}^{(n-k)} + D_{i,j}^{(n-k)}\right) \tag{3.3}$$

The propagation of a plane wave over the domain is represented in figure 3.12. The half-plane is represented by a black bar. The wave first propagates, then is reflected on the half-plane, and is diffracted at the tip of the half-plane. As the diffracted wave propagates, it is observed that the tip of the plane behaves as a source point. This is

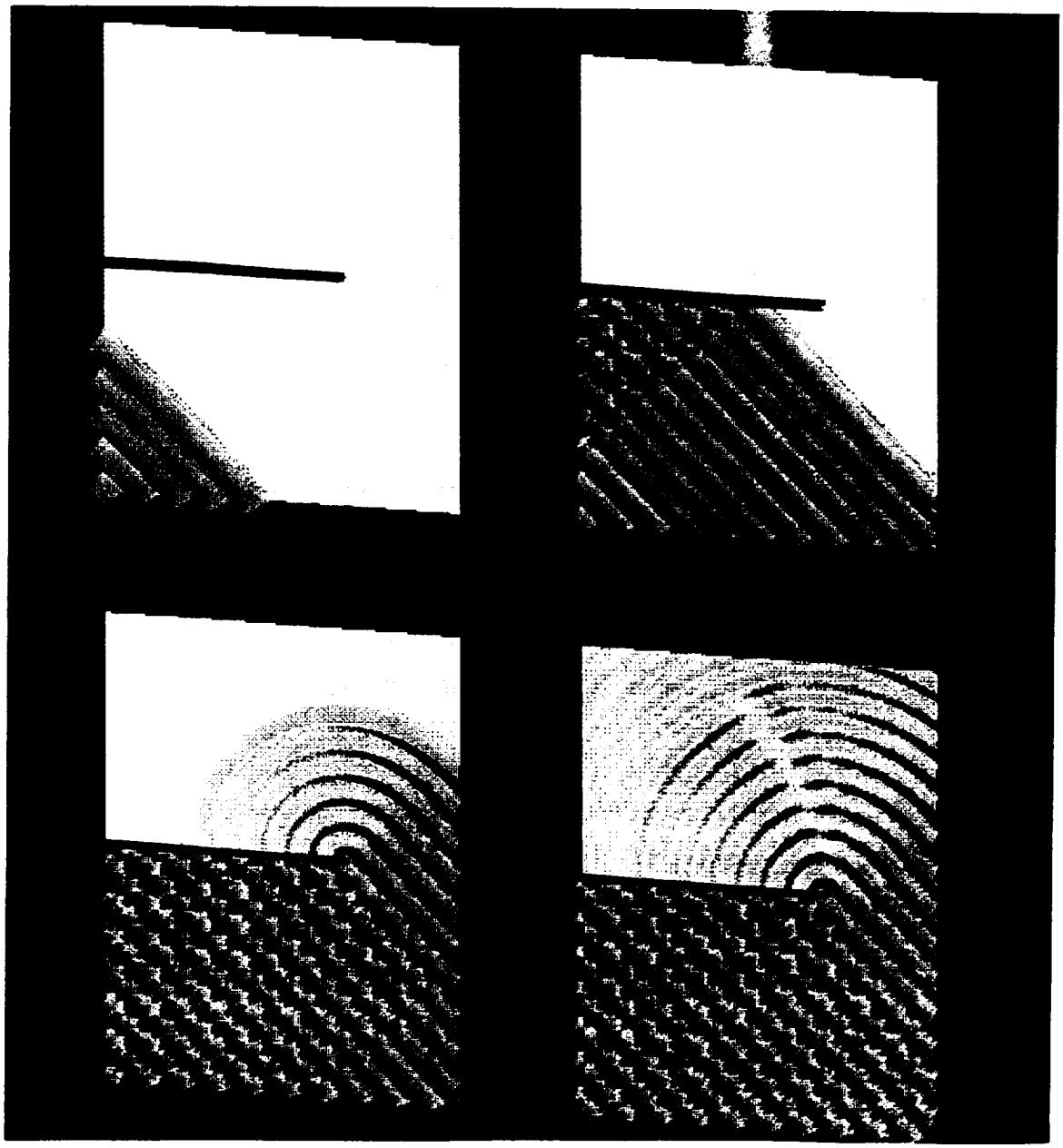

Figure 3.12: Diffraction of a plane wave: $\theta = \pi/4$, 10 points per wavelength, $c_0 = 1$, $\mu = 0.3$, number of iterations (a): , (b): , (c):6000

in agreement with the Huygen's principle.

Once the transient state has been eliminated from the domain, the solution can be compared with the analytical solution given by the Wiener-Hopf technique. A complete description of this technique can be found in the appendix. Here only the result for a plane wave is given.

If the incident wave p_i is given by $p_i(x,y,t) = \exp[i(k\ \cos\theta\ x + k\ \sin\theta\ y - \omega t)]$, the total wave is given by:

$$p_t(x,y,t) = p_i(x,y,t) \pm \frac{k^{1/2}\ \sin\theta\ e^{-i\omega t}}{2\pi\ (1+\cos\theta)^{1/2}} \int_{-\infty}^{\infty} \frac{\exp(-\gamma|y| - isx)}{(s-k\cos\theta)\ (s-k)^{1/2}}\ ds \qquad (3.4)$$

where $\gamma = (x^2+y^2)^{1/2}$

'+' stands for $y \geq 0$

'-' stands for $y \leq 0$

The half-plane extends in the x-direction from i=1 to i=100. The comparison between the two solutions is made along lines parallel to the wall. Each line can be considered as the intersections of the computational plane with an observation plane. These planes are represented in figure 3.13. The computational domain is grey. The half-plane is black. The incident wave is represented by the arrows. The two planes of observation are situated right below the half-plane ($S1$) and right above it ($S2$).

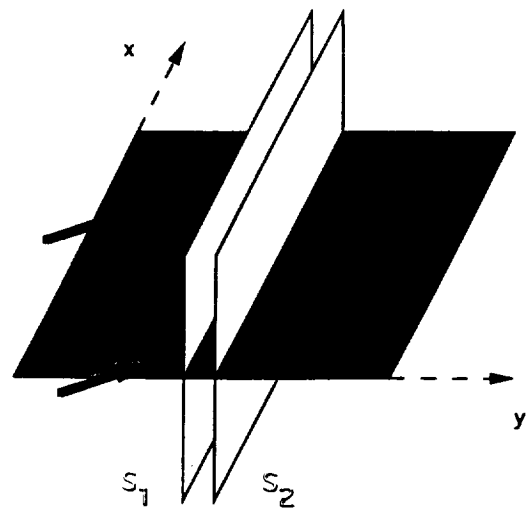

Figure 3.13: Comparison planes for the diffraction case

Figure 3.15 represents the analytical and numerical pressure n the plane $S1$. Figure 3.14 represents the same quantities in the plane $S2$. When comparing these two solutions, attention must be paid to the fact that, in the Wiener-hopf technique, the tip of the plane is well-defined. In the numerical solution, the tip of the plane is only known to be in between two nodes. This difference can induce some phase error. Nevertheless the agreement is very good. The oscillations close to $i = 100$ are due to the spurious waves generated by the tip of the plane. These oscillations disappear quickly when going away from the tip due to the damping added to the scheme.

These comparisons give some confidence both in the scheme and in the decomposition technique. The incident wave will now be changed. A priori, this is the only

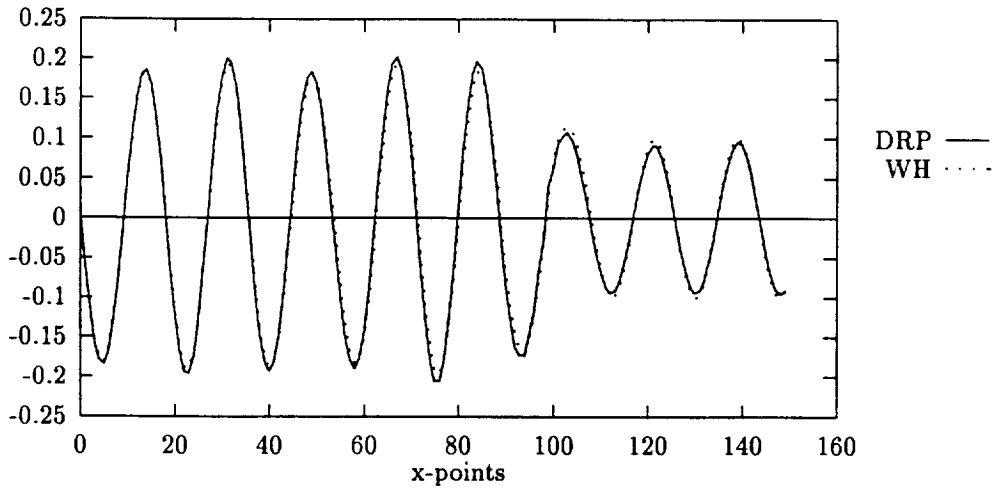

Figure 3.14: Comparaison between the Wiener-Hopf technique and the DRP numerical solution in the $S1$ plane: $\theta = \pi/4$, 10 points per wavelength, wall i=1-100

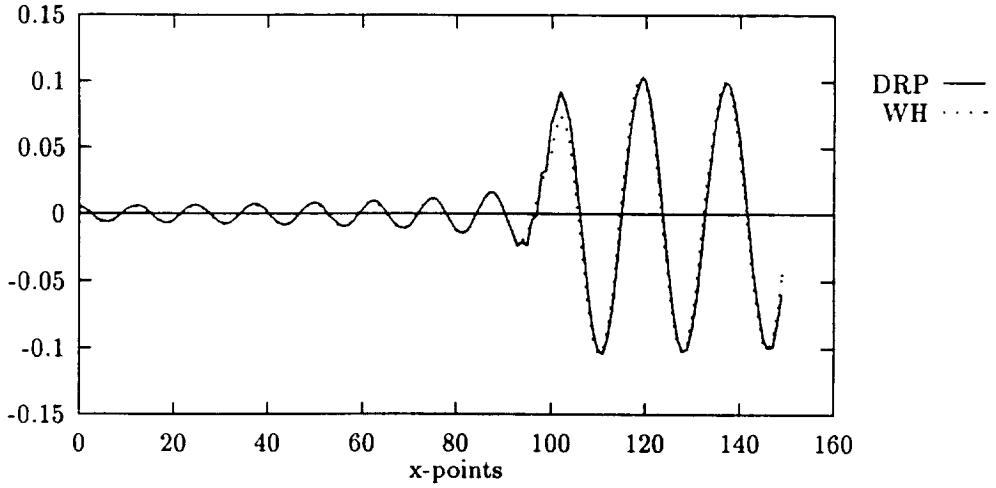

Figure 3.15: Comparaison between the Wiener-Hopf technique and the DRP in the $S2$ plane: $\theta = \pi/4$, 10 points per wavelength, wall i=1-100

change to be made.

3.4 Jet Noise Problem

Surrounding a jet by a shroud is an effective way to reduce the noise produced by the jet. In order to understand what effect diffraction has on this noise reduction, the half-plane diffraction will now be used as a simple model for a shroud surrounding a jet. The three main categories of noise in a supersonic jet have been recognized to be the mixing noise, the broadband shock assocated noise and the screech tones. The mixing noise is relateddirectly to the supersonically convecting turbulence existing in the plume of the jet. The broadband shock-associated noise is the product of an interaction between the shock-cell structure of an imperfectly expanded jet and the instabilities in the shear layer. The screech tones are a consequence of a phase-locked interaction between the shock-cell structure and the instability waves. So the instabilities seem to be at the center of all the mechanisms. They are well described by the instability waves of the jet. It is not unreasonable to propose that jet noise could be simulated simply as the propagation of an incident wave which is generated by these instability waves.

The incident wave is assumed to take the following form:

$$p(x,-h,t) = \exp\left[\frac{(x-x_0)^2}{b})\right] \quad \cos(kx-\omega t) \tag{3.5}$$

The parameters x_0, b, k and ω are functions of the Mach number M_j of the jet,

change to be made.

3.4 Jet Noise Problem

Surrounding a jet by a shroud is an effective way to reduce the noise produced by the jet. In order to understand what effect diffraction has on this noise reduction, the half-plane diffraction will now be used as a simple model for a shroud surrounding a jet. The three main categories of noise in a supersonic jet have been recognized to be the mixing noise, the broadband shock assocated noise and the screech tones. The mixing noise is relateddirectly to the supersonically convecting turbulence existing in the plume of the jet. The broadband shock-associated noise is the product of an interaction between the shock-cell structure of an imperfectly expanded jet and the instabilities in the shear layer. The screech tones are a consequence of a phase-locked interaction between the shock-cell structure and the instability waves. So the instabilities seem to be at the center of all the mechanisms. They are well described by the instability waves of the jet. It is not unreasonable to propose that jet noise could be simulated simply as the propagation of an incident wave which is generated by these instability waves.

The incident wave is assumed to take the following form:

$$p(x,-h,t) = \exp\left[\left(\frac{(x-x_0)^2}{b}\right)\right] \cos(kx-\omega t) \tag{3.5}$$

The parameters x_0, b, k and ω are functions of the Mach number M_j of the jet,

the Strouhal number St and the ratio of static temperatures T_a/T_j. All variables are scaled using the jet width d for a length scale and the speed of sound in the ambient medium c_0 for the velocity scale. Three intermediate variables are defined. c_j is the jet exit speed of sound, $\overline{u}_j$ is the jet exit velocity and, x_c is the length of the potential core.

The expressions for c_j, $\overline{u}_j$, ω may be written as:

$$c_j = c_0 \left[\frac{T_j}{T_a} \frac{1}{1 + \frac{\gamma-1}{2} M_j^2} \right] \tag{3.6}$$

$$\overline{u}_j = M_j c_j \tag{3.7}$$

$$\omega = \cancel{2}\pi \, \overline{u}_j \, St \tag{3.8}$$

By assuming that the phase velocity of the waves is 70% of the jet exit velocity, k and ω are related by the following expression.

$$k = \frac{\omega}{0.7\overline{u}_j} \tag{3.9}$$

The position of the maximum amplitude is a function of the Strouhal number [29].

$$x_0 = \overset{2}{\cancel{1}}(0.057St + 0.021St^2)^{-1/2} \tag{3.10}$$

Finally b is obtained using calculations taken from [20]. These calculations are extrapolated for any Mach number and any temperature ratio using the fact that b

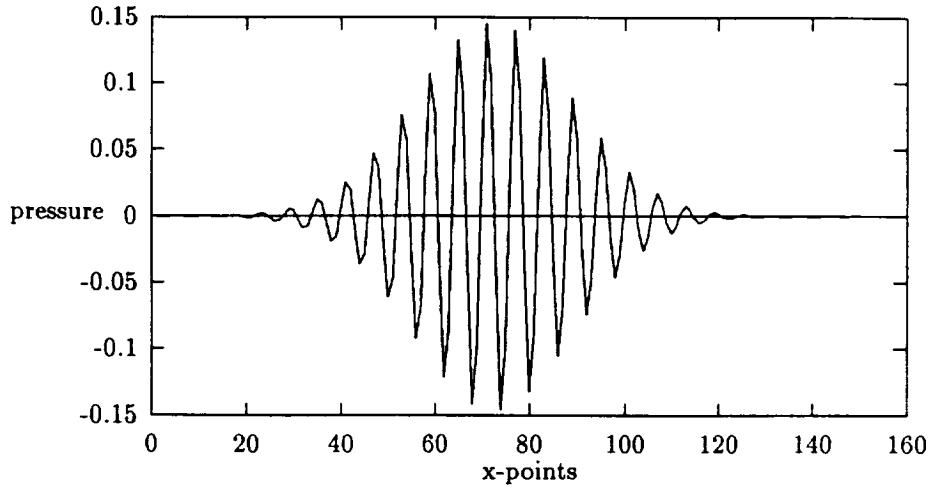

Figure 3.16: Example of incident wave for the jet noise problem

is a function of the length of the potential core x_c.

2. ok

$$x_c = (4.2 + 1.1M_j^2)(T_j/T_a)^{-0.2} \tag{3.11}$$

$$b(M_j, T_a/T_j, St) = b^*(St)\ \frac{x_c(M_j, T_a/T_j)}{x_c(1.4, 1)} \tag{3.12}$$

$b^*(1) = 1.4$ $\qquad$ $b^*(0.3) = 2.8$ 12 13 $\qquad$ $b^*(0.1) = 10$ 81

In figure 3.16, an example of the imposed wave is shown. The conditions are $M_j = 2$, $St = 1$ and, the jet is cold.

It is to be noted that this model is very simplified. In particular, it is known that the instability waves are greatly influenced by the presence of a shroud [30]. It has

been shown that the shroud acts as a selective amplifier for certain frequencies. In the present model, no account has been taken of the change in the instability waves due to the shroud. Therefore, it is not appropriate to consider shrouds close to the edge of the jet. The shrouds considered will be at least 4 to 5 jet widths.

Another simplification comes from the fact that only the first diffraction is considered. The reflected wave should be reflected on the other side of the shroud. Instead, in this model, the reflected wave simply radiates. A very simple way to solve this problem is to change the radiation condition imposed on the reflected wave to a reflection condition.

Nevertheless, the model gives an idea of how the diffraction effect by itself influences the noise radiation. It can be seen that this effect provides some noise reduction by redistributing the noise. Figures 3.17 and 3.18 show an example of a diffracted wave and of the corresponding incident wave. The incident wave corresponds to a cold jet with a Mach number of 2 and a Strouhal number of 1. The half-plane is parallel to the centerline of the jet at a distance of 5 jet width. The tip of the plane is placed downstream from the point of maximun amplitude of the incident wave. On the picture, the half-plane is at the left border. It extends from the the lower left corner to about two third of the left border. It can be seen that the pressure level has been greatly reduced by the presence of the half-plane. When looking at the solutions for large values of y (right border), one observes that the shape of the wave has been greatly transformed.

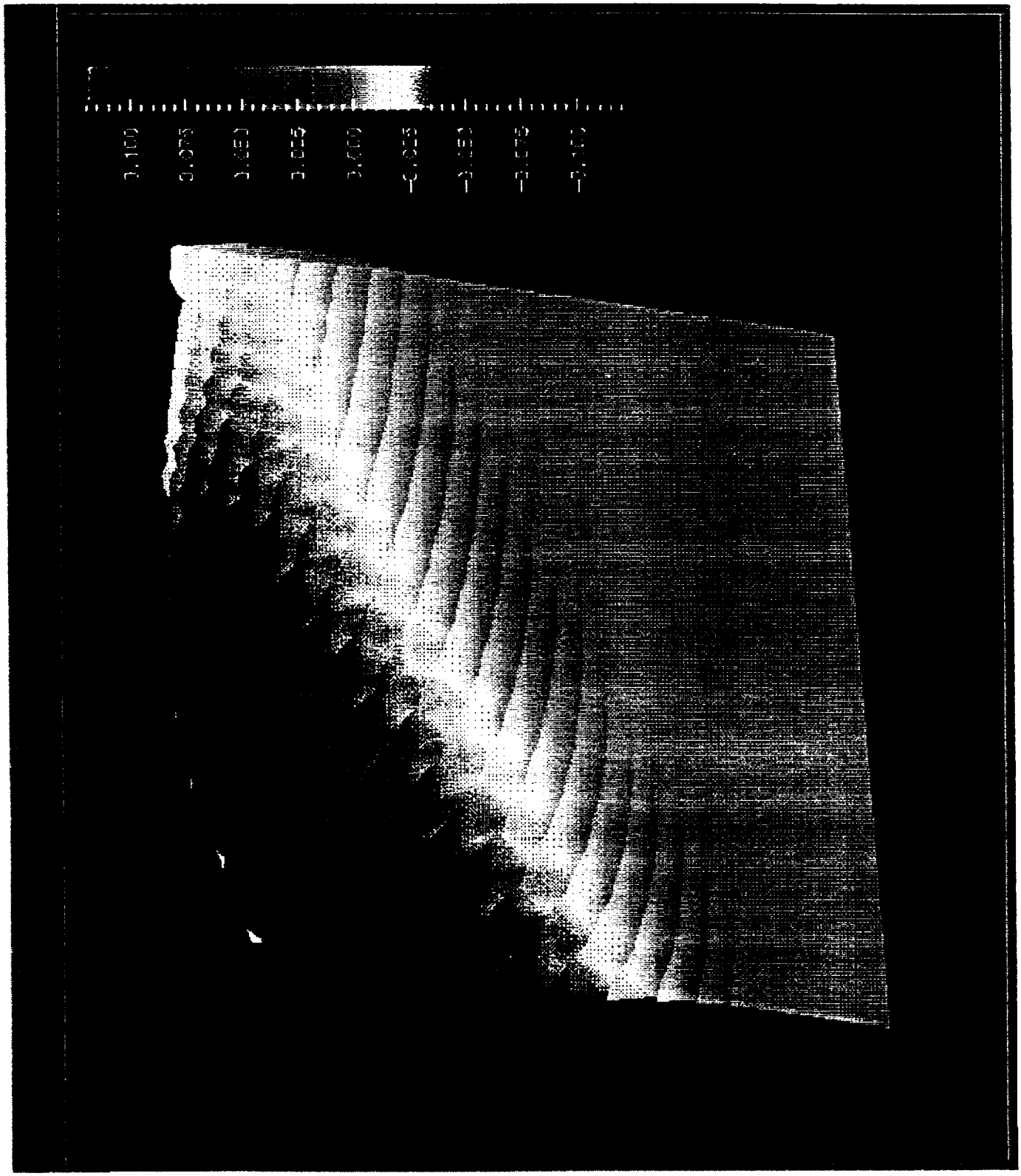

Figure 3.17: Propagation of the incident wave without the half-plane: $M_j = 2$, $St = 1$, cold jet

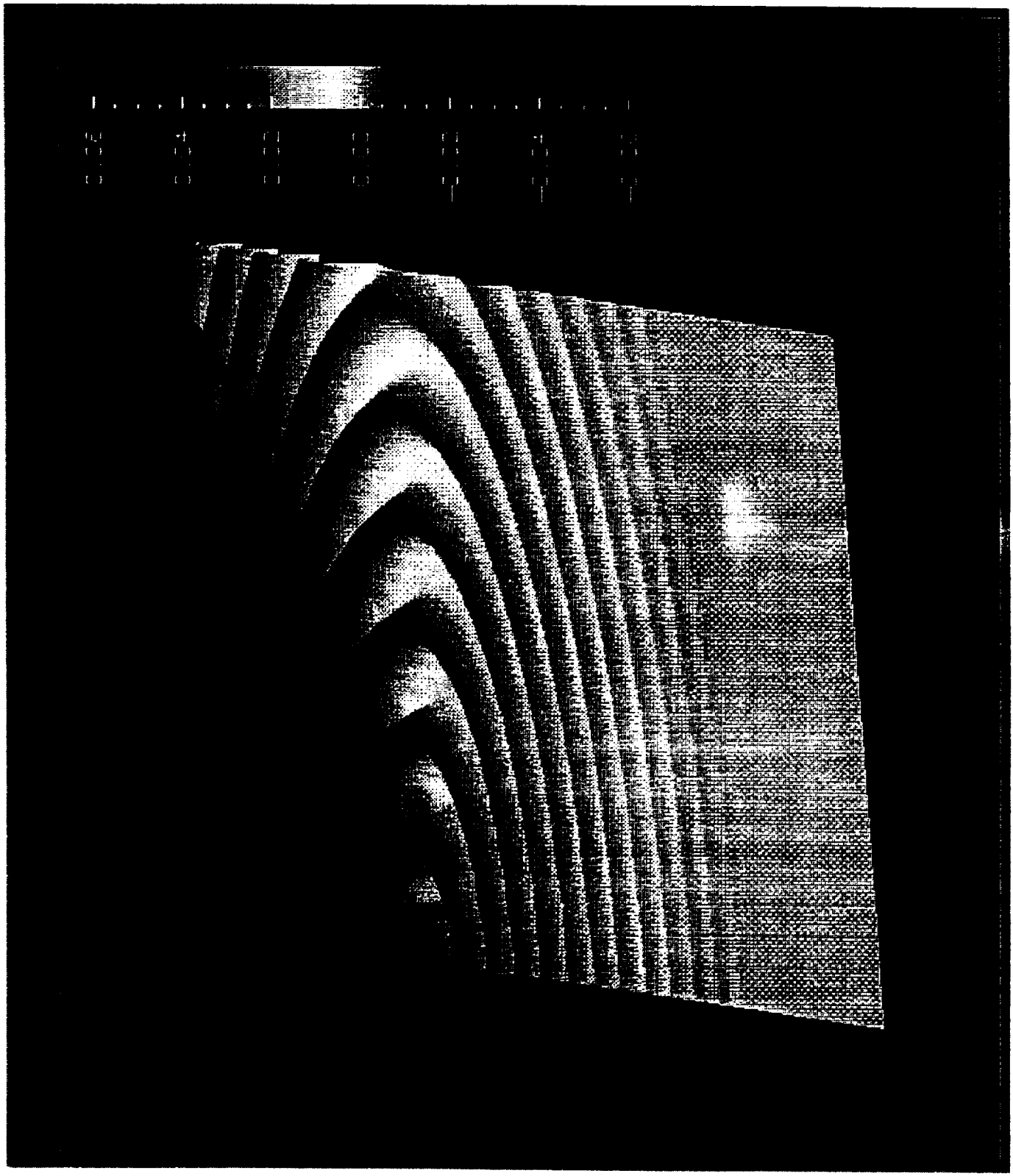

Figure 3.18: Propagation of the incident wave with the half-plane: $M_j = 2$, $St = 1$, cold jet

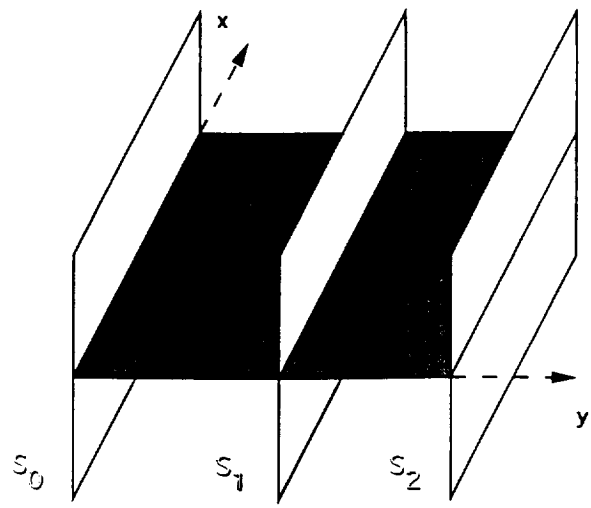

Figure 3.19: Observation planes for the jet noise problem

The influence of the position of the half-plane is now studied. The half-plane is placed at 5 jet width from the centerline of the jet. The tip of the half-plane is placed at three differents locations downstream. The influence of the downstream position of the plane is observed in two slices of the computational domain. The placement of these slices is illustrated by figure 3.19. The computational domain is grey. The half-plane is black. The incident wave is imposed in the plane $S0$. Figure 3.20 represents the waves in the plane $S1$. Figure 3.21 represents the same waves on a along the external boundary of the computational domain in the plane $S2$. half-plane (figure 3.20), and at the end of the computational domain (figure 3.21). In the three cases, there is a redistribution of the pressure: the intensity level is decreased and the solution is non-zero on a larger range on the x-axis. As expected, the further

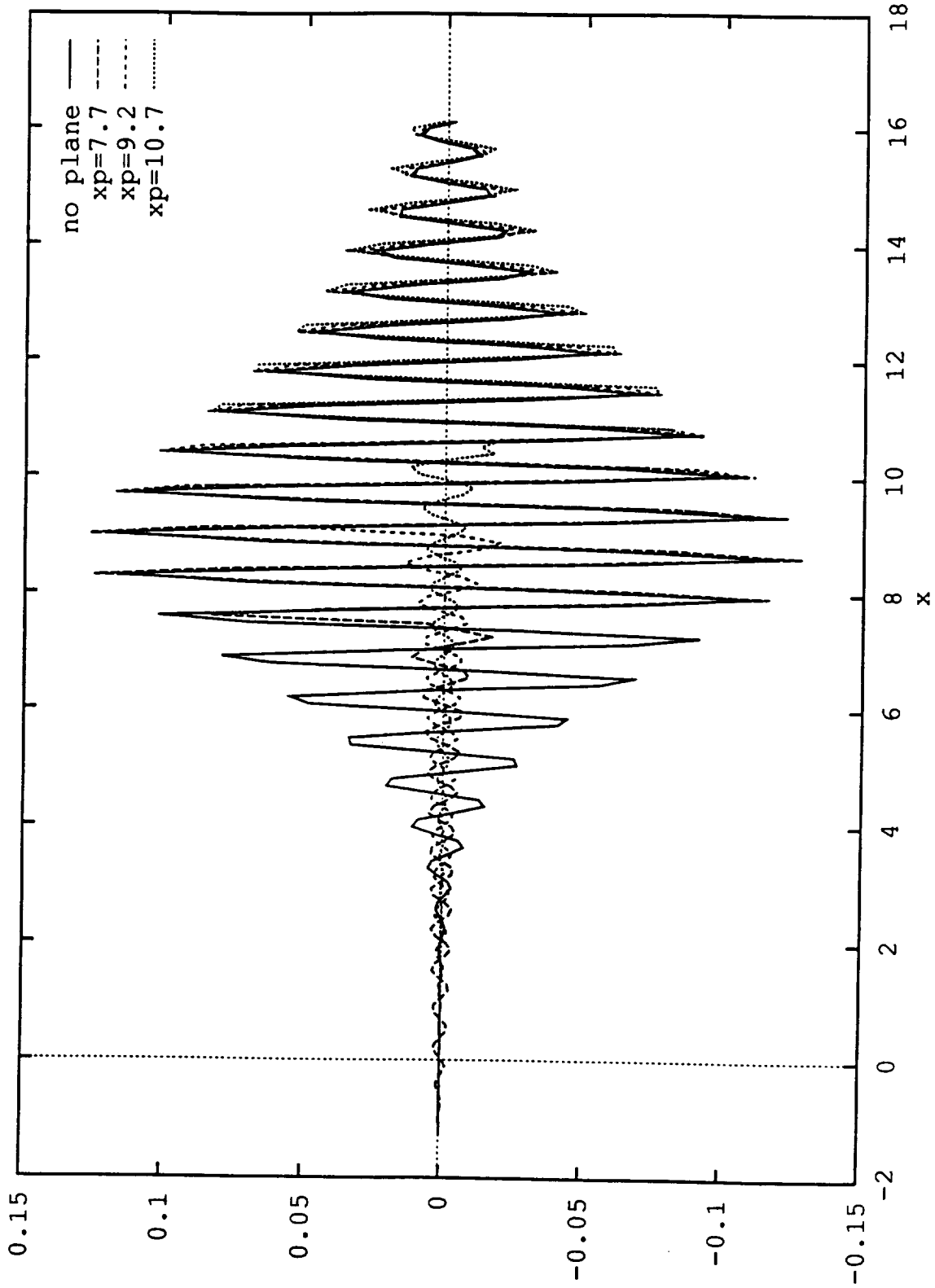

Figure 3.20: Diffracted waves in the half-plane plane $S1$

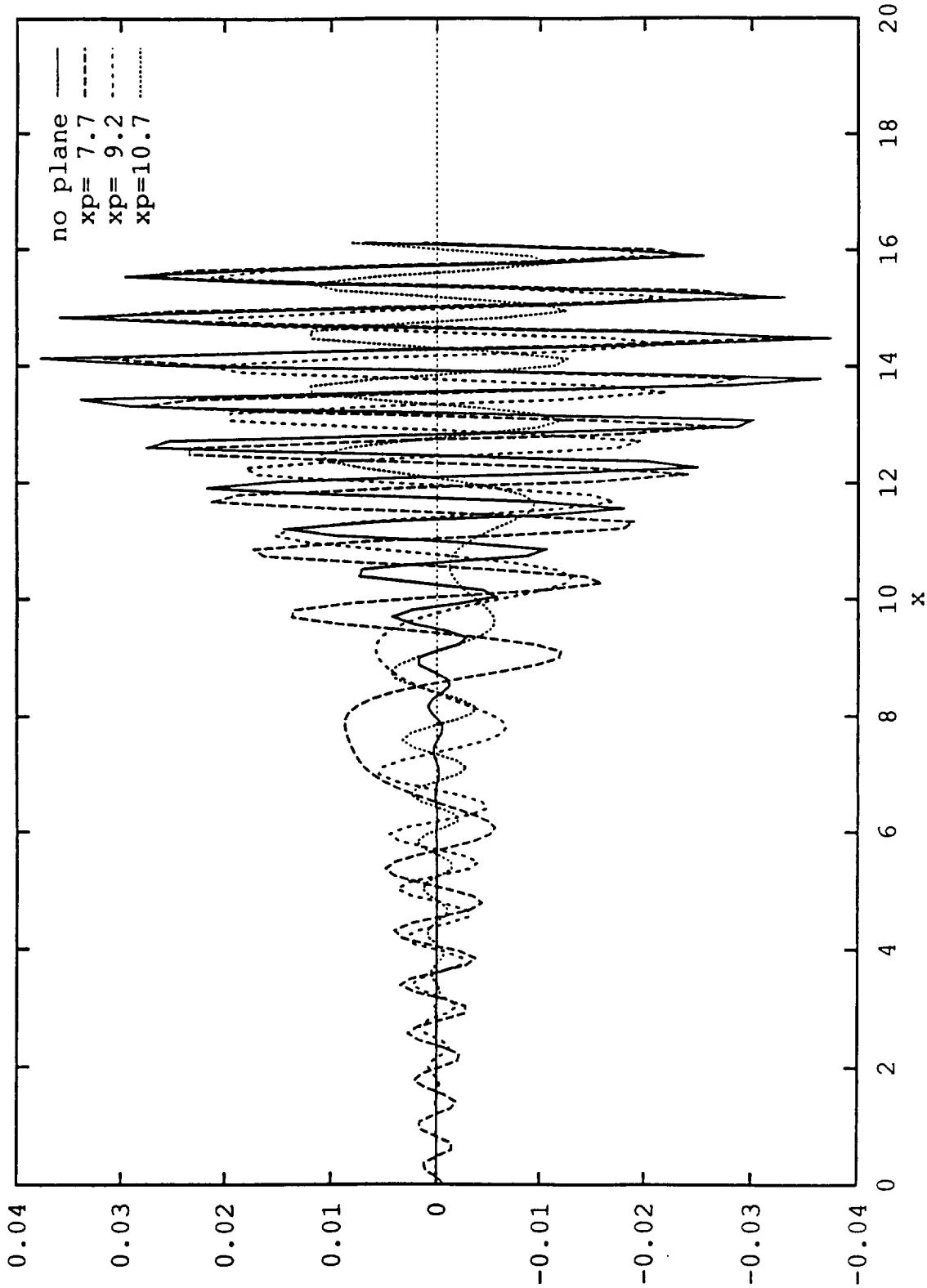

Figure 3.21: Diffracted waves in the far-field (plane $S2$)

downstream the tip of the plane is, the smaller the intensity is. Before drawing a conclusion, one has to remember that only the first diffraction is taken into account in these calculations. When the tip of the plane is moved further downstream, the secondary reflections will become more important. The range on the x-axis over which the wave is not equal to zero also depends on the position of the tip of the plane. The closer it is from the peak of the incident wave, the more the more this range is large. So, the best downstream position for the half-plane seems to be such that the tip is close to the peak of the wave. The redistribution of energy is then strong and, the secondary reflections not too strong.

To look at the influence of the position of the plane from the centerline of the jet, one can take a look at how the incident wave propagates. Away from the centerline, the intensity decreases, the wave is non-zero on a larger range of the x axis. Therefore, the further from the centerline the plane is, the less efficient the diffraction will be. To study in more details the influence of the position from the centerline, one would have to introduce the effect of the shroud on the instability waves.

In summary, part of the noise reduction observed when putting a shroud around a jet, is due to diffraction. Diffraction attenuates the intensity levels of the original wave by sending some of the energy in other directions. This process is greatly influenced by the position of the shroud. For best results, the end of the shroud has to be put exactly at the position of the maximum amplitude of the radiated noise.

Chapter 4

CONCLUSION AND RECOMMENDATIONS

4.1 Conclusion

The diffraction by a half-plane of a given incident wave has been studied. The final goal of this work is to be able to specify an incident wave related to the instability waves of a jet. The problem would then become a simple model problem that studies the diffraction effects, due to a shroud around a jet, on the noise radiation. Unfortunately, such an incident wave does not have a simple form. This had to be taken into account when looking for a way to solve the diffraction problem.

A technique to solve the diffraction problem analytically is the Wiener-Hopf technique. It is based on some properties of the Fourier transform. If the incident wave is a plane wave, the Wiener-Hopf technique provides a simple process to determine the diffracted wave. Unfortunately, when the incident wave becomes more complicated, parts of the analysis become too complex and have to be performed numerically. Therefore, a direct numerical solution is considered. The type of scheme chosen is a finite difference scheme. To ensure accuracy both in time and space, a scheme conserving the dispersion relation is preferred. The Dispersion Relation Preserving (DRP) scheme developed by Tam and Webb [27] is such a scheme.

A description of the numerical model that was implemented has been given. The governing equations are the linearized equation in absence of a mean flow. The main characteristic of the scheme is the fact that only 5 points per wavelength are required to obtain a good resolution. This should be compared with the classical 6th order finite diffrence scheme which performs with the same stencil. The 6th order scheme requires about 6.5 points per wavelengths. Furthermore the DRP scheme is isotropic for as little as 2 points per wavelength. The 6th order scheme requires at least 3 points per wavelength. The DRP scheme represents a net advantage over the 6th order scheme with no additional cost.

The major problem encountered in the implementation of the diffraction problem was the fact that one boundary generating the incident wave needs to let the reflected wave exit the domain. This problem occurs because the problem was solved for the total wave. A common solution would have been to solve only for the diffracted wave. In that case, the wall boundary condition would have to be changed. It would implicitly contain the expression for the incident wave at the wall. But this information might not be available, that is why it was decided to solve for the total wave. The problem with the boundary was solved using a decomposition technique close to the boundary. The total wave was decomposed into the incident wave and the reflected wave. At each time step these two waves were determined independently and then added to reconstruct the total wave. The imposed boundary and the non-reflecting boundary were then decoupled. The technique was used to solve the problem of a

plane wave impinging on a plane. Then it was applied to the diffraction of a plane wave by a half-plane. The results were compared with the analytical solution. The agreement was very good. In the last section, the incident wave was changed to simulate the noise radiation issuing from a supersonic jet. The incident wave was related to the instability waves of the jet. As was noted, only the diffraction effects were considered. In particular, the influence of the shroud on the instability waves has been neglected. It has been found that the radiated noise is redistributed in space because of the diffraction. As can be expected, this leads to a reduction of the noise levels.

4.2 Recommendations

This study was performed by solving the wave equation or linearized wave equation in the absence of a mean flow. It would be interesting to allow for a mean flow. This would lead to a more realistic model in the jet noise case. The only changes in the code would be in the definition of the vectors E and F, in the definition of the radiation conditions and, in the specification of the imposed boundaries. The decomposition technique would stay the same.

Another improvement could be made by changing the shape of the half-plane or its boundary conditions. In the study, it was taken as solid on both sides, and infinitely thin. Changing the plane boundary conditions is a fairly easy task. It only involves changing the calculation of the ghost points around the wall. Changing the thickness

of the wall is a more tedious problem. It requires the changing of the calculation of all the points in the vicinity of the wall.

REFERENCES

[1] S. ASHGAR. Acoustic diffraction by an absorbing finite strip in a moving fluid. *J. Acous. Soc. Am.*, **83** 2:812–816, 1988.

[2] H. ATKINS and J. CASPER. Nonreflective boundary conditions for high-order methods. *AIAA Journal*, **32** 3:512–518, 1994.

[3] A. BAYLISS and E. TURKEL. Radiation boundary conditions for wave-like equations. *Comm. on Pure and Appl. Math.*, **33**:707–725, 1980.

[4] A. BAYLISS and E. TURKEL. Far field boundary conditions for compressible flow. *J. Comput. Phys.*, **48**:182–199, 1982.

[5] J. BAZAR and S. N. KARP. Propagation of plane electromagnetic waves past a shoreline. *J. Res. Natl. Bur. Stand. Sec. D*, **66**:319–334, 1962.

[6] P. J. CLARK, P. BETTESS, G. E. HEARN, and M. J. DOWNIE. The application of finite element analysis to the solution of stokes wave diffraction problems. *International Journal for Numerical Methods in Fluids*, **12**:343–367, 1991.

[7] D. G. CRIGHTON, A. P. DOWLING, J. E. FFOWCS-WILLIAMS, M. HECKL, and F. G. LEPPINGTON. *Modern Methods in Analytical Acoustics.* Springer-Verlag, 1992.

[8] D. G. CRIGHTON and F. G. LEPPINGTON. Scattering of aerodynamic noise by a semi-infinite compliant plane. *J. Fluid Mech.*, **43** part 4:721–736, 1970.

[9] P. H. DAHL and G. V. FRISK. Low-frequency diffraction from a free surface coupled to a semi-infinite elastic surfaces as modeled by sea ice properties. *J. Acous. Soc. Am.*, Supp. 1, **85**:S50, 1989.

[10] P. H. DAHL and G. V. FRISK. Diffraction from the juncture of pressure release and locally reacting half-planes. *J. Acoust. Soc. Am.*, Pt. 1, **90** 2:1093–1100, 1991.

[11] J. E. FFOWCS-WILLIAMS and L. H. HALL. Aerodynamic sound generation by turbulent flow in the vicinity of a scattering half-plane. *J. Fluid Mech.*, **40** part 4 : 657–670, 1970.

[12] R. P. HANSEN. Finite element modeling of infinite domain acoustics problems. Master's thesis, The Pennsylvania State University, 1992.

[13] A. S. IL'INSKII and O. M. MASLOVSKAYA. The finite element method in the problem of diffraction by a periodic structure. *Comput. Maths. Math. Phys.*, **31** 11:57–63, 1991.

[14] P. JUHL. An axisymmetric integral equation formulation for free space non-axisymmetric radiation and scattering of a known incident wave. *Jounal of Sound and Vibration*, **163** 3:397–406, 1993.

[15] Y. KAGAWA, T. TSUCHIYA, T. YAMABUCHI, H. KAWABE, and T. FUJII. Finite element simulation of non-linear sound wave propagation. *Journal of Sound and Vibration*, **154** 1:125–145, 1992.

[16] R. P. KENDIG and S. H. HAYEK. Diffraction by a hard-soft barrier. *J. Acous. Soc. Am*, **70**:1156–1165, 1981.

[17] M. M. S. KHAN, W. H. BROWN, and K. K. AHUJA. Computational aeroacoustics as applied to the diffraction of sound by cylindrical bodies. *AIAA Journal*, **25**:949–956, 1987.

[18] H. S. KIM, J. S. KIM, and H. J. KANG. Acoustic wave scattering from axisymmetric bodies. *Jounal of Sound and Vibration*, **163** 3:385–396, 1993.

[19] S. K. LELE. Compact finite-difference schemes witk spectral-like resolution. *J.Comput. Phys.*, **103**:16–42, 1992.

[20] P. J. MORRIS. Flow charactheristics of the large scale wave-like structure of a supersonic round jet. *Journal of Sound and Vibration*, **53** 2:223–244, 1977.

[21] P. M. MORSE and K. U. INGARD. *Theoretical Acoustics.* Princeton University Press, 1968.

[22] B. NOBLE. *Methods Based on the Wiener-Hopf Technique for the Solution of Partial Differential Equations.* Chelsea Pub., 1988.

[23] A. D. PIERCE. *Acoustics, An Introduction to its Physical Principles and Applications.* Acoustical Society of America, 1981.

[24] A. D. RAWLINS. The solution of a mixed boundary value problem in the theory of diffraction by a semi-infinite plane. *Proc. R. Soc. Lond. A.*, **346**:469–484, 1975.

[25] C. K. W. TAM and Z. DONG. Wall boundary conditions for high order finite difference schemes in computational aeroacoustics. *Theoretical and Computational Fluid Dynamics*, to appear 1993.

[26] C. K. W. TAM and H. SHEN. Direct computation of nonlinear acoustic pulses using high order finite difference schemes. In *AIAA paper 93-4325*, 1993.

[27] C. K. W. TAM and J. C. WEBB. Dispersion-relation-preserving finite difference schemes for computational acoustics. *J. Comput. Phys.*, **107** 2:262–281, 1993.

[28] C. K. W. TAM, J. C. WEBB, and Z. DONG. A study of the short-wave components in computational acoustics. *J. Computational Acoustics*, **1** 1:1–30, 1993.

[29] H. K. TANNA and P. J. MORRIS. The noise from normal-velocity-profile coannular jets. *Journal of Sound and Vibration*, **98** 2:213–234, 1985.

[30] K. VISWANATHAN, P. J. MORRIS, and G. CHEN. Linear instability waves in supersonic jets confined in circular and non-circular ducts. *Journal of Sound and Vibration*, **171** 2:231–253, 1994.

[31] D. W. ZINGG and H. LOMAX. Finite-difference schemes on regular triangular grids. *Journal of Computational Physics*, **108**:306–313, 1993.

THE WIENER-HOPF TECHNIQUE

The aim of the the Wiener-Hopf technique is to solve linear partial differential equations subject to mixed boundary conditions on semi-infinite geometries. An extended discussion of its application to the so-called Sommerfeld half-plane diffraction problem is provide by NOBLE [22]. He described three ways to solve the problem using the Wiener-Hopf technique. The problem can be solved by a dual integral equation approach, formulated as an integral equation or solved using the so-called Jone's method. This last method is relatively straightforward and provides a technique taht may be extended to further problems. Therefore, this is the method described in the following.

The problem is represented in figure 1.1. The incident wave (arrow) impinges on the half-plane with an incidence angle θ. The domain then contains three types of waves: the incident wave, the reflected wave and the diffracted wave. The domains of existence of the incident wave (II) and of the reflected wave (I) are determined by geometric acoustics. The shadow zone (III) contains only the diffracted wave.

Assuming the time factor of the steady-state waves is $e^{-i\omega t}$, the incident wave is

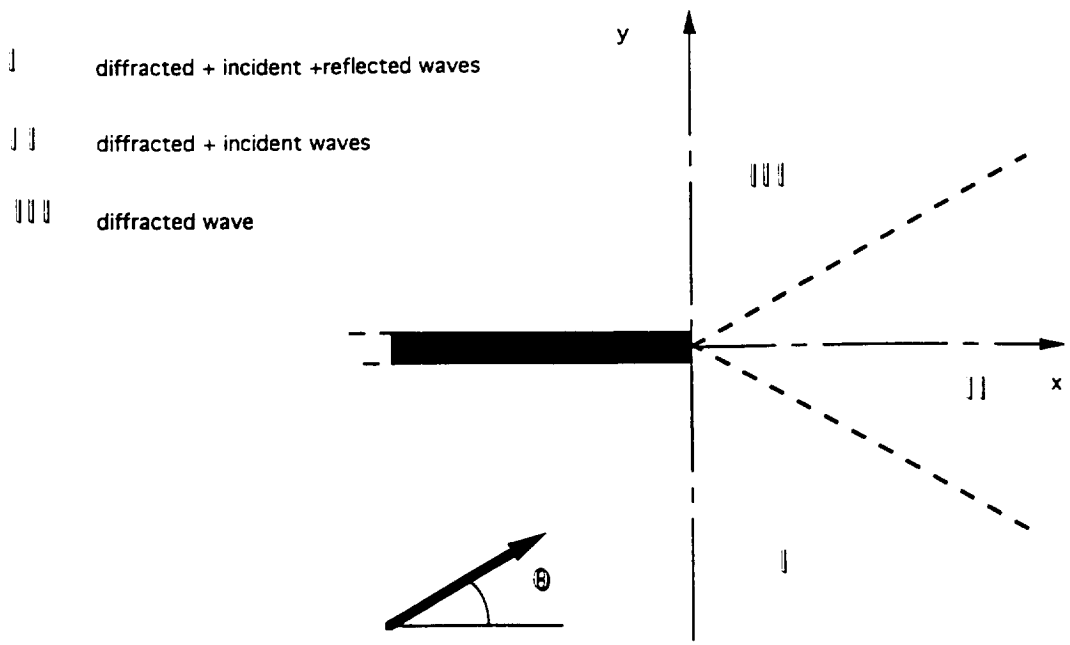

Figure 1.1: Diffraction problem

represented by:

$$\phi_i = \exp[ikx\cos\theta + iky\sin\theta] \tag{1.1}$$

The total field is represented by $\phi_t = \phi_i + \phi$. The function ϕ is an odd function in y. Thus the study may be limited to the region $y \geq 0$.

Then ϕ satisfies the Helmholtz equation:

$$\frac{\partial^2\phi}{\partial x^2} + \frac{\partial^2\phi}{\partial y^2} + k^2\phi = 0 \tag{1.2}$$

The conditions at the wall are defined by:

(i) for $y = 0$ and $x < 0, \frac{\partial\phi_t}{\partial y} = 0$ so $\frac{\partial\phi}{\partial y} = -ik\sin\theta\exp(ikx\cos\theta)$

(ii) for $y = 0$ and any x, $\frac{\partial\phi}{\partial y}$ is continuous

(iii) for $y = 0$ and $x \geq 0$, ϕ is continuous, and since ϕ is odd in y, $\phi(x, 0) = 0$

Some assumptions may be made about the behaviour of ϕ at infinity and near the tip of the plane. Conditions at infinity require cylindrical spreading waves as $x \to \infty$, cancelation of the incident wave plus cylindrically spreading waves as $x \to -\infty$. To ensure that no energy is created at the edge, the following assumptions are made ϕ bounded, $|\nabla\phi| = O(x^\alpha)$, for some $\alpha > -1$ as $x \to \pm 0$.

The following Fourier transform is introduced:

$$\Phi(s, y) = \int_{-\infty}^{\infty} \phi(x, y) e^{isx} dx \tag{1.3}$$

with $\Phi_+ = \int_0^\infty \phi(x, y) e^{isx} dx$, $\Phi_- = \int_{-\infty}^0 \phi(x, y) e^{isx} dx$

A small positive imaginary part is assigned to $k = \overline{k} + i\epsilon$ to improve the convergence of the Fourier integrals. Using the conditions at infinity, Φ_+ is found to be analytic for $s_2 > -\epsilon$, Φ_- for $s_2 < \epsilon \cos\theta$.

The Fourier transform is applied to the Helmholtz equation (1.2). $\Phi(s, y)$ satisfies

$$\frac{d^2\Phi}{dy^2} - \gamma^2 \Phi = 0 \tag{1.4}$$

with $\gamma = (s^2 - k^2)^{1/2}$

The choice of the square root is such that $\Re(\gamma) > 0$. The integration of equation

(1.4) can be performed. Since the solution is bounded as $y \to \infty$,

$$\Phi(s,y) = A(s)e^{-\gamma y} \tag{1.5}$$

At $y = 0$,

$$\begin{aligned} \Phi_+(x,0) + \Phi_-(x,0) &= A \\ \Phi'_+(x,0) + \Phi'_-(x,0) &= -\gamma A \end{aligned} \tag{1.6}$$

The wall conditions (i) and (iii) are defined by:

$$\begin{aligned} \Phi_+(s,0) &= 0 \\ \Phi_-(s,0) &= -\tfrac{k\sin\theta}{k\cos\theta - s} \end{aligned} \tag{1.7}$$

The system of equations (1.6) becomes:

$$\begin{aligned} \Phi_-(x,0) &= A \\ \Phi'_+(s,0) + \gamma\Phi_- &= \tfrac{k\sin\theta}{k\cos\theta - s} \end{aligned} \tag{1.8}$$

The second equation of the system is now rewritten in order to separate $\oplus$ functions, analytic for $s_2 > -\epsilon$, and $\ominus$ functions, analytic for $s_2 < \epsilon\cos\theta$.

The factorization of the kernel γ is straightforward:

$$\gamma = (s^2 - k^2)^{1/2} = \underbrace{(s+k)^{1/2}}_{\gamma_+} \; \underbrace{(s-k)^{1/2}}_{\gamma_-} \tag{1.9}$$

The system of equation (1.8) leads to the following equation:

$$(s+k)^{1/2}\Phi'_+(s,0) + (s-k)^{1/2}\Phi_-(s,0) = \frac{k\sin\theta}{(k\cos\theta - s)\,(s+k)^{1/2}} \tag{1.10}$$

The right hand side (RHS) of this equation has now to be sum decomposed. There is a branch cut in the $\ominus$ region and a pole in the $\oplus$ region. The pole is removed by doing the following arrangement:

$$\left[(k\cos\theta - s)\,(s+k)^{1/2}\right]^{-1} = \underbrace{[k\cos\theta - s]^{-1}\left\{\left[(s+k)^{1/2}\right]^{-1} - \left[(k+k\cos\theta)^{1/2}\right]^{-1}\right\}}_{\oplus}$$

$$+\underbrace{\left[(k+k\cos\theta)^{1/2}\,(k\cos\theta - s)\right]^{-1}}_{\ominus} \tag{1.11}$$

The first term is a $\oplus$ function (with no pole at $k\cos\theta$) and the seconf term is a $\ominus$ function. Finally the equation (1.10) becomes:

$$(s+k)^{1/2}\Phi'_+(s,0) - RHS_- = -(s-k)^{1/2}\Phi_-(s,0) + RHS_- = E(s) \tag{1.12}$$

E(s) is defined analytically over the whole s-plane since each side analytically continues the other. E(s) is determined by the behaviour of ϕ near the discontinuity at $x = 0$. Since $\phi(x,0)$ is bounded as $x \to +0$, the Abelian theorem guaranties that

$\Phi_- = O(1/s)$ as $|s| \to \infty$ $s_2 < \epsilon \cos\theta$. So the left hand side of the equation tends to zero as $|s| \to \infty$ in the lower half-plane. Similarly $[\phi_y(x,0) = O(x^\alpha)$ as $x \to -0$ with $\alpha > -1]$ will imply that the rigth hand side will also tends to zero as $|s| \to \infty$ in th eupper half-plane. Using the Liouville's theorem (ref. [22], 57 ; [7], 167) $E(s) \equiv 0$.

Using the system (1.8) and the equation (1.12), the amplitude $A(s)$ has been determined. Thus, Φ is known. The expression of ϕ is obtained by inversing the Fourier transform:

$$\phi(x,y) = \frac{k^{1/2}\sin\theta}{2\pi\ (1+\cos\theta)^{1/2}} \int_{-\infty}^{\infty} \frac{e^{-\gamma y - isx}}{(s-k\cos\theta)\ (s-k)^{1/2}} ds \tag{1.13}$$

This integral is then expressed in terms of Fresnels integrals defined by $F(v) = \int_v^\infty \exp(iu^2)du$.

$$\phi(x,y) = \pi^{-1/2} e^{i\pi/4} \left[-e^{-ikr\cos(\theta-\Theta)}\ F\left\{ (2kr)^{1/2} \cos\frac{1}{2}(\theta-\Theta) \right\} \right] \tag{1.14}$$

$$\left[+e^{-ikr\cos(\theta+\Theta)}\ F\left\{ (2kr)^{1/2} \cos\frac{1}{2}(\theta+\Theta) \right\} \right]$$

where θ is the angle of incidence

Θ is defined by $x = R\cos\Theta, \quad y = R\sin\Theta$

The Pennsylvania State University

The Graduate School

Department of Aerospace Engineering

INSTABILITY WAVE ANALYSIS OF CONFINED ASYMMETRIC SUPERSONIC JETS USING THE FINITE ELEMENT METHOD

A Thesis in

Aerospace Engineering

by

Chingwei M. Shieh

Submitted in Partial Fulfillment
of the Requirements
for the Degree of

Master of Science

August 1995

ABSTRACT

In this thesis, a novel approach to the solution of linear stability problems is studied. The perturbation equation governing the linear instability waves in supersonic jets is evaluated using a global scheme instead of the traditional shooting method. Typical global schemes such as the finite difference method and the boundary element method have been applied to solve related problems for circular and elliptic jets. To improve the robustness of the calculation for more complex jet exit geometries, the present study makes use of the finite element method (FEM). Different numerical techniques in solving the resulting non-linear matrix eigenvalue problem are studied, and the feasibility of implementing these numerical methods to two-dimensional calculations are assessed.

With the application of the FEM, the characteristics of the instability waves, such as the growth rate, phase velocity, and pressure eigenfunctions, are determined from local solutions of the compressible Rayleigh equation. Further refinement of the calculations is obtained through successive FEM grid generation and local iterative method. Favorable agreement between the FEM results and those from a shooting method is obtained. The effects of varying the shroud geometry on the instability wave characteristics of a confined circular jet are then analyzed. Calculations are also performed for both confined elliptic jets of aspect ratio 2:1 and 3:1 at Mach number 1.5. The effects of confinement on the different classes of instability modes in elliptic jets are documented. The mode that "flaps" about the jet major axis is found to be less influenced by the presence of a shroud than the "varicose" mode that is even about both the jet's major and minor axes.

TABLE OF CONTENTS

LIST OF FIGURES v

LIST OF TABLES ix

NOMENCLATURE x

ACKNOWLEDGMENTS xii

1 INTRODUCTION 1
- 1.1 Experimental Investigations 2
- 1.2 Theoretical and Numerical Analysis 5
- 1.3 Objectives and Scope of Present Study 7

2 MATHEMATICAL FORMULATION 9
- 2.1 General Form of the Compressible Rayleigh Equation 9
- 2.2 Compressible Rayleigh Equation for Axisymmetric Jets 12
- 2.3 Mean Flow Properties 13

3 NUMERICAL SOLUTION TECHNIQUES 15
- 3.1 Shooting Method 15
- 3.2 Finite Element Discretization 17
- 3.3 Numerical Methods for Non-Linear Eigenvalue Problems 21
  - 3.3.1 Linear Companion Matrix Method (LCMM) 22
  - 3.3.2 Matrix Factorization Method (MFM) 23
  - 3.3.3 Local Refinement Method 24
  - 3.3.4 Practical Implementation 25
- 3.4 Contour Deformation 26
- 3.5 Summary 29

4 RESULTS AND DISCUSSIONS 30
- 4.1 Circular Jets in Circular Shroud 30
- 4.2 Validation of FEM Stability Codes 43
- 4.3 Circular Jets in Non-Circular Shroud 46
- 4.4 Elliptic Jets in Circular Shroud 62

5 CONCLUSIONS AND FUTURE RESEARCH 69
- 5.1 Conclusions 69

5.2 Suggestions for Future Research 72

REFERENCES 73

A APPROPRIATE CHOICES OF BRANCH CUTS 79

B LOCAL ELEMENT MATRICES 82

B.1 One-Dimensional Linear Line Element 82

B.2 Two-Dimensional Linear Triangular Element 83

LIST OF FIGURES

1.1 Schematic representations of (a) the nearly quasi-periodic shock-cell system down stream of the jet flow, and (b) the shock-associated noise generation mechanism as Mach wave radiation. 5

2.1 Cylindrical coordinate system in (r, θ, z). 12

3.1 The cross-section and discretization of the solution domain. 18

3.2 A schematic of the choice of branch cut for the logarithmic function and the location of the critical point, ζ_c. 27

3.3 A schematic of the detoured integration contour. 28

4.1 A schematic of the mean flow velocity profile of a jet. 31

4.2 Variation of axial growth rate of the Kelvin-Helmholtz instabilities with Strouhal number for a confined and unconfined axisymmetric jet. $M_j = 4.0$, unheated, $b = 0.1$. (a) $n = 0$ axisymmetric mode, (b) $n = 1$ helical mode. . 32

4.3 Pressure perturbation amplitude of the Kelvin-Helmholtz and the supersonic instability waves. $M_j = 4.0$, unheated, $b = 0.1$, $r_w = 2.0$, $n = 0$ mode. . . . 34

4.4 Pressure perturbation amplitude of the Kelvin-Helmholtz and the supersonic instability waves. $M_j = 4.0$, unheated, $b = 0.1$, $r_w = 2.0$, $n = 1$ mode. . . . 34

4.5 Variation of axial growth rate with Strouhal number in a confined axisymmetric jet. $M_j = 4.0$, unheated, $b = 0.1$, $r_w = 2.0$, $n = 0$ mode. 35

4.6 Variation of axial phase speed with Strouhal number in a confined axisymmetric jet. $M_j = 4.0$, unheated, $b = 0.1$, $r_w = 2.0$, $n = 0$ mode. 35

4.7 Variation of axial growth with Strouhal number in a confined axisymmetric jet. $M_j = 4.0$, unheated, $b = 0.1$, $r_w = 2.0$, $n = 1$ mode. 36

4.8 Variation of axial phase speed with Strouhal number in a confined axisymmetric jet. $M_j = 4.0$, unheated, $b = 0.1$, $r_w = 2.0$, $n = 1$ mode. 36

4.9 Variation of axial growth rate with Strouhal number at different azimuthal modes. $M_j = 4.0$, unheated, $b = 0.1$, $r_w = 2.0$, Kelvin-Helmholtz instability waves. 37

4.10 Variation of axial growth rate with Strouhal number at different azimuthal modes. $M_j = 4.0$, unheated, $b = 0.1$, $r_w = 2.0$. supersonic instability waves. 37

4.11 Pressure perturbation amplitude of the $n = 0$ axisymmetric Kelvin-Helmholtz instability waves at various Strouhal numbers. 39

4.12 Pressure perturbation amplitude of the $(0, 1)$ axisymmetric supersonic instability waves at various Strouhal numbers. 39

4.13 Pressure perturbation amplitude of the $(0,2)$ axisymmetric supersonic instability waves at various Strouhal numbers. 40
4.14 Pressure perturbation amplitude of the $n = 1$ helical Kelvin-Helmholtz instability waves at various Strouhal numbers. 40
4.15 Pressure perturbation amplitude of the $(1,1)$ helical supersonic instability waves at various Strouhal numbers. 41
4.16 Pressure perturbation amplitude of the $(1,2)$ helical supersonic instability waves at various Strouhal numbers. 41
4.17 The effect of outer wall radius on the growth rates of the (1,KH) and (1,1) modes at (a) $St = 0.11$, and (b) $St = 1.50$. $M_j = 4.0$, $b = 0.1$, unheated jet. 42
4.18 The amplitude of the pressure eigenfunction distribution of a helical Kelvin-Helmholtz (1,KH) instability mode at $M_j = 4.0$, $b = 0.1$, $St = 1.50$, unheated jet. 42
4.19 Eigenvalue spectrum in the complex wavenumber plane for a circular confined jet. $M_j = 1.5$, unheated, $b = 0.1$, $r_w = 2.0$. 44
4.20 Variation of axial growth rate with Strouhal number in a confined circular jet. $M_j = 1.5$, unheated, $b = 0.1$, $r_w = 2.0$. 47
4.21 Variation of axial phase speed with Strouhal number in a confined circular jet. $M_j = 1.5$, unheated, $b = 0.1$, $r_w = 2.0$. 47
4.22 Variation of axial growth rate with Strouhal number in a confined circular jet with complex integration contour deformation. $M_j = 1.5$, unheated, $b = 0.1$, $r_w = 2.0$. 48
4.23 Variation of axial growth rate with Strouhal number for the (1,KH) instability mode in a confined circular jet with complex integration contour deformation. $M_j = 4.0$, unheated, $b = 0.1$, $r_w = 2.0$. 48
4.24 A semi-unstructured triangular finite element grid. 49
4.25 Contour plot of the perturbation pressure amplitude for $n = 0$ Kelvin-Helmholtz instability at $St = 0.50$. $M_j = 1.5$, unheated, $b = 0.1$, $r_w = 2.0$. . 49
4.26 Contour plot of the perturbation pressure amplitude for $n = 2$ helical Kelvin-Helmholtz instability at $St = 0.50$. $M_j = 1.5$, unheated, $b = 0.1$, $r_w = 2.0$. . 50
4.27 Perturbation pressure amplitude for $n = 0$ Kelvin-Helmholtz instability at $St = 0.50$ along the x- and y-axis. $M_j = 1.5$, unheated, $b = 0.1$, $r_w = 2.0$. . 50
4.28 Perturbation pressure amplitude for $n = 2$ helical Kelvin-Helmholtz instability at $St = 0.50$ along the x- and y-axis. $M_j = 1.5$, unheated, $b = 0.1$, $r_w = 2.0$. 51
4.29 Comparison of the growth rate curves from the shooting code and FEM2D for different Kelvin-Helmholtz azimuthal modes. $M_j = 1.5$, unheated, $b = 0.1$, $r_w = 2.0$. 51

4.30 Comparison of the phase speed curves from the shooting code and FEM2D for different Kelvin-Helmholtz azimuthal modes. $M_j = 1.5$, unheated, $b = 0.1$, $r_w = 2.0$. 52
4.31 A locally equilateral unstructured triangular finite element grid. 53
4.32 Effects of varying the shroud geometry on the axial growth rate of the $n = 0$ and $n = 2$ Kelvin-Helmholtz instability modes. $M_j = 4.0$, unheated, $b = 0.1$. 54
4.33 Contours of the amplitude of the pressure fluctuation for the $n = 0$ axisymmetric Kelvin-Helmholtz mode. $M_j = 4.0$, unheated, $b = 0.1$, $St = 0.50$, $AR = 1.0$. 56
4.34 Contours of the amplitude of the pressure fluctuation for the $n = 0$ axisymmetric Kelvin-Helmholtz mode. $M_j = 4.0$, unheated, $b = 0.1$, $St = 0.50$, $AR = 1.1$. 56
4.35 Contours of the amplitude of the pressure fluctuation for the $n = 0$ axisymmetric Kelvin-Helmholtz mode. $M_j = 4.0$, unheated, $b = 0.1$, $St = 0.50$, $AR = 1.2$. 57
4.36 Contours of the amplitude of the pressure fluctuation for the $n = 0$ axisymmetric Kelvin-Helmholtz mode. $M_j = 4.0$, unheated, $b = 0.1$, $St = 0.50$, $AR = 1.3$. 57
4.37 Contours of the amplitude of the pressure fluctuation for the $n = 0$ axisymmetric Kelvin-Helmholtz mode. $M_j = 4.0$, unheated, $b = 0.1$, $St = 0.50$, $AR = 1.4$. 58
4.38 Contours of the amplitude of the pressure fluctuation for the $n = 0$ axisymmetric Kelvin-Helmholtz mode. $M_j = 4.0$, unheated, $b = 0.1$, $St = 0.50$, $AR = 1.5$. 58
4.39 Contours of the amplitude of the pressure fluctuation for the $n = 2$ helical Kelvin-Helmholtz mode. $M_j = 4.0$, unheated, $b = 0.1$, $St = 0.50$, $AR = 1.0$. 59
4.40 Contours of the amplitude of the pressure fluctuation for the $n = 2$ helical Kelvin-Helmholtz mode. $M_j = 4.0$, unheated, $b = 0.1$, $St = 0.50$, $AR = 1.1$. 59
4.41 Contours of the amplitude of the pressure fluctuation for the $n = 2$ helical Kelvin-Helmholtz mode. $M_j = 4.0$, unheated, $b = 0.1$, $St = 0.50$, $AR = 1.2$. 60
4.42 Contours of the amplitude of the pressure fluctuation for the $n = 2$ helical Kelvin-Helmholtz mode. $M_j = 4.0$, unheated, $b = 0.1$, $St = 0.50$, $AR = 1.3$. 60
4.43 Contours of the amplitude of the pressure fluctuation for the $n = 2$ helical Kelvin-Helmholtz mode. $M_j = 4.0$, unheated, $b = 0.1$, $St = 0.50$, $AR = 1.4$. 61
4.44 Contours of the amplitude of the pressure fluctuation for the $n = 2$ helical Kelvin-Helmholtz mode. $M_j = 4.0$, unheated, $b = 0.1$, $St = 0.50$, $AR = 1.5$. 61
4.45 Appropriate boundary conditions to simulate the four general classes of instability wave. 63

4.46 Contours of the pressure perturbation amplitude of the ce_0, varicose mode. Elliptic jet, $M_j = 1.5$, unheated, $b_A = b_B = 0.2$, $r_w = 4.0$, $AR = 3$. 65
4.47 Contours of the pressure perturbation amplitude of the se_1, flapping mode. Elliptic jet, $M_j = 1.5$, unheated, $b_A = b_B = 0.2$, $r_w = 4.0$, $AR = 3$. 65
4.48 Variation of axial growth rate of ce_0 varicose mode with Strouhal number. Elliptic jet, $M_j = 1.5$, unheated, $b_A = b_B = 0.2$, $r_w = 4.0$, $AR = 2$. 66
4.49 Variation of axial growth rate of ce_0 varicose mode with Strouhal number. Elliptic jet, $M_j = 1.5$, unheated, $b_A = b_B = 0.2$, $r_w = 4.0$, $AR = 3$. 66
4.50 Variation of axial growth rate of se_1 flapping mode with Strouhal number. Elliptic jet, $M_j = 1.5$, unheated, $b_A = b_B = 0.2$, $r_w = 4.0$, $AR = 2$. 67
4.51 Variation of axial growth rate of se_1 flapping mode with Strouhal number. Elliptic jet, $M_j = 1.5$, unheated, $b_A = b_B = 0.2$, $r_w = 4.0$, $AR = 3$. 67
4.52 Variation of axial phase velocity of ce_0 varicose mode with Strouhal number. Elliptic jet, $M_j = 1.5$, unheated, $b_A = b_B = 0.2$, $r_w = 4.0$. 68
4.53 Variation of axial phase velocity of se_1 flapping mode with Strouhal number. Elliptic jet, $M_j = 1.5$, unheated, $b_A = b_B = 0.2$, $r_w = 4.0$. 68

A.1 Mapping of the branch cut from χ-plane to λ_2-plane. 81

B.1 Linear line element shape function. 83
B.2 Linear triangular element shape function. 84

LIST OF TABLES

3.1 Memory requirement of different numerical schemes. 26

4.1 Convergence history of the axisymmetric Kelvin-Helmholtz instability mode with number of grid points, N. $M_j = 1.5$, unheated, $b = 0.1$, $r_w = 2.0$, $St = 0.50$. The wavenumber obtained by the shooting method is $(2.1847164, -0.85869151)$. 43

4.2 Comparison of results from shooting code and FEM2D for different azimuthal modes. 46

4.3 Effects of varying the shroud geometry on the $n = 0$ axisymmetric mode. . 52

4.4 Effects of varying the shroud geometry on the $n = 2$ helical mode. 53

NOMENCLATURE

A	semi-major jet axis
A_e	area of a linear triangular element
a	speed of sound
B	semi-minor jet axis
b	mixing layer half-width
b_A	mixing layer half-width on the jet major axis
b_B	mixing layer half-width on the jet minor axis
$\mathbf{C_i}$	global element matrices, where $i = 0, 1, \ldots 3$
c	phase speed
$\mathbf{D}$	λ-matrix, or matrix polynomial
F_l	piece-wise constant coefficients of f
f	coefficients of the compressible Rayleigh equation
G_j	piece-wise constant coefficients of g
g	test function
$H_n^{(1)}$	Hankel function of the first kind of integer order n
$H_n^{(2)}$	Hankel function of the second kind of integer order n
h	potential core radius
h_A	potential core radius on the jet major axis
h_B	potential core radius on the jet minor axis
$\mathbf{I}$	identity matrix
J_n	Bessel function of the first kind of integer order n
$\mathbf{K_i}$	local element matrices, where $i = 1, 2, \ldots 5$
M	number of basis functions
M_j	jet exit Mach number
N	number of discretization points
$\hat{\mathbf{n}}$	outward normal
n	azimuthal mode number
$\hat{P}_i$	nodal values of $\hat{p}$
p	instantaneous static pressure
R	velocity ratio
R_j	equivalent jet radius
r_w	radius of the outer wall
$\mathbf{S}$	dominant solvent of $\mathbf{D}$
s	transformation factor
T	temperature

T_j	static temperature of the jet
T_2	static temperature of the external flow
T_∞	stagnation temperature of the ambient air
t	time
u	x-component of instantaneous velocity
v	y-component of instantaneous velocity
W_j	axial jet velocity
W_2	velocity of the external flow
w	z-component of instantaneous velocity
$\mathbf{Y}$	solvent or factor of $\mathbf{D}$
x, y, z	Cartesian coordinate system
r, θ, z	cylindrical coordinate system
η, ξ, z	elliptic coordinate system

Greek:

α	complex axial wavenumber
Γ	solution boundary
γ	ratio of specific heat constants
κ	distance from the origin to the focus of an ellipse
$\mathcal{L}$	differential operator
μ	transformed eigenvalue
Ω	solution domain
ω	real radian frequency
ϕ	shape function
ρ	instantaneous density
ρ_j	density of the jet
ρ_2	density of the ambient air
σ	eigenvalue spectrum

Superscripts/Subscripts:

$*$	dimensional quantity
$-$	mean quantity
$'$	fluctuating quantity
$\hat{}$	eigenfunction of the fluctuating quantity
i, j, k	summation indices in Cartesian tensor notation

ACKNOWLEDGMENTS

I would like to express my heartfelt appreciation to my thesis advisor, Dr. P. J. Morris, for his constant support and guidance throughout this work. Gratitude is also extended to Dr. L. N. Long for taking his time to review my thesis. I would also like to take this opportunity to thank Mr. L.-S. Lee, Mr. D. P. Lockard, and Mr. M. T. Mendonca for the discussions we had, and for giving me a helping hand when I needed it the most. Most of all, I would like to thank my parents. Without them, this opportunity would not be possible.

This work was partially supported by NASA Langley Research Center under Grant No. NAG-1-1047. The technical monitor is Dr. J. M. Seiner.

Chapter 1

INTRODUCTION

In 1986, studies initiated by NASA and the U.S. aerospace industry indicated a potential market for a long-range supersonic civil aircraft. All of these studies concluded that significant advances in technology would have to be achieved in order to develop this new generation of commercial aircraft, referred to as the High Speed Civil Transport (HSCT). While the development of the Concorde was a tremendous technological achievement, the HSCT is proposed to fly nearly twice the distance, carry three times as many passengers, and operate economically in both subsonic and supersonic regimes. However, with the new FAR 36-Stage 3 noise emission standard for subsonic transport aircraft, a 20-dB sideline noise reduction, or a 75% decrease in perceived loudness compared to the Concorde, is required of the HSCT. This poses a challenge that has to be addressed before the HSCT can be fully operational.

At the same time, the consideration of a new propulsion system utilizing supersonic combustion (SCRAMJET) for the future hypersonic aircraft, the National Aerospace Plane (NASP), has created a renewed interest in the studies of supersonic mixing processes. Many problems need to be overcome to make this propulsion system viable. For example, there are stringent regulations of the emission levels that will be required of the NASP. This is due to a heightened awareness of the potential impact of the NASP on the environment, in particular, the effects of the jet exhaust on ozone depletion. In addition, rapid mixing must be encouraged to minimize the engine length and weight.

It has been observed that rapid mixing of exhaust plumes with co-flowing air can lead to jet noise reduction. Moreover, as noted above, the SCRAMJET propulsion concept depends on rapid mixing of the air/fuel mixture in order to minimize combustor size and increase engine efficiency. Besides, with enhanced mixing, a high local peak temperature can be avoided, and the residence time for chemical reactions may be reduced. This results in a decrease in nitrous oxide formation, a primary cause of stratospheric ozone depletion. All this evidence shows that mixing enhancement of jets and shear layers offers an attractive solution to problems involving engine efficiency, exhaust emissions, and jet noise radiation. However, due in part to the incapability of disturbances to travel upstream in supersonic flows, supersonic shear layers are inherently more stable, and this leads to a decrease in mixing. Therefore, before mixing augmentation techniques can be developed for supersonic shear layers, detailed studies on the mixing characteristics of such flows have to be performed.

1.1 Experimental Investigations

The existence of large-scale coherent structures was observed experimentally in turbulent mixing layers at subsonic speeds by Brown and Roshko [1]. These large-scale structures may be viewed as co-rotating vortices that are initiated by the Kelvin-Helmholtz instability. Their amalgamation causes the shear layer to grow in the downstream flow direction. However, as the free-stream Mach number increases and becomes supersonic, the growth rate of the mixing layer decreases. While density ratio does play a role in the spreading rate, it is a relatively small effect compared to the effect of increasing Mach number. Therefore, Brown and Roshko [1] deduced that the trend of decreasing growth rate of the mixing layer as the Mach number increases is due to compressibility effects in the shear layer. To describe the effects of compressibility accurately, a new frame of reference that travels with the large-scale eddies was proposed by Papamoschou and Roshko [2]. Within this convective frame of reference, they defined a compressibility-correlation parameter called the convective Mach number and showed that the reduction in growth rate is indeed a compressibility phenomenon.

Similar large-scale coherent structures had also been observed in the mixing layers of axisymmetric jets by Crow and Champagne [3], Yule [4], and Dimotakis *et al.* [5] among others. Using hot-wire measurements, it was shown by McLaughlin *et al.* [6, 7], Troutt [8], and Troutt and McLaughlin [9] that the large-scale turbulent structures in the mixing layers of supersonic jets are in the form of instability waves. Moreover, at low and moderate Reynolds number, these large-scale turbulent structures are coherent and quasi-periodic over many jet diameters.

Jets have multiple azimuthal instability modes, equivalent to the oblique or three-dimensional modes in plane shear layers. These modes, in a circular jet, are referred to as "spinning modes." These multiple modes are more pronounced if the jet is asymmetric. In three-dimensional jets, the interesting phenomenon of axis switching that is not present in axisymmetric jets has been observed by Sforza *et al.* [10] and Sfeir [11] in their studies of three-dimensional jets from rectangular nozzles. This phenomenon is due to the different spreading rates in the major and minor axis planes, resulting in a cross-over point some distance downstream from the nozzle. The same phenomenon has also been observed in the case of the elliptic jet. Other experimental studies have been carried out: on subsonic small-aspect-ratio elliptic jets by Ho and Gutmark [12]; on controlled excitation of subsonic elliptic jets by Hussain and Husain [13, 14] and Gutmark and Ho [15]; on the dynamics and evolution of the large-scale coherent structures in elliptic air and water jets at low speeds by Husain and Hussain [16, 17]; on supersonic underexpanded elliptic and rectangular jets by Gutmark *et al.* [18, 19]; on mixing characteristics of high-aspect-ratio rectangular jets by Krothapalli *et al.* [20, 21] and Grandmaison *et al.* [22]; and on instability modes of low-aspect-ratio rectangular jets by Shih *et al.* [23] among others.

Measurements made by single hot-wire and cross-wire probes [12] indicate that the spreading characteristics in the two axis planes of the elliptic jet are quite different. While the shear layer spreads into the potential core in the major axis plane, spreading occurs into the stationary surroundings in the minor axis plane. Moreover, unlike two-dimensional mixing layers, axisymmetric jets or plane jets, there may be a continuous variation of momentum thickness around the elliptic nozzle, which introduces a non-uniform length-scale and complicates the instability wave development in the shear layer. There is also a significant increase of mass entrainment in an elliptic jet, as compared to that of a circular jet or a two-dimensional plane jet. The obvious parameter that influences the spreading enhancement is the aspect ratio, and the mechanism of this entrainment is due to the azimuthal distortion of the elliptic vortices or large structures caused by self-induction. Other flow properties, such as the turbulence intensities and Reynolds stress, are also very different in the major and minor axis planes, due to the asymmetric development of the large structures.

Under small excitation, elliptic jets respond at a preferred mode that may be defined as the non-dimensional frequency at which the fundamental r.m.s. longitudinal fluctuation velocity is mostly amplified [13, 14, 17]. The location at which axis switching occurs moves further upstream due to the excitation, and the spreading rate is increased dramatically in the minor axis plane. The jet cross-sectional area, mixing rate, and turbulence intensity are all enhanced through excitation. Moreover, flow visualization using dye traces [15, 14] shows that the large-scale vortices in the elliptic jets remain centered on the jet axis during evolution, and confirms mixing augmentation at both large- and fine-scales.

Similar flow characteristics from rectangular jets have also been observed by Sforza *et al.* [10], Krothapalli *et al.* [20] and Grandmaison *et al.* [22]. Besides axis switching, the velocity flow field can be differentiated into three distinct regions: the potential core region; the two-dimensional region; and the axisymmetric region. In the near field region of high-aspect-ratio jets, the flow is characterized by the presence of a saddle-back profile in the major axis plane. Some flow properties, such as spreading rates, are increased as compared to a round jet emanating from a nozzle of the same equivalent diameter. Other properties, like entrainment, do not exhibit significant improvement from those of two-dimensional flows when a large-aspect-ratio nozzle is used in the experiments.

Unlike subsonic jets, the flow field of supersonic underexpanded elliptic and rectangular jets are more complicated because of the presence of shock-cell structures. Using a spark schlieren photography technique, Krothapalli *et al.* [21], Gutmark *et al.* [18, 19, 24], and Shih *et al.* [23] observed the flapping motion of the large-scale structures in elliptic and rectangular jets at moderate Mach numbers. For the case of elliptic jets, as the Mach number increases, the spreading rate in the minor axis plane is enhanced, while the jet width in the major axis plane is reduced. Due to the thinner initial shear layer in the minor axis plane

of the jet, which results in a higher initial vorticity, the turbulence intensity in the minor axis plane increases dramatically. On the other hand, the Strouhal number of the preferred mode decreases as the Mach number increases. The presence of multiple instability peaks is also seen, similar to observations made in earlier studies [6]. The near-field pressure of the underexpanded jet is modified by the interaction between the shock-cell structures and the large-scale eddies, which results in higher pressure fluctuation levels. Mixing enhancement, which is observed in the subsonic jets, is greater in supersonic underexpanded jets. This is a consequence of an augmented self-induction mechanism due to the shock-cell and large-scale eddy interaction.

Observations made from experimental studies indicate that the use of three-dimensional jets is a promising technique in the control of mixing. The main advantage of using three-dimensional jets is that they are passive control devices, that involve less moving parts compared to those needed for active control. The advances in passive and active control of mixing layers have been reviewed recently by Schadow and Gutmark [25], Yu *et al.* [26], and Gutmark [27]. However, apart from mixing enhancement, elliptic and rectangular jets have also found many aeronautical applications in V/STOL aircraft, thrust-vectoring nozzles for high maneuverability planes and, most recently, supersonic jet noise reduction [28].

There is a close relation between mixing enhancement and jet noise reduction. In the pioneering work by Lighthill [29, 30], the turbulence in the mixing layers of jets was identified as a source of noise generation due to the fluctuating turbulent momentum flux. He proposed that the intensity of the noise scales as the eighth power of the jet velocity. Therefore, a naive argument would suggest that an increase in spreading rate of the jet would reduce the jet velocity, and consequently suppress noise radiation. However, though this argument has led to the successful development of subsonic jet noise suppressions, it may not apply so directly to supersonic jets. For example, from the experimental investigation by Krothapalli *et al.* [31], it was shown that a supersonic diamond jet exhibits striking features such as "corrugated" structures and lobed, large-scaled vertices, indicating the presence of streamwise vorticity. However, despite the presence of these distinct features in the flow field and the turbulent nature of the mixing layers, the far-field noise characteristics are quite similar to the corresponding axisymmetric jet. This observation further indicates that for supersonic jets, noise reduction cannot be simply achieved by reducing the jet velocity.

It is now generally recognized that there are three principal components of supersonic jet noise. They are the turbulent mixing noise, the broadband shock-associated noise, and screech [32]. For the latter two noise sources to exist, the jet must be imperfectly expanded so that it is shock containing. Due to the imperfect expansion of supersonic jets, a nearly periodic shock-cell system (as shown in Figure 1.1a) develops in the jet downstream of the nozzle exit. The large-scale coherent structures in the mixing layers of the supersonic jet interact with this shock-cell system as they propagate downstream, and shock-associated

noise is generated in the form of upstream traveling Mach wave radiation, as shown in Figure 1.1b.

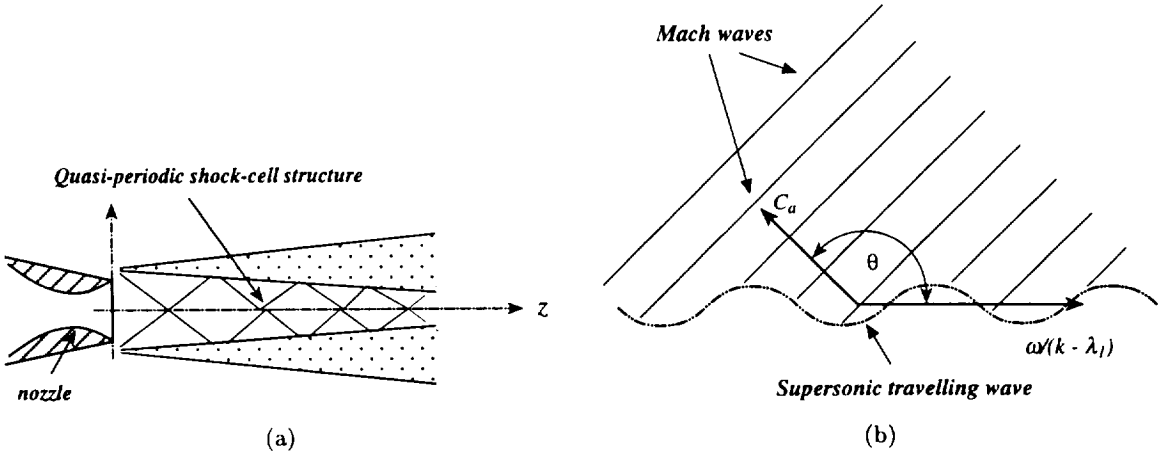

Figure 1.1. Schematic representations of (a) the nearly quasi-periodic shock-cell system down stream of the jet flow, and (b) the shock-associated noise generation mechanism as Mach wave radiation.

In supersonic underexpanded elliptic and rectangular jets, the near acoustic field was observed by Krothapalli *et al.* [21] and Gutmark *et al.* [19, 24] using a spark schlieren photography technique. Also, the overall sound pressure level is decreased significantly as compared to that of an axisymmetric jet (Kinzie and McLaughlin [33]). As the shock-associated noise propagates upstream, the acoustic waves modify the shear layer evolution near the nozzle exit, and may form a feed-back loop. This resonant interaction between the shock-associated noise and the large-scale turbulent eddies produces intense screech tones, and augments the spreading rate of the jets. This shock system/large coherent structure interaction becomes particularly significant in ducted jets since acoustic waves reflected from the shroud can further modify the shear layer evolution and enhance mixing. This is an alternative passive mixing enhancement technique.

1.2 Theoretical and Numerical Analysis

Analyses of large-scale turbulent structures based on linear stability theory (LST) have shown remarkable agreement with experimental results. The trend of decreasing instability of axisymmetric and helical modes in circular jets with an increase in Mach number was predicted by Michalke [34]. To study the instability characteristics of the growing and decaying modes of a slowly diverging turbulent shear layer, Tam and Morris [35] performed an inviscid calculation using a multiple-scale expansion model. In order to avoid the presence of singularities in the problem as the branch cut crosses the real axis, a complex integration contour deformation was used. It was shown that this method can produce the analytical continuation of the viscous, Orr-Sommerfeld solution in the limit of infinite Reynolds number, without the intensive computational effort needed to carry out a viscous

analysis. Later, a stochastic model was developed by Plaschko [36, 37] to calculate the statistical properties of the coherent turbulent structures in circular jets. Favorable agreement between the numerical predictions and experimental results were obtained.

To investigate the stability characteristics of elliptic jets, Morris and Miller [38] re-cast the problem in a natural orthogonal elliptic coordinate system, and solved the governing equation with a vortex sheet approximation for the jet flow. This work was later extended to include finite thickness shear layer effects [39], and the effects of compressibility with a realistic mean flow profile [40]. Four classes of instability wave modes were identified: ce_{2n} (varicose mode), se_{2n+1} (flapping mode), ce_{2n+1} (wagging mode), and se_{2n+2}. The flapping motion of elliptic jets have been observed in many experimental studies [21, 19, 24, 41, 23]. Similar investigations have been carried out by Tam and Thies on the instability of rectangular jets [42] using a vortex sheet model.

Extending their work on the instability wave characteristics of supersonic elliptic jets, Morris and Bhat [43] calculated the noise generated from supersonic elliptic jets by matching the inner instability wave solution with the outer acoustic solution in an intermediate region. The predicted overall sound pressure level and directivity compared favorably with experimental data. Similar analyses have been carried out by Tam and Burton [44, 45] on the radiation of sound by two-dimensional shear layers and axisymmetric jets.

In a series of studies by Koshigoe and Tubis [46], the characteristics of wave structures in jets of arbitrary shape were investigated using a linear spatial instability analysis. A Green function technique was used to carry out the instability analysis, instead of a typical shooting method utilizing a Runge-Kutta integration scheme. Using the Green function technique, the rigid restriction on the velocity profile, in order to ensure a separable form for the Rayleigh equation, is eliminated. Both circular and elliptic incompressible inviscid jets were studied, and in the case of elliptic jets, numerical results were compared with those previously calculated from the separable solutions of the Rayleigh equation in elliptic coordinates [38]. To reduce the computational time required for the integral-equation (Green function) approach, a generalized shooting method was developed by Koshigoe and Tubis [47]. This method was later used to study the stability characteristics of triangular jets [48].

Due to the recent interest in the passive control of supersonic jets and shear layers using dump combustors or ejector shrouds, the stability characteristics of confined supersonic jets and mixing layers was examined by Tam and Hu [49]. Using both a vortex sheet approximation and finite thickness shear layer model, two classes of supersonic instability wave modes and two neutral acoustic wave modes were identified at supersonic convective Mach numbers. Further investigations were performed by Viswanathan *et al.* [50] on the stability characteristics of ducted jets. In their analysis, a boundary element method was used to solve the perturbation equation and the effects of changes in the duct geometry

were examined.

With recent advances in computer technology, it is now feasible to investigate the mixing characteristics and noise generation mechanisms of supersonic jets and shear layers using direct numerical simulation (DNS). In studies based on LST, certain assumptions on the flow properties have to be made in order to perform the analysis. Moreover, mean flow quantities such as the velocity and density have to be specified *a priori*. Such stringent requirements are not needed in DNS, so it is possible to study flows that contain complex phenomena. Calculations on jet turbulence noise for both circular and rectangular jets have been performed by Berman*et al.* [51]. The phenomenon of axis switching has also been simulated in the studies by Grinstein [52] and Zaman [53]. Chyczewski and Long [54] extended the calculations to parallel computers using an efficient parallel computational aeroacoustics algorithm. Favorable results have been obtained as compared to the experimental data by Kinzie and McLaughlin [33].

1.3 Objectives and Scope of Present Study

This thesis focuses on the analysis of instability waves in confined elliptic jets using the finite element method (FEM). With the assumption of a locally parallel flow condition, detailed derivation of the governing equation of the instability waves based on LST is described in Chapter 2. To eliminate any constraint of the assumed mean velocity profile, so as to ensure separable form of the compressible Rayleigh equation, a global scheme is applied to discretize the governing equation, and transform the differential operator into a matrix polynomial. Typical global schemes such as the finite difference method [55] and the boundary element method [50] have been applied to solve related problems for circular and elliptic jets. However, to increase the robustness of the calculation for more complex jet exit geometries, the finite element Galerkin method is employed for such discretization. Since the resulting problem is a non-linear matrix eigenvalue problem, special numerical methods must be utilized to solve the system. All these numerical solution techniques are summarized in Chapter 3. Special attention is paid to the practical implementation of these techniques, and the assessments of applying these numerical methods to two-dimensional calculations are made.

To capture the oscillatory behavior of the growth rate curve due to the effects of confinement, the integration path has to be detoured in the complex plane in order to avoid the presence of singularities. While this deformation can be achieved rather straightforward in the shooting method by directly integrating numerically into the complex plane, a more elegant approach in the FEM is to used a transformation method. This complex transformation method is also described in Chapter 3.

In Chapter 4, numerical results from both the traditional shooting method and the FEM are presented. To understand the effects of confinement on jets, a circular jet is

studied first using the shooting method. This provides a case study to examine the various characteristics possessed in confined jets that are not present in free jets. Then, the axisymmetric form of the compressible Rayleigh equation is discretized using the FEM to assess the different numerical solution techniques for the solution of the non-linear eigenvalue problem. With a validated FEM code, various aspects of confined jets are examined. These consist of the effects of varying the aspect ratio of the shrouds and the jets. The stability characteristics of confined elliptic jets are then presented. To simulate the four general classes of instability modes in elliptic jets using only the first quadrant of the solution domain, appropriate boundary conditions have to be applied. The combinations of the Neumann and Dirichlet boundary condition to calculate the different classes of instability mode are described. Comparisons are made between these results and those of free elliptic jets calculated by Morris and Bhat [40]. Finally, in Chapter 5, the advantages and disadvantages of using the FEM to solve linear stability problems are made. Conclusions of the analysis for confined elliptic jets and suggestions for future research are also summarized.

Chapter 2

MATHEMATICAL FORMULATION

In this chapter, the governing equation of the development of instability waves in a compressible, inviscid flow, the compressible Rayleigh equation, is formulated. Assumptions used to simplify the Navier-Stokes equations in the derivation of the perturbation equation are also stated. The general form of the compressible Rayleigh equation in Cartesian coordinate system is derived in Section 2.1. If the jet is assumed to be axisymmetric, further simplifications can be performed, and a separable form of the governing equation is developed, as described in Section 2.2. Often, in linear stability theory, mean flow properties are needed in order to perform the calculation. Analytical expressions describing these mean flow properties are described in Section 2.3.

2.1 General Form of the Compressible Rayleigh Equation

The equations describing the development of a compressible fluid are the Navier-Stokes equations. Assuming an inviscid flow so that the viscous terms of the equations can be neglected, the Navier-Stokes equations are reduced to the Euler equations. For a calorically perfect gas, these equations, in Cartesian tensor notation, can be written as

$$\frac{\partial \rho^*}{\partial t^*} + \frac{\partial}{\partial x_k^*}\{\rho^* u_k^*\} = 0, \tag{2.1}$$

$$\rho^* \left\{ \frac{\partial u_i^*}{\partial t^*} + u_k^* \frac{\partial u_i^*}{\partial x_k^*} \right\} = -\frac{\partial p^*}{\partial x_i^*}, \tag{2.2}$$

$$\frac{\partial p^*}{\partial t^*} + u_i^* \frac{\partial p^*}{\partial x_i^*} + \gamma p^* \frac{\partial u_i^*}{\partial x_i^*} = 0, \tag{2.3}$$

where u_i^* is the instantaneous velocity, ρ^* is the instantaneous density, p^* is the instantaneous static pressure, and γ is the ratio of specific heat constants.

Assuming that the flow quantities such as the velocity, pressure, and density can be separated into a mean and a fluctuating component using the Reynolds decomposition,

$$u_j^*(x_i^*, t^*) = \bar{u}_j^*(x_i^*) + u_j^{*'}(x_i^*, t^*), \tag{2.4}$$

$$p^*(x_i^*, t^*) = \bar{p}^*(x_i^*) + p^{*'}(x_i^*, t^*), \tag{2.5}$$

$$\rho^*(x_i^*, t^*) = \bar{\rho}^*(x_i^*) + \rho^{*'}(x_i^*, t^*), \tag{2.6}$$

where the overbar and the prime represent the mean and fluctuating quantity respectively,

the Euler equations can be linearized by neglecting second- and higher order fluctuating terms. The linearized, unsteady, compressible Euler equations are found to be

$$\left\{\frac{\partial}{\partial t^*}+\bar{u}_k^*\frac{\partial}{\partial x_k^*}+\frac{\partial \bar{u}_k^*}{\partial x_k^*}\right\}\rho^{*'}+\bar{\rho}^*\frac{\partial u_k^{*'}}{\partial x_k^*}+u_k^{*'}\frac{\partial \bar{\rho}^*}{\partial x_k^*}=0, \tag{2.7}$$

$$\bar{\rho}^*\left\{\frac{\partial u_i^{*'}}{\partial t^*}+\bar{u}_k^*\frac{\partial u_i^{*'}}{\partial x_k^*}+u_k^{*'}\frac{\partial \bar{u}_i^*}{\partial x_k^*}\right\}+\rho^{*'}\,\bar{u}_k^*\frac{\partial \bar{u}_i^*}{\partial x_k^*}=-\frac{\partial p^{*'}}{\partial x_i^*}, \tag{2.8}$$

$$\left\{\frac{\partial}{\partial t^*}+\bar{u}_i^*\frac{\partial}{\partial x_i^*}\right\}p^{*'}+\gamma\bar{p}^*\frac{\partial u_i^{*'}}{\partial x_i^*}+\gamma p^{*'}\frac{\partial \bar{u}_i^*}{\partial x_i^*}=0, \tag{2.9}$$

with the assumption that the mean static pressure is constant.

To derive the general form of the compressible Rayleigh equation, only the momentum and the energy equations are needed for manipulation. In addition, it is assumed that there is no mean transverse flow, the jet axis is aligned with the z-direction, and the downstream velocity is only dependent on the x- and y-direction, that is,

$$\bar{u}^*=0,\quad \bar{v}^*=0,\quad \bar{w}^*=\bar{w}^*(x^*,y^*). \tag{2.10}$$

Then, the linearized Euler equations can be further simplified into

$$\bar{\rho}^*\left\{\frac{\partial u^{*'}}{\partial t^*}+\bar{w}^*\frac{\partial u^{*'}}{\partial z^*}\right\}=-\frac{\partial p^{*'}}{\partial x^*}, \tag{2.11}$$

$$\bar{\rho}^*\left\{\frac{\partial v^{*'}}{\partial t^*}+\bar{w}^*\frac{\partial v^{*'}}{\partial z^*}\right\}=-\frac{\partial p^{*'}}{\partial y^*}, \tag{2.12}$$

$$\bar{\rho}^*\left\{\frac{\partial w^{*'}}{\partial t^*}+\bar{w}^*\frac{\partial w^{*'}}{\partial z^*}+u^{*'}\frac{\partial \bar{w}^*}{\partial x^*}+v^{*'}\frac{\partial \bar{w}^*}{\partial y^*}\right\}=-\frac{\partial p^{*'}}{\partial z^*}, \tag{2.13}$$

$$\frac{\partial p^{*'}}{\partial t^*}+\bar{w}^*\frac{\partial p^{*'}}{\partial z^*}+\gamma\bar{p}^*\left(\frac{\partial u^{*'}}{\partial x^*}+\frac{\partial v^{*'}}{\partial y^*}+\frac{\partial w^{*'}}{\partial z^*}\right)=0. \tag{2.14}$$

In the analysis performed by Tam and Morris [35] and Tam and Burton [44, 45], a multiple-scale expansion model was used to represent the slowly-diverging shear layer. This method, however, will not be used in the present study. Instead, a locally-parallel flow approximation is assumed to describe the instability wave development. This is a good assumption for high speed jets, since the mixing rate decreases as Mach number increases. In fact, the locally-parallel approximation is the lowest order approximation in a multiple-scales expansion. For any given perturbation quantity, a normal mode representation is used,

$$\phi^{*'}(x^*,y^*,z^*,t^*)=\mathrm{Re}\left\{\hat{\phi}^*(x^*,y^*)\exp\left[\left(\alpha^*z^*-\omega^*t^*\right)\right]\right\}, \tag{2.15}$$

where α^* is the axial wavenumber, ω^* is the radian frequency, and the hat denotes the eigenfunction of the perturbation quantity. In a spatial analysis, the wavenumber is complex and the frequency is real. Substitution of the normal mode quantities into Equations (2.11), (2.12), (2.13), and (2.14), the time-dependent, linearized, perturbation momentum and energy equations of a compressible fluid may be written as

$$-i\omega^*\bar{\rho}^*\hat{u}^* + i\alpha^*\bar{\rho}^*\bar{w}^*\hat{u}^* = -\frac{\partial\hat{p}^*}{\partial x^*}, \tag{2.16}$$

$$-i\omega^*\bar{\rho}^*\hat{v}^* + i\alpha^*\bar{\rho}^*\bar{w}^*\hat{v}^* = -\frac{\partial\hat{p}^*}{\partial y^*}, \tag{2.17}$$

$$\bar{\rho}^*\left\{-i\omega^*\hat{w}^* + i\alpha^*\bar{w}^*\hat{w}^* + \hat{u}^*\frac{\partial\bar{w}^*}{\partial x^*} + \hat{v}^*\frac{\partial\bar{w}^*}{\partial y^*}\right\} = -i\alpha^*\hat{p}^*, \tag{2.18}$$

$$-i\omega^*\hat{p}^* + i\alpha^*\bar{w}^*\hat{p}^* + \gamma\bar{p}^*\left\{\frac{\partial\hat{u}^*}{\partial x^*} + \frac{\partial\hat{v}^*}{\partial y^*} + i\alpha^*\hat{w}^*\right\} = 0. \tag{2.19}$$

This system of four linear differential equations can then be combined and re-arranged into a second-order partial differential equation that governs the development of instability waves. In terms of $\hat{p}^*$, this equation can be written as

$$\left\{\frac{\partial^2\hat{p}^*}{\partial x^{*2}} + \frac{\partial^2\hat{p}^*}{\partial y^{*2}}\right\} + \left\{\frac{2\,\alpha^*}{(\omega^* - \alpha^*\bar{w}^*)}\frac{\partial\hat{w}^*}{\partial x^*} - \frac{1}{\bar{\rho}^*}\frac{\partial\bar{\rho}^*}{\partial x^*}\right\}\frac{\partial\hat{p}^*}{\partial x^*} \tag{2.20}$$

$$+\left\{\frac{2\,\alpha^*}{(\omega^* - \alpha^*\bar{w}^*)}\frac{\partial\hat{w}^*}{\partial y^*} - \frac{1}{\bar{\rho}^*}\frac{\partial\bar{\rho}^*}{\partial y^*}\right\}\frac{\partial\hat{p}^*}{\partial y^*} + \left\{\frac{\bar{\rho}^*}{\gamma\bar{p}^*}(\omega^* - \alpha^*\bar{w}^*)^2 - \alpha^{*2}\right\}\hat{p}^* = 0.$$

To non-dimensionalize these equations, the following parameters are used

$$x = \frac{x^*}{R_j}, \quad y = \frac{y^*}{R_j}, \quad z = \frac{z^*}{R_j},$$

$$\bar{\rho} = \frac{\bar{\rho}^*}{\rho_j}, \quad \bar{w} = \frac{\bar{w}^*}{W_j}, \quad \hat{p} = \frac{\hat{p}^*}{\rho_j W_j^2},$$

$$\alpha = \alpha^* R_j, \quad \omega = \frac{\omega^* R_j}{W_j}, \quad t = \frac{W_j t^*}{R_j},$$

where R_j is the equivalent jet radius, ρ_j is the jet exit density, and W_j is the jet exit axial velocity. The equivalent jet radius is defined by $R_j = \sqrt{A\,B}$, where A and B are the jet's semi-major and semi-minor axes respectively. The resulting non-dimensional compressible Rayleigh equation for the pressure fluctuation is

$$\nabla_\perp^2\hat{p} + \bar{\rho}\Omega^2\left[\nabla_\perp\left(\frac{1}{\bar{\rho}\Omega^2}\right)\right]\cdot[\nabla_\perp\hat{p}] + \left[\bar{\rho}\Omega^2 M_j^2 - \alpha^2\right]\hat{p} = 0, \tag{2.21}$$

where

$$\nabla_\perp \equiv \hat{\mathbf{i}}\frac{\partial}{\partial x} + \hat{\mathbf{j}}\frac{\partial}{\partial y}, \tag{2.22}$$

and

$$\Omega = \omega - \alpha\bar{w}(x, y). \tag{2.23}$$

This is the second-order partial differential equation that governs the development of the instability waves generated at the exit of a three-dimensional jet.

2.2 Compressible Rayleigh Equation for Axisymmetric Jets

In the case of axisymmetric jets, the compressible Rayleigh equation can be further simplified by writing the gradient, divergence, and Laplacian of Equation (2.21) in a cylindrical coordinate system (r, θ, z),

$$\nabla_\perp \phi \equiv \hat{\mathbf{e}}_\mathbf{r}\frac{\partial \phi}{\partial r} + \hat{\mathbf{e}}_\theta \frac{1}{r}\frac{\partial \phi}{\partial \theta}, \tag{2.24}$$

$$\nabla_\perp \cdot \mathbf{A} \equiv \frac{1}{r}\frac{\partial}{\partial r}(rA_r) + \frac{1}{r}\frac{\partial}{\partial \theta}(A_\theta), \tag{2.25}$$

$$\nabla_\perp^2 \phi \equiv \frac{1}{r}\frac{\partial}{\partial r}\left(r\frac{\partial \phi}{\partial r}\right) + \frac{1}{r^2}\frac{\partial^2 \phi}{\partial \theta^2}. \tag{2.26}$$

A typical cylindrical coordinate system is shown in Figure 2.1.

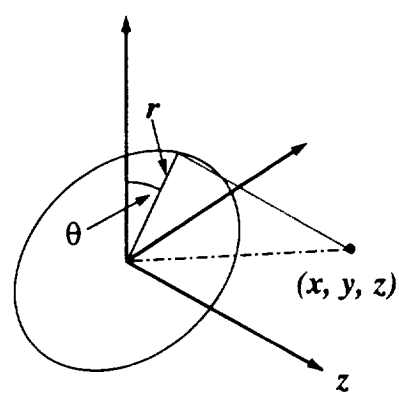

Figure 2.1. Cylindrical coordinate system in (r, θ, z).

Then, the assumption is made that there is no azimuthal variation in the mean velocity profile, $\frac{\partial \bar{w}}{\partial \theta} = \frac{\partial^2 \bar{w}}{\partial \theta^2} = 0$, so that the mean velocity profile is only dependent on the radial direction, $\bar{w} = \bar{w}(r)$. The governing equation, or the compressible Rayleigh equation, for an axisymmetric jet can therefore be written as a second-order ordinary differential equation,

$$\frac{d^2\hat{p}}{dr^2} + \left[\frac{1}{r} - \frac{1}{\bar{\rho}}\frac{d\bar{\rho}}{dr} + \frac{2\alpha}{(\omega - \alpha\bar{w})}\frac{d\bar{w}}{dr}\right]\frac{d\hat{p}}{dr} + \left[\bar{\rho}M_j^2(\omega - \alpha\bar{w})^2 - \alpha^2 - \frac{n^2}{r^2}\right]\hat{p} = 0, \tag{2.27}$$

where n is the azimuthal mode number.

2.3 Mean Flow Properties

In the earlier sections, the perturbation equation that governs the development of instability waves in a jet or shear layer was derived. The compressible forms of the Rayleigh equation for three-dimensional and axisymmetric jets are given by Equations (2.21) and (2.27) respectively. The compressible Rayleigh equation and associated boundary conditions constitute a boundary-value problem, where the complex wavenumber α is the eigenvalue and $\hat{p}$ is the eigenfunction. Since the real radian frequency, ω, is specified, the unknown variables in the governing equation are the mean velocity and density profiles. Usually, the mean velocity profile is obtained from either a curve-fit of experimental data, or an analytical expression that has a qualitative representation of the physical flow. Then, the only unknown variable that needs to be specified is the mean density profile. However, mean density profiles are not usually available from experimental data. To overcome this difficulty, the mean density profile is often related to the mean velocity profile through the Crocco-Busemann equation.

The main assumptions used in the derivation of this equation are: (1) negligible streamwise variation, that is, $\frac{\partial}{\partial z} = 0$; (2) frictionless external flow; and (3) no heat transfer at the outer edge of the boundary layer. In the case of free jets with no external flow, the Crocco-Busemann equation is given by,

$$\frac{\rho}{\rho_j} = \left(\frac{T}{T_j}\right)^{-1} = \left\{\frac{T_\infty}{T_j} + \left[1 - \frac{T_\infty}{T_j} + \left(\frac{\gamma-1}{2}\right)M_j^2\right]\left(\frac{\bar{w}}{W_j}\right) - \left(\frac{\gamma-1}{2}\right)M_j^2\left(\frac{\bar{w}}{W_j}\right)^2\right\}^{-1}, \tag{2.28}$$

where T_j is the static temperature of the jet, and T_∞ is the stagnation temperature of the ambient air. With external flow, the equation is given by

$$\frac{\rho}{\rho_j} = \left(\frac{T}{T_j}\right)^{-1} = \tag{2.29}$$
$$\left\{ -\frac{\gamma-1}{2} M_j^2 \left(\frac{\bar{w}}{W_j}\right)^2 + \left[\left(1 - \frac{T_2}{T_j}\right)\left(\frac{1}{1-R}\right) + \frac{\gamma-1}{2}(1+R) M_j^2\right]\left(\frac{\bar{w}}{W_j}\right)\right.$$
$$+\frac{1}{2}\left[\left(1 + \frac{T_2}{T_j}\right) + \frac{\gamma-1}{2} M_j^2 \left(1+R^2\right) - \left(1 - \frac{T_2}{T_j}\right)\left(\frac{1+R}{1-R}\right)\right.$$
$$\left.\left. -\frac{\gamma-1}{2}(1+R)^2 M_j^2\right]\right\}^{-1},$$

where R is defined by the ratio of the external and jet velocities, $R = W_2/W_j$. W_2 and T_2 are the velocity and static temperature of the external flow, respectively. For supersonic jets and shear layers, the assumptions used in deriving the relation between the mean density and velocity profiles are not violated. Therefore, although the Crocco-Busemann equation is derived to relate the mean density profiles to mean velocity profiles in boundary layers, it still provides a qualitative representation of the mean density profiles in supersonic jets and shear layers.

Chapter 3

NUMERICAL SOLUTION TECHNIQUES

In the previous chapter, the second-order differential equation that governs the instability wave characteristics of a compressible flow was derived. The governing equation, the compressible Rayleigh equation, and the associated boundary conditions form a boundary-value problem. In a spatial analysis, the complex wavenumber, α, is the eigenvalue and $\hat{p}$ is the eigenfunction. Unlike a temporal analysis, where the radian frequency is the complex eigenvalue, α varies non-linearly in the perturbation equation. To evaluate a non-linear eigenvalue problem, special numerical methods have to be utilized. In this chapter, some of these numerical methods are presented. The advantages and disadvantages of each scheme are described, and special attention is paid to the practical implementation of these schemes.

For the axisymmetric form of the compressible Rayleigh equation, Equation (2.27), can be solved efficiently using a shooting method. However, this is not possible for the general form of the compressible Rayleigh equation, Equation (2.21). Alternatively, a global method can be used to analyze the problem. This involves the discretization of the governing equation, resulting in a matrix eigenvalue problem. Different techniques can be utilized to convert the differential operator into a matrix system, such as the spectral method using Chebyshev series (Bridges and Morris [56], or the finite difference method (Liou and Morris [55]). If the coefficients in the perturbation equation are constants, the boundary element method (BEM) can be used for the discretization. This can be achieved by assuming a vortex sheet model for the mixing layer in the jet, and such analysis has been carried out by Viswanathan *et al.* [50]. In the present analysis, the finite element Galerkin method (FEM) is proposed for the discretization of the differential equations. This eliminates the stringent requirements on the mean velocity profiles, and thus more complex flows can be analyzed.

3.1 Shooting Method

For a confined axisymmetric jet, the instability wave characteristics of the flow are governed by the axisymmetric form of the compressible Rayleigh equation, Equation (2.27), re-written here for clarity,

$$\frac{d^2\hat{p}}{dr^2} + \left[\frac{1}{r} - \frac{1}{\bar{\rho}}\frac{d\bar{\rho}}{dr} + \frac{2\alpha}{(\omega - \alpha\bar{w})}\frac{d\bar{w}}{dr}\right]\frac{d\hat{p}}{dr} + \left[\bar{\rho}M_j^2\left(\omega - \alpha\bar{w}\right)^2 - \alpha^2 - \frac{n^2}{r^2}\right]\hat{p} = 0.$$

Inside the potential core region, $r \leq h$, where h is the potential core radius, and outside the mixing layer, the velocity is uniform and the equation reduces to

$$\frac{d\hat{p}_1}{dr^2} + \frac{1}{r}\frac{d\hat{p}_1}{dr} + \left[M_j^2(\omega-\alpha)^2 - \alpha^2 - \frac{n^2}{r^2}\right]\hat{p}_1 = 0, \tag{3.1}$$

$$\frac{d\hat{p}_2}{dr^2} + \frac{1}{r}\frac{d\hat{p}_2}{dr} + \left\{\left(\frac{\rho_2}{\rho_j}\right)M_j^2\left[\omega - \alpha\left(\frac{W_2}{W_j}\right)\right]^2 - \alpha^2 - \frac{n^2}{r^2}\right\}\hat{p}_2 = 0, \tag{3.2}$$

where $\hat{p}_1$ and $\hat{p}_2$ are the perturbation pressure eigenfunctions inside and outside the jet respectively. ρ_2 is the density of the ambient air, and n is the azimuthal mode number. The general solutions of these equations, with the imposition of finite jet centerline pressure, are given by

$$\hat{p}_1 = C_1 J_n(\lambda_1 r) \tag{3.3}$$

and

$$\hat{p}_2 = C_2 H_n^{(1)}(i\lambda_2 r) + C_3 H_n^{(2)}(i\lambda_2 r), \tag{3.4}$$

where

$$\lambda_1 = \left[M_j^2(\omega-\alpha)^2 - \alpha^2\right]^{\frac{1}{2}}, \quad \text{and} \tag{3.5}$$

$$\lambda_2 = \left\{\alpha^2 - \left(\frac{\rho_2}{\rho_j}\right)M_j^2\left[\omega - \alpha\left(\frac{W_2}{W_j}\right)\right]^2\right\}^{\frac{1}{2}}. \tag{3.6}$$

The branch cut for λ_2 is chosen to insure decaying solutions or outgoing waves as r approaches infinity, and in the present analysis, it is chosen so that

$$-\frac{\pi}{2} \leq \arg(\lambda_2) < \frac{\pi}{2}. \tag{3.7}$$

A detailed description of the choice of the appropriate branch cut is given in Appendix A. However, it should be noted that for the confined jet case, the choice of branch cut for λ_2 is arbitrary, and it is only enforced here for generality. J_n is the Bessel function of the first kind of integer order n, $H_n^{(1)}$ and $H_n^{(2)}$ are the Hankel functions of the first and second kind of integer order n respectively, and $H_n^{(2)}$ represents the incoming wave reflected from the outer wall. C_1, C_2, and C_3 are unknown constant coefficients. At the outer wall, r_w, the boundary condition is imposed as

$$\frac{\partial \hat{p}_2}{\partial r} = 0, \; r = r_w \tag{3.8}$$

and this condition can be used to eliminate one of the unknown constant coefficients, so that

$$C_3 = -C_2 \left\{ \frac{\frac{n}{r_w} H_n^{(1)}(i\lambda_2 r_w) - i\lambda_2 H_{n+1}^{(1)}(i\lambda_2 r_w)}{\frac{n}{r_w} H_n^{(2)}(i\lambda_2 r_w) - i\lambda_2 H_{n+1}^{(2)}(i\lambda_2 r_w)} \right\}. \tag{3.9}$$

In order to evaluate the eigenvalues for a given set of operating conditions, the compressible Rayleigh equation is re-written as a pair of first-order ordinary differential equations,

$$\left\{ \begin{array}{c} \frac{d\hat{p}}{dr} \\ \frac{d\mathcal{F}}{dr} \end{array} \right\} = \left[\begin{array}{cc} 0 & 1 \\ \mathcal{G}_1 & \mathcal{G}_2 \end{array} \right] \left\{ \begin{array}{c} \hat{p} \\ \mathcal{F} \end{array} \right\} \tag{3.10}$$

where

$$\mathcal{G}_1 = -\left[\bar{\rho} M_j^2 (\omega - \alpha\bar{w})^2 - \alpha^2 - \frac{n^2}{r^2} \right], \tag{3.11}$$

and

$$\mathcal{G}_2 = -\left[\frac{1}{r} - \frac{1}{\bar{\rho}} \frac{d\bar{\rho}}{dr} + \frac{2\alpha}{(\omega - \alpha\bar{w})} \frac{d\bar{w}}{dr} \right]. \tag{3.12}$$

Applying the shooting method, this system of first-order ordinary differential equations are integrated numerically from the potential core to the outer wall using a fifth-order variable step-size Runge-Kutta scheme [57]. The initial conditions inside and outside the jet are taken from Equations (3.3) and (3.4) respectively. In order to satisfy the condition of continuity of the integrated function and its derivative, the following condition,

$$C_1 \left\{ \begin{array}{c} \hat{p}_1 \\ \mathcal{F}_1 \end{array} \right\} = C_2 \left\{ \begin{array}{c} \hat{p}_2 \\ \mathcal{F}_2 \end{array} \right\}, \text{ or } \left[\begin{array}{cc} \hat{p}_1 & -\hat{p}_2 \\ \mathcal{F}_1 & -\mathcal{F}_2 \end{array} \right] \left\{ \begin{array}{c} C_1 \\ C_2 \end{array} \right\} = \left\{ \begin{array}{c} 0 \\ 0 \end{array} \right\}, \tag{3.13}$$

must hold. C_1 and C_2 are the unknown constant coefficients in Equations (3.3) and (3.4). For a non-trivial solution, the determinant of the 2 by 2 matrix must be zero, since the unknown constant coefficients are arbitrary. Therefore, the wavenumbers are varied iteratively until the two numerical solutions matched.

3.2 Finite Element Discretization

In order to analyze the instability wave characteristics of a jet using a global method, the different forms of the compressible Rayleigh equation, Equations (2.21) and (2.27), have to be discretized in the solution domain. There are many numerical schemes for such discretization. A very popular method, often used in the analysis of fluid problems, is the finite difference method. The advantage of this method is that it is very easy to understand and implement. However, for complex geometries, a transformation is required to convert the problem into a computational domain. This increases the complexity of the problem. The next choice is the boundary element method (BEM). This method does handle arbitrary geometries, and it only requires the discretization of the boundaries of the solution

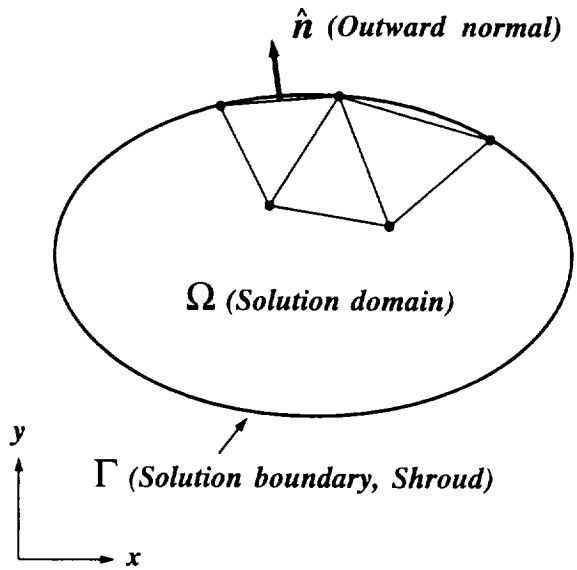

Figure 3.1. The cross-section and discretization of the solution domain.

domain. This significantly reduces the size of the problem to be solved. Unfortunately, in the compressible Rayleigh equation, the coefficients are not constant, and BEM is not able to handle this. Thus, BEM is not an ideal choice for studying jets of arbitrary geometries.

Unlike the finite difference approximation and the boundary element method, the finite element method (FEM) is able to handle complex physical geometries and non-constant coefficients in the governing equation. Moreover, the Neumann boundary condition that exists in the present analysis is naturally satisfied along the edge of the domain when applying the Green's theorem. This reduces the task of implementing the boundary conditions. In the present analysis, a finite element Galerkin method is employed for the discretization of the governing equation.

Consider a jet confined in a shroud, as shown in Figure 3.1. The governing equation of the instability waves in the jet is described by the general form of the compressible Rayleigh equation, Equation (2.21), re-written here for clarity.

$$\nabla_{\perp}^{2}\hat{p} + \bar{\rho}\Omega^{2}\left[\nabla_{\perp}\left(\frac{1}{\bar{\rho}\Omega^{2}}\right)\right]\cdot\left[\nabla_{\perp}\hat{p}\right] + \left[\bar{\rho}\Omega^{2}M_{j}^{2} - \alpha^{2}\right]\hat{p} = 0,$$

where

$$\nabla_{\perp} \equiv \hat{\mathbf{i}}\frac{\partial}{\partial x} + \hat{\mathbf{j}}\frac{\partial}{\partial y},$$

and

$$\Omega = \omega - \alpha\bar{w}(x, y).$$

For simplicity, the governing equation can be expressed as a differential operator, $\mathcal{L}$, acting

on the perturbation pressure, $\hat{p}$, such that

$$\mathcal{L}[\hat{p}] = -f^{(1)}\left(\frac{\partial^2\hat{p}}{\partial x^2} + \frac{\partial^2\hat{p}}{\partial y^2}\right) + f^{(2)}\frac{\partial\hat{p}}{\partial x} + f^{(3)}\frac{\partial\hat{p}}{\partial y} + f^{(4)}\hat{p} = 0, \tag{3.14}$$

where

$$f^{(1)} = -1, \tag{3.15}$$

$$f^{(2)} = \frac{2\alpha}{\omega - \alpha\bar{w}}\frac{\partial\bar{w}}{\partial x} - \frac{1}{\bar{\rho}}\frac{\partial\bar{\rho}}{\partial x}, \tag{3.16}$$

$$f^{(3)} = \frac{2\alpha}{\omega - \alpha\bar{w}}\frac{\partial\bar{w}}{\partial y} - \frac{1}{\bar{\rho}}\frac{\partial\bar{\rho}}{\partial y}, \tag{3.17}$$

$$f^{(4)} = \bar{\rho}M_j^2\left(\omega - \alpha\bar{w}\right)^2 - \alpha^2. \tag{3.18}$$

This is a boundary-value problem with Neumann boundary condition,

$$\frac{\partial p}{\partial \hat{\mathbf{n}}} = 0, \tag{3.19}$$

along the edges of the domain, where $\hat{\mathbf{n}}$ is the outward normal of the solution boundary, as shown in Figure 3.1.

The difficulty in solving Equation (2.21) is that the requirement of a solution $\hat{p}$ satisfying this equation at every point in the solution domain, Ω, is too strong. To overcome this difficulty, the boundary-value problem is reformulated in such a way that weaker conditions on the solution and its derivatives will be admitted. Such a formulation is called the weak, or variational formulation of the problem.

To derive the variational statement of the problem, the solution $\hat{p}$ is evaluated such that the differential equation, together with the boundary conditions, are satisfied in the sense of weighted averages. This means that

$$\int_\Omega \left\{ g\left[-f^{(1)}\left(\frac{\partial^2\hat{p}}{\partial x^2} + \frac{\partial^2\hat{p}}{\partial y^2}\right) + f^{(2)}\frac{\partial\hat{p}}{\partial x} + f^{(3)}\frac{\partial\hat{p}}{\partial y} + f^{(4)}\hat{p}\right]\right\} dx\, dy = 0 \tag{3.20}$$

for all members g of a suitable class of functions. The weight function, or the test function, g, is any function that is sufficiently well behaved in the integration. Using the Green's theorem and integration by parts, Equation (3.20) can be re-written as

$$\begin{aligned}\int_\Omega \Bigg[&\left(\frac{\partial g}{\partial x}f^{(1)} + g\frac{\partial f^{(1)}}{\partial x}\right)\frac{\partial\hat{p}}{\partial x} + \left(\frac{\partial g}{\partial y}f^{(1)} + g\frac{\partial f^{(1)}}{\partial y}\right)\frac{\partial\hat{p}}{\partial y} \\ &+ gf^{(2)}\frac{\partial\hat{p}}{\partial x} + gf^{(3)}\frac{\partial\hat{p}}{\partial y} + gf^{(4)}\hat{p}\Bigg]\, dx\, dy = 0.\end{aligned} \tag{3.21}$$

This is the variational statement of the original problem that satisfies the solutions of the original form without the stringent requirement on $\hat{p}$.

In order to derive the finite element formulation of the variational statement of the problem, a set of basis functions $\{\phi_1, \phi_2, \ldots, \phi_M\}$ has to be identified in the space H^1 that defines a finite dimensional subspace of test functions H^h in H^1. Each individual function ϕ is called the shape function and the space H^1 is known as the Sobolev space. Using these basis functions, $\hat{p}$, g, $f^{(1)}$, $f^{(2)}$, $f^{(3)}$ and $f^{(4)}$ can be defined as

$$\hat{p}_h = \sum_{i=1}^{M} \phi_i \hat{P}_i, \tag{3.22}$$

$$g_h = \sum_{j=1}^{M} \phi_j G_j, \tag{3.23}$$

$$f_l^{(k)} = \sum_{l=1}^{M} \phi_l F_l^{(k)}, \qquad k = 1, 2, \ldots 4. \tag{3.24}$$

where $\hat{P}_i$, G_j, and $F_l^{(k)}$ are the the nodal values of the pressure eigenfunction $\hat{p}$, the test function g, and the coefficients of the compressible Rayleigh equation respectively, and M is the number of the basis functions. If Equations (3.22), (3.23), and (3.24) are substituted into the weak variational statement, Equation (3.21), the variational form of the compressible Rayleigh equation becomes

$$\begin{aligned}\Bigg\{\int_\Omega \Bigg[&\frac{\partial \phi_j}{\partial x}\left(\phi_l F_l^{(1)}\right)\frac{\partial \phi_i}{\partial x} + \phi_j\left(\frac{\partial \phi_l}{\partial x}F_l^{(1)}\right)\frac{\partial \phi_i}{\partial x} \\ &+\frac{\partial \phi_j}{\partial y}\left(\phi_l F_l^{(1)}\right)\frac{\partial \phi_i}{\partial y} + \phi_j\left(\frac{\partial \phi_l}{\partial y}F_l^{(1)}\right)\frac{\partial \phi_i}{\partial y} \\ &+\phi_j\left(\phi_l F_l^{(2)}\right)\frac{\partial \phi_i}{\partial x} + \phi_j\left(\phi_l F_l^{(3)}\right)\frac{\partial \phi_i}{\partial y} + \phi_j\left(\phi_l F_l^{(4)}\right)\phi_i\Bigg]\,dx\,dy\Bigg\}\,\hat{P}_i = 0,\end{aligned} \tag{3.25}$$

where the summation signs are omitted and the Cartesian summation convention is adopted to simplify the notation. This is the finite element approximation of the variational form of the compressible Rayleigh equation.

In the present analysis, the shape functions of a linear triangular element are used. Evaluating the integrals in Equation (3.25), the local element matrices for the differential operators in Equation (3.25) are obtained:

$$\mathbf{K_1} = \int_\Omega \left[\frac{\partial \phi_j}{\partial x}\left(\phi_l F_l^{(1)}\right)\frac{\partial \phi_i}{\partial x} + \phi_j\left(\frac{\partial \phi_l}{\partial x}F_l^{(1)}\right)\frac{\partial \phi_i}{\partial x}\right]dx\,dy; \tag{3.26}$$

$$\mathbf{K_2} = \int_\Omega \left[\frac{\partial \phi_j}{\partial y}\left(\phi_l F_l^{(1)}\right)\frac{\partial \phi_i}{\partial y} + \phi_j\left(\frac{\partial \phi_l}{\partial y}F_l^{(1)}\right)\frac{\partial \phi_i}{\partial y}\right]dx\,dy; \tag{3.27}$$

$$\mathbf{K_3} = \int_\Omega \left[\phi_j\left(\phi_l F_l^{(2)}\right)\frac{\partial \phi_i}{\partial x}\right]dx\,dy; \tag{3.28}$$

$$\mathbf{K_4} = \int_\Omega \left[\phi_j\left(\phi_l F_l^{(3)}\right)\frac{\partial \phi_i}{\partial y}\right]dx\,dy; \text{ and} \tag{3.29}$$

$$\mathbf{K_5} = \int_\Omega \left[\phi_j\left(\phi_l F_l^{(4)}\right)\phi_i\right]dx\,dy. \tag{3.30}$$

A detailed derivation of the local element matrices of a triangular element for each of the integrals is given in Appendix B. To derive the local element matrices for the axisymmetric form of the compressible Rayleigh equation, a similar procedure can be carried out. However, instead of using a linear triangular element, the shape functions of a linear line element are used. These local element matrices are also given in Appendix B.

Usually, in finite element analyses, a Gaussian quadrature numerical integration scheme is employed to integrate the integrals in Equation (3.25) numerically. For non-constant coefficients, the piece-wise constant values of the coefficients are used within each element. For linear triangular elements, the values are usually taken from those corresponding to the centroid of each element. Another popular method is to integrate the coefficients at the weighted integration points in Gaussian quadrature numerically. In the present analysis, since the coefficient functions can also be represented by the same shape functions, as shown in Equation (3.24), the integrations are carried out analytically. Therefore, the element matrices are piece-wise linear instead of piece-constant, and no approximation is made in the derivation. This increases the accuracy of the solution.

By assembling the local element matrices, and re-arranging in terms of the complex wavenumber, α, the matrix form of the compressible Rayleigh equation is reduced to

$$[\mathbf{D}(\alpha)]\,\mathbf{p} = \left[\alpha^3\mathbf{C_0} + \alpha^2\mathbf{C_1} + \alpha\mathbf{C_2} + \mathbf{C_3}\right]\mathbf{p} = 0, \tag{3.31}$$

where $\mathbf{C_0}$, $\mathbf{C_1}$, $\mathbf{C_2}$, and $\mathbf{C_3}$ are N by N matrices, $\mathbf{p}$ is the eigenvector, and N is the number of discretization points in the solution domain. The original compressible Rayleigh equation is transformed into an eigenvalue problem in which the parameter, α, varies non-linearly. To solve this type of non-linear eigenvalue problem, special numerical methods have to be applied. These methods are described in the next section.

3.3 Numerical Methods for Non-Linear Eigenvalue Problems

In the previous section, a finite element Galerkin method is applied to discretize the governing equation, the compressible Rayleigh equation, over the solution domain. This discretization method converts the differential operators to a matrix system, and in the case of hydrodynamic stability problems, the resulting system is a matrix polynomial, also known as λ-matrix [58, 59]. A matrix polynomial, or λ-matrix, is a matrix-valued function of a complex variable of the form $L(\lambda) = \sum_{i=0}^{l} A_i\lambda^{l-i}$, where $A_0, A_1, \ldots, A_l$ are complex matrices of order N. If $A_l = I$, the identity matrix, then in this case, $L(\lambda)$ is said to be monic. However, in the present analysis, this is not necessarily true.

In most temporary stability analyses, the λ-matrix is reduced to an algebraic eigenvalue problem, since the frequency, ω, varies linearly. However, in spatial stability analyses, the complex wavenumber, α, appears non-linearly in the λ-matrix and the analysis

becomes more complicated. In this section, special numerical methods used to solve non-linear eigenvalue problems are outlined. Two global methods are discussed which evaluate the eigenvalue spectrum without an initial estimate, and a local refinement method using Newton iteration in compact matrix form is also considered.

3.3.1 Linear Companion Matrix Method (LCMM)

A very straight forward method to solve the non-linear eigenvalue problem given by Equation (3.31) is the Linear Companion Matrix Method (LCMM). A companion matrix for the matrix polynomial may be formed in the same way as that for a scalar polynomial. Two new vectors are defined such that

$$\mathbf{p_1} = \alpha \mathbf{p} \tag{3.32}$$

and

$$\mathbf{p_2} = \alpha \mathbf{p_1}. \tag{3.33}$$

With these definitions, the matrix eigenvalue problem may be re-written in block matrix form,

$$\left[\begin{pmatrix} \mathbf{C_1} & \mathbf{C_2} & \mathbf{C_3} \\ \mathbf{I} & \mathbf{0} & \mathbf{0} \\ \mathbf{0} & \mathbf{I} & \mathbf{0} \end{pmatrix} - \alpha \begin{pmatrix} \mathbf{C_0} & \mathbf{0} & \mathbf{0} \\ \mathbf{0} & \mathbf{I} & \mathbf{0} \\ \mathbf{0} & \mathbf{0} & \mathbf{I} \end{pmatrix}\right] \begin{pmatrix} \mathbf{p_2} \\ \mathbf{p_1} \\ \mathbf{p} \end{pmatrix} = \mathbf{0}. \tag{3.34}$$

This is a generalized eigenvalue problem, and can be solved using globally convergent algorithms such as the QZ algorithm. If $\mathbf{C_0}$ is not singular, it is more efficient to transform the generalized eigenvalue problem given by Equation (3.34) to the algebraic eigenvalue problem,

$$\left[\begin{pmatrix} -\mathbf{C_0^{-1}C_1} & -\mathbf{C_0^{-1}C_2} & -\mathbf{C_0^{-1}C_3} \\ \mathbf{I} & \mathbf{0} & \mathbf{0} \\ \mathbf{0} & \mathbf{I} & \mathbf{0} \end{pmatrix} - \alpha \mathbf{I}\right] \begin{pmatrix} \mathbf{p_2} \\ \mathbf{p_1} \\ \mathbf{p} \end{pmatrix} = \mathbf{0}. \tag{3.35}$$

These eigenvalues can be evaluated more efficiently and accurately using the QR algorithm.

However, $\mathbf{C_0}$ is almost singular in the present analysis, due to the FEM discretization. Therefore, Equation (3.34) cannot be converted to Equation (3.35) without first introducing a transformation,

$$\mu = \frac{1}{\alpha - s}, \tag{3.36}$$

where s is the transformation factor. In fact, any transformation can be applied for such conversion. The advantage of using the transformation given by Equation (3.36) becomes

apparent in the next section. The transformed matrix using the LCMM is

$$\left[\begin{pmatrix} \hat{\mathbf{C}}_1 & \hat{\mathbf{C}}_2 & \hat{\mathbf{C}}_3 \\ \mathbf{I} & \mathbf{0} & \mathbf{0} \\ \mathbf{0} & \mathbf{I} & \mathbf{0} \end{pmatrix} - \mu \begin{pmatrix} \hat{\mathbf{C}}_0 & \mathbf{0} & \mathbf{0} \\ \mathbf{0} & \mathbf{I} & \mathbf{0} \\ \mathbf{0} & \mathbf{0} & \mathbf{I} \end{pmatrix}\right] \begin{pmatrix} \mathbf{p}_2 \\ \mathbf{p}_1 \\ \mathbf{p} \end{pmatrix} = \mathbf{0}, \tag{3.37}$$

where

$$\hat{\mathbf{C}}_0 = \mathbf{C}_3 + s\mathbf{C}_2 + s^2\mathbf{C}_1 + s^3\mathbf{C}_0, \tag{3.38}$$

$$\hat{\mathbf{C}}_1 = \mathbf{C}_2 + 2s\mathbf{C}_1 + 3s^2\mathbf{C}_0, \tag{3.39}$$

$$\hat{\mathbf{C}}_2 = \mathbf{C}_1 + 3s\mathbf{C}_0, \tag{3.40}$$

$$\hat{\mathbf{C}}_3 = \mathbf{C}_0. \tag{3.41}$$

After the transformation, $\hat{\mathbf{C}}_0$ is no longer singular, and one is able to convert Equation (3.37) to the algebraic eigenvalue problem of Equation (3.35). Using the LCMM, the entire eigenvalue spectrum is calculated. However, the order of the matrix becomes $3N$, instead of N. This becomes computationally intensive as the size of the problem becomes larger.

3.3.2 Matrix Factorization Method (MFM)

In most hydrodynamic problems, only a subset of the eigenvalue spectrum is of physical interest. Therefore, it is not necessary to solve for the entire spectrum. Indeed, it is possible to calculate a subset of the eigenvalue spectrum if the matrix polynomial is factorized. This is the Matrix Factorization Method (MFM). To implement the MFM, the matrix polynomial, Equation (3.31) is transformed using the transformation Equation (3.36), and the resulting matrix polynomial is,

$$[\mathbf{D}(\mu)]\,\mathbf{p} = \left[\mu^3\mathbf{I} + \mu^2\mathbf{A}_1 + \mu\mathbf{A}_2 + \mathbf{A}_3\right]\mathbf{p} = \mathbf{0}, \tag{3.42}$$

where

$$\mathbf{A}_1 = \hat{\mathbf{C}}_0^{-1}\hat{\mathbf{C}}_1, \tag{3.43}$$

$$\mathbf{A}_2 = \hat{\mathbf{C}}_0^{-1}\hat{\mathbf{C}}_2, \tag{3.44}$$

$$\mathbf{A}_3 = \hat{\mathbf{C}}_0^{-1}\hat{\mathbf{C}}_3, \tag{3.45}$$

If the matrix equivalent of synthetic division is employed on Equation (3.42), the factored form of $\mathbf{D}$ is,

$$\mathbf{D}(\mu) = \{\mathbf{Q}_2(\mu)\}(\mu\mathbf{I} - \mathbf{Y}), \tag{3.46}$$

where

$$\mathbf{Q}_2 = \mu^2 + \mu(\mathbf{A}_1 + \mathbf{Y}) + \mathbf{A}_2 + \mathbf{A}_1\mathbf{Y} + \mathbf{Y}^2. \tag{3.47}$$

$\mathbf{Y}$ is the solvent or factor of the polynomial $\mathbf{D}$. Equation (3.46) will only be satisfied if $\mathbf{Y}$ is a root of the matrix polynomial, and the reminder of the division is zero, that is,

$$\mathbf{Y}^3 + \mathbf{A_1}\mathbf{Y}^2 + \mathbf{A_2}\mathbf{Y} + \mathbf{A_3} = \mathbf{0}. \tag{3.48}$$

Therefore, in order to calculate the eigenvalues of the problem, the roots of this matrix polynomial have to be evaluated first.

The method used to calculate the roots of the matrix polynomial is the Bernoulli iteration. The theorem of this method is stated below without proof. For further details, please refer to Gohberg *et al.* [59].

Theorem 3.1 *Let $L(\lambda) = I\lambda^l + \sum_{i=0}^{l-1} \lambda^i A_i$ be a monic matrix polynomial of degree l. Assume that $L(\lambda)$ has a dominant solvent S, and the transposed matrix polynomial $L^T(\lambda)$ also has a dominant solvent. Let $\{U_r\}_{r=1}^{\infty}$ be the solution of the system*

$$A_0U_r + A_1U_{r-1} + \cdots + A_{l-1}U_{r+l-1} + U_{r+1} = 0, \quad r = 1, 2, \ldots$$

where $\{U_r\}_{r=1}^{\infty}$ is a sequence of $n \times n$ matrices to be found, and is determined by the initial conditions $U_0 = \cdots = U_{l-1} = 0, U_l = I$. Then $U_{r+1}U_r^{-1}$ exists for large r and $U_{r+1}U_r^{-1} \to S$ as $r \to \infty$.

Simply stated, the Bernoulli iteration consists of a sequence of iterations:

$$\mathbf{X}_{i+1} + \mathbf{A_1}\mathbf{X}_i + \mathbf{A_2}\mathbf{X}_{i-1} + \mathbf{A_3}\mathbf{X}_{i-2} = \mathbf{0}, \tag{3.49}$$

with the initial conditions

$$\mathbf{X}_0 = \mathbf{X}_1 = \mathbf{0}, \text{ and } \mathbf{X}_2 = \mathbf{I}. \tag{3.50}$$

Thus,

$$\mathbf{S_1} = \lim_{n\to\infty} \mathbf{X}_n \left[\mathbf{X}_{n-1}\right]^{-1}, \tag{3.51}$$

where $\mathbf{S_1}$ is the dominant solvent of $\mathbf{D}$, that is, the factor that contains the eigenvalues with the maximum modulus. It is apparent that the transformation, Equation (3.36), controls the subset of the eigenvalue spectrum to be calculated, since the modulus of μ becomes very large if α is in the vicinity of s.

3.3.3 Local Refinement Method

A locally convergent algorithm can be utilized to find a single eigenvalue if a sufficiently good guess is available. One such algorithm is the Newton-Raphson iteration method in compact matrix form by Lancaster [58]. In this algorithm, the roots of the eigenvalue

spectrum, $\sigma(\alpha)$, are evaluated using the iterative formula

$$\alpha_{i+1} = \alpha_i - \frac{\Delta\sigma(\alpha_i)}{\Delta\sigma^{(1)}(\alpha_i)}, \tag{3.52}$$

where $\sigma^{(1)}$ is the first derivative of the eigenvalue spectrum with respect to α, and $i = 0, 1, \ldots,$ is the number of iteration steps. However, the determinant and its derivative are not calculated explicitly. Instead, the trace theorem of Davidenko [60] is used. Then, the Newton iteration method in compact matrix form can be written as

$$\alpha_{i+1} = \alpha_i - \frac{1}{f(\alpha_i)} \tag{3.53}$$

where

$$f(\alpha_i) = \mathrm{Tr}\left\{\mathbf{D}^{-1}(\alpha_i)\,\mathbf{D}^{(1)}(\alpha_i)\right\}.$$

Tr denotes the trace, $\mathbf{D}^{-1}$ is the inverse of $\mathbf{D}$ and $\mathbf{D}^{(1)}$ represents the first derivative of $\mathbf{D}$ with respect to α. This algorithm, Equation (3.53), is quadratically convergent.

To compute a single eigenvector, inverse iteration is used

$$\mathbf{D}(\alpha)\,\mathbf{p}_{i+1} = \lambda\mathbf{p}_i, \tag{3.54}$$

where λ is a scaling factor. In each iteration step, the evaluated eigenvector is normalized by the scaling factor to prevent numerical over-flow. Usually, the 2-norm or the ∞-norm is used as the scaling factor. This method is very effective in computing the eigenvector, even when $\mathbf{D}(\alpha)$ is nearly singular. Convergence is often obtained in a few iteration steps with an initial guess, $\mathbf{p}_0 = [1, 1, \ldots, 1]^T$.

3.3.4 Practical Implementation

In general, all three numerical schemes outlined in the earlier subsections can be used to solve the non-linear eigenvalue problem posed by Equation (3.31). Using the LCMM, the non-linear eigenvalue problem is converted into an algebraic one, and a globally convergent algorithm such as the QR algorithm can be used in the computation of the eigenvalues. The MFM, on the other hand, only solves for a subset of the entire eigenvalue spectrum, since in hydrodynamic problems, not all eigenvalues are of physical interest. If a good initial guess is available, obtained from either the LCMM or the MFM, the Newton iteration in compact matrix form can be used for the refinement of selected eigenvalues and the associated eigenvector.

For axisymmetric jets, the number of nodes required in order to obtain a converged solution is rather small. Typically, a sufficiently accurate solution, compared with the shooting method, is calculated with $N \leq 201$. Therefore, memory requirement and computation

time are not important issues. However, these become constraints in two-dimensional calculations. The increase in computation time becomes very significant when the problem is extended from axisymmetry to two-dimensions. For the QR algorithm, the number of floating point operation is of order $O(N^3)$, where N is the size of the matrix. In the LCMM, the order of the matrix is increased from N to $3N$, so the floating point operations are of order $O(27N^3)$. This can be very costly!

It is clear that in order to obtain a more accurate solution, more grid points should be used in the FEM discretization. However, the memory requirement limits the number of nodes that can be used. Table 3.1 shows the memory requirements for each of the schemes. To obtain an accurate solution in two-dimensional calculation, $N = 2501$ grid points have to be used. Under this condition, both the computation time and the memory requirement of using the LCMM is comparable to that of direct numerical simulations. This defeats the purpose of the present study. Therefore, the choice of using the MFM or Newton iteration to solve non-linear hydrodynamic problems is evidenced from the perspective of the reduction in computation time and memory requirement. However, at $N = 2501$, the memory requirement can still be a constraint for the MFM and the Newton iteration method.

Table 3.1. Memory requirement of different numerical schemes.

Method	Memory Requirement	$N = 2501$ (MB)
LCMM	$9N^2 + 6N$	450
MFM	$5N^2$	250
Newton Iteration	$4N^2$	200
Optimized MFM	$2N^2 + N$	100

It will be shown in the next chapter that even with one Bernoulli iteration step, the dominant solvent for the matrix polynomial is obtained with reasonable accuracy. This drastically reduces the memory requirements in the MFM. The inverse iteration method can then be used to calculate single eigenvalues and the associated eigenvectors. However, this method requires the inversion of the dominant solvent. To further reduce the computation time, the power iteration method is utilized instead. Since the dominant solvent contains the eigenvalue with the maximum modulus, convergence of the desired eigenvalue using the power iteration method can be ensured.

3.4 Contour Deformation

The evaluation of amplifying instability waves from the compressible Rayleigh equation is relatively straightforward. However, difficulty is encountered if neutral or decaying solutions are sought. This results from the mathematical dilemma, as the general form of

the solution, $\hat{p}$, is multiple-valued. A singularity occurs when the mean flow velocity is equal to the phase velocity of the instability waves, that is,

$$\bar{w} = c = \frac{\omega}{\alpha}. \tag{3.55}$$

This is known as the critical velocity. To determine the critical point, ζ_c, the phase velocity, c, is written as a Taylor series expansion,

$$c_r + ic_i = c_r + i\delta\frac{\partial\bar{w}(c_r)}{\partial\zeta} + O(\delta^2), \tag{3.56}$$

where δ is the distance in the complex plane, as shown in Figure 3.2. If the second- and higher-order terms are ignored, the Taylor series can be simplified into

$$\delta = c_i \Big/ \frac{\partial\bar{w}(c_r)}{\partial\zeta}. \tag{3.57}$$

This expression provides a functional relation between δ and the derivative of the mean velocity profile.

For growing modes, $\alpha_i < 0$ so that $c_i > 0$, the sign of the first derivative of the velocity profile determines the location of the critical point in the complex plane. If the sign is positive, then δ is greater then zero. This implies that the critical point lies above the real axis. If the sign is negative, the critical point is below the real axis. Since the choice of branch cut for the logarithmic function in the general form of the solution can be arbitrary, it is chosen such that the branch cut does not cross the real axis for growing modes (see Figure 3.2).

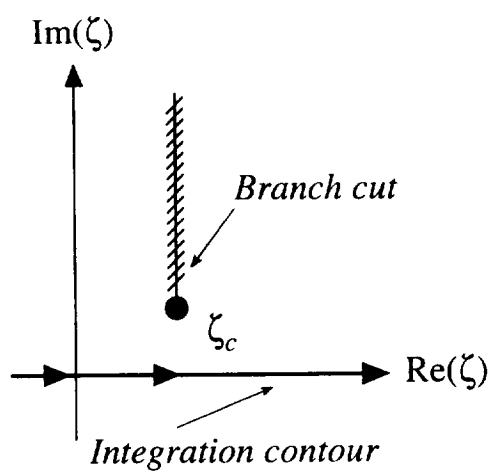

Figure 3.2. A schematic of the choice of branch cut for the logarithmic function and the location of the critical point, ζ_c.

However, as the solution approaches the neutral point and eventually becomes a decaying

mode, the critical point crosses the real axis and the branch cut intercepts the real axis. To avoid this singularity, the integration contour has to be deformed into the complex plane, as shown in Figure 3.3.

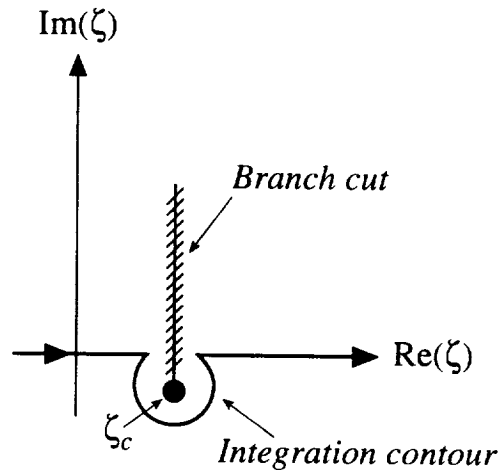

Figure 3.3. A schematic of the detoured integration contour.

The implementation of the detoured integration path in the shooting method is quite easy. A similar procedure also can be applied to derive the local element matrices in the FEM. However, a more elegant technique is to employ a complex mapping method by Boyd [61]. In this technique, any given second-order ordinary differential equation in the form

$$a_2(r)\frac{1}{r}\frac{d}{dr}\left(r\frac{d\hat{p}}{dr}\right) + a_1(r)\frac{d\hat{p}}{dr} + a_0(r)\hat{p} = 0, \tag{3.58}$$

with a mapping function such that

$$r = h(\zeta), \tag{3.59}$$

may be mapped into a computational plane such that the integration path in the computational plane is detoured in the physical plane. The transformed differential equation in the mapped plane is given by

$$\frac{a_2}{(h_\zeta)^2}\frac{d^2\hat{p}}{d\zeta^2} + \left\{\frac{a_2}{hh_\zeta} - \frac{a_2 h_{\zeta\zeta}}{(h_\zeta)^3} + \frac{a_1}{h_\zeta}\right\}\frac{d\hat{p}}{d\zeta} + a_0\hat{p} = 0, \tag{3.60}$$

where

$$h_\zeta = \frac{dh}{d\zeta} \text{ and } h_{\zeta\zeta} = \frac{d^2h}{d\zeta^2}.$$

In the current analysis, the following mapping function is chosen,

$$r = \zeta + i\delta\exp\left\{-\epsilon\left[\zeta - \mathrm{Re}(r_c)\right]^2\right\}, \tag{3.61}$$

where r is the detoured integration contour, r_c is the critical point in the physical plane, and

$\epsilon \gg 1$ to enforce the mapping to hug the real axis after the detour. The use of the mapping formula in Equation (3.60) thus provides the means to perform the contour deformation without re-deriving the local finite element matrices using a complex integration contour.

3.5 Summary

In this chapter, the weak formulations of the axisymmetric and the general form of the compressible equation is derived using the finite element Galerkin method. The shape functions of both the linear line element and linear triangular element can be readily employed to develop the local element matrices, and the derivation of these matrices are described in Appendix B. Different numerical solution techniques are outlined, and the feasibility of the practical implementation of these methods in two-dimensional calculations are discussed. A complex transformation method is also described. This method offers a more elegant approach to perform the complex integration contour deformation in the FEM. In the next chapter, the results from both the shooting method and the FEM are presented. Different numerical techniques outlined in this chapter are applied in the solution of the non-linear eigenvalue problem. The effects of confinement on jets with circular and elliptic exit geometries are discussed.

Chapter 4

RESULTS AND DISCUSSIONS

In this chapter, the instability waves of confined supersonic jets are analyzed using the numerical methods outlined in Chapter 3. Due to the simplicity and the ease of obtaining results using the shooting method, an axisymmetric jet is studied first in order to understand the effects of confinement on jets. Various characteristics exhibited in confined jets that are absent in free jets are discussed. Moreover, the numerical results from the shooting code are used to validate the FEM codes. Since it is computationally inexpensive to solve the axisymmetric form of the compressible Rayleigh equation using the axisymmetric formulation of the FEM, this provides the means to explore the different numerical techniques for the solution of the non-linear eigenvalue problem. Once the FEM code is benchmarked, various aspects of asymmetric confined jets are examined. These include the effects of varying the aspect ratio of the ducts and the jets. Finally, the stability properties of confined elliptic jets are presented, and comparisons are made between these results and those of free elliptic jets calculated by Morris and Bhat [40].

4.1 Circular Jets in Circular Shroud

In this section, the results from the instability wave analysis of a circular jet in a circular duct are presented. Due to the simple geometry of the problem, the axisymmetric form of the compressible Rayleigh equation is solved using the shooting method. In order to analyze the instability wave characteristics of a confined, axisymmetric jet, the mean velocity profile must be provided, as stated in Chapter 2. In the present analysis, the mean flow profiles and characteristic parameters of perfectly expanded supersonic jets measured by Eggers [62], Birch and Eggers [63], Lau *et al.* [64], and Lau [65] are used in the calculation of the instability waves. The mean flow profile can be approximated by

$$\bar{w}(r) = \begin{cases} \bar{W}_j, & r \leq h, \\ \bar{W}_j \exp\left[-\ln(2)\left(\dfrac{r-h}{b}\right)^2\right], & r > h, \end{cases} \tag{4.1}$$

where $\bar{W}_j$ is the centerline jet velocity, h is the radius of the potential core, and b is the half-width of the mixing layer. A schematic of the various regions in the mean flow velocity profile is shown in Figure 4.1.

Using this model, the radius of the uniform core, h, and the half-width of the mixing layer, b, have to be evaluated before the mean flow velocity profile can be employed. The

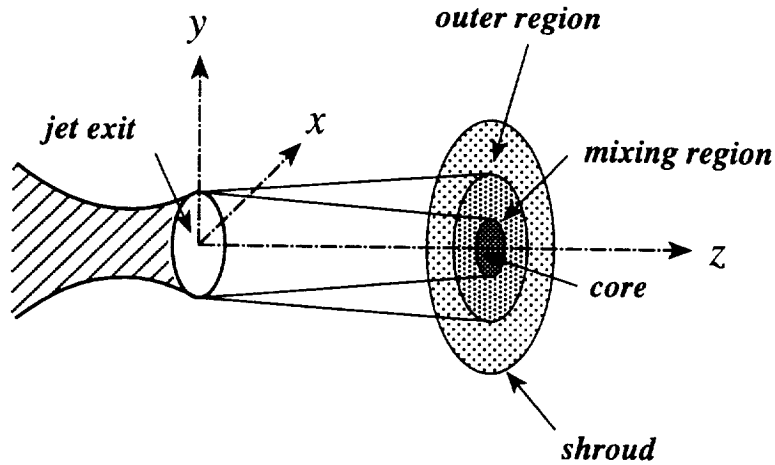

Figure 4.1. A schematic of the mean flow velocity profile of a jet.

conservation of momentum is used to derive a relation between the two parameters, b and h, given by

$$\int_0^\infty \int_0^{2\pi} \bar{\rho}\bar{w}^2 \, r d\theta \, dr = \int_0^{R_j} \int_0^{2\pi} \bar{\rho}_j \bar{w}_j{}^2 \, r d\theta \, dr, \tag{4.2}$$

where R_j is the radius of the jet. A local similarity variable is defined,

$$\eta = \frac{r-h}{b}, \tag{4.3}$$

and one part of the integration can be re-written as

$$\int_h^\infty \bar{\rho}\bar{w}^2 r dr = b^2 \int_0^\infty \bar{\rho}(\eta)\bar{w}^2(\eta)\, \eta \, d\eta + bh \int_0^\infty \bar{\rho}(\eta)\bar{w}^2(\eta)\, d\eta. \tag{4.4}$$

In fact, this gives a quadratic equation in terms of h and b such that

$$\frac{h^2}{2} + C_1 b^2 + C_2 hb = \frac{R_j^2}{2} \tag{4.5}$$

where

$$C_1 = \int_0^\infty \bar{\rho}(\eta)\bar{w}^2(\eta)\, \eta \, d\eta \tag{4.6}$$

and

$$C_2 = \int_0^\infty \bar{\rho}(\eta)\bar{w}^2(\eta)\, d\eta. \tag{4.7}$$

This quadratic equation provides the functional relation between the potential core radius, h, and the mixing layer half-width, b, and can be solved numerically.

To evaluate the effects of confinement on axisymmetric jets, the operating conditions in Reference [50] for a supersonic, unheated jet in a circular dump of 2 equivalent jet radii, $r_w = 2.0$, and with $M_j = 4.0$ are simulated. For the existence of supersonic instability

waves, the following condition must be satisfied:

$$\bar{W}_j^* - \bar{W}_2^* > \bar{a}_j^* + \bar{a}_2^*, \tag{4.8}$$

where $\bar{W}_j^*$ and $\bar{W}_2^*$ are the dimensional speed of the jets and the ambient air respectively. In the current study, the ambient air is assumed to be stationery, so $\bar{W}_2^* = 0$. $\bar{a}_1^*$ is the dimensional speed of sound in the jet and $\bar{a}_2^*$ is the sound in the ambient medium. Physically, the supersonic instability waves can be generated by heating the jet. However, to avoid introducing the effects of heating into the present analysis, a very high Mach number is chosen instead.

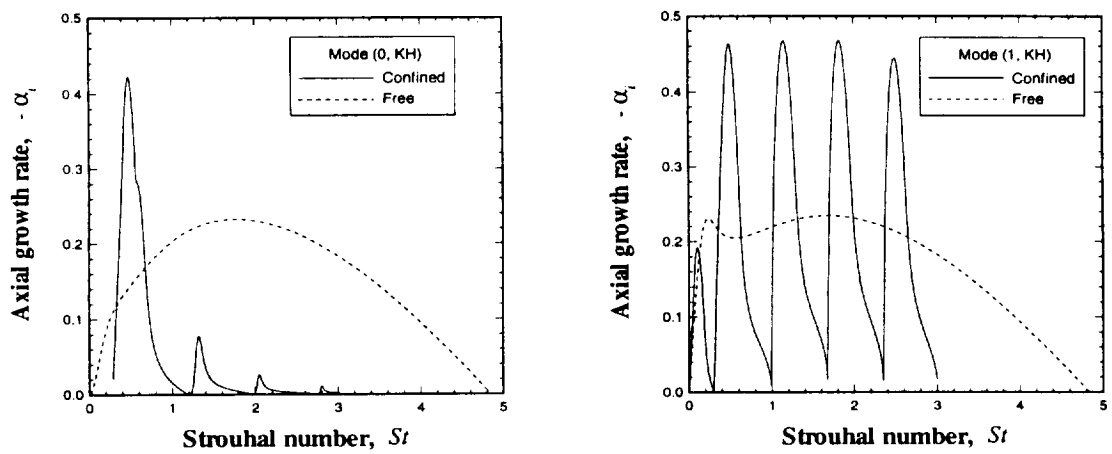

(a) (b)

Figure 4.2. Variation of axial growth rate of the Kelvin-Helmholtz instabilities with Strouhal number for a confined and unconfined axisymmetric jet. $M_j = 4.0$, unheated, $b = 0.1$. (a) $n = 0$ axisymmetric mode, (b) $n = 1$ helical mode.

In Figures 4.2a and 4.2b, the axial growth rate of the axisymmetric and $n = 1$ helical Kelvin-Helmholtz instability waves for both a confined and an unconfined supersonic jets are shown. The low spreading rates of high Mach number, free jets have been observed both experimentally and analytically. However, in the presence of a dump, the growth rates of the Kelvin-Helmholtz instability waves are increased by almost 100% for both the axisymmetric mode and the helical modes. Moreover, the growth rates have a highly oscillatory behavior with the Strouhal number. At high frequencies, the Kelvin-Helmholtz instability waves for a free jet become decaying waves. One the other hand, for a confined jet, the waves become almost neutral and then start to increase again. This is especially evident in the $n = 1$ helical mode as shown in Figure 4.2b. This characteristic is due to the reinforcement and cancelation of the instability waves by the interaction of the internal Mach wave system of the jet and the external reflected waves from the outer wall. Since the growth rate curve is almost neutral at certain frequencies, the complex integration contour deformation

described in Chapter 3 has to be employed in order to capture this oscillatory behavior. It is interesting to note that Kelvin-Helmholtz instability waves do not exist at very low frequencies for the axisymmetric mode, and the peak of the growth rate curve decreases at high frequencies.

Due to the influence of the outer wall, additional instability waves can be found if the existence condition of Equation (4.8) is satisfied [49]. Since the additional waves are traveling at supersonic speeds, they are known as the supersonic instability waves. As in Reference [66], the radial mode number of the instability waves is determined by the number of antinodes in the amplitude of the perturbation pressure eigenfunction inside the jet potential core. The pressure perturbation eigenfunctions for the $n = 0$ axisymmetric and the $n = 1$ helical mode are shown in Figures 4.3 and 4.4. The growth rate and the phase speed curves of the Kelvin-Helmholtz and supersonic instability waves for various azimuthal modes ($n = 0$ and $n = 1$) are shown in Figures 4.5, 4.6, 4.7, 4.8 respectively. Unlike the observations made by Viswanathan *et al.* [50], the oscillatory characteristics of the growth rate curves are also present in the supersonic instability modes, and are not just confined to the low frequency range. The Kelvin-Helmholtz instability waves are dominant for both azimuthal modes, while the growth rate of the supersonic modes is comparable to that of the Kelvin-Helmholtz instabilities in the unconfined case.

Comparisons of the growth rates between the different azimuthal modes for the Kelvin-Helmholtz and the supersonic instability waves are shown in Figures 4.9 and 4.10. For the Kelvin-Helmholtz instability waves with $b = 0.1$, the $n = 2$ helical mode is the most unstable in the low frequency range, that is, $St < 1.0$. At high frequency, the $n = 1$ helical mode becomes the most unstable one. Over the entire frequency spectrum, the $n = 0$ axisymmetric mode is the most stable. In contrast, the growth rates of the different azimuthal modes are approximately of the same magnitude for the supersonic instability modes. As the frequency increases, the growth rate of the supersonic instability waves decreases. The reinforcement and cancelation of the instability waves caused by the interaction of the internal Mach waves and the external reflected waves can be illustrated by examining the pressure perturbation eigenfunctions.

In Figures 4.11, 4.12, 4.13, 4.14, 4.15, and 4.16, the amplitude of the pressure perturbation eigenfunctions for different instability waves at various Strouhal numbers are plotted. In order to make a qualitative comparison of the different pressure perturbation eigenfunctions, the amplitude of the fluctuation pressures have been normalized by the absolute maximum value to ensure that the values lie in the range of 0.0 to 1.0. The Strouhal numbers correspond to the peaks in the growth rate curves. While the pressure fluctuations decay exponentially in the exterior region for unconfined jets, it is observed that pressure oscillations exist in the outer region for confined jets. As the Strouhal number increases, the number of antinodes in the pressure perturbation outside the jets increases, indicating the

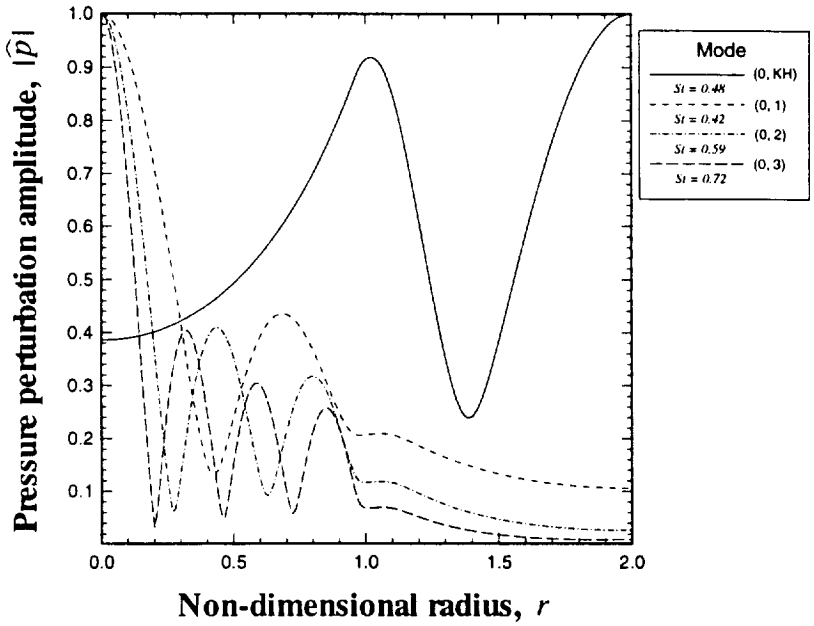

Figure 4.3. Pressure perturbation amplitude of the Kelvin-Helmholtz and the supersonic instability waves. $M_j = 4.0$, unheated, $b = 0.1$, $r_w = 2.0$, $n = 0$ mode.

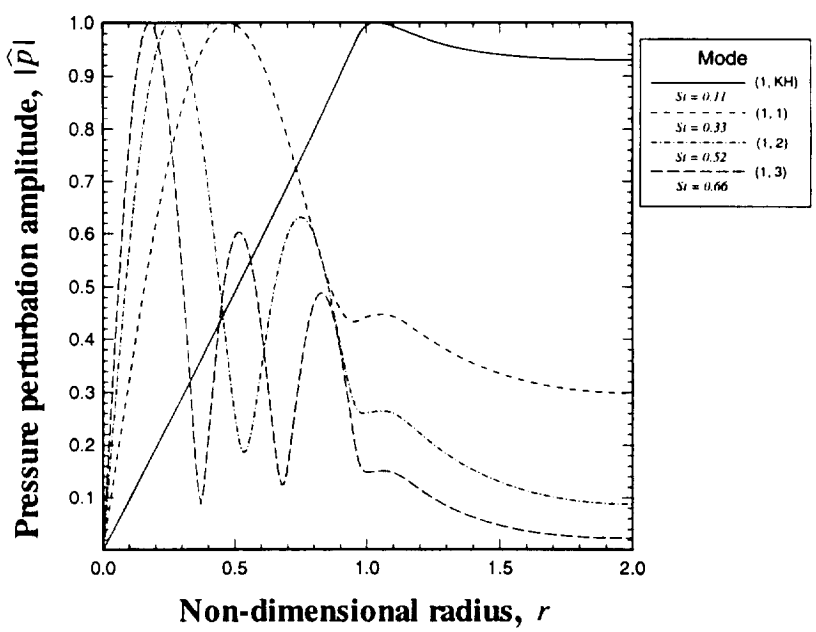

Figure 4.4. Pressure perturbation amplitude of the Kelvin-Helmholtz and the supersonic instability waves. $M_j = 4.0$, unheated, $b = 0.1$, $r_w = 2.0$, $n = 1$ mode.

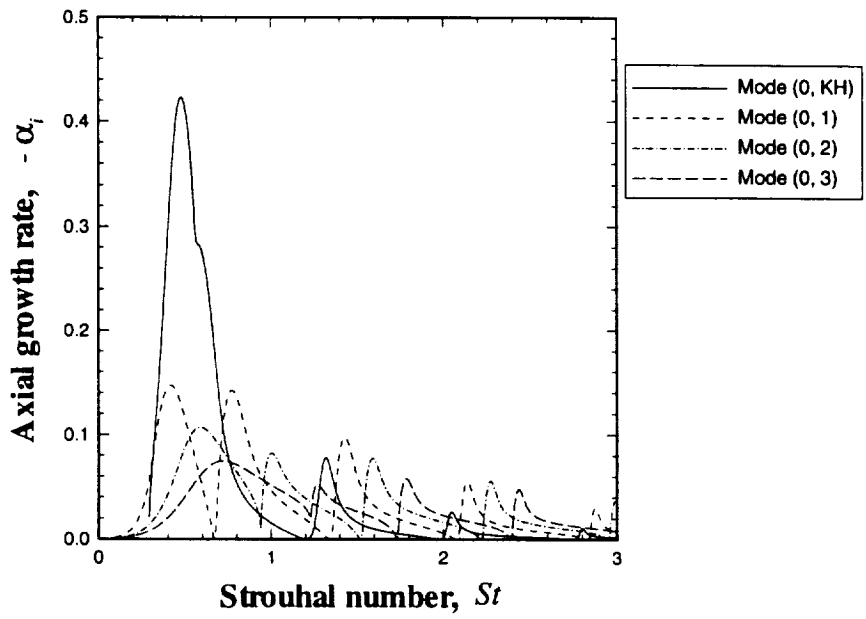

Figure 4.5. Variation of axial growth rate with Strouhal number in a confined axisymmetric jet. $M_j = 4.0$, unheated, $b = 0.1$, $r_w = 2.0$, $n = 0$ mode.

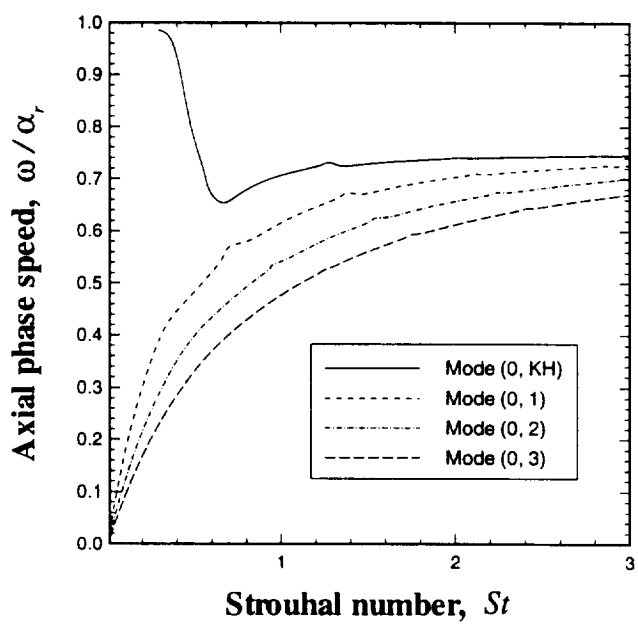

Figure 4.6. Variation of axial phase speed with Strouhal number in a confined axisymmetric jet. $M_j = 4.0$, unheated, $b = 0.1$, $r_w = 2.0$, $n = 0$ mode.

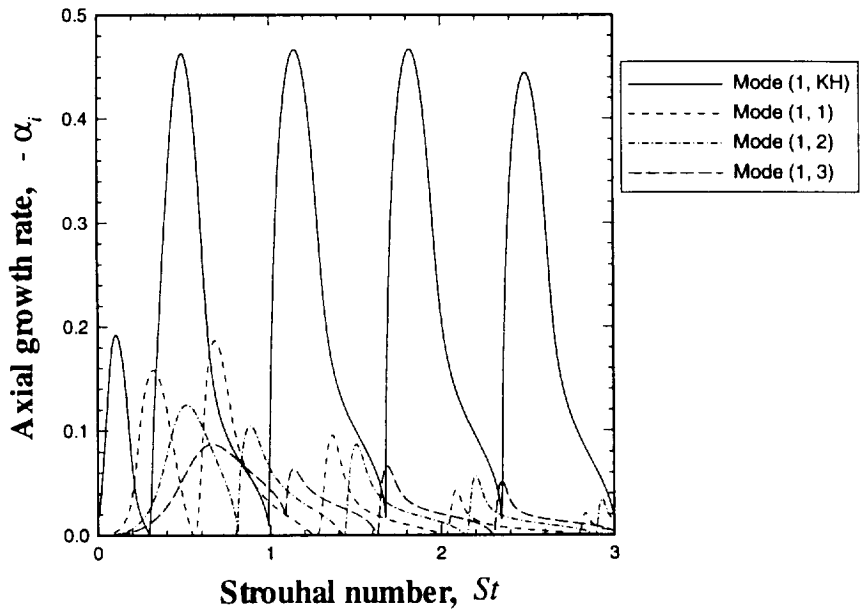

Figure 4.7. Variation of axial growth with Strouhal number in a confined axisymmetric jet. $M_j = 4.0$, unheated, $b = 0.1$, $r_w = 2.0$, $n = 1$ mode.

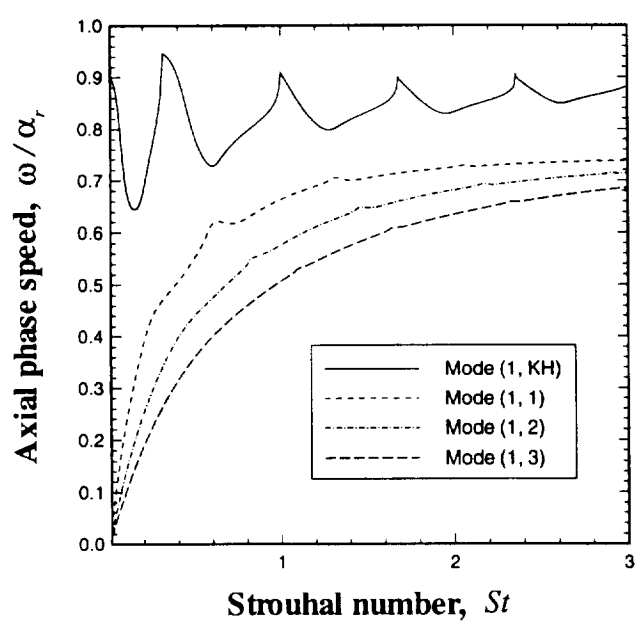

Figure 4.8. Variation of axial phase speed with Strouhal number in a confined axisymmetric jet. $M_j = 4.0$, unheated, $b = 0.1$, $r_w = 2.0$, $n = 1$ mode.

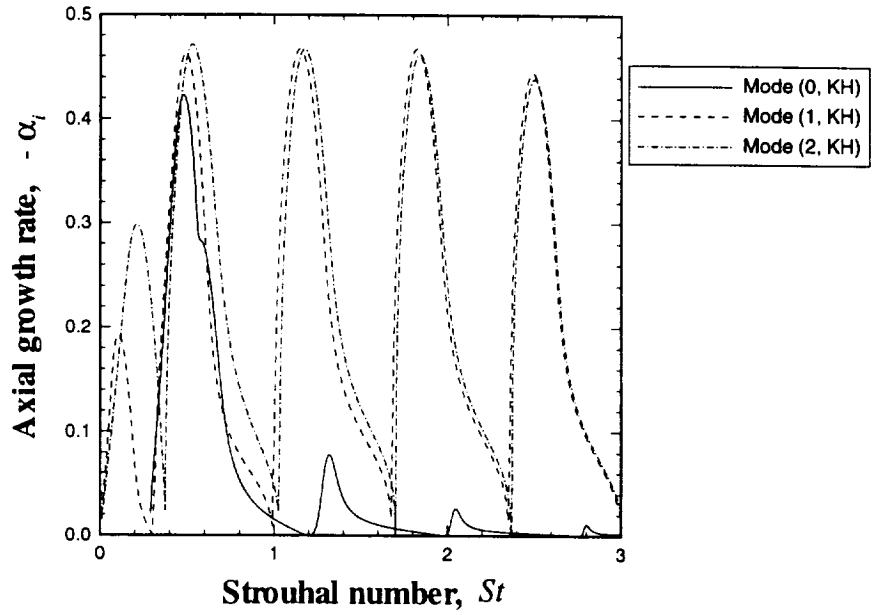

Figure 4.9. Variation of axial growth rate with Strouhal number at different azimuthal modes. $M_j = 4.0$, unheated, $b = 0.1$, $r_w = 2.0$, Kelvin-Helmholtz instability waves.

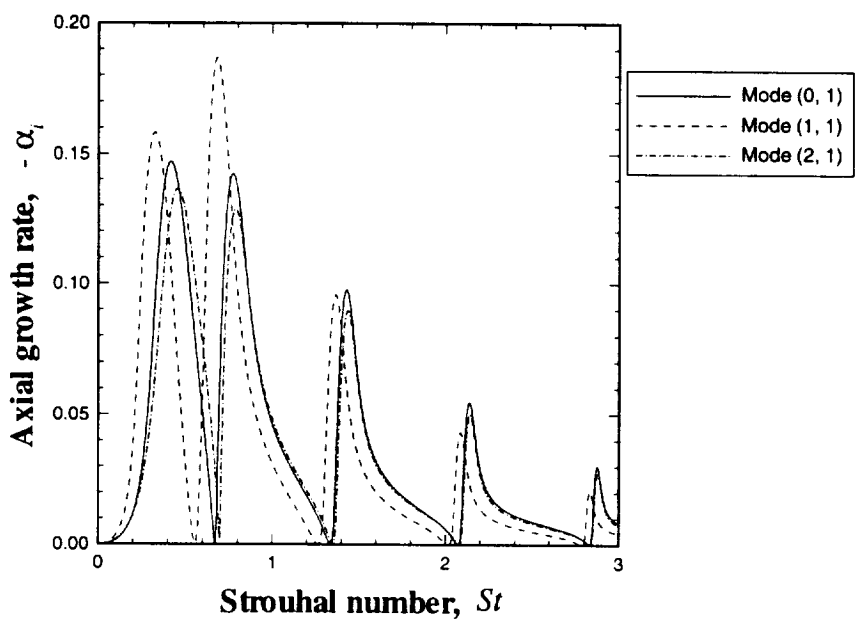

Figure 4.10. Variation of axial growth rate with Strouhal number at different azimuthal modes. $M_j = 4.0$, unheated, $b = 0.1$, $r_w = 2.0$. supersonic instability waves.

interaction between the instability waves and the reflected waves. The lower radial modes, with longer radial wavelengths, are more susceptible to the reflections due to the outer wall than the higher radial modes with shorter wavelengths. This can be shown from the relative amplitude of the pressure oscillations inside and outside the jets.

To examine the effect of outer wall radius, the growth rate of the helical Kelvin-Helmholtz (1,KH) and (1,1) supersonic instability waves, as a function of wall height, are shown in Figure 4.17. The oscillations in the growth rate curves are very significant at high frequency ($St = 1.50$) for both the helical Kelvin-Helmholtz and supersonic instability modes. At low frequency ($St = 0.11$), the oscillatory behavior is still present, but not as dramatic as in the high frequency case. The amplitude of the pressure eigenfunctions at various radii associated with the helical Kelvin-Helmholtz mode at $St = 1.50$ are shown in Figure 4.18. As the radius of the wall is decreased, the external pressure oscillations moves towards the mixing layer. This observation has also been made by Viswanathan *et al.* [50] using a vortex sheet model to represent the jet.

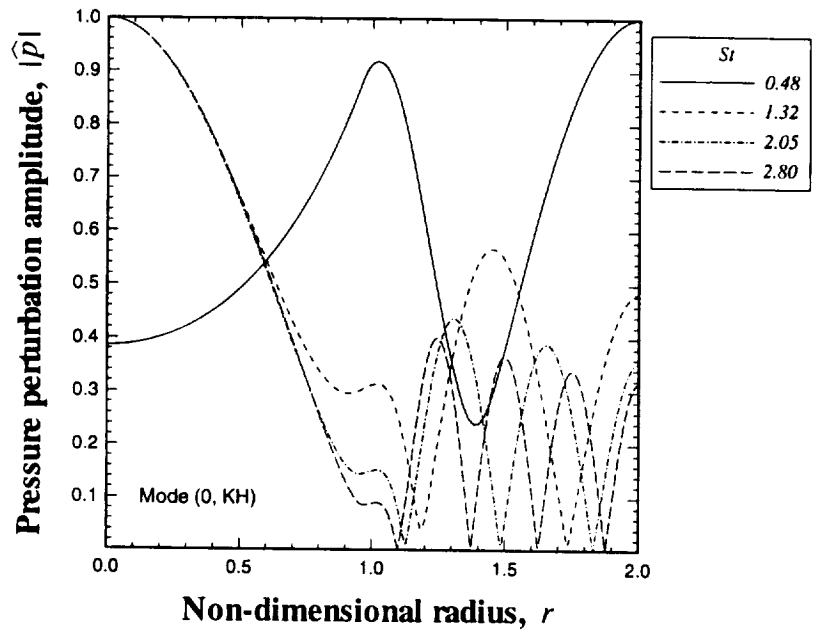

Figure 4.11. Pressure perturbation amplitude of the $n = 0$ axisymmetric Kelvin-Helmholtz instability waves at various Strouhal numbers.

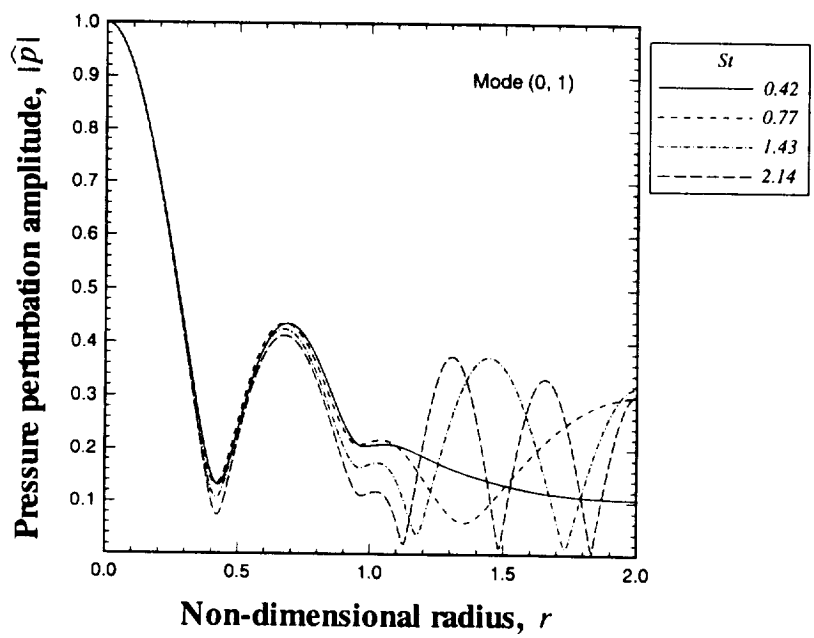

Figure 4.12. Pressure perturbation amplitude of the $(0, 1)$ axisymmetric supersonic instability waves at various Strouhal numbers.

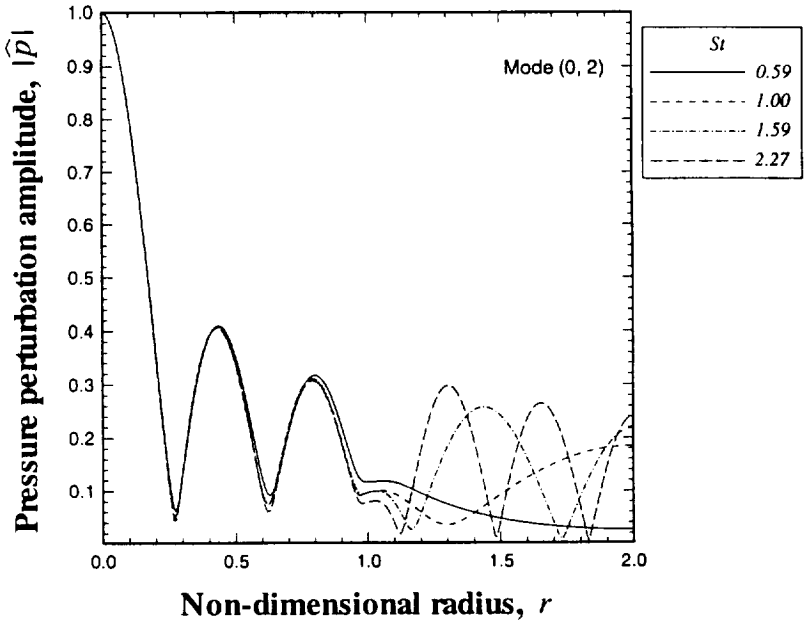

Figure 4.13. Pressure perturbation amplitude of the $(0, 2)$ axisymmetric supersonic instability waves at various Strouhal numbers.

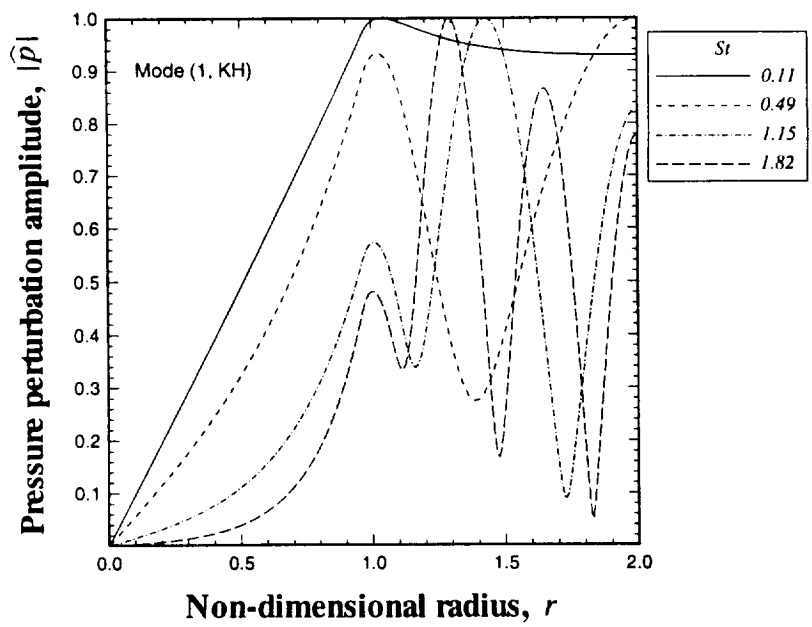

Figure 4.14. Pressure perturbation amplitude of the $n = 1$ helical Kelvin-Helmholtz instability waves at various Strouhal numbers.

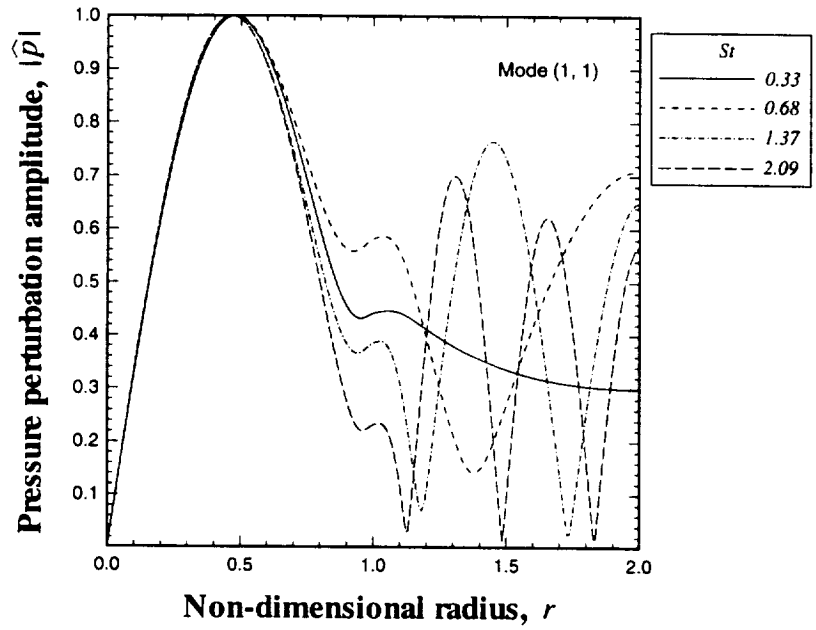

Figure 4.15. Pressure perturbation amplitude of the $(1,1)$ helical supersonic instability waves at various Strouhal numbers.

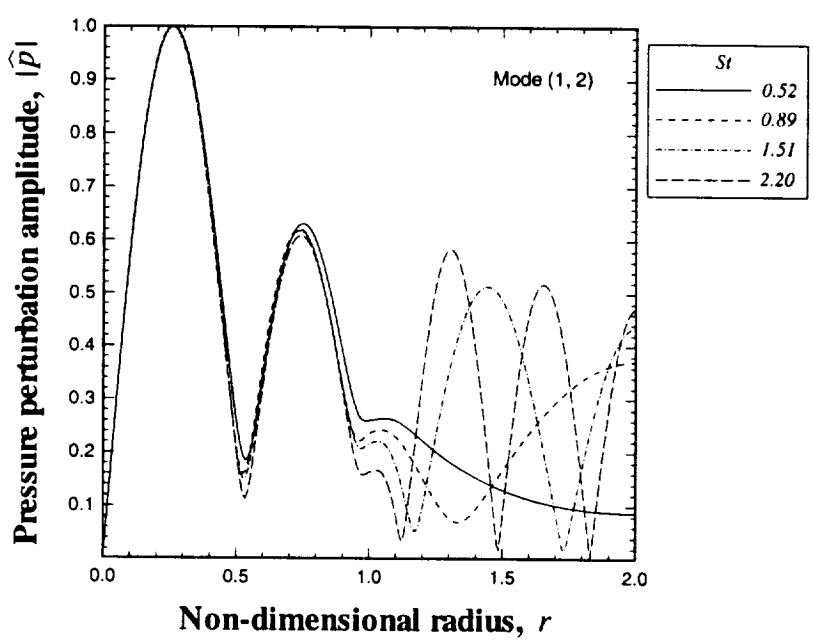

Figure 4.16. Pressure perturbation amplitude of the $(1,2)$ helical supersonic instability waves at various Strouhal numbers.

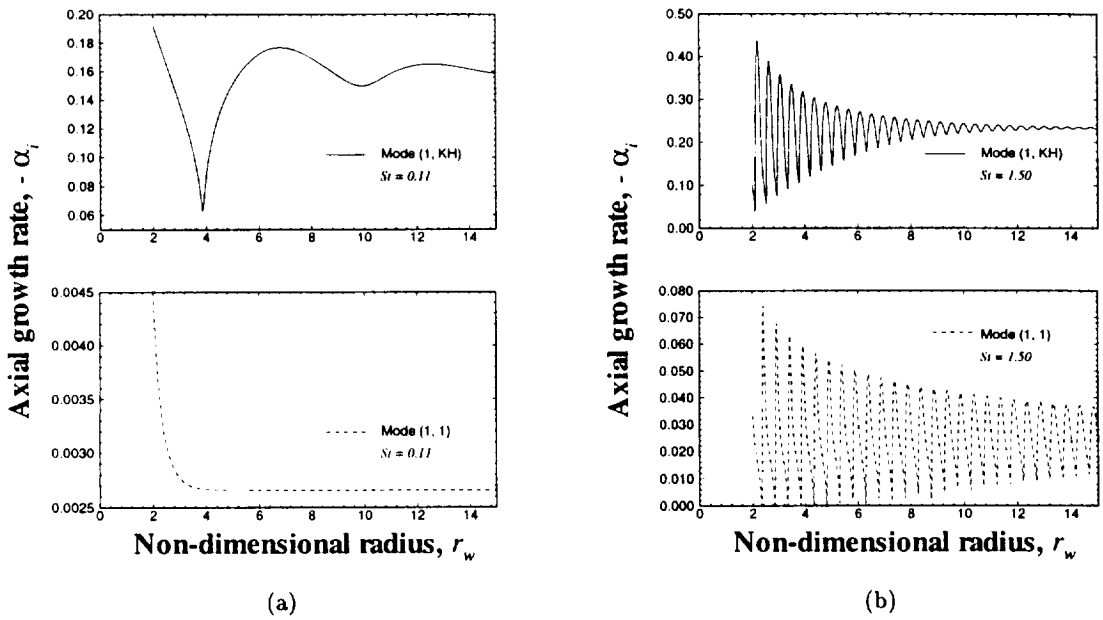

Figure 4.17. The effect of outer wall radius on the growth rates of the (1,KH) and (1,1) modes at (a) $St = 0.11$, and (b) $St = 1.50$. $M_j = 4.0$, $b = 0.1$, unheated jet.

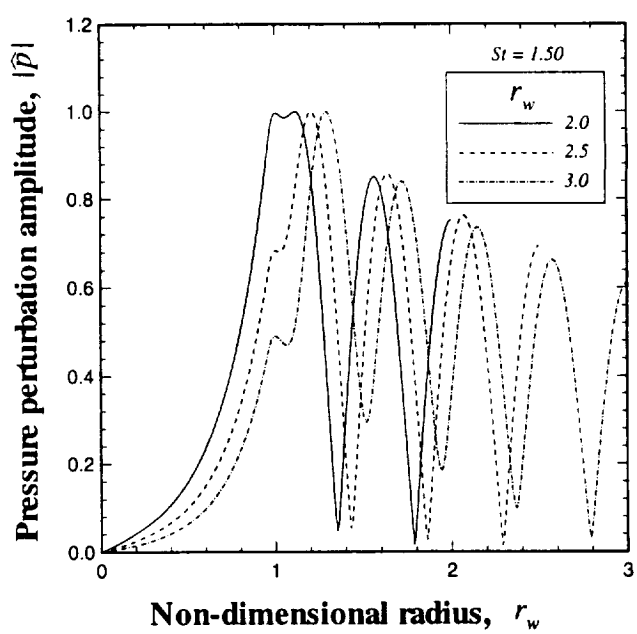

Figure 4.18. The amplitude of the pressure eigenfunction distribution of a helical Kelvin-Helmholtz (1,KH) instability mode at $M_j = 4.0$, $b = 0.1$, $St = 1.50$, unheated jet.

4.2 Validation of FEM Stability Codes

In this section, the results obtained using the FEM are benchmarked with those from the shooting code. Since the problem is axisymmetric for a circular jet confined in a circular duct, the axisymmetric formulation of the compressible Rayleigh equation is examined first. $N = 251$ nodes along the radial direction are used in the FEM with 1D linear shape functions. For a $M_j = 1.5$, unheated circular jet in a circular dump, a table of the convergence history of the wavenumber with the number of grid points is shown in Table 4.1. The percentage error, as shown in the table, is defined as

$$\% \text{ error } = \frac{|\alpha_{\text{anal}} - \alpha_{\text{num}}|}{|\alpha_{\text{anal}}|} \times 100. \tag{4.9}$$

The entire eigenvalue spectrum is calculated using the LCMM and LAPACK subroutines, and is shown in Figure 4.19. The wavenumber associated with the Kelvin-Helmholtz mode is indicated by the arrow. It is interesting to note that not all the wavenumbers in the eigenvalue spectrum are of physical interest. In fact, additional wavenumbers are generated due to the finite element discretization. Moreover, evanescent waves have to be distinguished from amplifying waves. This is done by applying the Briggs-Bers criterion [67, 68]. Under this criterion, it is found that the apparent amplifying waves near the imaginary axis are actually evanescent waves.

Table 4.1. Convergence history of the axisymmetric Kelvin-Helmholtz instability mode with number of grid points, N. $M_j = 1.5$, unheated, $b = 0.1$, $r_w = 2.0$, $St = 0.50$. The wavenumber obtained by the shooting method is (2.1847164, −0.85869151).

N	Wavenumber	Error (%)
51	(2.1568215, −0.84839238)	1.27
101	(2.1705975, −0.84616542)	0.804
151	(2.1734386, −0.84580505)	0.730
201	(2.1745269, −0.84573286)	0.702
251	(2.1750756, −0.84572981)	0.688

It is interesting to note from Table 4.1 the apparent slow convergence of the the numerical wavenumber to the analytical result from the shooting method. As the number of nodes increases, the error should approach machine precision. Further study reveals that this slow convergence is due to the quality of the grid, and in this case, the clustering of the grid points. It is not possible to cluster the grid precisely to capture the oscillation in the pressure eigenfunction *a priori*, unless an adaptive FEM solver is used. However, this type of adaptive scheme is quite expensive to implement computationally, and is not employed in the present study. For Kelvin-Helmholtz instability modes, the oscillations of

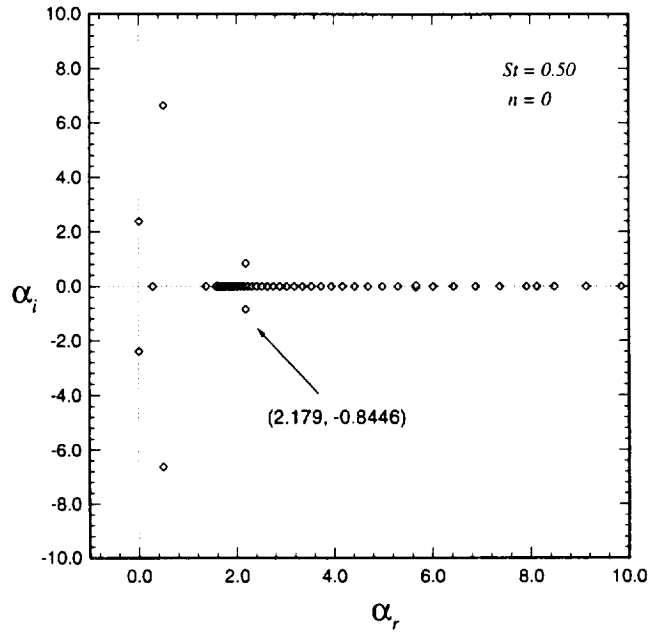

Figure 4.19. Eigenvalue spectrum in the complex wavenumber plane for a circular confined jet. $M_j = 1.5$, unheated, $b = 0.1$, $r_w = 2.0$.

the fluctuation pressures occur inside the shear layer, so the grid is clustered in this region. Since this clustering is not optimized, this causes the apparent slow convergence of the wavenumber.

The advantage of using the LCMM is that the entire eigenvalue spectrum of the wavenumbers at a fixed frequency is computed. However, to evaluate the characteristics of the instability waves over a frequency range, it is more efficient to solve the equation using a local iterative method. In the present study, the Newton iteration method is employed to evaluate the complex wavenumber at each frequency. The grid points are also clustered at the mixing layer in order to resolve the oscillations in the pressure eigenfunctions. Compared with the shooting method, which makes use of a fifth-order variable step-size Runge-Kutta integration scheme, favorable agreement is achieved. In fact, the percentage of error is less than 1.0% when more than $N = 101$ number of grid points are used. In Figures 4.20 and 4.21, the growth rate and the phase speed curves for the $n = 0$ axisymmetric and $n = 1$ helical instability waves are shown. The FEM solutions compare very well with those of the shooting method. To compute the decaying modes in the limit of infinite Reynolds number, an integration contour has to be detoured into the complex plane to avoid the branch cut. In the shooting method, this is accomplished by integrating numerically in the complex plane. Although the same procedure can be performed using the FEM by re-deriving the local finite element matrices, a more elegant way is to use the mapping method explained in Chapter 3. Using the mapping technique, the growth rate curves from both the shooting

method and the FEM are shown in Figure 4.22. Again, the comparison is remarkably good, with a percentage error less than 1.0%.

At very high Mach numbers, the growth rate of the instability waves for axisymmetric jets exhibit an oscillatory behavior, as discussed in the previous section. Since the instability waves become almost neutral at certain frequencies, the singular point in the governing equation has to be avoided using a complex integration contour deformation. Using the mapping method, the growth rate curve for a $M_j = 4.0$, unheated, axisymmetric jet is obtained using the FEM, as shown in Figure 4.23. While the gross features of the curve can be captured when the growth rates are away from the neutral points, the FEM fails to converge at the frequencies of very low growth rates, ($0.2 < St < 0.3$ and $0.9 < St < 1.0$).

In order to validate the general formulation of the FEM code, FEM2D, the axisymmetric problem is evaluated and compared with that from the shooting method. $N = 1501$ number of nodes are discretized in the solution domain, as shown in Figure 4.24, with Neumann boundary conditions applied at all the boundaries. It has been argued in the previous chapter that it is not feasible to calculate the wavenumbers using the LCMM for the general FEM formulation. This is due to the constraint on memory requirement and the execution time. Therefore, in FEM2D, the wavenumber and the eigenfunction are evaluated using the MFM and the power iteration method. To further reduce the memory requirement, the dominant solvent is computed using only one Bernoulli iteration step. It will be shown that one Bernoulli iteration step provides a very good approximation to the "theoretical" dominant solvent of the matrix polynomial, since numerical results within reasonable accuracy are achieved.

A comparison of the results from the shooting code and FEM2D is shown in Table 4.2 for the $n = 0$ axisymmetric and $n = 2$ helical Kelvin-Helmholtz instability mode of a $M_j = 1.5$, unheated, confined circular jet at $St = 0.50$. Since the same grid is used in the calculation, it is not surprising that the wavenumber of $n = 0$ mode is more accurate than the $n = 2$ mode. From the perspective of azimuthal grid points per wavelength, the $n = 0$ mode has approximately four times the number of azimuthal grid points than the $n = 2$ mode to resolve the perturbation pressure wave. Contour plots of pressure eigenfunctions are shown in Figure 4.25 and 4.26 for the $n = 0$ axisymmetric and $n = 2$ helical modes respectively. A comparison of the pressure eigenfunction amplitudes along the x- and y-axis (see Figures 4.27 and 4.28) with those from the shooting code illustrates the fact that more azimuthal grid points are indeed needed to resolve the higher order instability modes. For the $n = 2$ Kelvin-Helmholtz instability mode, there is a slight discrepancy in the pressure eigenfunction along the y-axis, as shown in Figure 4.28.

Comparisons between the growth rate and phase speed curves from the shooting code and the FEM2D are shown in Figures 4.29 and 4.30. It is possible to analyze the characteristics of the instability waves over a range of frequencies using the FEM2D. However,

Table 4.2. Comparison of results from shooting code and FEM2D for different azimuthal modes.

n	Shooting Code	FEM2D	Error (%)
0	(2.1847164, −.85869151)	(2.1852509, −0.83504361)	1.10
2	(2.3557033, −1.0272056)	(2.3823597, −0.98729568)	1.87

the advantage of using a global method to solve hydrodynamic instability problems clearly becomes a disadvantage when the desired instability wave properties are traced over a frequency range. The use of a global method (finite difference, boundary element, finite element, or spectral method) provides the entire eigenvalue spectrum. In the general finite element formulation of the compressible Rayleigh equation, all the radial and azimuthal modes are contained in the resulting matrix system. In theory, there are infinite number of such modes. As the Strouhal number becomes large, and in this case when $St > 1.2$, the wavenumbers become so clustered that the FEM2D is not able to trace the wavenumber of the desired instability mode. However, below this threshold non-dimensional frequency, favorable agreement with the shooting code is obtained.

4.3 Circular Jets in Non-Circular Shroud

In this section, the instability of axisymmetric jets confined in non-circular shrouds is considered. Due to the large number of parameters involved, the jet operating conditions are fixed and taken to be the same as in Section 4.1, that is, $M_j = 4.0$, with no heating and no external flow. The effects of variations in the geometry of the outer shroud on the instability waves are examined, while the primary jet is taken to be circular. Similarly, the effects of duct geometry variations on asymmetric jets can be treated accordingly. However, to eliminate the introduction of additional parameters in the present analysis, a circular jet is chosen instead.

In order to quantify the effects of the duct geometry variations, the shroud is varied from a circular to an elliptic shape of aspect ratio 1.5, while maintaining the same cross-sectional area. It becomes apparent during the study that the quality of the unstructured triangular grid plays a very important role in the convergence of the desired instability modes. It has been discussed earlier that grid clustering is essential in the resolution of the oscillation of the pressure eigenfunction in the confined axisymmetric jet case. In the two-dimensional calculations of circular jets in circular ducts, grids with very skewed elements, as shown in Figure 4.24, can be used, since there is very little azimuthal variations in the pressure eigenfunction. However, as the shroud geometry varies, the interaction between the internal Mach waves and the external reflected waves causes azimuthal variations in the pressure eigenfunctions. These variations have to be resolved by the use of a more locally equilateral mesh, as shown in Figure 4.31.

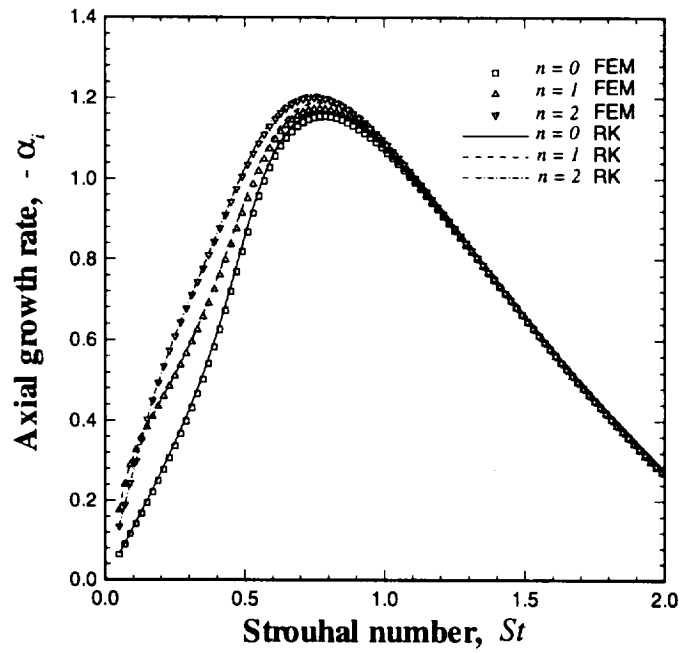

Figure 4.20. Variation of axial growth rate with Strouhal number in a confined circular jet. $M_j = 1.5$, unheated, $b = 0.1$, $r_w = 2.0$.

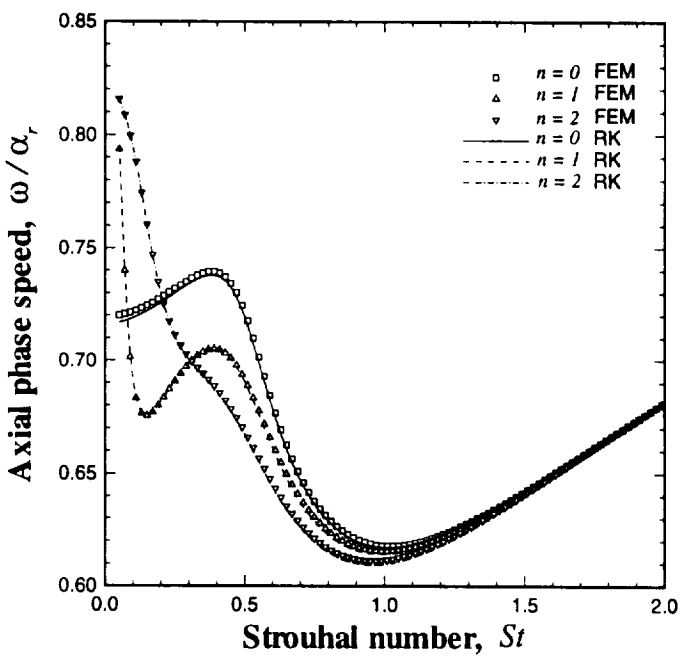

Figure 4.21. Variation of axial phase speed with Strouhal number in a confined circular jet. $M_j = 1.5$, unheated, $b = 0.1$, $r_w = 2.0$.

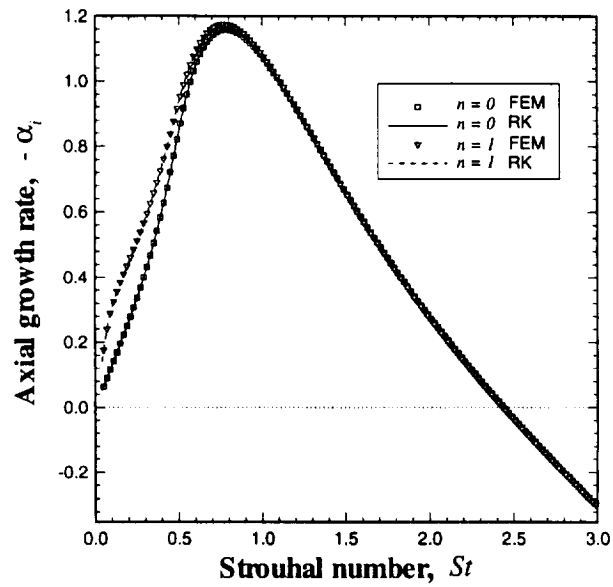

Figure 4.22. Variation of axial growth rate with Strouhal number in a confined circular jet with complex integration contour deformation. $M_j = 1.5$, unheated, $b = 0.1$, $r_w = 2.0$.

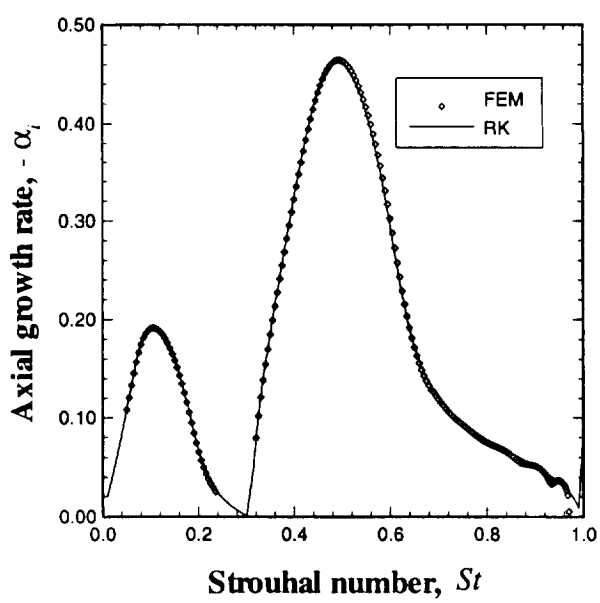

Figure 4.23. Variation of axial growth rate with Strouhal number for the (1,KH) instability mode in a confined circular jet with complex integration contour deformation. $M_j = 4.0$, unheated, $b = 0.1$, $r_w = 2.0$.

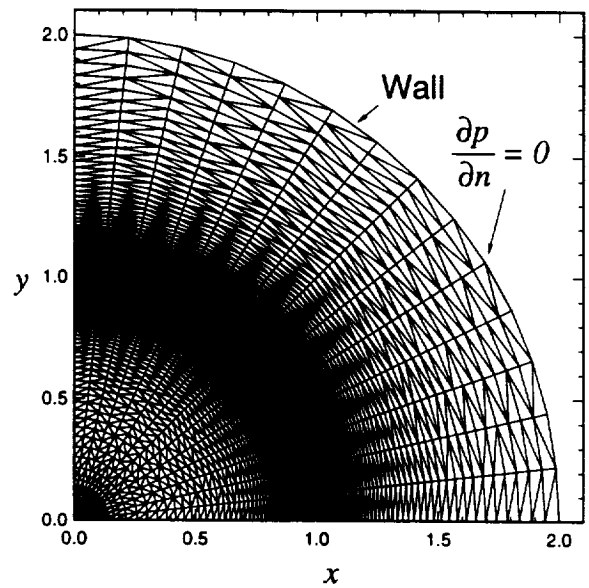

Figure 4.24. A semi-unstructured triangular finite element grid.

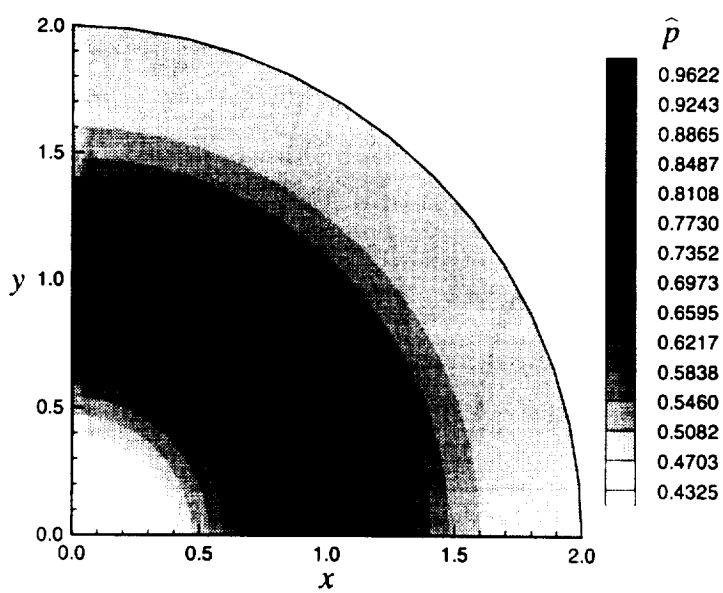

Figure 4.25. Contour plot of the perturbation pressure amplitude for $n = 0$ Kelvin-Helmholtz instability at $St = 0.50$. $M_j = 1.5$, unheated, $b = 0.1$, $r_w = 2.0$.

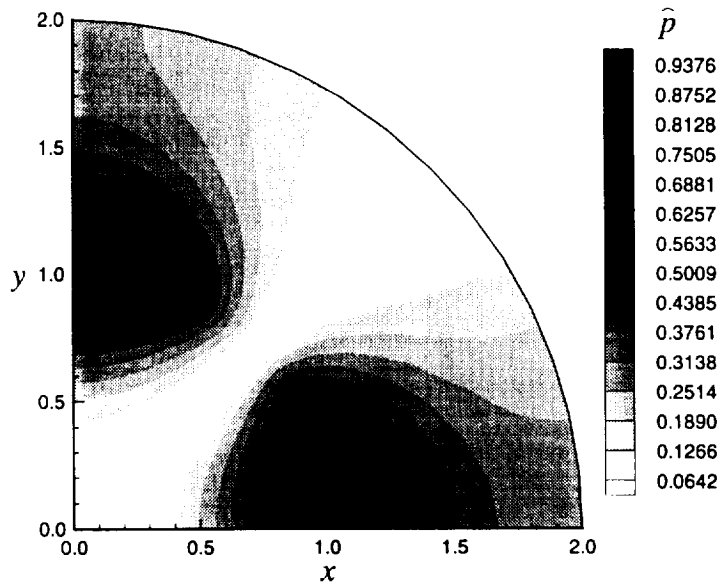

Figure 4.26. Contour plot of the perturbation pressure amplitude for $n = 2$ helical Kelvin-Helmholtz instability at $St = 0.50$. $M_j = 1.5$, unheated, $b = 0.1$, $r_w = 2.0$.

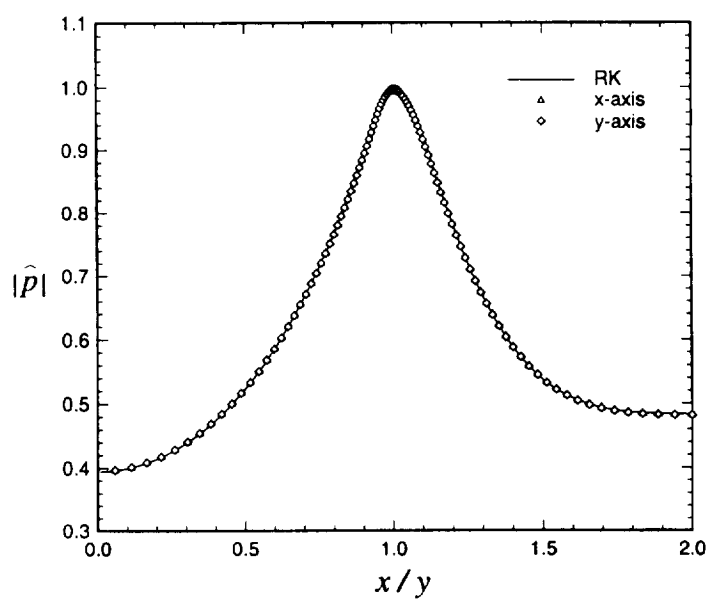

Figure 4.27. Perturbation pressure amplitude for $n = 0$ Kelvin-Helmholtz instability at $St = 0.50$ along the x- and y-axis. $M_j = 1.5$, unheated, $b = 0.1$, $r_w = 2.0$.

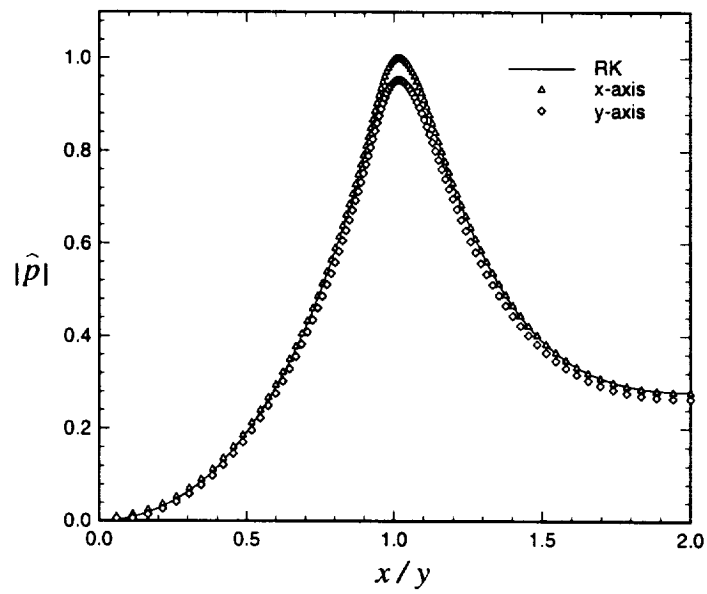

Figure 4.28. Perturbation pressure amplitude for $n = 2$ helical Kelvin-Helmholtz instability at $St = 0.50$ along the x- and y-axis. $M_j = 1.5$, unheated, $b = 0.1$, $r_w = 2.0$.

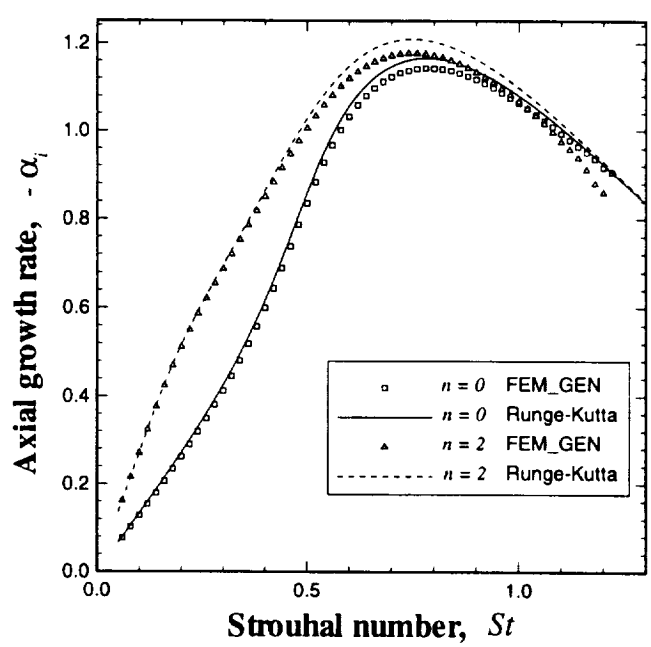

Figure 4.29. Comparison of the growth rate curves from the shooting code and FEM2D for different Kelvin-Helmholtz azimuthal modes. $M_j = 1.5$, unheated, $b = 0.1$, $r_w = 2.0$.

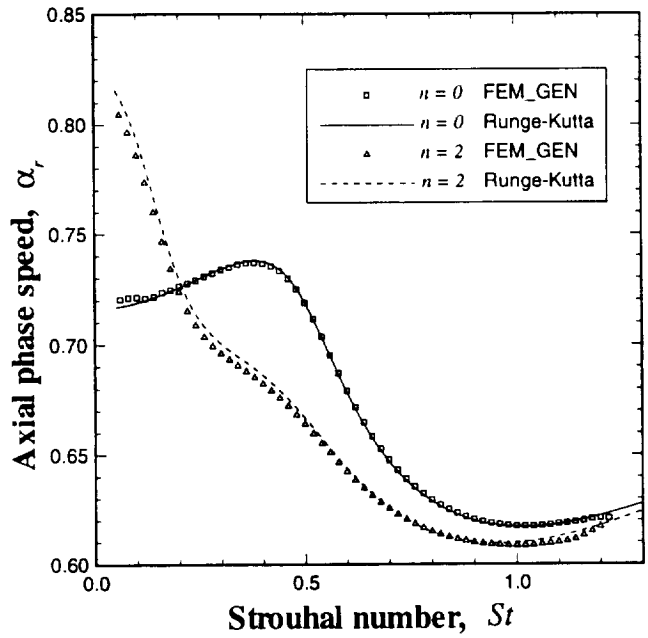

Figure 4.30. Comparison of the phase speed curves from the shooting code and FEM2D for different Kelvin-Helmholtz azimuthal modes. $M_j = 1.5$, unheated, $b = 0.1$, $r_w = 2.0$.

Two Kelvin-Helmholtz instability waves found in the case of the circular duct, the $n = 0$ axisymmetric and the $n = 2$ helical modes at $St = 0.50$, have been considered. $N = 3070$ number of nodes are generated in the unstructured FEM grid in order to obtain results of reasonable accuracy. The variations of the complex wavenumbers with changes in the aspect ratio of the shroud geometry is listed in Table 4.3 for the $n = 0$ axisymmetric mode. It can be seen that the growth rate decreases as the aspect ratio of the shroud increases. The real part of the complex wavenumber, on the other hand, is only affected slightly. Results obtained for the $n = 2$ helical mode are also given in Table 4.4. The same trend of decreasing axial growth rate with increasing aspect ratio is also observed in the $n = 2$ helical mode. A similar observation was made by Viswanathan *et al.* [50] using a vortex sheet model to represent the jet.

Table 4.3. Effects of varying the shroud geometry on the $n = 0$ axisymmetric mode.

AR	Wavenumber, α
1.000	(2.043236, −0.409981)
1.102	(2.105604, −0.407820)
1.199	(2.163010, −0.389827)
1.300	(2.178121, −0.365309)
1.404	(2.171335, −0.361235)
1.500	(2.170207, −0.361784)

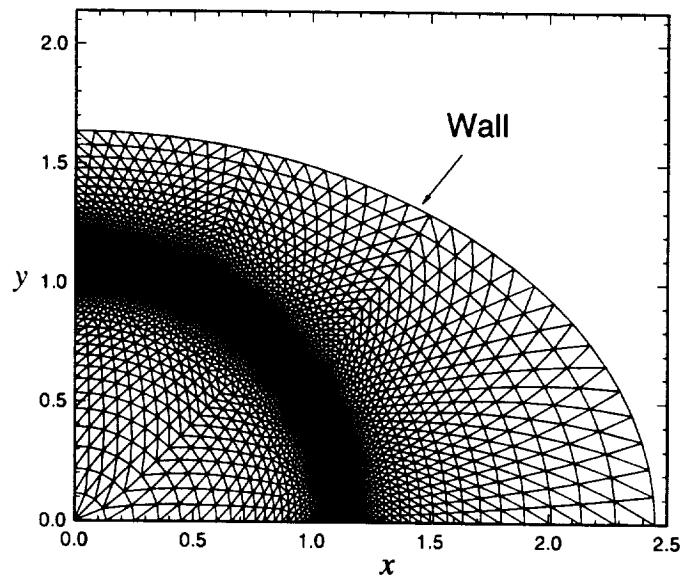

Figure 4.31. A locally equilateral unstructured triangular finite element grid.

Table 4.4. Effects of varying the shroud geometry on the $n = 2$ helical mode.

AR	Wavenumber, α
1.0	(1.984690, −0.454023)
1.1	(1.913138, −0.423662)
1.2	(1.832175, −0.376839)
1.3	(1.778470, −0.320662)
1.4	(1.747926, −0.268821)
1.5	(1.732502, −0.227809)

A comparison of the axial growth rates of the $n = 0$ and $n = 2$ mode indicates that the $n = 2$ helical mode exhibits a more significant reduction in growth rates as the aspect ratio of the shroud increases, as shown in Figure 4.32. Moreover, a closer examination on the growth rate curve for the $n = 0$ axisymmetric mode shows that the axial growth rate actually increases slightly first and then decreases to an asymptotic value. In order to understand the physics of the flow, the amplitude of the pressure fluctuations is examined. The perturbation pressure field is computed in the first quadrant only since it is possible to simulate the $2n$ mode, where $n = 0, 1, \ldots$, by applying Neumann boundary conditions at all the boundaries. The amplitude of the fluctuation pressure field has been normalized by the absolute maximum value to ensure that the values lie in the range of 0.0 and 1.0.

Contour plots of the fluctuation pressure amplitude associated with the $n = 0$ axisymmetric Kelvin-Helmholtz mode at different aspect ratios of the shroud are shown in Figure

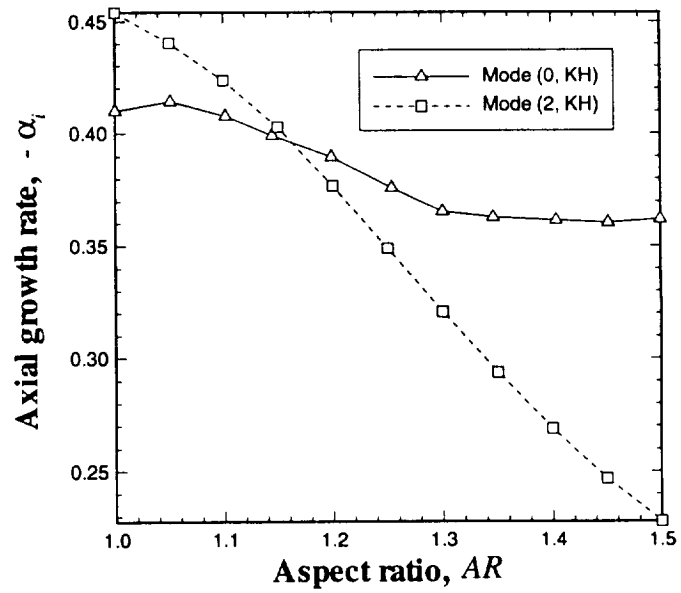

Figure 4.32. Effects of varying the shroud geometry on the axial growth rate of the $n = 0$ and $n = 2$ Kelvin-Helmholtz instability modes. $M_j = 4.0$, unheated, $b = 0.1$.

4.33 to Figure 4.38. The pressure amplitude contours in Figure 4.33 are typical of those associated with an axisymmetric instability mode, with concentric patterns. For the case where the shroud is of two equivalent jet radii, the maxima of the pressure fluctuations are at the shear layer and the outer wall. However, as the aspect ratio of the shroud increases and becomes more elliptic, the perturbation pressure field loses its concentric pattern. The "finger-like" contours mentioned in Reference [50] are also observed in the present study, extending from the major and minor axes. The pressure maxima are seen to shift away from the minor axis and the outer wall. As the length of the major axis increases, the presence of the wall becomes less significant in the development of the instability waves. In contrast, along the minor axis, the length decreases as the aspect ratio increases, and the presence of the wall is felt by the instability waves. The initial cancelation of the instability waves due to the external reflected waves causes the shift in pressure maxima along the minor axis. However, as the aspect ratio of the shroud increases further, the external reflected waves reinforce the instability waves and cause the formation of local pressure maxima along the minor axis. This reinforcement and cancelation of the instability waves by the interaction of the internal Mach waves and the external reflected waves from the outer wall is demonstrated distinctly in the $AR = 1.5$ case, as shown in Figure 4.38.

Figure 4.39 to Figure 4.44 display the pressure amplitude contours of the $n = 2$ helical Kelvin-Helmholtz instability mode at different aspect ratio of the shroud. Unlike the $n = 0$ axisymmetric mode, as the aspect ratio of the shroud increases, the pressure maxima moves

away from both the major and minor axes. Moreover, the pressure oscillations inside the shear layer are smoothed out as the aspect ratio increases. In fact, at $AR = 1.5$, most of the pressure fluctuations for the $n = 2$ helical mode occur outside the shear layer. From this observation, it may be possible to explain the significant reduction in the growth rates of the $n = 2$ helical Kelvin-Helmholtz mode as compared to the $n = 0$ axisymmetric mode.

In the case of a circular outer shroud, the reinforcement of the instability waves by the external reflected waves manifest itself. This leads to an increase in the growth rate of both the axisymmetric and helical instability mode. For both modes, the perturbation pressure gradient is large near the region where the shear layer is located ($r \approx 1.0$). However, as the aspect ratio of the shroud increases, the interference caused by the reflections from the outer wall effectively smooths out the perturbation pressure gradient near the shear layer. For the axisymmetric mode, this smoothing effect is not significant. However, for the $n = 2$ helical mode, this effect is very drastic. In fact, there are hardly any perturbation pressure fluctuations inside the shear layer. In light of the above observations, it is possible to argue that the dramatic decrease in the growth rate for the $n = 2$ helical mode is due to the decrease in the perturbation pressure gradient inside the shear layer. However, further study is needed to confirm this hypothesis.

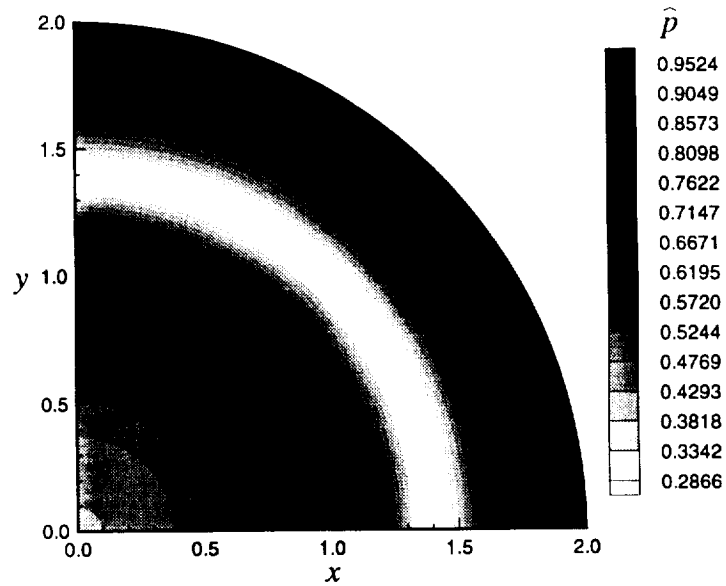

Figure 4.33. Contours of the amplitude of the pressure fluctuation for the $n = 0$ axisymmetric Kelvin-Helmholtz mode. $M_j = 4.0$, unheated, $b = 0.1$, $St = 0.50$, $AR = 1.0$.

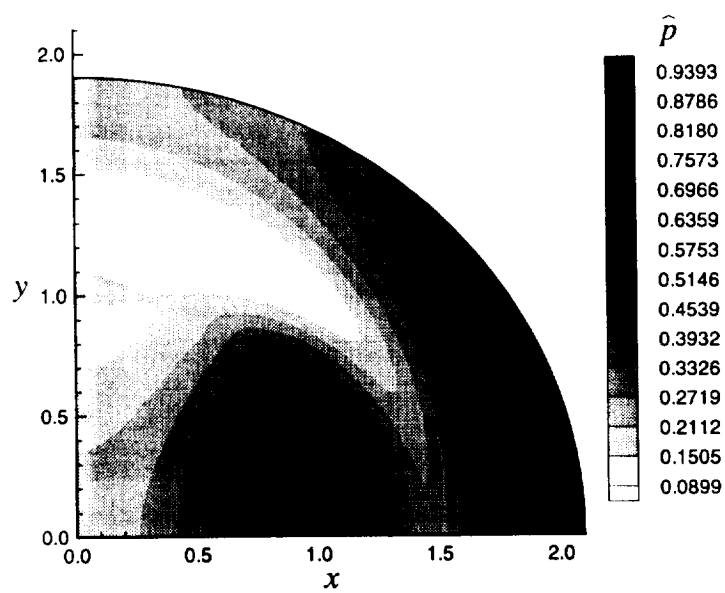

Figure 4.34. Contours of the amplitude of the pressure fluctuation for the $n = 0$ axisymmetric Kelvin-Helmholtz mode. $M_j = 4.0$, unheated, $b = 0.1$, $St = 0.50$, $AR = 1.1$.

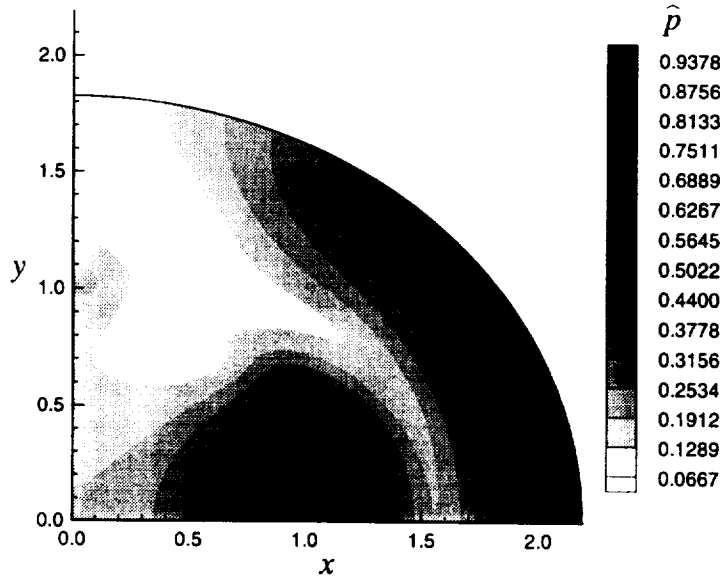

Figure 4.35. Contours of the amplitude of the pressure fluctuation for the $n = 0$ axisymmetric Kelvin-Helmholtz mode. $M_j = 4.0$, unheated, $b = 0.1$, $St = 0.50$, $AR = 1.2$.

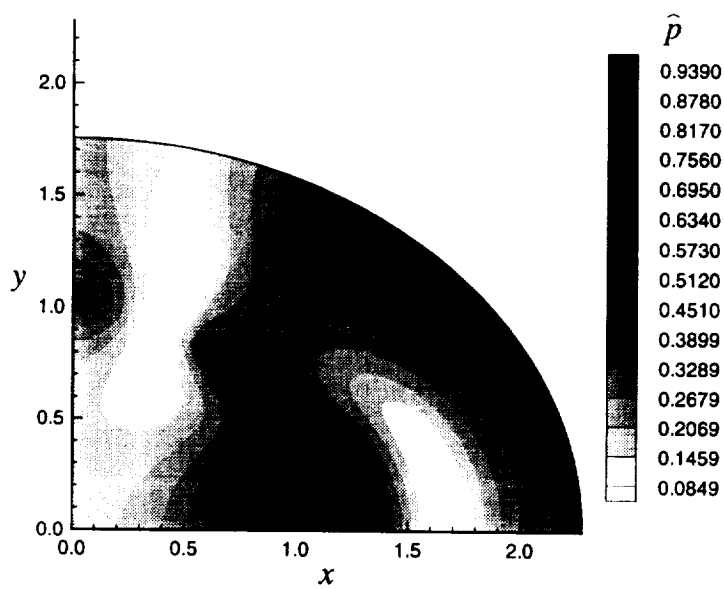

Figure 4.36. Contours of the amplitude of the pressure fluctuation for the $n = 0$ axisymmetric Kelvin-Helmholtz mode. $M_j = 4.0$, unheated, $b = 0.1$, $St = 0.50$, $AR = 1.3$.

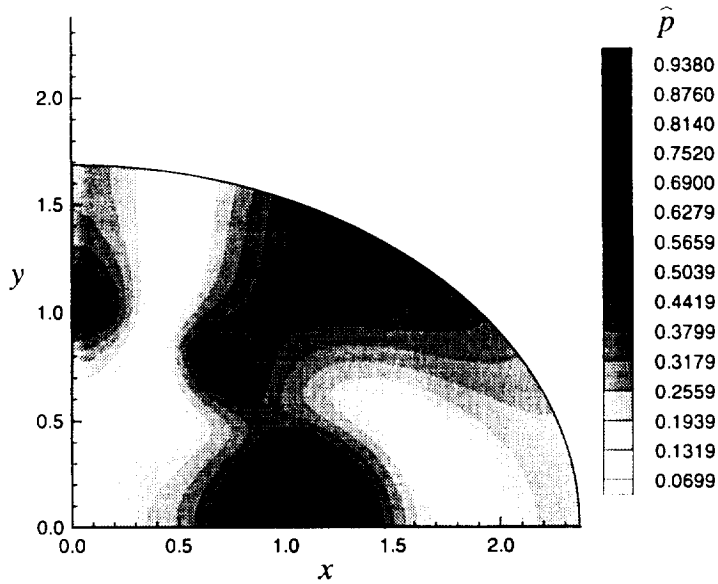

Figure 4.37. Contours of the amplitude of the pressure fluctuation for the $n = 0$ axisymmetric Kelvin-Helmholtz mode. $M_j = 4.0$, unheated, $b = 0.1$, $St = 0.50$, $AR = 1.4$.

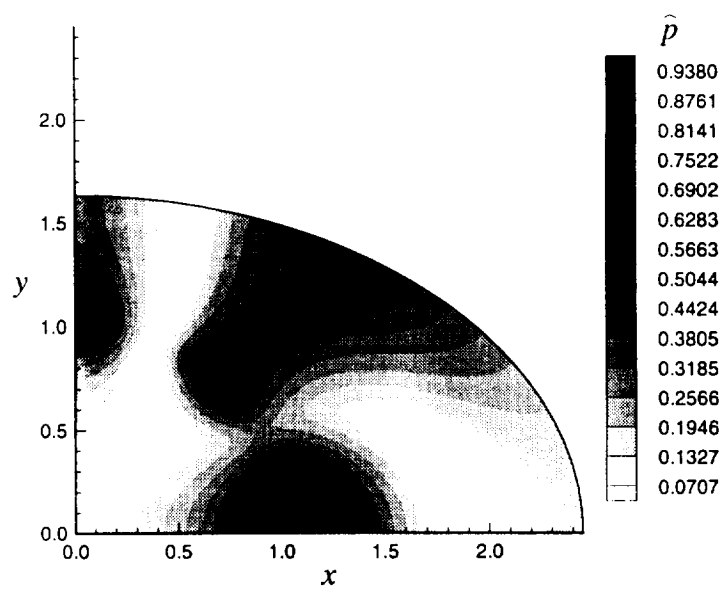

Figure 4.38. Contours of the amplitude of the pressure fluctuation for the $n = 0$ axisymmetric Kelvin-Helmholtz mode. $M_j = 4.0$, unheated, $b = 0.1$, $St = 0.50$, $AR = 1.5$.

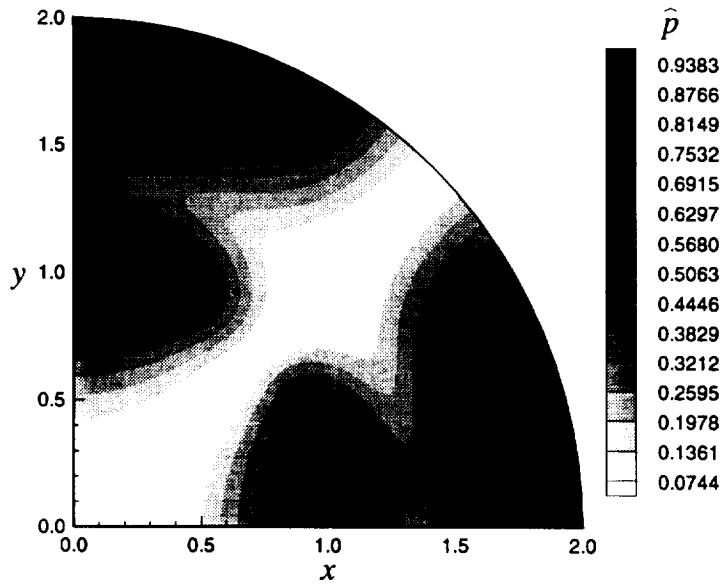

Figure 4.39. Contours of the amplitude of the pressure fluctuation for the $n = 2$ helical Kelvin-Helmholtz mode. $M_j = 4.0$, unheated, $b = 0.1$, $St = 0.50$, $AR = 1.0$.

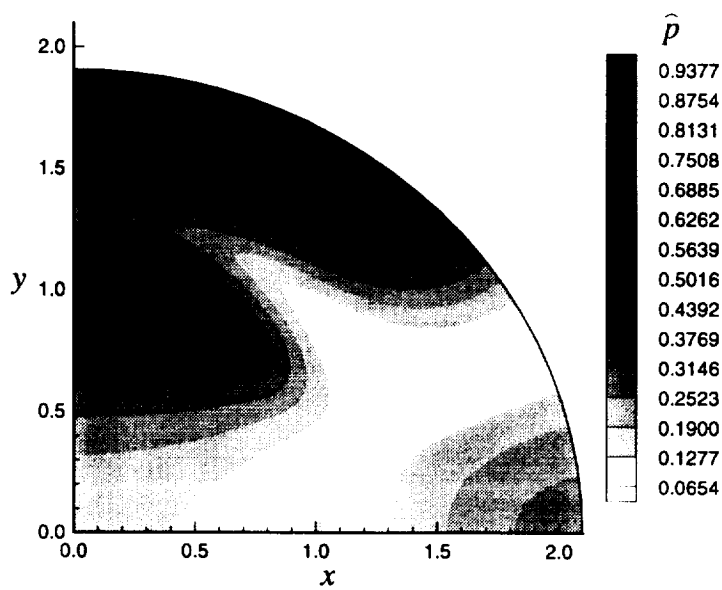

Figure 4.40. Contours of the amplitude of the pressure fluctuation for the $n = 2$ helical Kelvin-Helmholtz mode. $M_j = 4.0$, unheated, $b = 0.1$, $St = 0.50$, $AR = 1.1$.

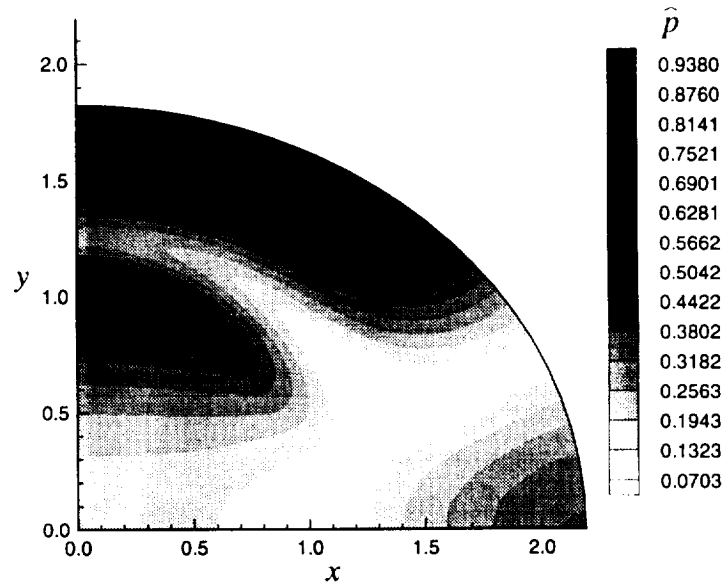

Figure 4.41. Contours of the amplitude of the pressure fluctuation for the $n = 2$ helical Kelvin-Helmholtz mode. $M_j = 4.0$, unheated, $b = 0.1$, $St = 0.50$, $AR = 1.2$.

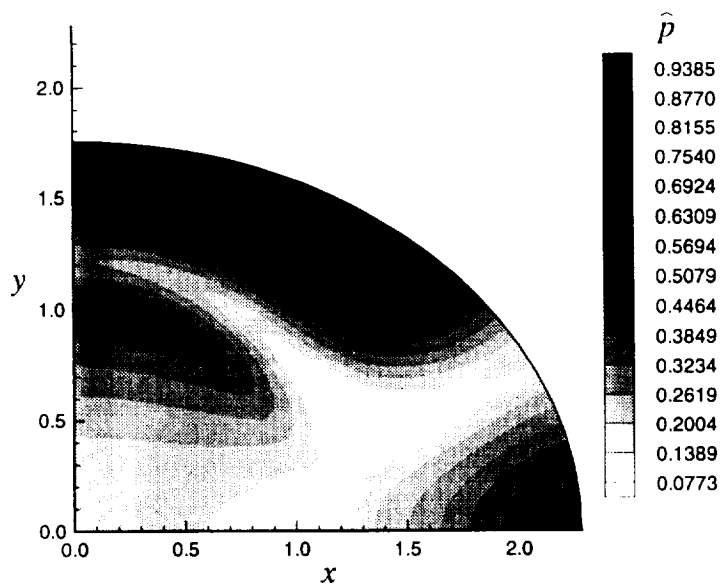

Figure 4.42. Contours of the amplitude of the pressure fluctuation for the $n = 2$ helical Kelvin-Helmholtz mode. $M_j = 4.0$, unheated, $b = 0.1$, $St = 0.50$, $AR = 1.3$.

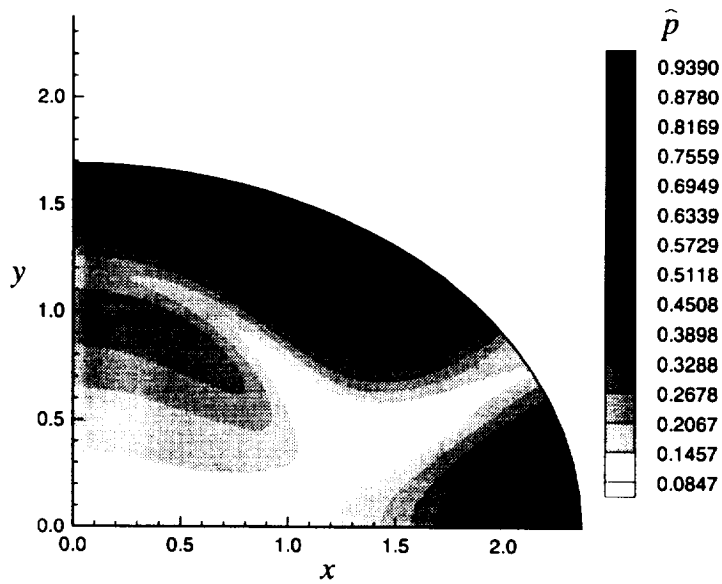

Figure 4.43. Contours of the amplitude of the pressure fluctuation for the $n = 2$ helical Kelvin-Helmholtz mode. $M_j = 4.0$, unheated, $b = 0.1$, $St = 0.50$, $AR = 1.4$.

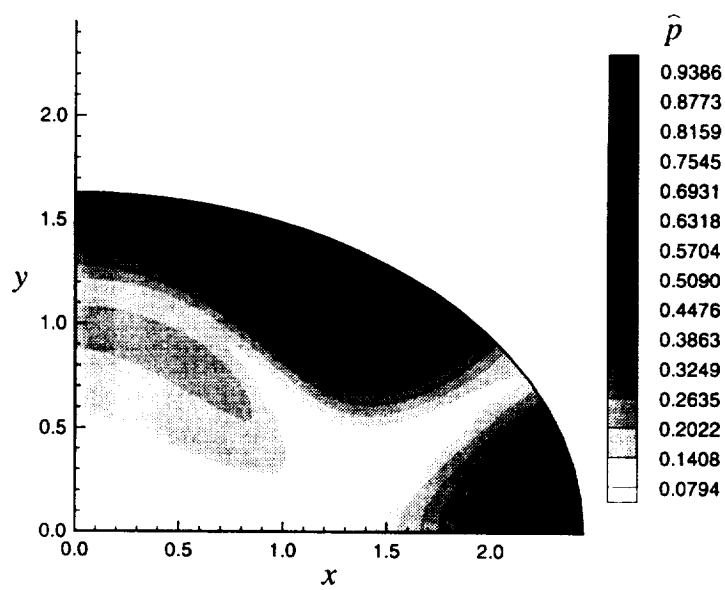

Figure 4.44. Contours of the amplitude of the pressure fluctuation for the $n = 2$ helical Kelvin-Helmholtz mode. $M_j = 4.0$, unheated, $b = 0.1$, $St = 0.50$, $AR = 1.5$.

4.4 Elliptic Jets in Circular Shroud

In this section, the stability characteristics of a confined elliptic jet are examined. The operating conditions are taken from Morris and Bhat [40] for a supersonic, unheated jet with $M_j = 1.5$ and $\rho_\infty = 0.6897$. The elliptic jet is confined in a circular shroud of four equivalent jet radii. Before linear stability analyses can be performed, it is necessary to specify the mean velocity and density profile *a priori*. In this study, the velocity profile of an elliptic jet proposed by Morris and Bhat [40] is employed. With the introduction of an elliptic coordinate system (η, ξ, z),

$$x = \kappa \cosh(\eta)\cos(\xi), \quad y = \kappa \sinh(\eta)\sin(\xi), \quad z = z, \tag{4.10}$$

where κ is the distance from the origin to the focus of the ellipse, the mean flow velocity profile is describe by

$$\bar{w}(\eta, \xi) = \begin{cases} 1 & \text{for } \zeta < 0, \\ W_j \exp\left[-\ln(2)\zeta^2\right] & \text{for } \zeta \geq 0, \end{cases} \tag{4.11}$$

where

$$\zeta = f(\xi)\left(\frac{\kappa \sinh(\eta) - h_B}{b_B}\right), \tag{4.12}$$

and

$$f(\xi) = \frac{1 + f(0)}{2} - \frac{1 - f(0)}{2}\cos(2\xi). \tag{4.13}$$

h_B and b_B are the potential core radius and the mixing layer half-width on the jet minor axis respectively. By matching the half-width on the jet major axis, b_A, and the value of κ to the potential core radius on the jet major axis, h_A, the expression, $f(0)$, is given by

$$f(0) = \frac{b_B}{\sqrt{(h_A + b_A)^2 - \kappa^2} - h_B}. \tag{4.14}$$

The aspect ratio of the jet is defined by

$$AR = \frac{h_A + b_A}{h_B + b_B}. \tag{4.15}$$

For this analytic velocity profile, the agreement with the measured velocity profiles of Kinzie *et al.* [69] is reasonable.

In elliptic jets, there are four general classes of instability wave; modes that are odd or even about the jet's major and minor axes. This classification was first proposed by Morris and Miller [38]. The modes that are even about both the major and minor axes are termed the ce_{2n} modes. The lowest order ce_0 mode is called the "varicose" mode. The modes that are odd about the jet's major axis and even about the minor axis are termed the se_{2n+1}

modes. The lowest order se_1 mode is known as the "flapping" mode. The modes that are even about the major axis and odd about the minor axis is termed the ce_{2n+1} modes, and the lowest order ce_1 mode is referred to as the "wagging" mode. Finally, the modes that are odd about both the major and minor axes are denoted as the se_{2n+2} modes.

In studies made by Morris and Miller [38] and Morris and Bhat [40], these four general classes of instability waves are related to the odd and even Mathieu functions. In the present analysis, since the FEM is employed, the four classes of instability wave are contained in the solution if the entire jet is discretized. However, if the entire jet is discretized, the resulting matrix system becomes very large due to the number of nodes required to resolve the pressure fluctuations. Therefore, in order to reduce the resulting matrix system, it is possible to take advantage of the symmetry of the domain and only simulate the first quadrant of the jet by applying the appropriate boundary conditions at the edges of the domain.

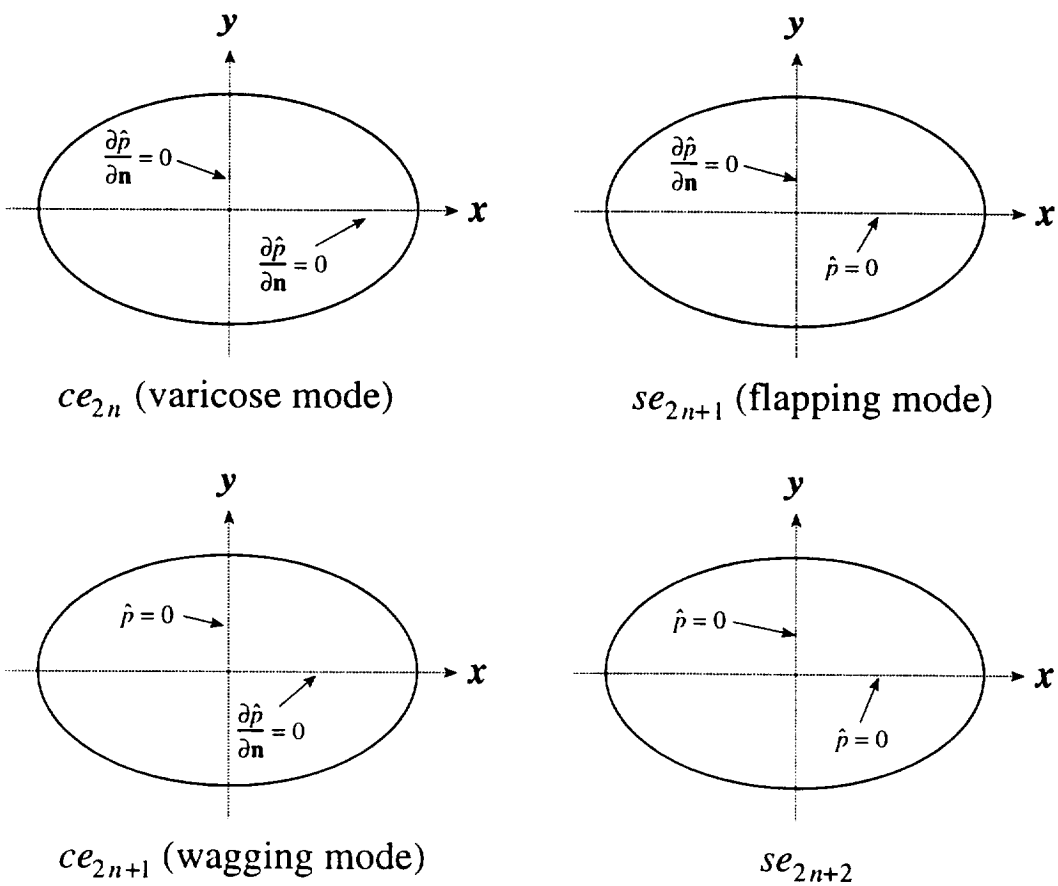

Figure 4.45. Appropriate boundary conditions to simulate the four general classes of instability wave.

Figure 4.45 illustrates the implementation of the appropriate boundary conditions to simulate the four classes of instability wave. Different combinations of the Neumann and Dirichlet boundary condition applied at the jet's major and minor axes are used to

simulate the odd and even characteristics of the four classes of instability wave. Contours of the pressure fluctuation amplitude for the ce_0 varicose and se_1 flapping mode of an $AR = 3.0$ elliptic jet are shown in Figures 4.46 and 4.47 respectively. For the ce_0 varicose mode, most of the pressure oscillations occur along the major axis. In contrast, the se_1 flapping mode has a pressure maxima at the jet's minor axis, since it is odd about the jet's major axis. The same observations were made by Morris and Bhat [40].

In Figure 4.48, the axial growth rate of the ce_0 varicose mode for a confined and unconfined elliptic jet of aspect ratio 2.0 is shown. At low frequencies ($St < 3.0$), the growth rate of the confined jet is lower than that of a free jet. Beyond this cross-over frequency, there is a slight increase in the axial growth rate of this instability mode. This variation in the axial growth rate is due to the interaction of the instability wave with the external reflected waves. However, this phenomenon is not as drastic as the confined axisymmetric jet case, since the shroud is considerably further away ($r_w = 4.0$), and the Mach number of the elliptic jet is lower. Figure 4.49 shows the axial growth rate of the ce_0 mode for an elliptic jet of aspect ratio 3.0. While the presence of cross-over frequencies can also be observed in this case, the stability characteristics are significantly different for the confined jet at higher frequencies. Even though the growth rate starts to decrease at high frequencies, the variation is not as drastic as in the unconfined jet case. Apparently, for the ce_0 mode, jets of high aspect ratio are affected by the presence of the shroud. This is because at high aspect ratio, the shroud is less than four jet radius along the major axis due to the increase in the potential core radius on the jet's major axis. Therefore, the reinforcement and cancelation of the instability mode is more significant at high aspect ratio.

The axial growth rates of the se_1 flapping mode for a confined and unconfined elliptic jet of aspect ratio 2.0 and 3.0 are shown in Figure 4.50 and Figure 4.51 respectively. Unlike the ce_0 varicose mode, the se_1 flapping mode seems to be unaffected by the presence of the shroud, even for jets with high aspect ratio. Since the mode is odd about the jet's major axis and even about the jet's minor axis, most of the pressure fluctuations occur in the minor axis (see Figure 4.47). The radius of the shroud is more than four jet radii on the minor axis, so the presence of the outer wall has very little influence on the development of the se_1 instability mode. This accounts for the apparent similar instability characteristics of the flapping mode for a confined elliptic jet. The axial phase velocity for both the ce_0 and se_1 mode is similar to the confined circular jet case. The variations of the axial phase velocity for these two modes are shown in Figure 4.52 and Figure 4.53 for completeness.

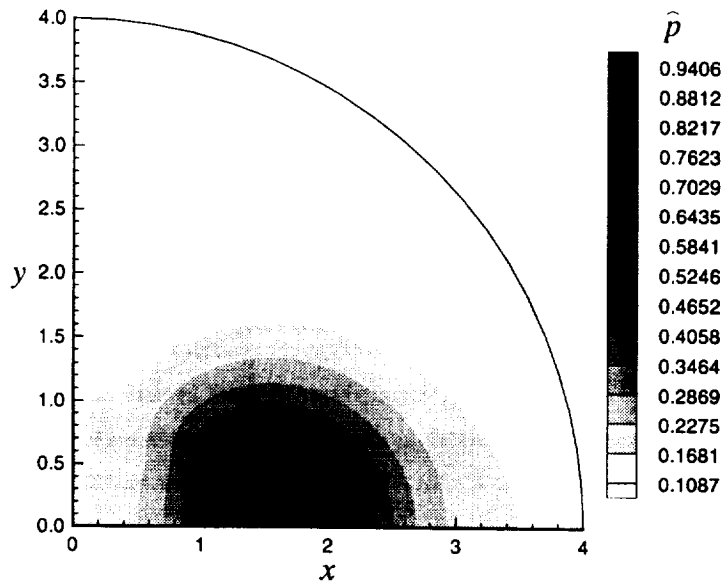

Figure 4.46. Contours of the pressure perturbation amplitude of the ce_0, varicose mode. Elliptic jet, $M_j = 1.5$, unheated, $b_A = b_B = 0.2$, $r_w = 4.0$, $AR = 3$.

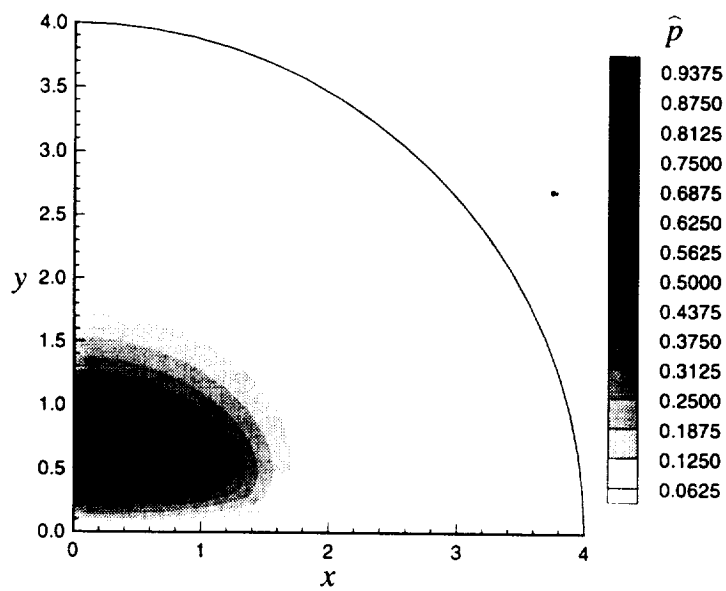

Figure 4.47. Contours of the pressure perturbation amplitude of the se_1, flapping mode. Elliptic jet, $M_j = 1.5$, unheated, $b_A = b_B = 0.2$, $r_w = 4.0$, $AR = 3$.

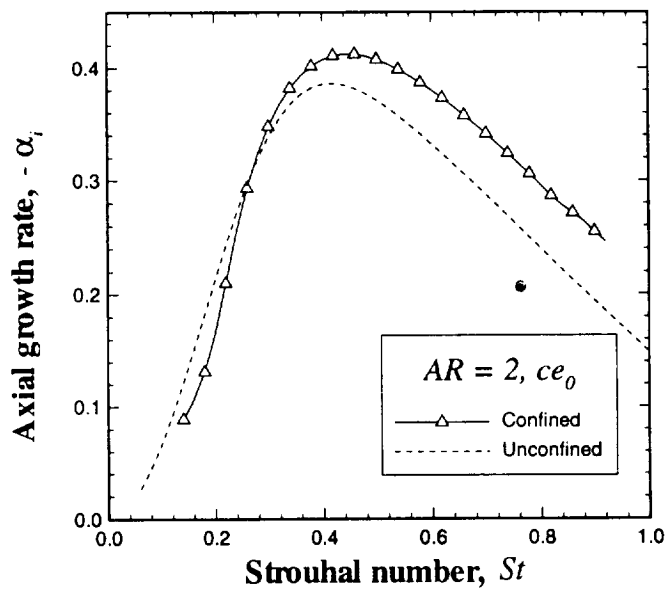

Figure 4.48. Variation of axial growth rate of ce_0 varicose mode with Strouhal number. Elliptic jet, $M_j = 1.5$, unheated, $b_A = b_B = 0.2$, $r_w = 4.0$, $AR = 2$.

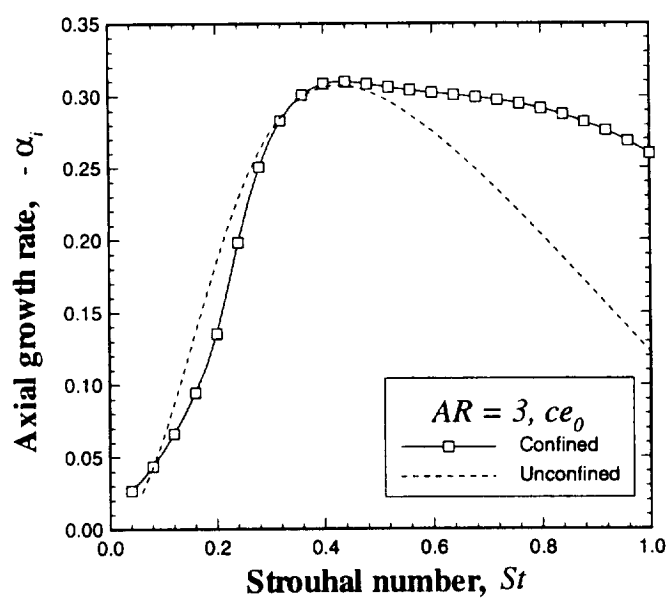

Figure 4.49. Variation of axial growth rate of ce_0 varicose mode with Strouhal number. Elliptic jet, $M_j = 1.5$, unheated, $b_A = b_B = 0.2$, $r_w = 4.0$, $AR = 3$.

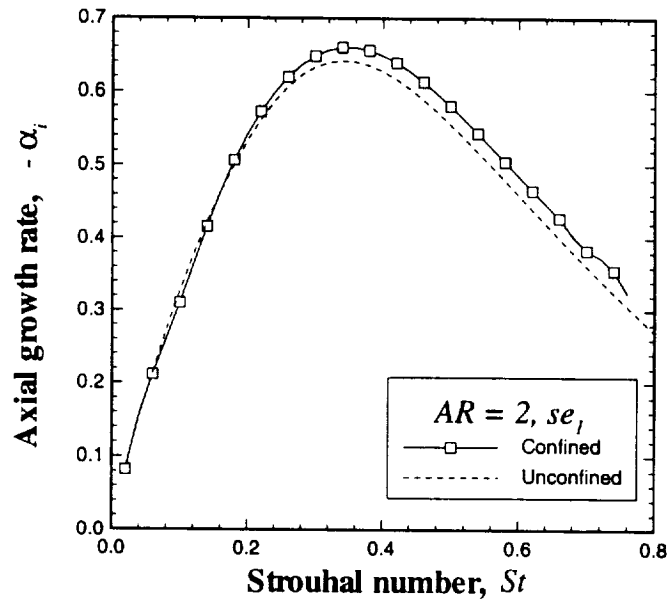

Figure 4.50. Variation of axial growth rate of se_1 flapping mode with Strouhal number. Elliptic jet, $M_j = 1.5$, unheated, $b_A = b_B = 0.2$, $r_w = 4.0$, $AR = 2$.

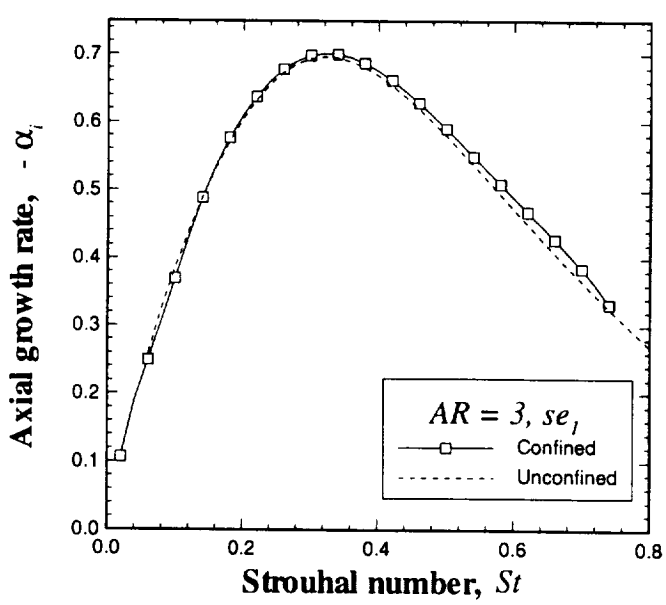

Figure 4.51. Variation of axial growth rate of se_1 flapping mode with Strouhal number. Elliptic jet, $M_j = 1.5$, unheated, $b_A = b_B = 0.2$, $r_w = 4.0$, $AR = 3$.

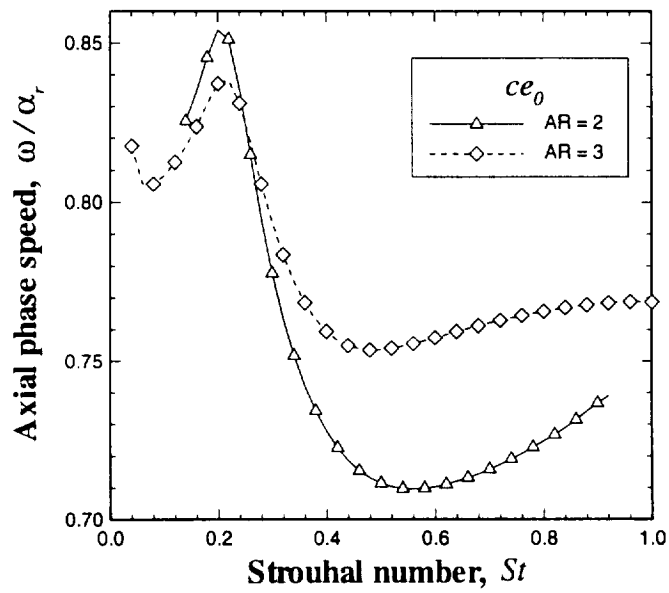

Figure 4.52. Variation of axial phase velocity of ce_0 varicose mode with Strouhal number. Elliptic jet, $M_j = 1.5$, unheated, $b_A = b_B = 0.2$, $r_w = 4.0$.

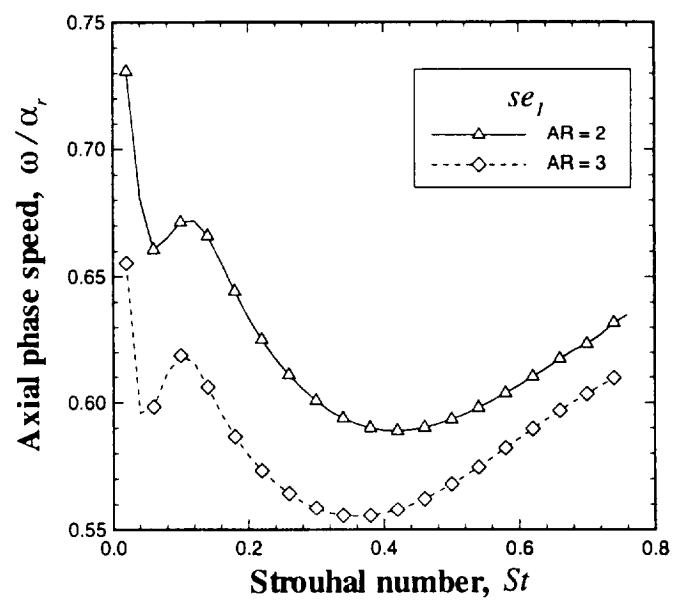

Figure 4.53. Variation of axial phase velocity of se_1 flapping mode with Strouhal number. Elliptic jet, $M_j = 1.5$, unheated, $b_A = b_B = 0.2$, $r_w = 4.0$.

Chapter 5

CONCLUSIONS AND FUTURE RESEARCH

In this chapter, conclusions are drawn from results presented throughout this thesis. The advantages and disadvantages of the use of the FEM to solve linear stability problems are discussed. Using the validated FEM code, FEM2D, the effects of confinement on supersonic asymmetric jets are analyzed and summarized. Finally, recommendations for future research are given.

5.1 Conclusions

Asymmetric jets with elliptic and rectangular exit geometries have found many aeronautical applications in V/STOL aircraft, thrust-vectoring nozzles for high maneuverability planes, mixing enhancement of combustion, and most recently, supersonic jet noise reduction. Previous studies on axisymmetric jets have shown that linear stability theory yields keen insight into the mixing process and noise generation mechanism of supersonic jets and shear layers. However, due to the stringent requirement of the assumed velocity profile, so as to ensure separable form of the governing equation, studies based on linear stability theory are only capable of analyzing flows with relatively simple mean flow profile. Therefore, to analyze the instability wave characteristics of asymmetric jets, the only alternative up to now is to perform direct numerical simulations (DNS). The obvious drawback in DNS, though, is the enormous requirement of computational resources. To circumvent these obstacles, a new approach to the solution of linear stability problems is proposed in the present analysis.

The objectives of this thesis are two fold: to assess the feasibility of the implementation of the finite element method (FEM) in the solution of linear stability problems, and to study the effects of confinement of supersonic jets with arbitrary exit geometries. The perturbation equation that describes the development of instability waves in supersonic jets, the compressible Rayleigh equation, is discretized using the FEM. Previous analyses based on this type of global scheme, such as the finite difference method (Liou and Morris [55]) and the boundary element method (Viswanathan *et al.* [50]) have been performed to calculate related problems for circular and elliptic jets. To increase the robustness of the calculation for more complex jet exit geometries, the present study makes use of the FEM instead. This is essentially an operator that converts the partial differential equation to a matrix system. In a spatial analysis, the complex wavenumber, α, is the eigenvalue and varies nonlinearly. This results in a matrix polynomial called the λ-matrix, and the problem becomes

a non-linear matrix eigenvalue problem.

Special numerical solution techniques have to be applied to solve the non-linear matrix eigenvalue problem. They are the Linear Companion Matrix Method (LCMM), the Matrix Factorization Method (MFM), and the Newton iteration method in compact matrix form. Due to the simplicity of the axisymmetric form of the compressible Rayleigh equation, this provides the means to explore the different numerical schemes for the solution of the non-linear matrix eigenvalue problem, and assess the viability of using the FEM in the solution of linear stability problems.

A very straightforward method to solve the non-linear eigenvalue problem is to implement the LCMM. In this method, new vectors are defined to set up the companion matrix of the original system. Depending on the order of the λ-matrix, the size of the companion matrix increases accordingly. A globally convergent scheme such as the QR method can be applied to solve the entire eigenvalue spectrum. However, in most hydrodynamic stability problems, not all eigenvalues are of physical interest. To calculate only a subset of the eigenvalue spectrum, the matrix polynomial is factorized using the MFM. In the MFM, the roots of the matrix polynomial have to be evaluated first, and Bernoulli iteration is performed for this calculation. If only a single eigenvalue is desired, a locally convergent method such as the Newton iteration in compact matrix form can be applied. The trace theorem of Davidenko [60] is used in order to avoid the calculation of the determinant and its derivative explicitly.

All three methods are able to calculate the desired eigenvalue with reasonable accuracy. For calculations of the axisymmetric jet case, the memory requirement and computational time are not important issues. However, these becomes crucial in the selection of the appropriate numerical schemes for two-dimensional calculations. Since results with reasonable accuracy can be achieved even with one Bernoulli iteration step, the MFM is clearly the choice for two-dimensional calculations. To further reduce the computation time, the power iteration method is utilized instead of the Newton iteration method. Since the dominant solvent from the MFM contains the eigenvalue with the maximum modulus, the convergence of the power iteration method is ensured.

It has been stated throughout this thesis that there are many advantages to solve linear stability problems using the FEM. The robustness of the calculations using the FEM becomes evident from the calculations of confined asymmetric jets. With a validated FEM code, FEM2D, instability characteristics of confined elliptic jets can be readily analyzed by prescribing the appropriate mean velocity profiles and generating the FEM grids. In fact, it is possible to analyze jets with any arbitrary geometries as long as the mean flow velocity profiles can be specified *a priori*. Unlike the finite difference method, the finite element discretization is carried out in the physical domain. Hence, no transformation is necessary to convert the problem into a computational domain. While the finite difference method can

still be implemented in a similar manner to solve the present problem, the use of the FEM significantly reduces the complexity of the analysis. Moreover, the FEM is able to handle non-constant coefficients in the governing equation, in contrast to the boundary element method. This enables the use of a more realistic mean flow profile.

On the other hand, the use of the FEM to solve linear stability problems is not without disadvantages. The resulting matrices due to the finite element discretization are not symmetric and positive-definite, so even though the matrices are sparse, accelerated methods such as the Lanczos subspace iteration method cannot be applied. To overcome this problem, the Arnoldi iteration method or the unsymmetric Lanczos tridiagonalization can be employed to solve the unsymmetric, sparse eigenvalue problem. However, in the present analysis, these methods are not implemented. In addition, computational memory becomes a constraint for two-dimensional calculations, since large matrices have to be stored in the present analysis. It should be noted that this is the artifact of the spatial analysis and the use of a global scheme for such computation. While it is possible to store the matrix coefficients in the λ-matrix in banded storage form, the matrix inversion in both the LCMM and MFM destroys this property. Therefore, the entire matrix has to be stored. This is regardless of the discretization method used in the present analysis.

Comparisons of results from the shooting method and those from the FEM have been made, and favorable agreement is achieved. For two-dimensional calculations, the apparent advantage of using a global scheme (finite difference, boundary element, finite element, or spectral method) becomes a disadvantage when the instability characteristics are traced over a frequency range. This is because the use of a global scheme provides the entire eigenvalue spectrum and, at high frequencies, the eigenvalues are so clustered that a converged solution cannot be obtained. For confined supersonic jets at very high Mach number, the growth rate curve exhibits an oscillatory behavior. At certain frequencies, the instability waves become almost neutral. To avoid the presence of singularities, a complex contour deformation has to be performed. Instead of re-deriving the local element matrices, a more elegant method of using a complex transformation method by Boyd [61] is implemented. However, this transformation is only carried out in the analyses of axisymmetric jets.

In order to understand the effects of outer shroud geometry variations on the stability characteristics of a confined circular jet, the shroud is varied from a circular to an elliptic shape of aspect ratio 1.5, while keeping the cross-sectional area constant. As the aspect ratio of the shroud increases, the interference caused by the reflections from the outer wall effectively smooths out the perturbation pressure gradient near the shear layer of the jet, and the axial growth rates of the Kelvin-Helmholtz modes decrease. It is proposed in the present study that such a decrease in growth rate is due to the decrease in the perturbation pressure gradient inside the mixing layer. However, further investigation is needed to confirm this hypothesis.

To simulate the four general classes of instability modes in elliptic jets using only the first quadrant of the solution domain, combinations of the Neumann and Dirichlet boundary conditions can be applied along the jet's major and minor axes. This further decreases the size of the problem, thus reducing the memory constraint and the computation time. For an elliptic jet at Mach 1.5, confined in a shroud of four equivalent jet radii, the ce_0 varicose mode is influenced by the effects of confinement, especially at high aspect ratio. In contrast, the se_1 flapping mode remains unaffected by the presence of the shroud. This is because the instability characteristics of the se_1 mode are controlled by the oscillations along the jet's minor axis, and at high aspect ratio, the wall is relatively far away from the jet shear layer in the minor axis plane.

5.2 Suggestions for Future Research

It has been shown in the present study that the implementation of the FEM for the solution of linear stability problems provides an attractive alternative to study the mixing characteristics of confined asymmetric jets. Although the memory requirement in the solution of the stability problems using the FEM is comparable to that of a typical direct numerical simulation, the computation time is reduced significantly. In fact, the validated code provides a powerful tool to analyze the instability characteristics of jets with arbitrary exit geometries. Therefore, it is now possible to extend the current work to document the stability properties of confined rectangular jets if a realistic mean velocity profile can be prescribed.

Another possible extension to the current research is to study the noise radiation from jets of arbitrary exit geometries. A detailed description of this analysis is given by Morris and Bhat [43]. By matching the inner instability wave solution with the outer acoustic solution in an intermediate region, the noise radiation from these jets can be predicted. Therefore, instead of using a typical shooting method to calculate the inner instability wave solution, the FEM can be applied. However, to perform this calculation, the Robin or mixed boundary condition has to be applied on the outer boundary in order to simulate the infinite domain. Alternatively, the shape functions of a infinite element (see Zienkiewicz and Talyor [70]) could be employed.

REFERENCES

[1] Brown, G. L., and Roshko, A. On density effects and large structure in turbulent mixing. *Journal of Fluid Mechanics*, **64**, pp. 775–781, 1974.

[2] Papamoschou, D., and Roshko, A. The compressible turbulent shear layer: an experimental study. *Journal of Fluid Mechanics*, **197**, pp. 453–477, 1988.

[3] Crow, S. C., and Champagne, F. H. Orderly structure in jet turbulence. *Journal of Fluid Mechanics*, **48**, pp. 547–591, 1971.

[4] Yule, A. J. Large-scale structure in the mixing layer of a round jet. *Journal of Fluid Mechanics*, **89**, pp. 413–432, 1978.

[5] Dimotakis, P. E., Miake-Lye, R. C., and Papantoniou, D. A. Structure and dynamics of round turbulent jets. *Physics of Fluids*, **26**, pp. 3185–3192, 1983.

[6] McLaughlin, D. K., Morrison, G. L., and Troutt, R. R. Experiments on the instability waves in a supersonic jet and their acoustic radiation. *Journal of Fluid Mechanics*, **69**, pp. 73–95, 1975.

[7] McLaughlin, D. K., Morrison, G. L., and Troutt, R. R. Reynolds number dependence in supersonic jet noise. *AIAA Journal*, **15**, pp. 526–532, 1977.

[8] Troutt, R. R. *Measurements on the Flow and Acoustic Properties of a Moderate Reynolds Number Supersonic Jet.* Ph.D. Thesis, Oklahoma State University, 1978.

[9] Troutt, R. R., and McLaughlin, D. K. Experiments on the flow and acoustic properties of a moderate-Reynolds-number supersonic jet. *Journal of Fluid Mechanics*, **116**, pp. 123–156, 1982.

[10] Sforza, P. M., Steiger, M. H., and Trentacoste, N. Studies on three-dimensional viscous jets. *AIAA Journal*, **4**, pp. 800–806, 1966.

[11] Sfeir, A. A. Investigation of three-dimensional turbulent rectangular jets. *AIAA Journal*, **16**, pp. 1055–1060, 1978.

[12] Ho, C.-M., and Gutmark, E. Vortex induction and mass entrainment in a small-aspect-ratio elliptic jet. *Journal of Fluid Mechanics*, **179**, pp. 383–405, 1987.

[13] Husain, H. S., and Hussain, A. K. M. F. Controlled excitation of elliptic jets. *Physics of Fluids*, **26**, pp. 2763–2766, 1983.

[14] Hussain, F., and Husain, H. S. Elliptic jets. Part 1. Characteristics of unexcited and excited jets. *Journal of Fluid Mechanics*, **208**, pp. 257–320, 1989.

[15] Gutmark, E., and Ho, C.-M. Visualization of an elliptical jet. *AIAA Journal*, **24**, pp. 684–685, 1986.

[16] Husain, H. S., and Hussain, F. Elliptic jets. Part 2. Dynamics of coherent structures: pairing. *Journal of Fluid Mechanics*, **233**, pp. 439–482, 1991.

[17] Husain, H. S., and Hussain, F. Elliptic jets. Part 3. Dynamics of preferred mode coherent structure. *Journal of Fluid Mechanics*, **248**, pp. 315–361, 1993.

[18] Gutmark, E., Schadow, K. C., and Wilson, K. J. Noncircular jet dynamics in supersonic combustion. AIAA Paper 87-1878. AIAA/SAE/ASME/ASEE 23rd Joint Propulsion Conference, 1987.

[19] Gutmark, E., Schadow, K. C., Wilson, K. J., and Bicker, C. J. Near-field pressure radiation and flow characteristics in low supersonic circular and elliptic jets. *Physics of Fluids*, **31**, pp. 2524–2532, 1988.

[20] Krothapalli, A., Baganoff, D., and Karamcheti, K. On the mixing of a rectangular jet. *Journal of Fluid Mechanics*, **107**, pp. 201–220, 1981.

[21] Krothapalli, A., Hsia, Y., Baganoff, D., and K., K. The role of screech tones in mixing of an underexpanded rectangular jet. *Journal of Sound and Vibration*, **106**, pp. 119–143, 1986.

[22] Grandmaison, E. W., Pollard, A., and Ng, S. Scalar mixing in a free, turbulent rectangular jet. *International Journal of Heat and Mass Transfer*, **34**, pp. 2653–2662, 1991.

[23] Shih, C., Krothapalli, A., and Gogineni, S. Experimental observations of instability modes in a rectangular jet. *AIAA Journal*, **30**, pp. 2388–2394, 1991.

[24] Gutmark, E., Schadow, K. C., and Bicker, C. J. Near acoustic field and shock structure of rectangular supersonic jets. *AIAA Journal*, **28**, pp. 1163–1170, 1990.

[25] Schadow, K. C., and Gutmark, E. Review of passive shear-flow control research for improved subsonic and supersonic combustion. AIAA Paper 89-2789. AIAA/ASME/SAE/ASEE 25th Joint Propulsion Conference, 1989.

[26] Yu, K. H., Gutmark, E., and Schadow, K. C. Passive control of coherent vortices in compressible mixing layers. AIAA Paper 93-3262. AIAA Shear Flow Conference, 1993.

[27] Gutmark, E. J., Schadow, K. C., and Yu, K. H. Mixing enhancement in supersonic free shear flows. *Annual Review of Fluid Mechanics*, **27**, pp. 375–417, 1995.

[28] Morris, P. J. Noise radiation from non-circular supersonic jets. DGLR/AIAA Paper 92-02-061. DGLR/AIAA 14th Aeroacoustics Conference, 1992.

[29] Lighthill, M. J. On sound generated aerodynamically, I: General theory. *Proceedings of Royal Society of London*, **211**, pp. 564–587, 1952.

[30] Lighthill, M. J. On sound generated aerodynamically, II: Turbulence as a source of sound. *Proceedings of Royal Society of London*, **222**, pp. 1–32, 1954.

[31] Krothapalli, A., Alvi, F. S., Washington, D., and King, C. J. Aeroacoustic characteristics of a supersonic diamond-shaped jet. CEAS/AIAA Paper 95-170. AIAA 16th Aeroacoustics Conference, 1995.

[32] Tam, C. K. W. Jet noise generated by large-scale coherent motion. In Hubbard, H. H., editor, *Aeroacoustics of Flight Vehicles: Theory and Practice, Volume 1: Noise Sources*, NASA Reference Publication 1258, pp. 311–390, 1991.

[33] Kinzie, K. W., and McLaughlin, D. K. Noise radiated from asymmetric supersonic jets. CEAS/AIAA Paper 95-014. AIAA 16th Aeroacoustics Conference, 1995.

[34] Michalke, A. Instability of compressible circular free jet with consideration of the influence of the jet boundary layer thickness. NASA TM 75190, 1971.

[35] Tam, C. K. W., and Morris, P. J. The radiation of sound by the instability waves of a compressible plane turbulent shear layer. *Journal of Fluid Mechanics*, **98**, pp. 349–381, 1980.

[36] Plaschko, P. Stochastic model theory for coherent turbulent structures in circular jets. *Physics of Fluids*, **24**, pp. 187–193, 1981.

[37] Plaschko, P. Axial coherence functions of circular turbulent jets based on an inviscid calculation of damped modes. *Physics of Fluids*, **26**, pp. 2368–2373, 1983.

[38] Morris, P. J., and Miller, D. G. Wavelike structures in elliptic jets. AIAA Paper 84-0399. AIAA 22nd Aerospace Sciences Meeting, 1984.

[39] Morris, P. J. Instability of elliptic jets. *AIAA Journal*, **26**, pp. 172–178, 1986.

[40] Morris, P. J., and Bhat, T. R. S. The spatial stability of compressible elliptic jets. *Physics of Fluids*, **7**, pp. 185–194, 1995.

[41] Baty, R. S., Seiner, J. M., and Ponton, M. K. Instability of a supersonic shock-free elliptic jet. AIAA Paper 90-3959. AIAA 13th Aeroacoustics Conference, 1990.

[42] Tam, C. K. W., and Thies, A. T. Instability of rectangular jets. DGLR/AIAA Paper 92-02-043. DGLR/AIAA 14th Aeroacoustics Conference, 1992.

[43] Morris, P. J., and Bhat, T. R. S. Supersonic elliptic jet noise. AIAA Paper 93-4409. AIAA 15th Aeroacoustics Conference, 1993.

[44] Tam, C. K. W., and Burton, D. E. Sound generated by instability waves of supersonic flows. Part 1. Two-dimensional mixing layers. *Journal of Fluid Mechanics*, **138**, pp. 249–271, 1984.

[45] Tam, C. K. W., and Burton, D. E. Sound generated by instability waves of supersonic flows. Part 2. Axisymmetric jets. *Journal of Fluid Mechanics*, **138**, pp. 273–295, 1984.

[46] Koshigoe, S., and Tubis, A. Wave structures in jets of arbitrary shape. I. Linear inviscid spatial instability analysis. *Physics of Fluids*, **29**, pp. 3982–3992, 1986.

[47] Koshigoe, S., and Tubis, A. Wave structures in jets of arbitrary shape. II. Application of a generalized shooting method to linear instability analysis. *Physics of Fluids*, **30**, pp. 1715–1723, 1987.

[48] Koshigoe, S., Gutmark, E., Schadow, K. C., and Tubis, A. Wave structures in jets of arbitrary shape. III. Triangular jets. *Physics of Fluids*, **31**, pp. 1410–1419, 1988.

[49] Tam, C. K. W., and Hu, F. Q. The instability and acoustic wave modes of supersonic mixing layers inside a rectangular channel. *Journal of Fluid Mechanics*, **203**, pp. 51–76, 1989.

[50] Viswanathan, K., and Morris, P. J. Linear instability waves in supersonic jets confined in circular and non-circular ducts. *Journal of Sound and Vibration*, **171**, pp. 231–253, 1994.

[51] Berman, C., Gordon, G., Karniadakis, G., and Orszag, S. Jet turbulence noise computations. AIAA Paper 93-4365. AIAA 15th Aeroacoustics Conference, 1993.

[52] Grinstein, F. F. Vorticity dynamics in spatially-developing rectangular jets. AIAA Paper 93-3286. AIAA Shear Flow Conference, 1993.

[53] Zaman, K. B. M. Q. Axis switching and spreading of an asymmetric jet–role of vorticity dynamics. AIAA Paper 95-0889. AIAA 33rd Aerospace Sciences Meeting and Exhibit, 1995.

[54] Chyczewski, T. S., and Long, L. N. Applications of an efficient parallel computational aeroacoustics algorithm. CEAS/AIAA Paper 95-011. AIAA 16th Aeroacoustics Conference, 1995.

[55] Liou, W. W. W., and Morris, P. J. The eigenvalue spectrum of the rayleigh equation for a plane shear layer. *International Journal for Numerical Methods in Fluids*, **15**, pp. 1407–1415, 1992.

[56] Bridges, T. J., and Morris, P. J. Differential eigenvalue problems in which the parameter appears nonlinearly. *Journal of Computational Physics*, **55**, pp. 437–460, 1984.

[57] Press, W. H., Teukolsky, S. A., Vetterling, W. T., and Flannery, B. P. *Numerical Recipes in Fortran: The Art of Scientific Computing.* Cambridge University Press, 2nd edition, 1992.

[58] Lancaster, P. Algorithms for lambda-matrices. *Numerische Mathematik*, **6**, pp. 388–394, 1964.

[59] Gohberg, I., Lancaster, P., and Rodman, L. *Matrix Polynomials.* Academic Press, 1982.

[60] Davidenko, D. F. The evaluation of determinants by the method of variation of parameters. *Soviet Mathematics-Doklady*, **1**, pp. 316–319, 1960.

[61] Boyd, J. P. Complex coordinate methods for hydrodynamic instabilities and Sturm-Liouville eigenproblems with an interior singularity. *Journal of Computational Physics*, **57**, pp. 454–471, 1985.

[62] Eggers, J. M. Velocity profile and eddy viscosity distributions downstream of a Mach 2.2 nozzle exhausting to quiescent air. NASA TN D-3601, 1966.

[63] Birch, S. F., and Eggers, J. M. A critical review of the experimental data for developed turbulent free shear layers. NASA SP-321, Volume 1, 1972.

[64] Lau, J. C., Morris, P. J., and Fisher, M. J. Measurements in subsonic and supersonic free jets using a laser velocimeter. *Journal of Fluid Mechanics*, **93**, pp. 1–27, 1979.

[65] Lau, J. C. Effects of exit Mach number and temperature on mean flow and turbulence characteristics in round jets. *Journal of Fluid Mechanics*, **105**, pp. 193–218, 1981.

[66] Tam, C. K. W., and Hu, F. Q. On the three families of instability waves of high-spped jets. *Journal of Fluid Mechanics*, **201**, pp. 447–483, 1989.

[67] Briggs, R. J. *Electron-Stream Interaction with Plasma.* M.I.T. Press, 1964.

[68] Bers, A. Space-time evolution of plasma instabilities—absolute and convective. In Galeev, A. A., and Sudan, R. N., editors, *Basic Plasma Physics, Volume 1*, pp. 451–517. North-Holland Publishing Co., 1983.

[69] Kinzie, K., Martens, S., and McLaughlin, D. K. Supersonic elliptic jet noise: experiments with and without an ejector shroud. AIAA Paper 93-4349. AIAA 15th Aeroacoustics Conference, 1993.

[70] Zienkiewicz, O. C., and Taylor, R. L. *The Finite Element Method, Volume 1: Basic Formulation and Linear Problems.* McGraw-Hill Book Co., 4th edition, 1989.

Appendix A

APPROPRIATE CHOICES OF BRANCH CUTS

Inside the potential core region and outside the mixing layer, the velocity is uniform. The general solutions, with the imposition of finite jet centerline pressure, are given by

$$\hat{p}_1 = C_1 J_n(\lambda_1 r) \tag{A.1}$$

and

$$\hat{p}_2 = C_2 H_n^{(1)}(i\lambda_2 r) + C_3 H_n^{(2)}(i\lambda_2 r), \tag{A.2}$$

where

$$\lambda_1 = \left[M_j^2 (\omega - \alpha)^2 - \alpha^2\right]^{\frac{1}{2}}, \tag{A.3}$$

$$\lambda_2 = \left\{\alpha^2 - \left(\frac{\rho_2}{\rho_j}\right) M_j^2 \left[\omega - \alpha \left(\frac{W_2}{W_j}\right)\right]^2\right\}^{\frac{1}{2}}. \tag{A.4}$$

J_n is the Bessel function of the first kind of integer order n, $H_n^{(1)}$ and $H_n^{(2)}$ are the Hankel functions of the first and second kind of integer order n respectively, and C_1, C_2, and C_3 are unknown constant coefficients.

In Equation (A.4), the argument of the Hankel function is written as $(i\lambda_2 r)$. To ensure decaying solutions as r approaches infinity, the asymptotic form of the Hankel function for large arguments has to converge to zero. For large arguments, the asymptotic form of the Hankel function is

$$H_n^{(1)}(i\lambda_2 r) \approx (i\lambda_2 r)^{-\frac{1}{2}} \exp\left[i(i\lambda_2 r)\right]. \tag{A.5}$$

The limit of $(i\lambda_2 r)^{-\frac{1}{2}}$ is zero as r approaches infinity. Since λ_2 is a complex number, it can be expressed as $\lambda_2 = \lambda_{2_R} + i\lambda_{2_I}$ where λ_{2_R} and λ_{2_I} are the real and imaginary part of λ_2, and the asymptotic form of the Hankel function can be re-written as

$$H_n^{(1)} \approx \exp\left(-\lambda_{2_R} r\right) \exp\left(-i\lambda_{2_I} r\right). \tag{A.6}$$

The second term, $\exp\left(-i\lambda_{2_I} r\right)$, is a transcendental function, so it is neither growing nor decaying. Hence, the Hankel function can only converge to zero if the limit of the first exponential function, $\exp\left(-\lambda_{2_R} r\right)$, approaches to zero as r approaches infinity. This is only possible if the real part of λ_2 is positive, that is,

$$\lambda_{2_R} > 0. \tag{A.7}$$

In the case when λ_{2_R} is zero, the solution is neutral. To ensure the neutral wave propagates outwards, the phase speed of the neutral wave has to be positive, that is,

$$\left.\frac{dr}{dt}\right|_{\text{constant phase}} > 0. \tag{A.8}$$

To determine the phase speed, the total derivative of the argument of the exponential function is taken so that

$$\lambda_{2_I} dr + \omega dt = 0. \tag{A.9}$$

The phase speed, c, is defined by $c = \dfrac{dr}{dt} = -\dfrac{\omega}{\lambda_{2_I}}$ and, for c to be positive,

$$\lambda_{2_I} < 0. \tag{A.10}$$

The two inequalities, Equations (A.7) and (A.10), will determine the choice of the branch cut for λ_2 in order to ensure decaying or outgoing solution in the limit of infinite r. λ_2 can be expressed as the square root of a complex number, χ, so that

$$\lambda_2 = \sqrt{\chi}, \text{ where } \chi = \left\{\alpha^2 - \left(\frac{\rho_2}{\rho_j}\right) M_j^2 \left[\omega - \alpha\left(\frac{W_2}{W_j}\right)\right]^2\right\}.$$

In complex polar coordinates,

$$\chi = r \exp\left[i\left(\theta + 2k\pi\right)\right], \text{ and}$$

$$\lambda_2 = \sqrt{r} \exp\left[i\left(\frac{\theta}{2} + k\pi\right)\right] = r_0 \exp\left[i\beta\right],$$

where k is an integer. A branch cut,

$$-\pi \leq \theta < \pi$$

is chosen in the principal χ-plane in order to ensure it is single-valued. Therefore, the branch cut in the λ_2-plane is determined by mapping the branch cut of the χ-plane to the λ_2-plane, as shown in Figure A.1.
In this way, the branch cut in the λ_2-plane,

$$-\frac{\pi}{2} \leq \arg(\lambda_2) < \frac{\pi}{2} \tag{A.11}$$

satisfies the inequalities given by Equations (A.7) and (A.10). This ensures that the solutions of the Hankel function is either decaying or outgoing in the limit of infinite distance, r.

As mentioned earlier in Chapter 3, the representation of the argument of the Hankel

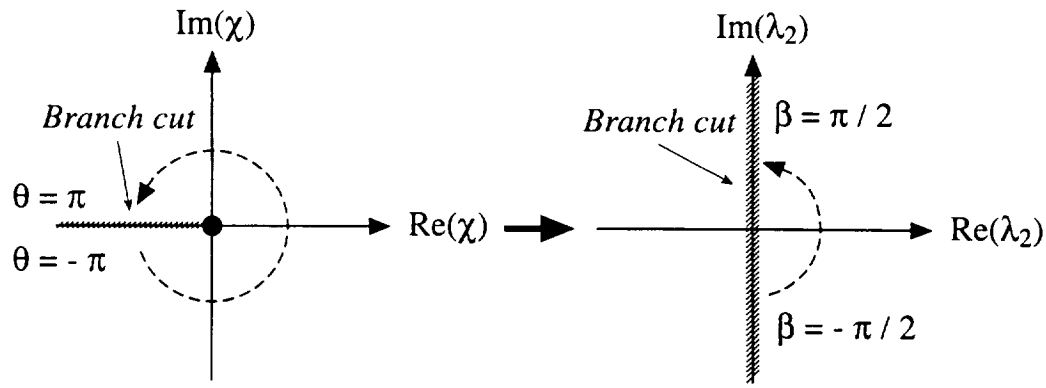

Figure A.1. Mapping of the branch cut from χ-plane to λ_2-plane.

function in Equation (A.4) will determine the appropriate choice of the branch cut. If λ_2 is re-written as

$$\lambda_2 = \left\{ \left(\frac{\rho_2}{\rho_j} \right) M_j^2 \left[\omega - \alpha \left(\frac{W_2}{W_j} \right) \right]^2 - \alpha^2 \right\}^{\frac{1}{2}}, \tag{A.12}$$

so that the general solution outside the mixing layers is given by

$$\hat{p}_2 = C_2 H_n^{(1)}(\lambda_2 r) + C_3 H_n^{(2)}(\lambda_2 r), \tag{A.13}$$

then the appropriate choice of the branch cut is

$$0 \leq \arg(\lambda_2) < \pi \tag{A.14}$$

in order to ensure the condition of decaying or outgoing solutions at infinity.

Appendix B

LOCAL ELEMENT MATRICES

In this appendix, the local element matrices for both the one-dimensional linear line element and the two-dimensional linear triangular element are derived. For both elements, the coefficients are assumed to be piece-wise linear instead of piece-wise constant to improve the accuracy of the solution.

B.1 One-Dimensional Linear Line Element

For any given homogeneous, second-order ordinary differential equation of the form

$$-f^{(1)}\frac{d^2\hat{p}}{dx^2} + f^{(2)}\frac{d\hat{p}}{dx} + f^{(3)}\hat{p} = 0, \tag{B.1}$$

the variational form can be derived accordingly as described in Chapter 3. Using the the interpolation polynomial for a linear line element (as shown in Figure B.1), given by,

$$\hat{p}_h = \alpha_1 + \alpha_2 x, \tag{B.2}$$

the local element matrices for the one-dimensional linear line element can be derived. The interpolation polynomial can re-written in terms of the shape functions, ϕ_1 and ϕ_2, such that

$$\hat{p} = \phi_1 P_1 + \phi_2 P_2 \tag{B.3}$$

where

$$\phi_1 = \frac{X_j - x}{L} \text{ and } \phi_2 = \frac{x - X_i}{L}. \tag{B.4}$$

The resulting local element matrices are

$$\mathbf{K_1} = \int_L \left[\frac{d\phi_j}{\partial x}\left(\phi_l F_l^{(1)}\right)\frac{\partial \phi_i}{\partial x}\right] dx = \frac{1}{L}\begin{bmatrix} F_1^{(1)} & -F_1^{(1)} \\ -F_2^{(1)} & F_2^{(1)} \end{bmatrix}; \tag{B.5}$$

$$\mathbf{K_2} = \int_L \left[\phi_j\left(\phi_l F_l^{(2)}\right)\frac{\partial \phi_i}{\partial x}\right] dx = \frac{1}{6}\begin{bmatrix} \left(-2F_1^{(2)} - F_2^{(2)}\right) & \left(2F_1^{(2)} + F_2^{(2)}\right) \\ \left(-F_1^{(2)} - F_2^{(2)}\right) & \left(F_1^{(2)} + 2F_2^{(2)}\right) \end{bmatrix}; \tag{B.6}$$

$$\mathbf{K_3} = \int_L \left[\phi_j\left(\phi_l F_l^{(3)}\right)\phi_i\right] dx = \frac{L}{12}\begin{bmatrix} \left(3F_1^{(3)} + F_2^{(3)}\right) & \left(F_1^{(3)} + F_2^{(3)}\right) \\ \left(F_1^{(3)} + F_2^{(3)}\right) & \left(F_1^{(3)} + 3F_2^{(3)}\right) \end{bmatrix}. \tag{B.7}$$

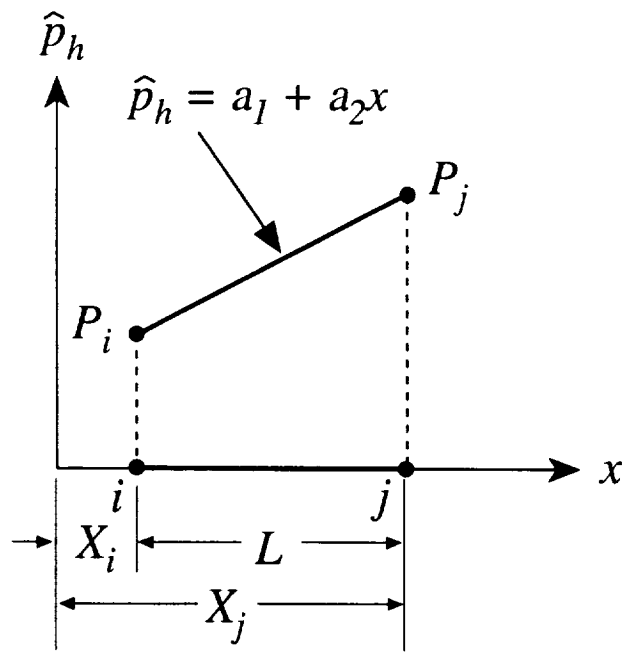

Figure B.1. Linear line element shape function.

B.2 Two-Dimensional Linear Triangular Element

The local element matrices evaluated from Equation (3.25) are given in this section. The shape functions of a linear triangular element are used, as shown in Figure B.2. The interpolation polynomial is given by

$$\hat{p}_h = \alpha_1 + \alpha_2 x + \alpha_3 y, \tag{B.8}$$

and this can be re-written in terms of the shape functions, ϕ_1, ϕ_2, and ϕ_3, such that

$$\hat{p}_h = \phi_1 P_1 + \phi_2 P_2 + \phi_3 P_3 \tag{B.9}$$

where P_1, P_2, and P_3 are the nodal values at each individual element. The shape functions are defined by

$$\phi_1 = \frac{1}{2A_e}(a_1 + b_1 x + c_1 y), \tag{B.10}$$

$$\phi_2 = \frac{1}{2A_e}(a_2 + b_2 x + c_2 y), \tag{B.11}$$

$$\phi_3 = \frac{1}{2A_e}(a_3 + b_3 x + c_3 y), \tag{B.12}$$

where A_e is the area of the triangular element and

$$a_1 = X_2Y_3 - X_3Y_2, \quad b_1 = Y_2 - Y_3, \quad \text{and} \quad c_1 = X_3 - X_2,$$

$$a_2 = X_3Y_1 - X_1Y_3, \quad b_2 = Y_3 - Y_1, \quad \text{and} \quad c_2 = X_1 - X_3,$$

$$a_3 = X_1Y_2 - X_2Y_1, \quad b_3 = Y_1 - Y_2, \quad \text{and} \quad c_3 = X_2 - X_1.$$

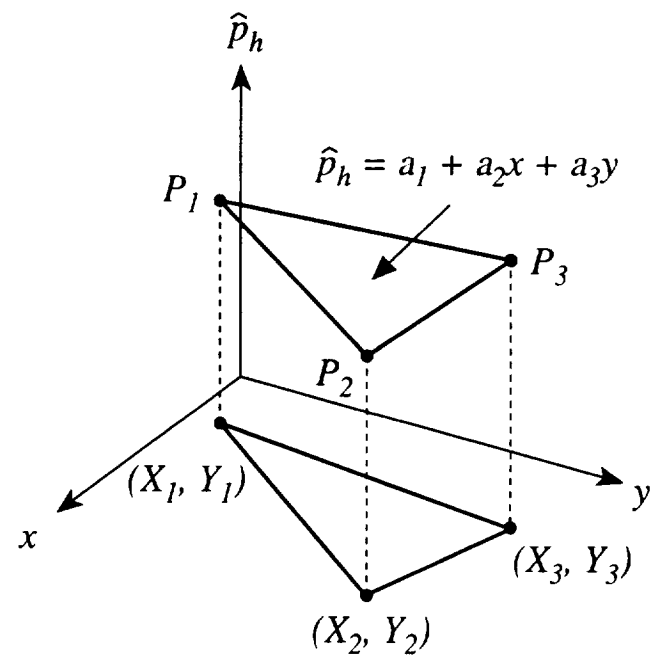

Figure B.2. Linear triangular element shape function.

The local element matrices are calculated by integrating Equation (3.25) analytically using these shape functions. The resulting matrices are given below:

$$\mathbf{K_1} = \int_{A_e} \left[\frac{\partial \phi_j}{\partial x}\left(\phi_l F_l^{(1)}\right)\frac{\partial \phi_i}{\partial x} + \phi_j \left(\frac{\partial \phi_l}{\partial x} F_l^{(1)}\right)\frac{\partial \phi_i}{\partial x}\right] dx\,dy \tag{B.13}$$

$$= \frac{F_1^{(1)} + F_2^{(1)} + F_3^{(1)}}{12A_e}\begin{bmatrix} b_1^2 & b_1b_2 & b_1b_3 \\ b_2b_1 & b_2^2 & b_2b_3 \\ b_3b_1 & b_3b_2 & b_3^2 \end{bmatrix} + \frac{b_1F_1^{(1)} + b_2F_2^{(1)} + b_3F_3^{(1)}}{12A_e}\begin{bmatrix} b_1 & b_2 & b_3 \\ b_1 & b_2 & b_3 \\ b_1 & b_2 & b_3 \end{bmatrix};$$

$$\mathbf{K_2} = \int_{A_e} \left[\frac{\partial \phi_j}{\partial y}\left(\phi_l F_l^{(1)}\right)\frac{\partial \phi_i}{\partial y} + \phi_j \left(\frac{\partial \phi_l}{\partial y} F_l^{(1)}\right)\frac{\partial \phi_i}{\partial y}\right] dx\,dy \tag{B.14}$$

$$= \frac{F_1^{(1)} + F_2^{(1)} + F_3^{(1)}}{12A_e}\begin{bmatrix} c_1^2 & c_1c_2 & c_1c_3 \\ c_2c_1 & c_2^2 & c_2c_3 \\ c_3c_1 & c_3c_2 & c_3^2 \end{bmatrix} + \frac{c_1F_1^{(1)} + c_2F_2^{(1)} + c_3F_3^{(1)}}{12A_e}\begin{bmatrix} c_1 & c_2 & c_3 \\ c_1 & c_2 & c_3 \\ c_1 & c_2 & c_3 \end{bmatrix};$$

$$\mathbf{K_3} = \int_{A_e} \left[\phi_j \left(\phi_l F_l^{(2)} \right) \frac{\partial \phi_i}{\partial x} \right] dx\, dy \tag{B.15}$$

$$= \frac{1}{24} \begin{bmatrix} b_1(2F_1^{(2)} + F_2^{(2)} + F_3^{(2)}) & b_2(2F_1^{(2)} + F_2^{(2)} + F_3^{(2)}) & b_3(2F_1^{(2)} + F_2^{(2)} + F_3^{(2)}) \\ b_1(F_1^{(2)} + 2F_2^{(2)} + F_3^{(2)}) & b_2(F_1^{(2)} + 2F_2^{(2)} + F_3^{(2)}) & b_3(F_1^{(2)} + 2F_2^{(2)} + F_3^{(2)}) \\ b_1(F_1^{(2)} + F_2^{(2)} + 2F_3^{(2)}) & b_2(F_1^{(2)} + F_2^{(2)} + 2F_3^{(2)}) & b_3(F_1^{(2)} + F_2^{(2)} + 2F_3^{(2)}) \end{bmatrix};$$

$$\mathbf{K_4} = \int_{A_e} \left[\phi_j \left(\phi_l F_l^{(3)} \right) \frac{\partial \phi_i}{\partial y} \right] dx\, dy \tag{B.16}$$

$$= \frac{1}{24} \begin{bmatrix} c_1(2F_1^{(3)} + F_2^{(3)} + F_3^{(3)}) & c_2(2F_1^{(3)} + F_2^{(3)} + F_3^{(3)}) & c_3(2F_1^{(3)} + F_2^{(3)} + F_3^{(3)}) \\ c_1(F_1^{(3)} + 2F_2^{(3)} + F_3^{(3)}) & c_2(F_1^{(3)} + 2F_2^{(3)} + F_3^{(3)}) & c_3(F_1^{(3)} + 2F_2^{(3)} + F_3^{(3)}) \\ c_1(F_1^{(3)} + F_2^{(3)} + 2F_3^{(3)}) & c_2(F_1^{(3)} + F_2^{(3)} + 2F_3^{(3)}) & c_3(F_1^{(3)} + F_2^{(3)} + 2F_3^{(3)}) \end{bmatrix};$$

$$\mathbf{K_5} = \int_{A_e} \left[\phi_j \left(\phi_l F_l^{(4)} \right) \phi_i \right] dx\, dy \tag{B.17}$$

$$= \frac{A_e}{60} \begin{bmatrix} 6F_1^{(4)} + 2F_2^{(4)} + 2F_3^{(4)} & 2F_1^{(4)} + 2F_2^{(4)} + F_3^{(4)} & 2F_1^{(4)} + F_2^{(4)} + 2F_3^{(4)} \\ 2F_1^{(4)} + 2F_2^{(4)} + F_3^{(4)} & 2F_1^{(4)} + 6F_2^{(4)} + 2F_3^{(4)} & F_1^{(4)} + 2F_2^{(4)} + 2F_3^{(4)} \\ 2F_1^{(4)} + F_2^{(4)} + 2F_3^{(4)} & F_1^{(4)} + 2F_2^{(4)} + 2F_3^{(4)} & 2F_{11}^{(4)} + 2F_{12}^{(4)} + 6F_{13}^{(4)} \end{bmatrix}.$$

Note that $\mathbf{K_5}$ is locally symmetric.